Observations of Coherence in Bacterial Reaction Centers Using Two-Dimensional Electronic Spectroscopy

by

Veronica R. Policht

A dissertation submitted in partial fulfillment
of the requirements for the degree of
Doctor of Philosophy
(Applied Physics)
in the University of Michigan
2018

Doctoral Committee:

Professor Jennifer P. Ogilvie, Chair
Professor Eitan Geva
Professor Kevin J. Kubarych
Professor Theodore B. Norris
Professor Roseanne J. Sension

Veronica R. Policht

vpolicht@umich.edu

ORCID iD: 0000-0002-1781-7258

DEDICATION

I would like to dedicate this thesis to my family.

ACKNOWLEDGMENTS

I want to begin by thanking Jennifer Ogilvie, my Ph.D advisor, for her hard work, dedication, and guidance throughout the course of my doctoral studies. In addition to running an excellent research lab with exciting experimental apparatuses and projects, Jennifer is an incredibly considerate and empathetic advisor. I feel extremely fortunate to have joined Jennifer's lab my first semester.

I would like to thank my parents, Ann and Rich, for their ongoing support throughout grad school, and for setting a good example of how to a be caring, hard-working (balanced with fun-loving), and ambitious person. I am inspired by my parents as well as my two siblings, Dr. Katie and Alex. I would like to thank Aaron Ross for always being incredibly supportive, for his friendship, and for providing a secluded subbasement space from which I wrote this thesis.

I would like to thank the rest of the Ogilvie group for their help and conversation. Specifically, Seckin Senlik who I shadowed for my first two years of lab and who was my mentor in all things 2D (2DES), coherences, and sample preparation, and Andrew Niedringhaus who was an excellent lab partner on the BRC studies. Jie Pan was a huge help in getting the BRC project off the ground, lending her expertise on BRC sample preparation. Thank you to Frank Fuller, Daniel Wilcox, Yin Song, and Vivek Tiwari for their mentorship and help, and to Anton Loukianov for helpful discussions and diverting conversations. Elizabeth Maret and Riley Sechrist are excellent scientists who challenge me in what I think I understand and are always fun to talk to about hiking and/or Star Trek.

I’m very grateful for the communities I’ve been apart of during grad school, both in- and outside of the physics department. I’ve been very fortunate to have a community of supportive friends that have helped make Ann Arbor into a home. I would also like to acknowledge all the graduate students in the physics department for their dedication and hard work to build and strengthen the community within the department and in the physics community beyond. Specifically, members of the Society for Women in Physics, the Coalition of Students and Student Groups, and the Physics and Applied Physics Graduate Student Councils. I would also like to thank the Graduate Employees Organization, for their dedicated efforts to secure benefits and salary for Graduate Student Instructors, which sets the bar for how Graduate Research Assistants like myself are compensated.

I would like to thank Cagliyan Kurdak, Cyndi Abraham, and Lauren Segall in the Applied Physics Program office for their help and support, as well as Brad Orr and Elise Bodei for their support. Finally, I would like to thank the employees of the University of Michigan Health Services and the Counseling and Psychological Services.

TABLE OF CONTENTS

LIST OF TABLES

LIST OF FIGURES

LIST OF APPENDICES

LIST OF ABBREVIATIONS

2DES – Two-dimensional Electronic Spectroscopy
AOPDF – Acousto-Optic Programmable Dispersive Filter
BBO – β-Barium Borate
BChla – Bacteriochlorophyll a
BPheoa – Bacteriopheophytin a
BRC – Bacterial Reaction Center
BS – Beam Splitter
Chla – Chlorophyll a
CM – Chirped Mirrors
DO – Diffractive Optic
DOPA – Degenerate Optical Parametric Amplifier
DSFD – Double-sided Feynman Diagrams
ESA – Excited State Absorption
FTIR – Fourier Transform Infrared Spectroscopy
GSB – Ground state bleach
LMID – Light-Matter Interaction Diagrams
LO – Local Oscillator
OPA – Optical Parametric Amplifier
PP – Pump probe
SE – Stimulated Emission
SHG – Second Harmonic Generation
TA – Transient Absorption
Ti:Sapphire – Titanium Sapphire
TG – Transient Grating

ABSTRACT

Photosynthesis is the process by which plants and photosynthetic bacteria convert absorbed sunlight into usable chemical energy. In the first steps of photosynthesis, light energy absorbed by molecules embedded in photosynthetic proteins is rapidly transferred to a low-energy state in a type of protein called the reaction center. In the reaction center, this energy then converted into a charge separation which is followed by rapid and efficient movement of an electron out of the protein. Recent observations of coherent oscillatory signals (coherences) in photosynthetic proteins have been suggested to be responsible for the rapidity and efficiency of the energy and charge transfer processes in these systems.

The reaction center of photosynthetic purple bacteria, the Bacterial Reaction Center (BRC), has long served as a model protein for understanding charge transfer processes due in part to the relatively well separated electronic peaks in its absorption spectrum and the availability of many mutants. Coherent oscillations previously observed in the BRC have been attributed to multiple conflicting origins. In this work we characterize the coherences present in the BRC using broadband Two-Dimensional Electronic Spectroscopy (2DES) with a nonlinear light source capable of generating pulses spanning the visible-NIR portion of the BRC spectrum. These 2DES experiments are some of the first to be performed on BRCs which undergo charge separation. Through comparison of

the coherences in the BRC with a monomer of one of its main constituent pigments, Bacteriochlorophyll a (BChla), we assign multiple coherence origins, including those due to excited vibrational modes and those due to vibronic coupling between molecules inside of the BRC. The results presented in this thesis serve as the first direct comparison of monomeric BChla and BRC coherences.

The coherence analysis detailed in this thesis presents several novel results. We significantly observe many prominent coherence modes in monomeric BChla; previous studies of coherence in this system have yielded conflicting reports of few or no coherences. We assign the observed BChla coherences to both excited and ground electronic state vibrational origins. We similarly observe a large number of coherence modes in two BRC mutants. These signals show strong signatures of vibrational coherence, similarly to in BChla, and additionally show signatures which are not explained by either purely vibrational or purely electronic origins. These signatures can be described by a mixed vibrational-electronic, or vibronic, model which has recently been used to describe coherences in a variety of photosynthetic proteins, including the BRC. We assign several of the signatures to the upper excitonic state of the strongly-coupled special pair, which has historically been difficult to resolve directly due to its low oscillator strength and proximity to other broad, strong transitions. The upper excitonic state is better resolved in this work due to vibronic coupling of the special pair states to neighboring monomeric BChla molecules. This vibronic coupling implies a stronger degree of coupling between these molecules than previously thought, providing a new perspective of the BRC as a system in which excitonic states are strongly delocalized over the special pair and monomeric BChla pigments. Accurate modeling of these signatures additionally requires inclusion of special pair charge transfer states. The results presented in this thesis should inform future efforts to model both Bacteriochlorophyll a and BRC electronic structures and the charge separation process in the BRC.

CHAPTER 1 INTRODUCTION

Photosynthesis is the process by which plants and other organisms produce sugars, beginning with the absorption of sunlight. Our current understanding of this complex reaction is the product of nearly two centuries of dedicated research, beginning with the discovery of plant oxygen production by Joseph Priestly in 1775 [1]. The majority of our understanding was developed in the 20th century; in this time ten Nobel prizes were awarded for discoveries related to photosynthesis, including the determination of the structure one of the main light absorbing molecules, chlorophyll a, and the structure of the protein which performs the primary steps of photosynthetic energy conversion in bacteria, called the Bacterial Reaction Center (BRC) [2]. The experiments in the first half of the 20th century determined much about the structure and overall reaction scheme of photosynthesis, but until the development of the laser (Light-amplification by stimulated emission) in the 1960s [3], the detailed mechanism of photosynthetic light-harvesting and energy conversion were limited by low-temporal resolution flash-bulb experiments [2]. With the development of high-power ultrafast (10^{-12} -10^{-15} s timescales) pulsed lasers, we now understand that the primary steps in converting absorbed light energy into chemical energy occur on ultrafast timescales and that the process is highly efficient [2]. As will be described in detail in Section 1.1, the initial steps in converting this absorbed light energy into chemical energy take place in proteins like the BRC which are generally referred to as reaction center proteins. Two types of processes take place in reaction center proteins: downhill electronic energy transfer and charge separation.

There are still many open questions about how the process of energy conversion takes place in reaction center proteins. For example, there is ongoing debate about the exact mechanisms of energy and charge transfer, and we lack a detailed understanding of the electronic structure of the reaction center. These questions are described briefly in Section 1.3 and are also addressed in a recent publication related to the work presented in this thesis [4]. Numerous studies have recently observed long lived oscillatory signals in several photosynthetic proteins, including the BRC; these signals show evidence of long-lived coherence between quantum superposition states [5,6] but we do not yet understand if and how they impact energy and charge transfer processes in photosynthetic proteins. Several studies have suggested that coherences enhance these processes [7], which would have important implications for the fundamental physics taking place in these systems (Section 1.4, Chapter 3). The rapidity and efficiency of energy and charge transfer in the reaction centers have also made photosynthetic protein complexes enticing systems for developing a set of design principles for artificial light harvesting devices [8–11], including dye-sensitized solar cells.

The main focus of this thesis are coherent dynamics in BRCs from photosynthetic purple bacteria *Rhodobacter capsulatus* studied using ultrafast two-dimensional electronic spectroscopy (2DES). Two-dimensional electronic spectroscopy is an ultrafast nonlinear spectroscopy technique which is well suited to observing energy and charge transfer dynamics as well as coherent dynamics [12–14]. In order to better characterize the coherences observed in 2DES of the BRC, we also perform coherence studies on monomeric Bacteriochlorophyll a, the most abundant chromophore in the BRC. We compare the monomer and BRC data within the context of several simple models to gain insight into the physical origin of the coherent signals.

Section 1.1 Introduction to Photosynthesis

Photosynthesis describes a series of photochemical and chemical reactions that take place in a variety of organisms, including plants and certain bacteria, which ultimately uses absorbed light to convert carbon dioxide (CO_2) into carbohydrates. The majority of organisms that perform photosynthesis are photoautotrophs, acquiring the energy they need to live via photosynthesis, though symbiotic organisms like lichen can gather energy by other means. This process of converting and storing absorbed light energy as chemical energy is responsible for the majority of life on Earth, as plants and other photosynthetic organisms sit at the bottom of the food chain.

In photosynthetic bacteria, photosynthesis takes place in and around an intracellular membrane called the intracytoplasmic membrane. In plants, photosynthesis takes place in an organelle called the chloroplast which contain stacks of membrane called the thylakoid membrane. Similar to the mitochondria in many eukaryotic cells the chloroplast has its own genome and is a result of evolutionary endosymbiosis of photosynthetic cyanobacteria [2,15,16]. The membrane is embedded with various protein complexes and delineates distinct intracellular spaces that are used to build up a charge gradient.

Photosynthetic processes are typically divided into reactions which involve the absorption of light and reactions that can take place in the absence of light. The light-driven reactions generate an electron which is used in the phosphorylation of ADP to ATP and hydration of NADP to NADPH. These cofactors are then used in the Calvin Cycle which converts CO_2, or other sources of carbon [17], into sugars. The total reaction is summarized by (1.1),

$$CO_2 + 2H_2A + \hbar\omega \rightarrow [CH_2O] + 2A + H_2O \quad (1.1)$$

where A is an electron donor. In plant photosynthesis, oxygen serves as an electron donor in the only naturally-occurring instance of water-splitting in the water evolving complex in the photosystem II reaction center. Bacterial systems use a variety of electron donors including oxygen, but most are anoxygenic instead utilizing sulfide, molecular hydrogen or similar molecules [2,17]. The focus of this thesis are the initial steps of the light-driven process, where light is absorbed and converted into usable chemical energy.

Light is absorbed by transmembrane proteins containing embedded light-absorbing molecules (also referred to as pigments or chromophores). These complexes are generally referred to as pigment-protein complexes and are categorized into two groups: light-harvesting (LH) or antenna complexes and reaction center proteins (RC). Light-harvesting complexes have a large number of chromophores, often of more than one type, and possess a large absorption cross section to harvest incident light over a broad spectral range. Reaction center proteins have a few chromophores, typically 6 or so, and their primary function is to convert absorbed light energy into a stable charge separation. Photosynthetic organisms live in a variety of environments with different light conditions, for example purple bacteria live near the bottom of lakes and in microbial mats where the incident light is redder than the incident light on the surface where plants live. The adaptation of photosynthetic organisms is reflected in the different photosynthetic machinery used and it is worth noting that not all photosynthetic organisms implement a light-harvesting → reaction center structure [18]. This adaptability is well demonstrated by the great variety in structure and spectral properties of light-harvesting proteins [2,18], whereas reaction center protein structure and function is remarkably conserved across species and types of organisms [15,19].

Light-harvesting complexes are arranged next to reaction centers so that the absorbed energy can be efficiently transferred to the reaction center (Figure 1.1). The arrangement and ratio of light-harvesting proteins and reaction centers is adapted by the cell depending on the light conditions during growth [20]. In the intracytoplasmic membrane of purple bacteria two types of light-harvesting complexes, called Light-

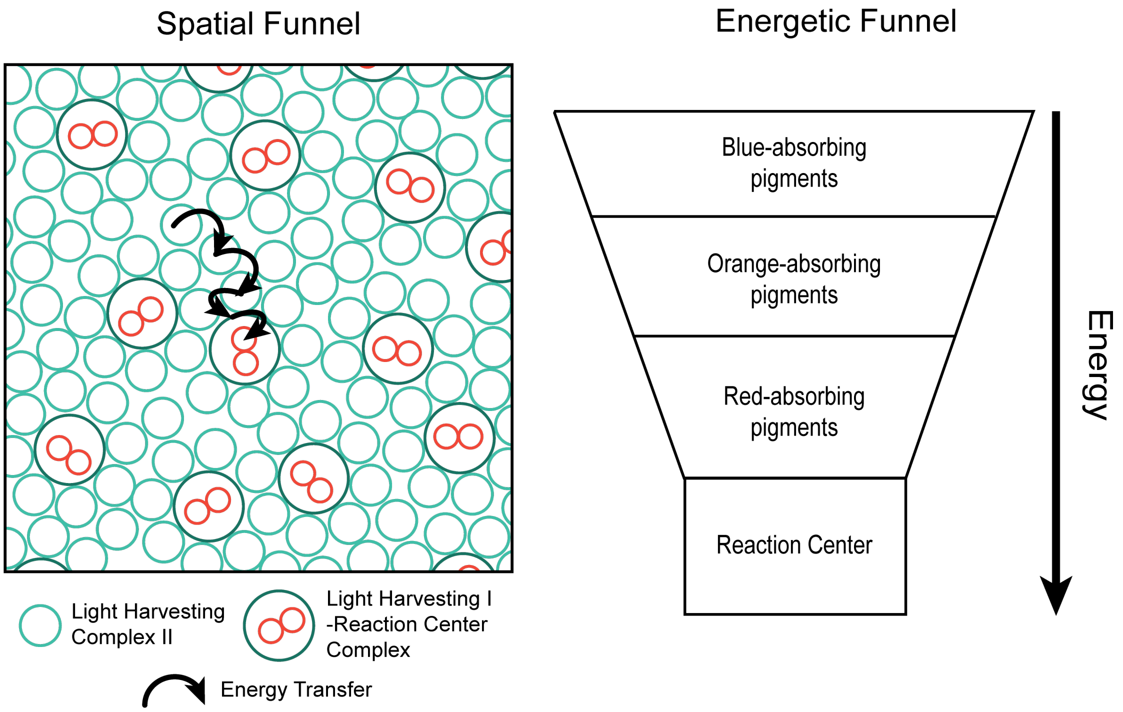

Figure 1.1 Cartoon diagram of spatial configuration of pigment-protein complexes for a purple bacteria (left) and Energy Funnel Diagram (right). (Left) Cartoon of the pigment-protein complexes in the intracytoplasmic membrane of a purple bacteria. Light-harvesting protein complexes (LHI and LH2) surround Reaction Center (RC) proteins, absorbing a large cross section of incident light and rapidly transferring absorbed energy between one another until reaching the RC. The ratio LH:RC depends on light conditions the bacteria is grown in [20]. Membrane figure adapted from [21]. (Right) Energetic funnel of absorbed light in light-harvesting complexes. Funnel figure adapted from [2].

Harvesting Complex I and II (LHI, LHII), are arranged in an antenna-like configuration around reaction center proteins. This arrangement of proteins functions like an energetic and spatial funnel, transferring absorbed energy inward towards the reaction center in a downhill energy fashion (Figure 1.1) [21]. Once the absorbed energy reaches the reaction center, it is rapidly transferred to a low-energy state where it is transformed into a charge separation. The electron of this charge separated state is transferred away from the hole, where it can remain for several tens of milliseconds before charge recombination occurs [2]. Before charge recombination, the electron is transported out of the reaction center and is introduced into the electron transport chain, which produces the cofactors used in the Calvin Cycle. In wild type BRCs the quantum efficiency of removing an electron following absorption of light is nearly unity [2], making this initial light-driven process extremely efficient.

Photosynthetic energy transfer processes occur on ultrafast (10^{-12} – 10^{-15} s, picosecond – femtosecond) timescales. Intra-protein energy transfer in LHI complexes occurs in a few ps [22] and inter-protein energy transfer from light-harvesting complexes to the reaction center proceeds within 10-100 ps [8,23]. In the BRC, the conversion of the absorbed energy to a charge separation is complete in a few ps, with downhill energy transfer taking place within a few hundred fs [2,4]. The details of the energy and charge transfer kinetics will be discussed in the following section.

Section 1.2 The Bacterial Reaction Center

Function & Structure

The Bacterial Reaction Center (BRC) (Figure 1.2) is a large multidomain transmembrane protein found in the intracytoplasmic membrane of photosynthetic purple bacterial [2]. Embedded in BRC protein domains L and M, or A and B in reference to charge separation, are 6 bacteriochlorin molecules, two ubiquinones, a carotenoid, and an iron ion. The 6 bacteriochlorins and two ubiquinones are arranged into two nearly mirror-symmetric branches. The two branches of chromophores are about ~24 Å across the BRC and ~31 Å from the special pair to the quinone [24]. Four of the six bacteriochlorins are Bacteriochlorophyll a (BChla) molecules and the remaining two are Bacteriopheophytin a (BPheoa) molecules, which are similar in structure to BChla but lack the central magnesium ion. These 6 bacteriochlorin molecules are weakly Coulombically coupled to one another via dipole-dipole interactions and are weakly coordinated to the surrounding amino acids.

Moving from the top to bottom of the BRC structure in Figure 1.2, two strongly coupled BChla molecules are referred to as the Special Pair or P (previously have been referred to as D). The Special Pair are the most strongly coupled out of any of the bacteriochlorins; this strong coupling is attributed to the small separation between the two molecules and their near parallel alignment [24], such that their electronic transitions are excitonically split and delocalized across the two molecules. Excitonic splitting occurs when electronic coupling strengths, J, perturb the electronic transition energies of the interacting molecules' site energies, ε_n and ε_m, to excitonic energies defined by $\varepsilon_{\pm} = 1/2(\varepsilon_n + \varepsilon_m) \pm \sqrt{(\varepsilon_n - \varepsilon_m)^2 + 4J^2}$ [25,26]. Two more BChla molecules with localized electronic character are referred to as the monomeric BChla or B. Two Bacteriopheophytin a molecules are referred to as H (previously have been referred to as Φ). In most models of the electronic structure of the BRC, the special pair electronic transitions are very delocalized across both special pair BChlas as well as the neighboring

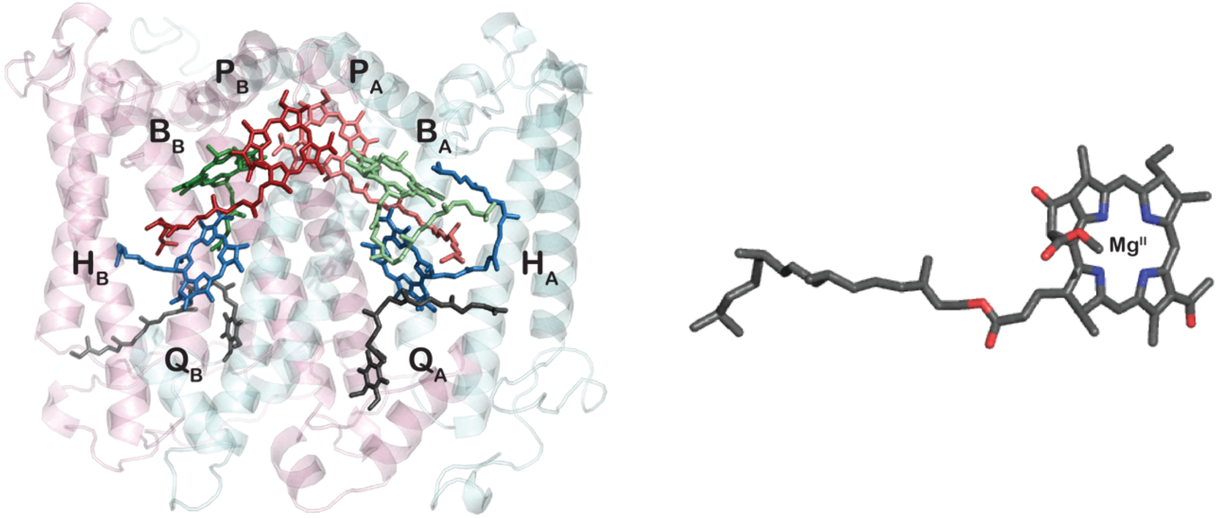

Figure 1.2 Structure of the Bacterial Reaction Center (BRC) and Bacteriochlorophyll a (BChla). (Left) BRC structure highlighting the two protein domains which contain 6 bacteriochlorins and 2 quinone molecules, labeled as described in the text. (Right) Structure of a BChla molecule (More detailed structure in Figure 4.1). Structure from 2.6 Å X-ray crystallography of neutral BRC of *Rhodobacter sphaeroides.* Carotenoid and Iron ion not pictured. Figure produced from Protein Data Bank entry 1AIJ using PyMOL.

monomeric BChlas (B) and are referred to as the excitonic transitions P_{-}^{*} and P_{+}^{*} [27]. The B and H molecules are more electronically localized such that the 4 other excitonic basis states are commonly referred to by their dominant site basis states contributors (B_A^*,B_B^*,H_A^*,H_B^*) [27].

The linear absorption spectra for a BRC mutant W(M250)V and BChla in isopropanol are shown in Figure 1.3. Figure 1.3 shows the lowest energy electronic transitions, the Qy band, for BChla and the BRC. These transitions span the visible to near-IR spectra and are the electronic states most involved in the light-dependent steps of photosynthesis. The three groupings of bacteriochlorins, P*, B*, and H*, have distinct electronic bands listed in order of increasing transition energy. The lower-excitonic peak of the special pair (P_{-}^{*}) forms the lowest energy state in the BRC; the upper-excitonic peak of the special pair (P_{+}^{*}) is very weak and has been historically difficult to identify [4].

When energy is transferred into the reaction center from a neighboring light harvesting complex, or the RC absorbs light directly, the energy is rapidly transferred in a downhill energy fashion (similar to in Figure 1.1) to the lower-exciton state of P (P_-*), which serves as an energetic trap, within a few hundred fs. After energy transfer to P_-* a charge separated state forms and an electron is transferred to the L-side quinone ($P^+Q_A^-$). While energy transfer to P_-* occurs along either branch of chromophores, charge transfer only occurs along one branch nearly 100% of the time in wild type (WT) BRCs. Because of this functional asymmetry, the pigments near the L-domain are referred to as the Active branch (A) and the other branch is labeled (B) (Figure 1.1). The excitonic states with dominant contributions from the A- and B-branch monomeric BChlas (B_A*,B_B*) and

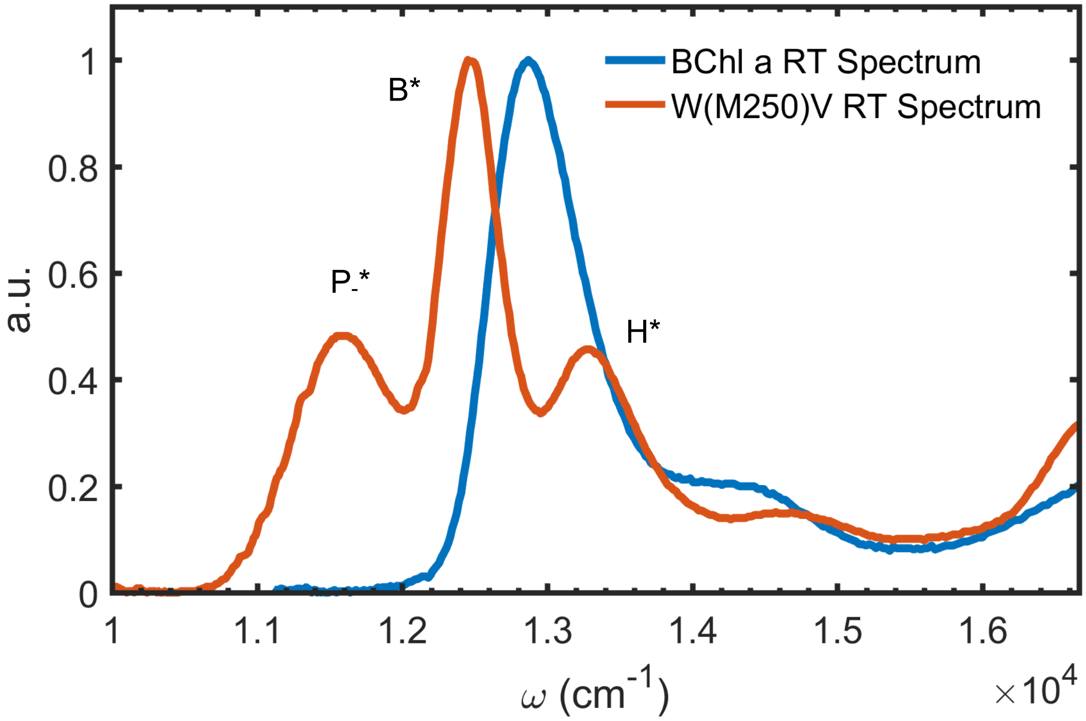

Figure 1.3 Room temperature linear absorption spectrum of W(M250)V BRC (orange) and BChla in isopropanol (blue). The BChla Qy band is peaked near 12,700 cm^{-1} with a vibrational shoulder. The BRC shows three distinct Qy bands which correspond to three groupings of bacteriochlorins present in the BRC, the P_-*, B*, and H* bands listed in order of increasing transition energy.

BPheoas (H_A*,H_B*) have nearly degenerate electronic transition frequencies but slight differences in the branches' protein environments perturb the individual chromophores such that they are distinguishable [28]. The electronic transitions of B_A* and B_B* exhibit moderate Stark shifts of a few hundred wavenumbers following charge separation [4,29–31], with the Stark shift of the A-branch B* transition larger than the B-branch. The final step in this cyclic process of energy and charge transfer is the reduction of P^+ by cytochrome c_2 [32].

The asymmetry in charge transfer has been a topic of intense study, with several biochemistry groups working to develop BRC mutants that could activate energy transfer along the B-branch to attempt to understand the origin of the asymmetry. One result of attempts to activate B-branch charge transfer is a mutant lacking the A-branch BPheoa called D_{LL} [33,34], which does not perform any charge separation due to shifting of the oxidative potentials into an energetically unfavorable configuration [35]. The D_{LL} BRC mutant does, however, perform downhill energy transfer among the chromophores present. The W(M250)V BRC mutant of *Rhodobacter capsulatus* (Figure 1.3) is missing the primary electron acceptor (Q_A) achieved by a single point mutation. This mutant functions similarly to wild-type BRCs and charge separation proceeds to form the $P^+H_A^-$ charge separated state while avoiding a long lived $P^+Q_A^-$ state that would make data acquisition difficult with our experimental apparatus [36]. Both the D_{LL} and W(M250)V BRC mutants for *Rh. capsulatus* purple bacteria are studied and discussed in this thesis. The D_{LL} BRC serves as a control for signatures of A-branch charge separation, whereas the W(M250)V BRC mutant allows us to study WT energy and charge transfer dynamics with high repetition-rate spectroscopic experiments.

Section 1.3 Recent Research Developments & Present Questions

Much of the summary from the previous section is the result of several decades of research on BRCs using various spectroscopic techniques. Antenna proteins and reaction centers from purple bacteria have long served as model systems for understanding photosynthetic energy and charge transfer generally. Some of the reasons are experimental; the BRC was the first of any membrane protein to be successfully crystalized [37] and there are many high-resolution X-ray crystallography structures [24,37,38] available on databases like the Protein Data Bank. Additionally, the BRC genome is well understood and numerous mutant strains of the BRC have been developed and well characterized [33,35,39,40]. From a more fundamental perspective, the BRC is easier to study than its plant analogue, the PSII D1D2 Reaction Center (PSII RC); despite very similar structure and functions, the PSII RC linear absorption spectrum shows a much higher degree of spectral congestion than the BRC. All Chlorophyll a (Chl a) and Pheophytin a (Pheo a) molecules in the PSII RC absorb in a relatively narrow peak. For these reasons, the BRC is a good model for studying photosynthetic energy and charge transfer. While our understanding of the structure and function of the BRC has advanced greatly in the past few decades, there are still topics of debate and unanswered questions that require further study. As spectroscopic and theoretical tools have advanced, researchers have returned repeatedly to the BRC as a model system to improve our understanding of photosynthetic charge separation.

Special Pair Spectral Assignment

The special pair (P) is a dimer of strongly coupled Bacteriochlorophyll a (BChla) molecules with excitonic character (Figure 1.2). Because of the orientation of each

BChla's transition dipole moment, the lower of the excitonic peaks has a much stronger transition dipole strength than the upper excitonic peak, as evident in Figure 1.3. Because of its weak dipole strength and the presence of other electronic transitions in the same region (spectral congestion) as the upper excitonic P band (P_+*) has been difficult to assign a transition frequency. A contributing factor to this difficult is that the upper and lower excitonic states are primarily delocalized across the two BChla molecules [27] and rapidly transfer energy between one another via internal conversion.

Many experimental studies have attempted to locate P_+* using various spectroscopy methods and several theoretical studies have attempted to model the electronic structure of the special pair by using X-ray crystallography-determined structures. Despite all these studies, the location of P_+* as well as the coupling strength that gives rise to these excitonic peaks is still a matter of debate. Generally though, the coupling strength is thought to be on the order of $J \cong 276 - 400\ cm^{-1}$ at room temperature [27,41] with P_+* assignments in the range of 11,905 – 12,121 cm^{-1} (825 – 840 nm) at room temperature [27,41]. At cryogenic temperatures, the P_-* band red shifts indicating an increased coupling of $J \cong 500 - 618\ cm^{-1}$ [27], which is generally attributed to decreased interchromophore spacing [27]. P_+* is assigned in the range of 12,225 – 12,642 cm^{-1} (791 – 818 nm) at these cryogenic temperatures [27,33,42–44]. These assignments for P_+* are in the spectral region of the strong B*-band (Figure 1.3) making it difficult to resolve these features even with multidimensional spectroscopy techniques.

It has been shown that including charge transfer states in simulations of the special pair electronic structure leads to electronic band shifts [45]; none of the theoretical studies mentioned above take charge transfer states into account. It has also been demonstrated experimentally that the choice of detergent for the buffer solution of BRCs samples can perturb the electronic transitions of the special pair by nearly 300 cm^{-1} (20 nm) [36]. In our recent work studying energy and charge transfer in the BRC at 77 K, we assigned the P_+* to 11,900 cm^{-1} by fitting the linear absorption spectrum and 2DES spectra simultaneously [4]. This assignment for P_+* is much lower in energy than previous assignments of P_+*, but is additionally supported by independent analysis of the coherent signals described in this thesis (Discussed in Chapters 5 & 6).

Energy & Charge Transfer Pathways

A large body of spectroscopic research on photosynthesis has been devoted to uncovering the ultrafast population dynamics in the BRC using ultrafast transient absorption and multidimensional spectroscopies. Recounting the progress made in understanding these processes is outside the scope of this thesis, but we will briefly discuss the recent debates regarding energy and charge transfer. The reader is referred to several review papers for a more complete discussion [46–50]

Figure 1.4 shows the energy and charge separation pathways and rates for the W(M250)V BRC from *Rhodobacter capsulatus* determined from 2DES via a multiexponential global fitting approach [4]. These are the results of a sister study to the

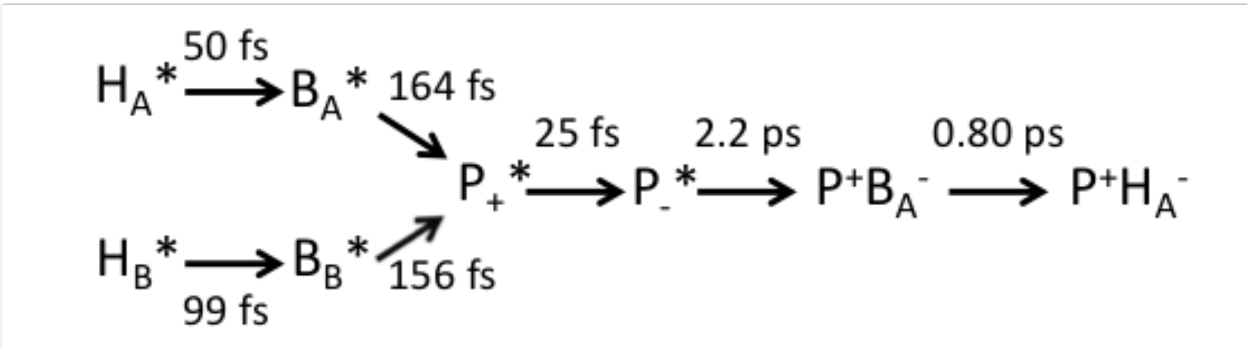

Figure 1.4 Energy and Charge Transfer Pathways and Rates for the BRC. From Niedringhaus, et al. [4].

coherence data presented in this thesis. The left half of the diagram in Figure 1.4 details the rates and pathways of the downhill energy transfer process which reaches the low-energy P_-^* within a few hundred fs; these results are in good agreement with previous observations of energy transfer in the BRC though the internal conversion rate (25 fs) is faster than previous proposals which had reduced time resolution [4].

The latter half of the diagram in Figure 1.4 details the charge separation pathways and rates. This study found that the data was fit well using this single sequential model of charge separation [4], contrary to recent proposals of multiple possible charge separation pathways [51–55]. Charge separation begins on the special pair (P_-^*) and proceeds to move the electron to the A-branch monomeric BChla followed sequentially to transfer to the A-branch BPheoa. In this study, Q_A was removed to prevent the buildup of the $P^+Q_A^-$ state, which has a 1 ms lifetime.

Coherent Oscillatory Signals

In the early 1990s, the ultrafast pump-probe spectroscopy group of Jean-Louis Martin observed coherent oscillatory signals (coherences) in several BRC mutants which remained coherent for several picoseconds at cryogenic temperatures [5] and room temperature [56]. These and follow-up studies' [5,57–63] observations were assigned to quantum superposition states of delocalized vibrations on the special pair BChla molecules and the surrounding protein [57]. The presence of vibrational coherences which persisted on the same timescales as charge separation was striking as it posed the question that they may be important to charge transfer processes. Additionally, these terms were expected to decohere rapidly due to the protein and solvent environments surrounding the BChla molecules. These conclusions are contrasted with more recent observations of coherence in BRCs using 2DES, which have either proposed the oscillatory signals resulted from quantum superpositions of electronic states [58,59] or superpositions of states that showed significant mixing between electronic and nuclear (vibrational) degrees of freedom [60–63]. A more detailed description of the results of these studies is discussed in Chapter 3 and Chapter 5.

At this point, most experiments studying coherences in the BRC have only examined portions of the Qy spectrum (the B*- and H*-bands together, or the P*-band). The work presented in this thesis presents 2DES coherence results covering nearly the entire Qy band of the BRC. In addition, most of the previous studies have examined the oxidized BRC, which does not perform charge separation. By comparing the coherence signals observed in the BRC with similar studies of BChla we will be able to better determine the physical origin of the coherence dynamics in the BRC.

Section 1.4 Coherences in Photosynthetic Systems

In the late 2000s a series of 2DES experiments on the Fenna-Matthews-Olson (FMO) antenna complex of green sulfur bacteria observed long lived coherences at cryogenic [6] and room temperatures [64]. The coherent signals from these studies were attributed to superposition states of excitonic states given the apparent match between the frequency of the oscillatory signals and exciton difference frequencies from electronic structure models of the FMO. These studies started a wave of experimental and theoretical work investigating the origins and implications of coherent dynamics in photosynthetic protein complexes. These efforts have been well summarized in several review articles [7,8,13] and will be discussed in more detail in Chapter 3.

The excitement regarding coherences in photosynthetic proteins was generated by proposals that coherences could be functionally important for ultrafast energy transfer in light-harvesting proteins and for the ultrafast and efficient energy and charge transfer in reaction center proteins [7,8]. Some studies have proposed that the superposition states of delocalized electronic states could more efficiently sample the environmental fluctuations to seek out the most energetically favorable path, or even employ pathway interference to enhance energy transfer efficiency. These studies differ in the degree to which coherence is preserved by the surrounding protein [58,64–66]. Not long after the 2DES studies of coherence in the FMO, several 2DES studies observed oscillatory signals due to vibrational coherences which showed similar behavior as the signals assigned as electronic coherence in the FMO [67,68]. Several groups then proposed a third model of coherences which involved superposition states of an electronically coupled dimer with excited state vibrational modes. This proposed mixed vibrational-electronic, or vibronic, model was proposed in part because of the observation that coherence frequencies matched known vibrational frequencies as well as exciton difference frequencies [26,69,70]. In vibronic coupling, where coupling between states results in mixing between electronic and vibrational degrees of freedom, an excitonic energy gap between two states is bridged resonantly by a vibrational mode. The vibrationally-assisted resonance has been shown to enhance energy transfer in simulations of plant reaction center dynamics [71,72]. It is still unclear whether these proposed effects are present, due to inherent approximations in the models used, and difficulties in interpreting the data in these spectrally congested systems. In the case of vibronic coupling, it may be true that the coupling enhances energy transfer, but it is not clear whether coherence is necessary to produce that enhancement.

While coherences have been observed in photosynthetic proteins at room temperature [56,63,64] the majority of coherence studies are conducted at cryogenic temperatures where homogeneous widths are narrower and perturbations from the solvent and protein environments are smaller. The observation of coherences primarily at cryogenic temperatures and the fact that these studies are performed using coherent pulsed light have called into question whether or not the coherent dynamics observed using these methods could actually be functionally relevant. The broadband coherent excitation used in 2DES experiments on vibronically coupled systems leads to readily observed coherent dynamics. These coherent dynamics may reflect functionally important electronic-vibrational resonances, but are more likely not representative of the dynamics that are initiated by the absorption of sunlight. This question remains a matter of debate [73–75].

Section 1.5 Thesis Overview

There is much we can learn about photosynthesis by studying coherences. Coherences can tell us about the electronic and vibrational structure in systems with weak or dark transitions [76] and help us understand how models of electronic structure fall short for both the BRC (discussed in Chapter 6) and molecules [77,78]. Additionally, studying how coherences are affected by and affect the structure of a system may help us to design more efficient artificial light harvesting devices [7,8,10,11].

Chapter 2 describes the theory and experimental setup of Two-dimensional electronic spectroscopy (2DES) and describes the basic signals we observe. Chapter 3 provides an overview of coherence signals, including several key models used in simulating and interpreting 2DES coherence data: the purely-vibrational displaced oscillator, purely-electronic electronic dimer, and the mixed vibrational-electronic vibronic models. Chapter 3 also reviews previous observations of coherences in the Bacterial Reaction Center and monomeric Bacteriochlorophyll a. In Chapter 4 and Chapter 5 we present 2DES results on Bacteriochlorophyll a and BRCs and present our analysis of the coherences signals in each system. In Chapter 6 we compare the coherence signals of these two systems and discuss observations of vibronic coupling in the BRC. Chapter 7 provides a brief summary of this thesis and proposes several experiments to follow-up on the work presented.

CHAPTER 2 TWO-DIMENSIONAL ELECTRONIC SPECTROSCOPY

The experimental challenges inherent in studying photosynthetic energy and charge transfer - including ultrafast timescales, large inhomogeneous broadening, and spectral congestion - have made it historically difficult to characterize these systems. Ultrafast transient absorption spectroscopies, which measure the temporal evolution of a given system by probing the third order nonlinear material polarization, could achieve the necessary time resolution using pulses with duration on the order of tens of fs. This method suffers, however, from time-frequency uncertainty, either retaining time resolution using spectrally broad pump and probe pulses but losing certainty of which transition was excited or using narrowband pump pulses with longer temporal width and therefore lower temporal resolution. Two-dimensional electronic spectroscopy (2DES) is a method which studies the same types of signals as transient absorption spectroscopy but with an additional frequency axis due to the addition of a second pump pulse. The time-domain Fourier transform version of this method allows for simultaneous high frequency and high temporal resolution and is well suited to studying photosynthetic energy and charge transfer processes. 2DES is a type of multidimensional spectroscopy particularly suited for studying electronic dynamics.

2DES was developed in the late 1990s [12,79] based on a vibrational analogue, two-dimensional infrared spectroscopy, which in turn was based on Nuclear Magnetic

Resonance techniques. 2DES is a four-wave mixing experiment whereby a series of three pulses measures the temporal dynamics of an induced electronic nonlinear material polarization in a system (Figure 2.1) by scanning interpulse delay times and Fourier transforming into the frequency domain. Fourier transforming with respect to the first time delay between two pump pulses, t_1, yields the excitation frequency axis, ω_1; the detection axis, ω_3, is directly measured in a spectrometer using a heterodyne detection technique called spectral interferometry [80]. This allows us to track the electronic dynamics as a function of excitation and detection frequencies for a given t_2 delay.

This chapter will review the basic theory of the 2DES method, will discuss the experimental apparatus and broadband pulse generation techniques using nonlinear optics, and will briefly review the 2DES signal analysis. For a more detailed theoretical treatment, the reader is referred to several texts on nonlinear optics [81], ultrafast optics [82], quantum optics [83], and nonlinear spectroscopies [14,84–86].

Section 2.1 Theory

Semiclassical Response Theory

Two-dimensional electronic spectroscopy measures the third-order nonlinear material polarization, $\boldsymbol{P}^{NL}(t)$, through a series of three interactions of the electric field of the exciting laser pulses, $\boldsymbol{E}(t)$, with the material, approximated as an electric dipole in most formulations of 2DES. The standard formalism in describing the theory of 2DES uses semiclassical response theory, treating the electric field classically and the material quantum mechanically. In this discussion, the material will be described in the density matrix representation, ϱ_{ij}, where indices i and j correspond to eigenstates represented by the ket, $|i\rangle$, and bra, $\langle j|$. This representation is particularly useful for describing the

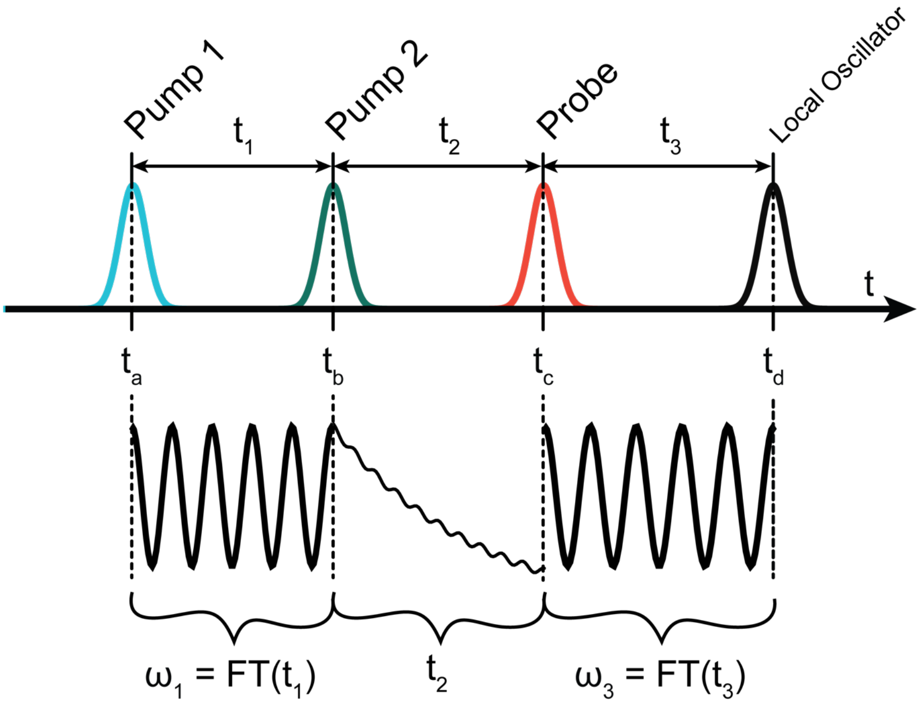

Figure 2.1 Pulse sequence used in 2DES. Three pulses, two pumps and a probe, induce a third order polarization generating a signal which is heterodyne detected with a fourth pulse serving as a local oscillator. A 2DES spectrum for a given t_2 is collected by scanning the inter-pump time, t_1, and detecting the emitted signal at t_3; Fourier transformation of t_1 yields the excitation frequency axes, ω_1, and the detection frequency axes, ω_3, is detected directly in a spectrometer. Scanning the waiting time, t_2, allows for detection of dynamical behavior.

evolution of the system using the Liouville formalism, in which the Hamiltonian is commuted with the density matrix, such that the system can be acted on by the ket or bra sides;

$$\begin{aligned}\frac{d}{dt}\varrho &= -\frac{i}{\hbar}\left[\hat{H}\varrho - \varrho\hat{H}\right] \\ &= -i\hat{\mathcal{L}}\varrho\end{aligned} \qquad (2.1)$$

where $\hat{\mathcal{L}}$ is the Liouville superoperator. Just as the Hamiltonian is often grouped into the material component, the perturbative interaction component, and system-bath coupling, so can the Liouville superoperator be grouped.

The material polarization can be described by expanding in a power series with respect to the incident electric field in the frequency domain, $\boldsymbol{E}(\omega)$,

$$\boldsymbol{P}(\omega) = \epsilon_0\left(\chi^{(1)}\boldsymbol{E}(\omega) + \chi^{(2)}\boldsymbol{E}^2(\omega) + \chi^{(3)}\boldsymbol{E}^3(\omega) + \cdots\right) \qquad (2.2)$$

$$
\begin{aligned}
&= \boldsymbol{P}^{(1)}(\omega) + \boldsymbol{P}^{(2)}(\omega) + \boldsymbol{P}^{(3)}(\omega) + \cdots \\
&= \boldsymbol{P}^{(1)}(\omega) + \boldsymbol{P}^{NL}(\omega)
\end{aligned}
$$

where susceptibility, $\chi^{(n)}$, represents the material response. Expressions for each order of $\boldsymbol{P}^{(n)}(\omega) = \epsilon_0 \chi^{(n)} \boldsymbol{E}^n(\omega)$ can be derived using a perturbative approach with the electromagnetic wave equation in Equation 2.3 to solve for orders of $\chi^{(n)}$. The linear polarization term, $\boldsymbol{P}^{(1)}(\omega) = \epsilon_0 \chi^{(1)} \boldsymbol{E}(\omega)$, is responsible for linear absorption and for linear dispersion, or the linear index of refraction. The second order term, $\boldsymbol{P}^{(2)}(\omega)$, is only nonzero in noncentrosymmetric materials due to inversion symmetry and is responsible for second harmonic generation and other three-wave mixing processes. The systems studied in this manuscript are isotropically oriented molecules and protein complexes so $\chi^{(2)}$ is neglected. The third order term, $\boldsymbol{P}^{(3)}(\omega)$, is responsible for four wave mixing as observed in pump-probe and 2DES spectroscopies, as well as third harmonic generation and cross wave polarization. The nonlinear polarization, $\boldsymbol{P}^{NL}(\omega)$, is also responsible for effects such as self-focusing and self-phase modulation that lead to supercontinuum generation. Nonlinear susceptibilities, χ^{NL}, are very weak; in condensed matter $\chi^{(2)} \sim 10^{-12}\, m/V$ and $\chi^{(3)} \sim 10^{-24} \left(\frac{m}{V}\right)^2$, with higher order susceptibilities decreasing in strength in a similar fashion. The linear susceptibility, however, is on the order of 1; we are not able to study temporal electronic dynamics but only absorptive and dispersive properties with this term. Thus, to study the electronic dynamics, the susceptibility with the largest signal strength is the third order term. Higher order terms have been studied in other spectroscopies but will not be discussed here.

Time-domain experiments measure the optical response function of a material via an induced polarization, $\boldsymbol{P}(\boldsymbol{r}, t)$, which is related to susceptibility via Fourier transformation. The induced polarization acts as the source term in the electromagnetic wave equation, which generates a signal field that we can measure, $\boldsymbol{E_s}$,

$$\nabla^2 \boldsymbol{E_s}(\boldsymbol{r},t) - \mu_o \epsilon \frac{\partial^2}{\partial t^2} \boldsymbol{E_s}(\boldsymbol{r},t) = \mu_0 \frac{\partial^2}{\partial t^2} \boldsymbol{P}(\boldsymbol{r},t) \qquad (2.3)$$

where ϵ is the material dielectric response, $\epsilon = (1+\chi)\epsilon_0$. Solutions to the homogeneous form of the wave equation in vacuum are electromagnetic plane waves of the form

$$\boldsymbol{E}(\boldsymbol{r},t) = \hat{\boldsymbol{e}} E_0 e^{-i\omega t + i\boldsymbol{k}\cdot\boldsymbol{r} + i\phi} + c.c. \quad (2.4)$$

where ω is the frequency of the plane wave oscillation, $\boldsymbol{k}$ is the wave vector, ϕ is some arbitrary phase factor, and $\hat{\boldsymbol{e}}$ is the polarization direction. From here on we will neglect the polarization direction of the electric fields and the transition dipole moments.

For an arbitrary n^{th}-order of the polarization, the time-dependent polarization depends on the sample response function, $S^{(n)}(t_n, t_{n-1}, \dots, t_1)$, as well as the n electric fields from each individual light-matter interaction [14]

$$\begin{gathered} P^{(n)}(t) = \int_0^\infty d\tau_n \int_0^\infty d\tau_{n-1} \int_0^\infty d\tau_1 S^{(n)}(t_n, t_{n-1}, \dots, t_1) \quad (2.5) \\ \times E(t-\tau_n) E(t-\tau_n-\tau_{n-1}) \dots E(t-\tau_n-\tau_{n-1}-\dots-\tau_1) \end{gathered}$$

where τ_n are the absolute interaction times of each light-matter interaction. The n^{th} order response function, $S^{(n)}(t_n, t_{n-1}, \dots, t_1)$, includes the material response and is related to the n^{th} order susceptibility. Using Liouville formalism to represent the quantum system, the response function is given by

$$S^{(n)}(t_n, t_{n-1}, \dots, t_1) = \left(\frac{i}{\hbar}\right)^n Tr[\hat{\mu} U_{mat}(\tau_n) \mathcal{V}_{\mathrm{n}} U_{mat}(\tau_{n-1}) \mathcal{V}_{\mathrm{n-1}} \dots U_{mat}(\tau_1) \mathcal{V}_1 \hat{\varrho}_{eq}] (2.6)$$

where $\hat{\mu} = \boldsymbol{n} \cdot \hat{\boldsymbol{\mu}}$ is the transition dipole oriented along the $\boldsymbol{n}$ direction of a given incident electric field, $U_{mat}(\tau_n) \equiv \exp(-i\mathcal{L}_{mat} t)$ is the free evolution operator that describes how the system behaves between pulses and is defined by the material Liouville superoperator, $\mathcal{L}_{mat}$, which is a construct of the material Hamiltonian, $\hat{H}_{mat}$, defined as

$$\mathcal{L}_{mat} \hat{A} = \frac{1}{\hbar} [\hat{H}_{mat}, \hat{A}] \quad (2.7)$$

In Equation 2.6, $\hat{\varrho}_{eq}$ is the equilibrium density matrix state before the perturbation, usually taken to be in the ground state $\hat{\varrho}_{eq} = |g\rangle\langle g|$, and, finally, $\mathcal{V}_n$ is the transition dipole superoperator which is describes the interaction of the n^{th} electric field with the material transition dipole, defined in the interaction Liouville superoperator,

$$\mathcal{L}_{int}\hat{A} = -\frac{1}{\hbar}\left[\hat{\mu}, \hat{A}\right]E(t) = -\hat{\mathcal{V}}\hat{A}E(t) \quad (2.8)$$

The expression inside the trace of Equation 2.6 describes the successive action of electric fields, first acting on the equilibrium system $\hat{\varrho}_{eq}$ with transition dipole superoperator $\mathcal{V}$, followed by system evolution during τ, repeated by additional fields moving right to left. Taking the trace of the equilibrium state acted upon by the transition dipole superoperators and evolution operators extracts only those pathways that end in a population, generating a correlation function. If we assume the electric field interactions are sufficiently short that they can be described by a delta function we can work in the impulsive limit and make a change of variable to the time between light matter interactions. The third order polarization from the expression in Equation 2.5 then becomes

$$\begin{gathered} P^{(3)}(t) = \int_0^\infty d\mathrm{t}_3 \int_0^\infty d\mathrm{t}_2 \int_0^\infty dt_1 S^{(3)}(\mathrm{t}_3, \mathrm{t}_2, \mathrm{t}_1) \qquad (2.9) \\ \times E(t - \mathrm{t}_3)E(t - \mathrm{t}_3 - t_2) \ldots E(t - \mathrm{t}_3 - \mathrm{t}_2 - \mathrm{t}_1) \end{gathered}$$

with response function

$$\begin{gathered} S^{(3)}(t_3, t_2, t_1) = i^3 Tr\left[\hat{\mu}_4 U_{mat}(t_3)\mathcal{V}_3 U_{mat}(t_2)\mathcal{V}_2 U_{mat}(t_1)\mathcal{V}_1\hat{\varrho}_{eq}\right] \quad (2.10) \\ = \left(\frac{i}{\hbar}\right)^3 \theta(t_3)\theta(t_2)\theta(t_1) \times \sum_{\alpha=1}^{4} \left(R_\alpha(t_3, t_2, t_1) - R_\alpha^*(t_3, t_2, t_1)\right) \end{gathered}$$

where Equation 2.10 results from expansion of the operators in Equation 2.6. $\theta(t_n)$ are Heaviside functions to enforce temporal ordering of the three electric field interactions. The system response functions are given by R_α and R_α^*, four-point correlation functions for a given ordering of light-matter interactions within the trace, for example:

$$R_4(t_3,t_2,t_1) = Tr[\hat{\mu}(t_1+t_2+t_3)\hat{\mu}(t_1+t_2)\hat{\mu}(t_1)\hat{\mu}(0)\varrho_{eq}] \qquad (2.11)$$

The solutions to the wave equation in Equation 2.3 with polarization, $P^{(3)}(t)$, as the source can be derived after making the temporal and spatial slowly varying envelope approximation (SVEA) which says that the envelope of the resulting field does not vary much during an optical period. We can solve for the electric field generated by the induced polarization, $\boldsymbol{E_s}(t)$, using the wave equation and find that it is proportional to $P^{(3)}(t)$ and therefore related to the response function and the incident electric fields,

$$\boldsymbol{E_s}(t) \approx i\omega P^{(3)}(t) \qquad (2.12)$$
$$\approx iS^{(3)}(t_3,t_2,t_1) \times E(t-t_3)E(t-t_3-t_2)E(t-t_3-t_2-t_1)$$

We now focus our attention on the incident electric fields and assume they each can be described as plane waves in Equation 2.4. Substituting plane wave expressions for each field into Equation 2.9, including the complex conjugate terms, would yield $(3!)^3 = 6^3 = 216$ possible combinations. Each combination will have some exponential term $exp\left(i(\Sigma_i \pm \boldsymbol{k_i}\cdot\boldsymbol{r_i} - \Sigma_i \pm \omega_i t + \Sigma_i \pm \phi_i)\right)$, where the emitted signal will have wave vector $\boldsymbol{k_s} = \pm\boldsymbol{k_1} \pm \boldsymbol{k_2} \pm \boldsymbol{k_3}$, frequency $\omega_s = \pm\omega_1 \pm \omega_2 \pm \omega_3$, and phase $\phi_s = \pm\phi_1 \pm \phi_2 \pm \phi_3$. We can initially eliminate many of these possible combinations with a few assumptions; if we assume that the emitted field will have a similar frequency as the absorbed frequency and that we will be able to detect any oscillations during t_2, we can eliminate third harmonic terms like $\omega_s = \pm(\omega_1+\omega_2+\omega_3)$ and double quantum terms like $\omega_s = \pm(\omega_1+\omega_2-\omega_3)$, leaving only $\omega_s = -\omega_1+\omega_2+\omega_3$ and $\omega_s = \omega_1-\omega_2+\omega_3$. This then also imposes $\phi_s = \mp\phi_1 \pm \phi_2 + \phi_3$ and $\boldsymbol{k_s} = \mp\boldsymbol{k_1} \pm \boldsymbol{k_2} + \boldsymbol{k_3}$ and in a diffractive-optic noncollinear geometry defines the emitted signal types.

Many 2DES experiments utilize a noncollinear beam geometry of which there are typically two types, a pump-probe and box-CARS geometry. In the pump probe geometry, the signal field is emitted in the same direction as the probe beam which allows for detection of the real absorptive signal directly. This method suffers from reduced signal to noise ratios compared to “background-free” approaches [87,88]. Several box-CARS geometry experiments use a diffractive optic to create spatially separated beams for each light-matter interaction [89]. The resulting signal field is then emitted in a direction different than any input beams for background-free signal detection. For the diffractive-optic based setup there are two signal types resulting from one light-matter interaction per beam, the rephasing (R) and nonrephasing (NR) signals defined by the respective phase matching conditions:

$$k_R = -k_1 + k_2 + k_3 \quad (2.13)$$
$$k_{NR} = k_1 - k_2 + k_3$$

With these limited conditions applied, the expression for the third order polarization in Equation 2.9 can be reduced to

$$P^{(3)}(t) = \int_0^\infty dt_3 \int_0^\infty dt_2 \int_0^\infty dt_1 (S_R^{(3)}(t_3,t_2,t_1) + S_{NR}^{(3)}(t_3,t_2,t_1)) \quad (2.14)$$
$$\times E(t - t_3)E(t - t_3 - t_2) \ldots E(t - t_3 - t_2 - t_1)$$

where the rephasing and nonrephasing response functions can be described by

$$S_R^{(3)}(t_3,t_2,t_1) \propto \boldsymbol{E_1^* E_2 E_3} = E_1 E_2 E_3 \quad (2.15)$$
$$\times \exp\left[i\left((-\boldsymbol{k_1} + \boldsymbol{k_2} + \boldsymbol{k_3}) \cdot \boldsymbol{r} + (-\phi_1 + \phi_2 + \phi_3) + \omega_s t\right)\right]$$
$$S_{NR}^{(3)}(t_3,t_2,t_1) \propto \boldsymbol{E_1 E_2^* E_3} = E_1 E_2 E_3$$
$$\times \exp\left[i\left((\boldsymbol{k_1} - \boldsymbol{k_2} + \boldsymbol{k_3}) \cdot \boldsymbol{r} + (\phi_1 - \phi_2 + \phi_3) + \omega_s t\right)\right]$$

where subscript n refers to the pulse interaction ordering, and $\omega_s = \mp\omega_1 \pm \omega_2 + \omega_3$ for rephasing and nonrephasing, respectively. The total response function of the system can be measured by measuring the rephasing and nonrephasing signals and adding them together.

Coupling to a Bath

In many theoretical treatments of molecular systems, decay and dephasing contributions are included by modeling interactions of the system with a fluctuating bath. A common assumption is that the bath is composed of harmonic oscillators and can be described by some spectral density function. Coupling between the system and bath is responsible for different spectral broadening contributions including homogeneous and inhomogeneous broadening. Homogeneous broadening can be modelled by fast bath fluctuations and inhomogeneous contributions by slower bath fluctuations [14,84].

Features of 2DES

Two-dimensional electronic spectroscopy measures the complex third order response function of the material with a series of three pulses with controlled time delays (Figure 2.1). We can study the evolution of the absorptive portion of the response function by taking the real part of this signal. The real absorptive signal is the same signal that is measured in wavelength-resolved pump probe spectroscopy, but 2DES additionally resolves the excitation frequency, providing two-dimensional correlation maps of excitation and detection frequency as a function of waiting time, t_2.

One of the main advantages of using 2DES over other spectroscopies is the ability to distinguish between different broadening contributions. This is particularly important for molecular systems and ensembles of molecules where broadening contributions can be large and can be difficult to distinguish from independent transitions with a similar frequency. Homogeneous broadening is distributed along the antidiagonal in 2DES spectra (Figure 2.2). In the condensed phase, the homogeneous width is primarily determined by coupling of the electronic transition to fast fluctuations of the surrounding bath (e.g. solvent molecules, protein amino acids) [90]. There are many possible sources of inhomogeneous broadening in atomic and molecular optics, but the main contributors in solution are different solvent environments, or in the case of photosynthetic proteins, variations in the surrounding protein matrix. Inhomogeneous effects result in different sub-ensembles with shifted transition frequencies so that the ensemble measurement is elongated along the diagonal (Figure 2.2). Chlorins in solution, like Bacteriochlorophyll a, are very inhomogeneously broadened due to multiple cofactors which can interact via

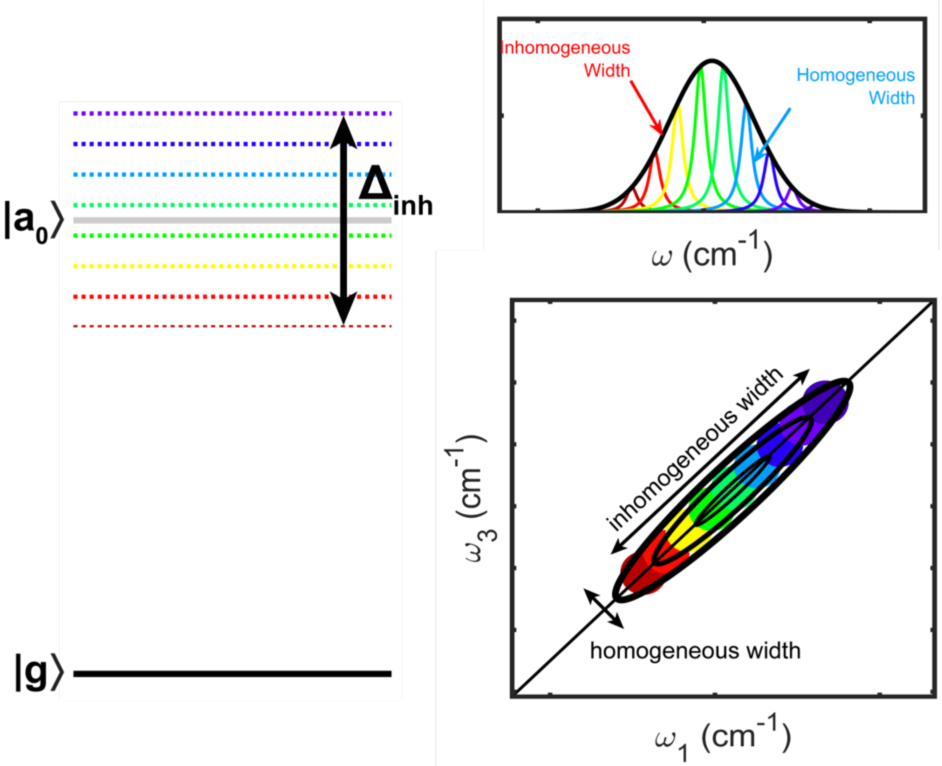

Figure 2.2 Cartoon ensemble of monomeric molecules. (Left) Jablonski diagram of molecule with electronic mean excited state $|a_0\rangle$ and shifted excited states due to different microenvironments. (Top right) Cartoon linear absorption spectrum of this ensemble showing the Gaussian distribution of transition energies each with some Lorentzian homogeneous linewidth. Without prior knowledge of the homogeneous linewidth, linear absorption spectra cannot distinguish between the contributions of these two broadening sources to the overall measured spectra (black). (Bottom right) Cartoon 2DES spectrum at early t_2 demonstrating the ability of 2DES to resolve inhomogeneous and homogeneous broadening contributions separately. Fast environmental fluctuations are experienced for the entire ensemble and are measured along the antidiagonal. Before dephasing effects are prominent the inhomogeneous width is distributed along the diagonal line. As dephasing effects take place the molecules lose correlation and the peak will round out, obscuring the homogeneous linewidth.

hydrogen bonding and coordination with solvent molecules. These molecules are similarly inhomogeneously broadened in protein environments.

2DES is capable of resolving many properties of monomeric systems including dephasing of electronic coherences, population decay, dynamical interactions with the environment that lead to fluctuations in frequency (spectral diffusion). Additionally, 2DES can resolve energy transfer between coupled transitions and can also be used to

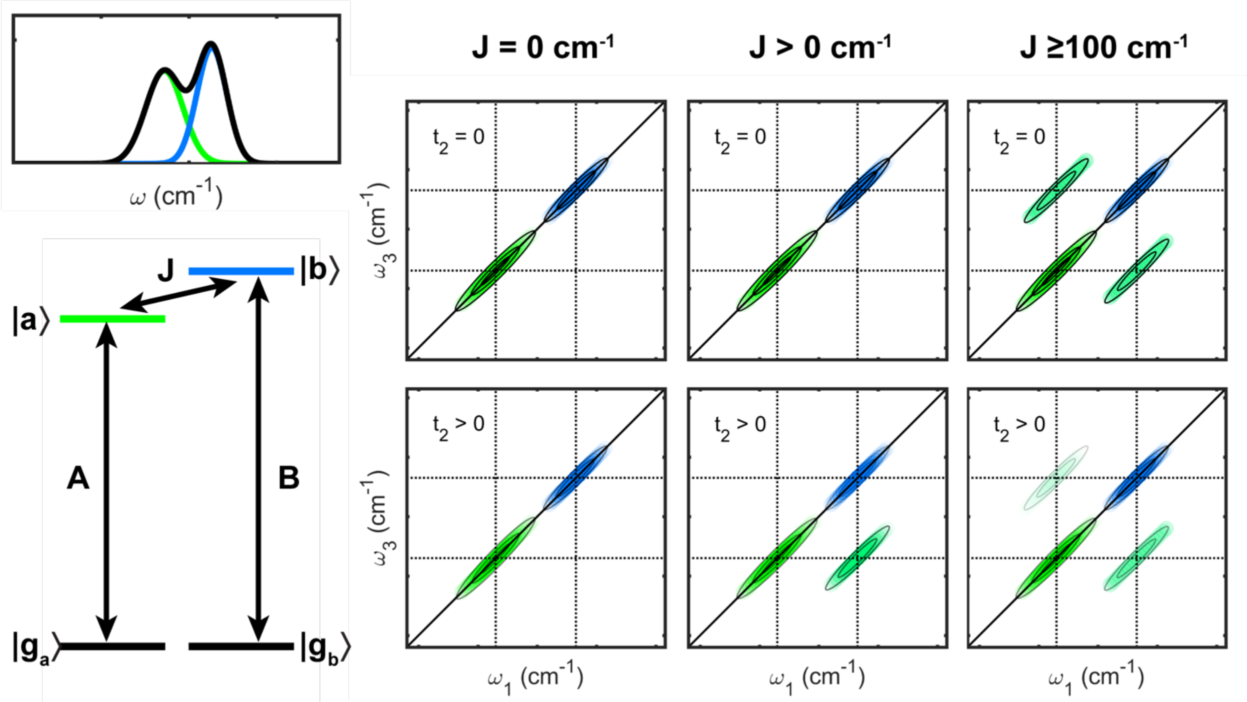

Figure 2.3 Cartoon molecular system with two electronic transitions and unknown electronic coupling. (Top left) Cartoon linear absorption spectrum for a system with two electronic transitions with frequencies A and B, shown by a Jablonski diagram (Bottom left). The black curve in the absorption spectrum shows what is measured using linear absorption spectroscopy and the green and blue curves shows two peaks which may be recovered from fitting. The linear absorption spectrum may look similar for three distinct systems, where there is no coupling between |a⟩ and |b⟩, weak electronic coupling ($J > 0$ cm^{-1}), and strong electronic coupling ($J \geq 100$ cm^{-1}). (Right) 2DES cartoon maps at $t_2 = 0$ fs (top row) and $t_2 > 0$ fs (bottom row) are able to distinguish these three scenarios and directly measure the homogeneous and inhomogeneous broadenings present in the system. ($J = 0$ cm^{-1}) Two diagonal peaks corresponding to |a⟩ and |b⟩ transitions decay with increasing t_2 and no cross peaks are present. ($J > 0$ cm^{-1}) The same two diagonal peaks are present at $t_2 = 0$ fs as in the uncoupled case, but an additional cross peak grows in at $t_2 > 0$ fs indicating energy transfer and weak coupling between the transitions. The positioning below the diagonal indicates downhill energy transfer. ($J \geq 100$ cm^{-1}) At $t_2 = 0$ fs two cross peaks are already present indicating a shared ground state between |a⟩ and |b⟩, due to strong excitonic coupling.

distinguish between weak and strong coupling regimes (Figure 2.3). A solution of uncoupled molecules would have 2D spectra with signals along the diagonal ($\omega_1 = \omega_3$), corresponding to populations which remain in the same transition and which decay with the excited state lifetime. The main signatures that indicate couplings in 2D spectra are cross peaks or signals off of the main diagonal line ($\omega_1 \neq \omega_3$). For a weakly coupled system where each electronic transition remains localized and can be described in the site basis, cross peaks grow in as a function of waiting time, t_2, as the energy is transferred between transitions. In a strongly coupled system with excitonic character, the shared ground state leads to cross peaks which appear at $t_2 = 0$, and decay with similar timescales as the excitonic state lifetimes. This is especially useful for photosynthetic protein complexes where we expect a mixture of strongly and weakly coupled transitions.

Up until this point we've treated the signals resulting from the sequence of three light-matter interactions by the pulses of light in a very general way. There are three types of signals present in third-order polarization spectroscopies like transient absorption and multidimensional spectroscopies; they are referred to as stimulated emission (SE), ground state bleach (GSB), and excited state absorption (ESA). Before going into detail about each type of signal, it is useful to describe two types of diagrams which describe the material response function (like in Equation 2.9) in terms of individual light-matter interactions. Figure 2.4 shows two types of diagrams, Double-Sided Feynman Diagrams (DSFD) and one I will be referring to as Light-Matter Interaction Diagrams (LMID), which present the pertubative third-order response function induced by the 2DES pulse sequence in different ways.

The DSFD presents the state of the system in the density function form, where $|a\rangle\langle a| = \varrho_{aa}$, in the vertical box and tracks the transitions probed by each individual pulse, represented by arrows. Time progresses vertically with horizontal bars indicating a light-matter interaction event and the space between vertical bars corresponding to free evolution of the system. In these DSFDs, the phase-matching condition for the rephasing signal can be invoked to restrict the possible diagrams that will contribute to the rephasing signal. The direction each arrow points (left vs right) is related to the sign in the phase-

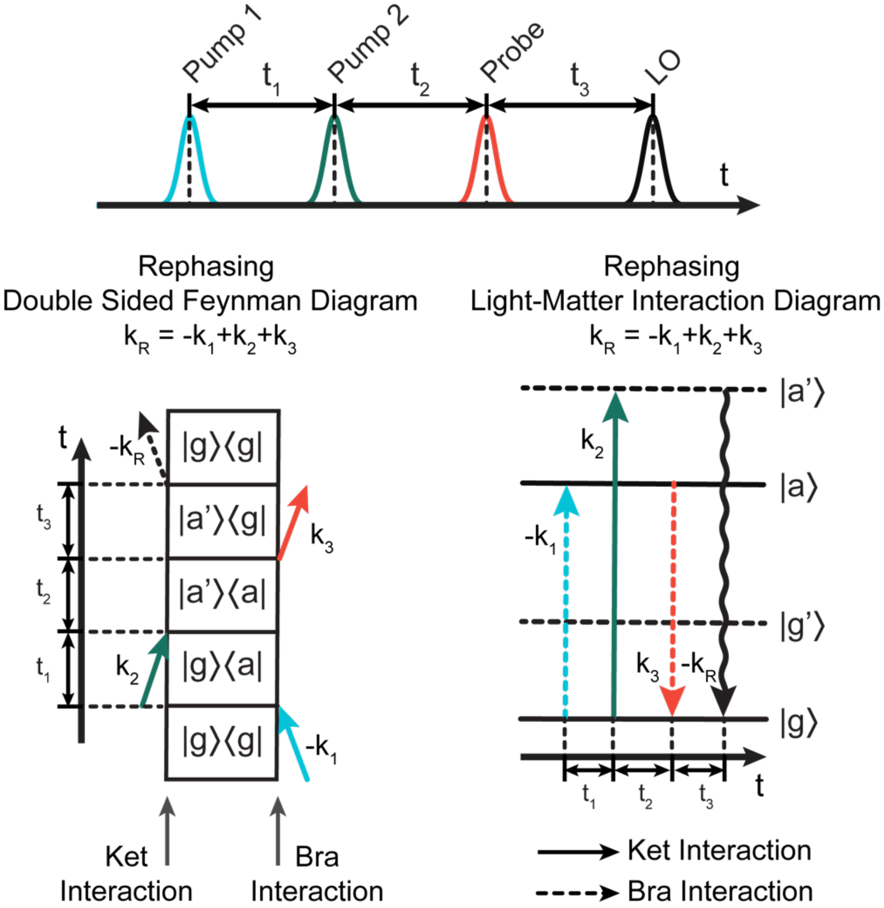

Figure 2.4 Double-sided Feynman Diagrams (DSFD) (bottom left) and Light-matter interaction diagrams (bottom right) are useful tools for interpreting possible light-matter interaction pathways observed in two-dimensional electronic spectroscopy (2DES). For a given 2DES pulse sequence (top) and arbitrary system with four states, |g⟩, |g'⟩, |a⟩, and |a'⟩, each pulse interacts with the system once either with the bra (⟨.|) or ket (|.⟩) direction of the density matrix. This is represented directly in the DSFD case and by either solid or dashed lines, respectively, in the light-matter interaction diagram. During each interpulse waiting time the systems freely evolves.

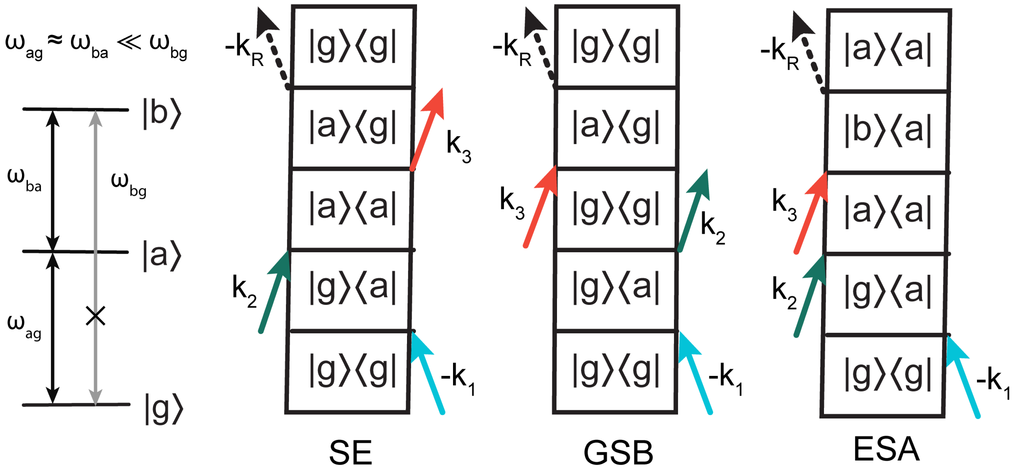

Figure 2.5 Double-sided Feynman Diagrams (DSFD) depicting rephasing signals. (Left) Jablonski diagram of an arbitrary system with electronic states |g⟩, |a⟩, and |b⟩. State |b⟩ is far from resonance with the pulses used. (Right) Double-sided Feynman diagrams (DSFD) depicting stimulated emission (SE), ground state bleach (GSB), and excited state absorption (ESA) signals in a population during t_2.

matching equation, $k_R = -k_1 + k_2 + k_3$, and its position relative to the system describes whether the interaction is absorptive (exciting a transition) or emissive (stimulating emission). The second diagram type presents the system in a Jablonski diagram and each light-matter interaction is represented by vertical arrows with time progressing along the horizontal axis. This representation contains the same information about phase-matching and the state of the system as the DSFDs but is better for representing systems with states of mixed character.

Figure 2.5 shows three DSFDs depicting stimulated emission, ground state bleach, and excited state absorption signals for the rephasing signal. For stimulated emission and excited state absorption pathways, the two pumps initially excite the system to an electronic excited state population (Figure 2.5); if the probe interaction acts on the bra-side of the density matrix it will stimulate emission which results in an increase in probe transmission and will produce a positive signal. Alternatively, if the probe interacts on the ket-side of the density matrix and is absorbed by a transition to a higher lying state, the probe transmission decreases and results in a negative signal. Ground state bleach signals result from the two pumps both interacting with the bra-side of the density matrix, corresponding to absorption and emission from the same transition, the probe can only be absorbed by the system. GSB pathways result in a decrease in probe absorption, but due to the odd number of interactions with the ket-side, acquire another negative sign such that the GSB signals are also positive.

In systems where the nonradiative relaxation of the excited state is small, the SE and GSB signals will significantly overlap. In this example (Figure 2.5) the state resulting in a ESA signature was a higher-lying electronic state far from resonance with our pulses so that it could not be excited directly. Generally, ESA signatures can also arise from the formation of new states that form over the course of the waiting time, t_2.

Section 2.2 Experimental Setup

Interferometer Setup

We use a hybrid diffractive-optic and pulse-shaping based 2DES spectrometer (Figure 2.6) which combines the phase-stability of the pump-probe geometry and the high S/N from the background-free signal detection of the box-CARS geometry [91]. A Ti:Sapphire regenerative amplifier (Spitfire Pro, Spectra Physics) produces 4 mJ of 40 nm pulses centered at 800 nm at 500 Hz. 1 mJ of the regen light is fed into a home-built Degenerate Optical Parametric Amplifer (DOPA) (Figure 2.9), based on a design by Siddiqui, et al. [92], which generates 8 μJ of broadband near-IR light centered at 800 nm. The DOPA light is split by an 80/20 beam splitter into pump and probe paths, respectively. Both beams are partially compressed using chirped mirrors and partially by pulse shapers. The pump beam is compressed by an acousto-optic programmable dispersive filter pulse shaper (Dazzler, Fastlite) which is also used to create a copy of the pump pulse with a controllable time delay, t_1. The Dazzler is also used in phase cycling by applying a constant phase factor to the two pump pulses. The pump beam is compressed by a spatial light modulator (femtoJock, Biophotonics) and is delayed from the pump pulses by a retroreflecting computer controlled delay stage.

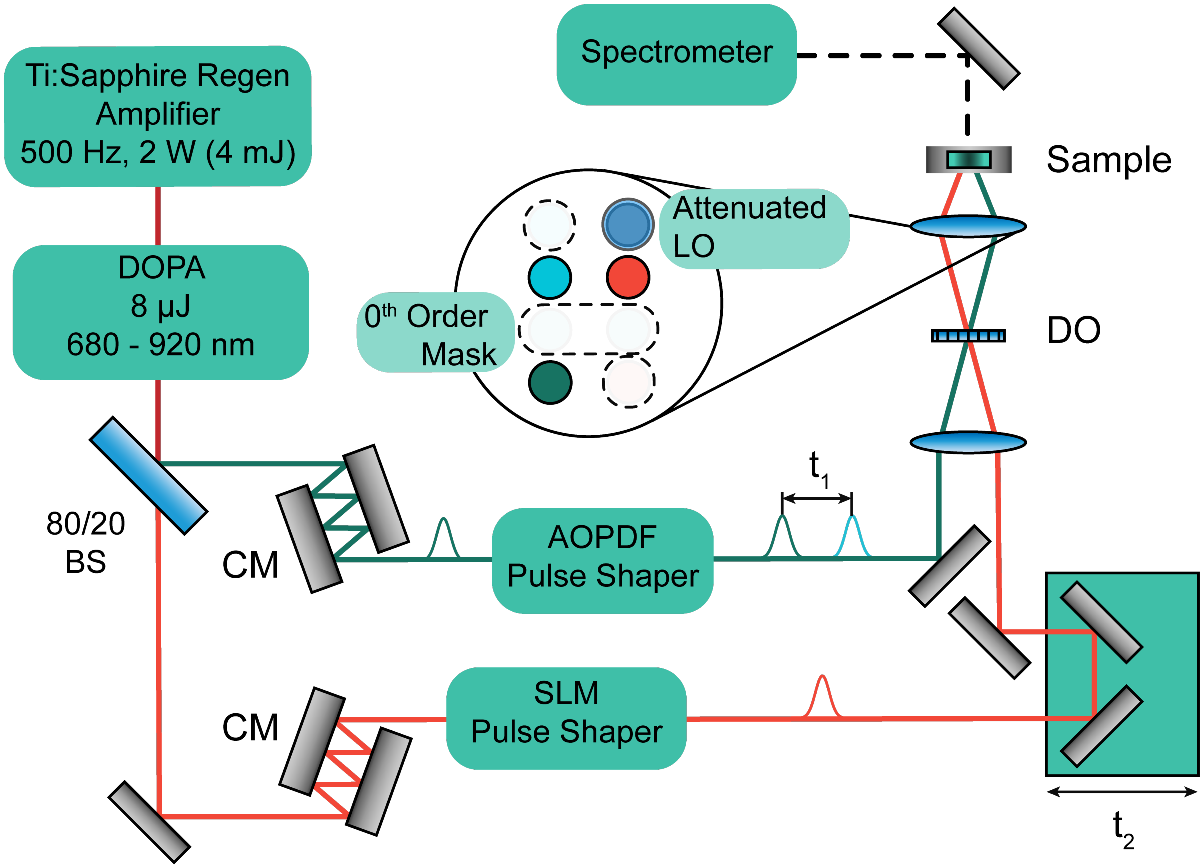

Figure 2.6 Hybrid diffractive optic and pulse-shaping based 2DES setup [91]. Light from a 500 Hz Ti:Sapphire regenerative amplifier is fed into a Degenerate Optical Parametric Amplifier (DOPA) (Figure 2.9) which generates 8 μJ of light spanning 680 – 920 nm. DOPA light is split by a 80/20 beam splitter into the pump and probe beams. Pump and probe beams are partially compressed with Chirped Mirrors (CM) before traversing an acousto-optic programmable dispersive filter (AOPDF) pulse shaper and spatial light modulator (SLM) pulse shaper, respectively. The AOPDF pulse shaper also generates a copy of the pump pulse at a controllable time delay, t_1. Scanning The probe beam is delayed from the two pump pulses using a retroreflecting stage with controllable time delay, t_2. Both beams are then focused onto a Diffractive Optic (DO) which diffracts beams along the plane perpendicular to the page; a mask filters all but the ±1 pump orders and the -1 and -3 probe orders. The -3 probe beam is attenuated and passes through a 0.5 mm fused silica delay plate. These four beams are focused to the sample plane and the generated four-wave mixing signal is heterodyne detected in a spectrometer. Figure adapted from [93].

The pump beam with two pump pulses and the probe beam are collimated and focused by a 50 cm curved mirror to a transmissive diffractive optic to generate the beam geometry needed for the box-CARs configuration (Figure 2.7). A transmission mask is applied at $2f$ and filters all but the ± 1st orders of the pump path and the -1st and -3rd orders of the probe path. The -1st probe beam is used as the probe pulse and the -3rd order is used as the local oscillator, delayed by a 0.5 mm thick delay plate and attenuated. These four beams are focused to the sample plane and the scattered four wave mixing signal is collected in the local oscillator direction in a spectrometer.

Spectral Interferometry & Signal Phasing

For a diffractive optic based experiment, the rephasing and nonrephasing signals are emitted into different phase-matching directions. These separate contributions can be

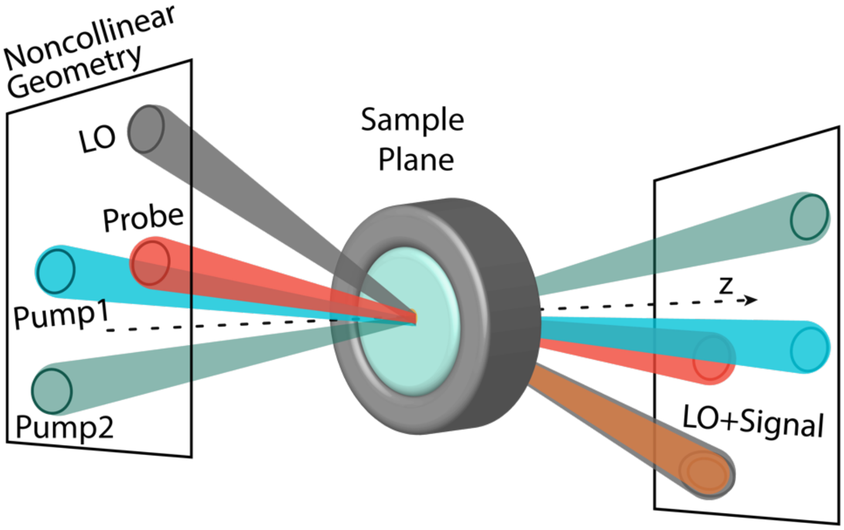

Figure 2.7 Cartoon 2DES beam configuration demonstrating the noncollinear box-CARS beam geometry. After pump and probe beams traverse a transmissive diffractive optic, the ± 1 orders of the pump and -1 & -3 orders of the probe are focused to the sample plane where they interact with the sample. The -3 order passes through a 0.5 mm fused silica delay plate (~800 fs delay) and is attenuated to serve as the local oscillator (LO) and is assumed to not to contribute to the measured third order polarization given the temporal isolation. The four-wave mixing signal is scattered into the LO direction due to phase matching; the rephasing and nonrephasing will scatter into the LO direction when either the +1 or -1 order pump pulses arrives first given the phase matching conditions $k_R = -k_1 + k_2 + k_3$ and $k_{NR} = k_1 - k_2 + k_3$.

measured by collecting the different phase-matched signals or by switching the interaction ordering of the two pump pulses. Experimentally, the latter approach is typically easier to implement.

Following the two pump pulses and the probe pulse is an attenuated pulse at a fixed time delay following the probe called the local oscillator (LO). This pulse has the same wave vector as the signal emitted from the third order polarization and is used to heterodyne detect the signal field in the spectrometer in a process referred to as spectral interferometry first proposed by Lepetit, et al. [80]. After reflecting off the spectrometer diffraction grating the LO and four wave mixing signal interfere in the frequency domain

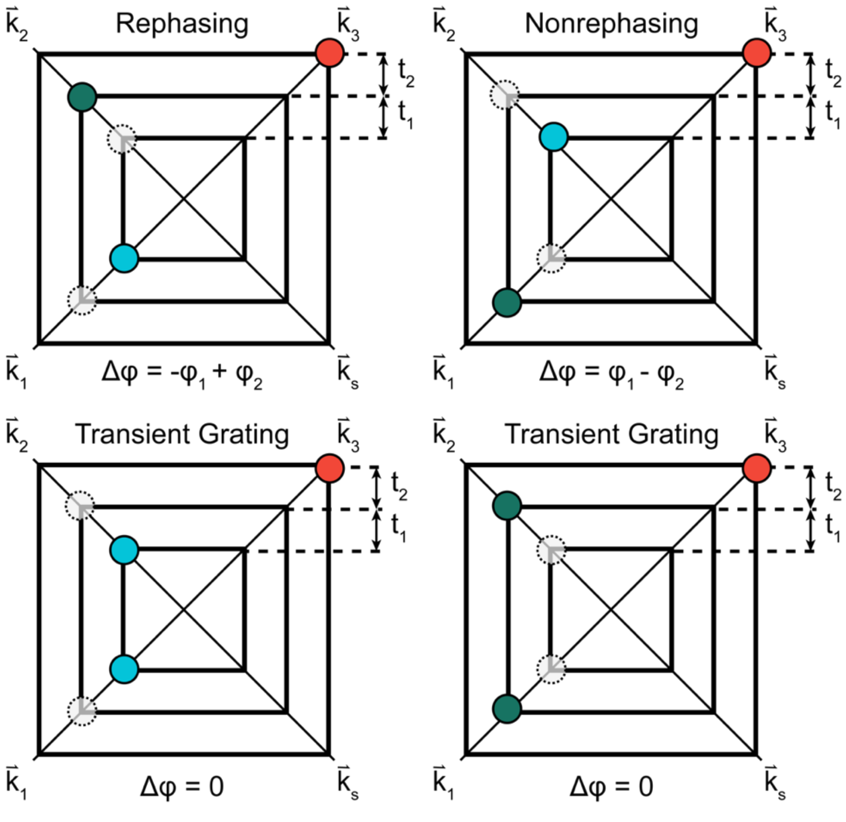

Figure 2.8 6-Pulse Timing and Phase Matching Scheme. The 6-pulse train used in the hybrid diffractive-optic and pulse-shaping 2DES setup is able to simultaneously measure rephasing, nonrephasing, and transient grating third order signals simultaneously from the different phase-matched pulse-interactions depicted above. Interaction ordering starts nearest the center of the box moving outwards. Transparent circles with dashed outlines represent the two pump pulses not involved in the given signal. Figure adapted from [91].

which manifests as interference fringes. The spectrum measured in the spectrometer has the form

$$
\begin{aligned}
I_{tot} &= |E_s(t) + E_{LO}(t)|^2 \qquad (2.16)\\
&= |E_s(t)|^2 + |E_{LO}(t)|^2 + 2Re[E_s(t)E_{LO}^*(t)]
\end{aligned}
$$

The complex signal field is detected in the frequency domain, $E_s(\omega)$, and can be recovered by Fourier transforming the spectrum to the time-domain, windowing out the time-delayed signal field which is separated from the other contributions at the DC peak, and inverse Fourier transforming back, [80]

$$E_s(\omega) \propto \mathcal{F}^{-1}[\theta(t_3)\mathcal{F}[I_{tot}(\omega)]] \qquad (2.17)$$

In experiments which utilize a local oscillator for heterodyne detection it is also necessary to determine the phase acquired by local oscillator, ϕ_{LO}, due to differences in its path compared to the probe pulse so that the signal field can be accurately determined. This phase is determined by comparing the real absorptive signal at $t_1 = 0$ projected along the detection axis, which is related to the transient grating signal S_{TG}, with the pump probe spectrum and finding a phase factor, $\Delta\phi$, which minimizes the difference between these two signals

$$\min\left|\mathrm{Re}\left[\mathrm{S_{TG}}(\omega)e^{i\Delta\phi}\right] - S_{PP}(\omega)\right|^2 \qquad (2.18)$$

After detection of the emitted signal field it is sometimes necessary to separate out the rephasing and nonrephasing signals so that the real absorptive signal can be constructed. This can be done by exploiting the different phase dependences of the rephasing and nonrephasing signals, $\phi_R = -\phi_1 + \phi_2 + \phi_3$ and $\phi_{NR} = \phi_1 - \phi_2 + \phi_3$, in a process called phase cycling. If we apply a constant phase factor, φ_n, to the first and second pump pulses such that

$$
\begin{aligned}
\phi_R &= -(\phi_1 + \varphi_1) + (\phi_2 + \varphi_2) + \phi_3 \qquad (2.19)\\
&= -\phi_1 + \phi_2 + \phi_3 - \Delta\varphi
\end{aligned}
$$

$$\begin{aligned}\phi_{NR} &= (\phi_1 + \varphi_1) - (\phi_2 + \varphi_2) + \phi_3 \\ &= \phi_1 - \phi_2 + \phi_3 + \Delta\varphi\end{aligned}$$

where $\Delta\varphi = \varphi_1 - \varphi_2$, we can distinguish the rephasing and nonrephasing signals by filtering the total signal by its dependence on the added constant phase factors.

Following phase cycling to distinguish the rephasing and nonrephasing contributions, the data is Fourier transformed with respect to t_1. Experimentally, we are able to resolve the excitation frequency axes while sampling t_1 sparsely by detecting the signal in the rotating frame with respect to some lock frequency ω_{lock}. For a given t_2 we can plot the excitation frequency, ω_1, against the detection frequency, ω_3 in frequency-frequency correlation plots.

For a given shot of the experiment there are 6 pulses at the sample plane, 2 pump pulses per pump beam in addition to the probe and local oscillator pulses. This 6-pulse scheme means for any shot of the experiment we are exciting rephasing, nonrephasing, and two transient grating signals simultaneously (Figure 2.8). We can extract the individual signals by using phase cycling described briefly above. We can use the signal phases from Equation 2.19 for the rephasing, $S_R \propto e^{-i\Delta\varphi}$, and nonrephasing signals, $S_{NR} \propto e^{i\Delta\varphi}$, to distinguish them from the transient grating signals where the constant phase contributions cancel out, $\phi_{TG} = (\phi_n + \varphi_n) - (\phi_n + \varphi_n) + \phi_3 = \phi_3$, where n is either the first or second pump pulse. Phase cycling is also used to suppress some scattering contributions. The total phase scheme is comprised of 6 pairs of phases:

$$\{\varphi_1, \varphi_2\} \in \{\{0,0\}, \{0, 2\pi/3\}, \{0, 4\pi/3\}, \{\pi, \pi\}, \{\pi, 5\pi/3\}, \{\pi, 7\pi/3\}\} \qquad (2.20)$$

which does not significantly increase the acquisition time of the experiment [91].

The experiments presented in this manuscript were all performed using an all-parallel pulse polarization scheme but it is also possible to control the relative polarization between the pump and probe pulses using a combination of $\lambda/2$ waveplates and wire grid polarizers. In our work studying the population kinetics of bacterial reaction centers we have demonstrated our ability to measure the magic angle polarization components which are independent of the angle between transition dipoles probed [4,93]. There are also many schemes to control the pulse polarization of each pulse in 2DES setups which control the coherence time, t_1, with glass wedges [59,61,94]. Such schemes have been used to enhance weak cross-peak features and suppress unwanted vibrational coherence signals.

Coherence Experiments

The data presented in this manuscript were collected scanning the coherence time from $10 \leq t_1 \leq -390\ fs$ in 10 fs steps and the local oscillator was delayed from the three pulse-sequence by about 830 fs. The waiting time was scanned -50 $\leq t_2 \leq 3{,}500\ fs$ in 10 fs steps, which after Fourier transformation yields a coherence frequency, ω_2, resolution of $1/(3{,}420\ fs\ *\ c) = 9.75\ cm^{-1}$. The highest possible frequency we can excite depends on either the longest pulse duration or the sampling rate, whichever is largest. Oscillatory signals with periods shorter than this limiting parameter cannot be resolved. The Nyquist criterion requires sampling at twice a given frequency in order to reliably resolve it. Given this definition, the Nyquist frequency using the t_2 sampling spacing of $10\ fs$ is $\omega_{2,\mathrm{max}} = 1/(2 * 10fs * c) = 1{,}667\ cm^{-1}$. The frequency resolution is only dependent on the length of the coherence scan, whereas the Nyquist frequency also depends on the duration of the pulses used. The numbers presented here give an upper limit on the Nyquist frequency and pulse-duration-limited numbers are presented at the beginning of each results section. Coherence signals are typically ≤10% of the total signal strength and can be difficult to resolve in low signal to noise experiments; increasing the averaging time can help improve the S/N to a point, but there are several other ways to improve the signal to noise that focus on the light source stability.

Phase stability during t_2 is very important in 2DES studies of coherence as is general spectral stability. Some of the main contributors to noise in coherence scans are air currents, which can be mitigated by using an enclosed setup, and chirp drift. Chirp drift occurs when the motor controlling the compressor inside of the regen moves slightly or due to other small changes internal to the regen; a small chirp drift has a very dramatic impact on the light produced by nonlinear light sources, such as the DOPA, where pulse signal generation is optimized at specific chirp values. Chirp drift can manifest as large laser power fluctuations which show up in the signals or as a decrease in spectral stability, which can wash out weak oscillatory signals. Chirp drift can be mitigated by optimizing the regen and the nonlinear light source and, in the case of slow chirp drift over the course of a few hours, can be corrected in between experimental scans.

Light Sources

All of the experiments presented here were performed using light from a home built Degenerate Optical Parametric Amplifier (DOPA) based on a design by Siddiqui, et al. [92] and depicted in Figure 2.9. This particular DOPA design has been discussed in detail elsewhere [93]. Briefly, 1 mJ of 800 nm 500 Hz light from a Ti:Sapphire regenerative amplifier is split into two paths, white light seed generation and second harmonic generation pump path. Along the white light seed path, the 800 nm light is first focused to a YAG crystal to produce spectrally broadened white light which is pumped by 800 nm light in a collinear optical parametric amplifier (OPA) to generate a 1.3 μm signal.

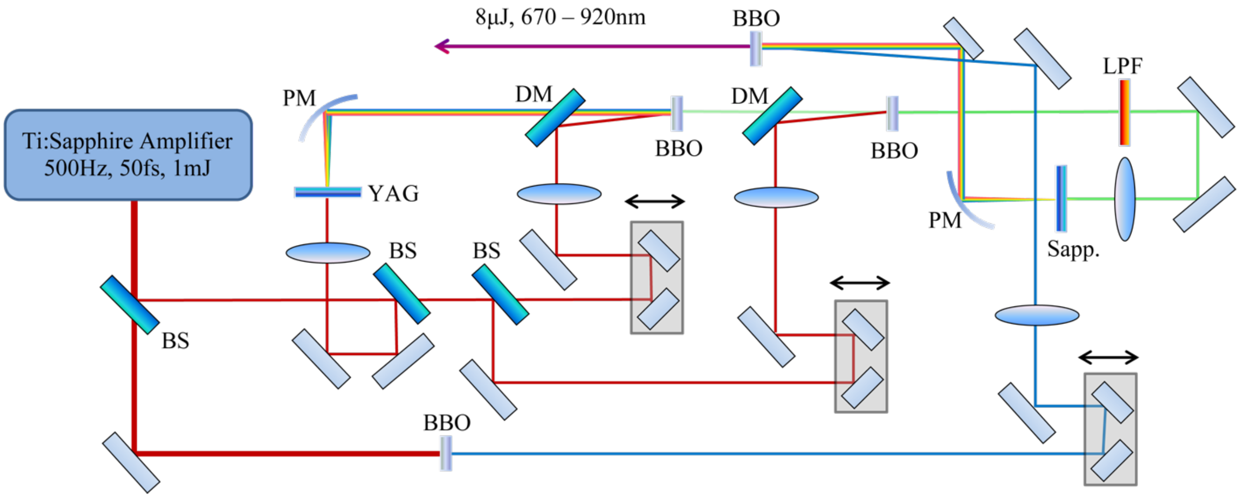

Figure 2.9 Degenerate Optical Parametric Amplifier (DOPA) Setup. DOPA light source design based on design by Siddiqui, et al. [92]. 1 mJ of 500 Hz light from a Ti:Sapphire regenerative amplifier is split into white light and pump beam baths. The white light is generated by focusing the output of a two-stage collinear optical parametric amplifier which generates, 5 μJ between 1.2 – 1.6 μm, to a sapphire plate. Using the OPA output to generate the white light avoids instability that would result from using the regen light directly. The pump beam is generated via second harmonic generation in a BBO crystal to 400 nm. The final DOPA signal is generated by collinear amplification of the white light with the strong 400 nm beam. Typical DOPA output is 8 μJ with stable spectrum from 670 – 920 nm. Figure by Andrew Niedringhaus [93].

The signal is amplified again by 800 nm light in a second OPA; the 1.3 μm signal passes through a long pass filter and is focused to a sapphire crystal to generate white light. Many Noncollinear Optical Parametric Amplifiers (NOPA) [95] use the 800 nm regen light directly to generate white light but this results in substantial spectral structure and instability around 800 nm. Using the 1.3 μm OPA output to generate the seed white light yields a stable and smooth spectrum over the region from about 650 – 950 nm. The portion of the regen light directed along the pump path is sent through a nonlinear BBO crystal to generate a strong 400 nm beam to be used as a pump in the final stages in the DOPA. The white light seed is then pumped in a final OPA stage by the strong 400 nm pump to produce broadband light from about 680 – 920 nm (Figure 2.10) with ≤1% “long-term” stability. The DOPA spectra shown in Figure 2.10 are from the final pump and probe spectra used in the Bacterial Reaction Center experiments in Chapter 5; these spectra are narrower-band than the output of the DOPA due to the pulse shapers used in compression and phase cycling.

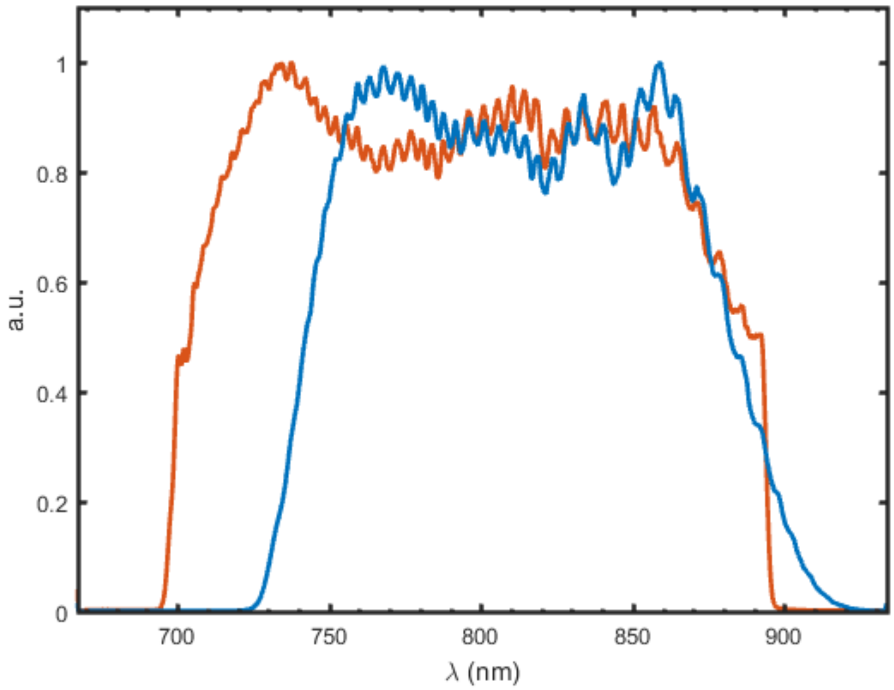

Figure 2.10 DOPA Spectra. DOPA Spectra from the pump (blue) and probe (orange) arms of the 2DES experimental setup (Figure 2.6). The output of the DOPA spans 680 – 920 nm, however the pulse shapers used to compress the pulses reduce the pump and probe bandwidths.

CHAPTER 3 COHERENT OSCILLATORY SIGNALS

The first observations of coherences in photosynthetic protein complexes were performed using ultrafast pump-probe spectroscopy [5]; this study resolved long-lived phase-stable oscillatory signals in photosynthetic bacterial reaction centers which persisted for several picoseconds. These long-lived phase-stable oscillatory signals were resolved during the pump-probe waiting time, t_2, appearing as weak periodic modulations of a strong exponentially decaying signature from energy transfer and population decay. Prior to this observation it was assumed that systems would be excited into electronic populations following two light-matter interactions with the pump pulse and that any off-diagonal coherence terms would decay very rapidly on account of strong coupling with the bath; because of these assumptions this time delay is sometimes referred to as the population time.

Oscillatory signals observed after two light-matter interactions – during the pump-probe delay time in pump-probe experiments or during t_2 in 2DES – have been referred to as coherences, zero electronic quantum coherences, quantum beats, or coherent oscillations almost interchangeably. For clarity, this use of the term *coherence* is different than the coherences excited by a single light-matter interaction. When exciting with visible-near IR light, such coherences typically correspond to one quantum electronic coherences and decay with the electronic dephasing rate. In this thesis we will use coherences or coherent oscillations, and coherent dynamics when describing the time-dependent behavior of oscillatory signals. We are able to analyze the coherences following subtraction of a fit to the population signals by Fourier transforming from t_2 to the coherence frequency axis, ω_2. Because of the time-frequency uncertainty relation, we typically analyze coherence signals in a static way, looking for prominent frequencies and mapping the FT amplitude as a function of (ω_1,ω_3) or coherence maps. Time-frequency analysis methods are being increasingly used to analyze dynamical behavior of these oscillations.

A quick historical note regarding the observation of coherences using ultrafast spectroscopy: the first observation of coherence in photosynthetic proteins in 1991 were performed using state of the art dye-based colliding-pulse ring lasers [96] which generated 45 & 80 fs pulses [5]. These studies were performed only a few years after the first commercial Titanium Sapphire lasers were made available in 1988 and one year after the development of Kerr lens mode locking, which made femtosecond pulse generation more readably attainable [3]. Our ability to resolve coherences is directly tied to our ability to make shorter and shorter pulses (and broader and broader pulse spectra) and we can correlate the rise in observations of coherences in various systems with the progress of stable femtosecond laser technology.

Coherence signals have been observed in a wide variety of systems using ultrafast spectroscopy techniques over the past several decades, including a variety of photosynthetic proteins from various organisms including bacterial reaction centers [5,30,41,51,56–63,97–104], the plant analogue Photosystem II D1D2 Reaction center [71,72], and antenna complexes [6,64,73,105–109], monomeric molecular

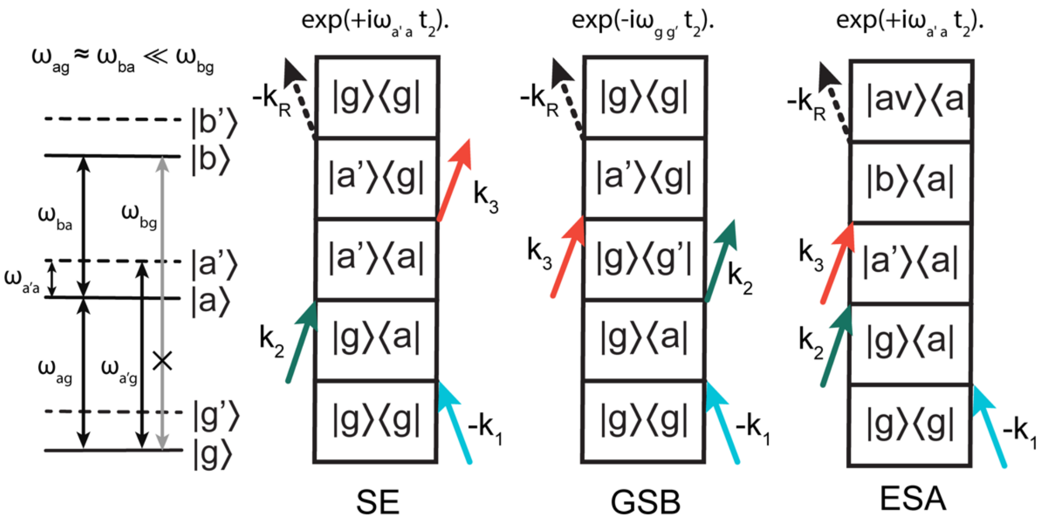

Figure 3.1 Double-sided Feynman Diagrams (DSFD) depicting signals evolve as coherent oscillation during the waiting time, t_2. (Left) Jablonski diagram of an arbitrary system with electronic states |g⟩, |a⟩, and |b⟩ and vibrational states |g'⟩, |a'⟩, and |b'⟩. (Right) Double-sided Feynman diagrams (DSFD) depicting stimulated emission (SE), ground state bleach (GSB), and excited state absorption (ESA) signals in a coherence during t_2. Coherence signals corresponding to superposition states between combinations of electronic or nuclear states, oscillating at the difference frequency. Above each DSFD is the oscillatory term that arises from the superposition, oscillating at some frequency with some sign. Coherences can be prepared by the first two pump pulses in excited (SE & ESA) and ground states (GSB) directly.

systems [110] including porphyrins [77,78,105,111–116], polymers [117], metal nanoclusters [118], organic photovoltaic materials [119], and quantum dots [120]. The first 2DES experiment to observe coherences in photosynthetic proteins [6] helped to launch the current fervent community of spectroscopists and theorists working to understand coherence dynamics in these systems. There have been numerous theoretical studies which have sought to provide guidance for the types of signals that should be observable in 2DES spectroscopy for different modes and have also modeled the impacts coherent dynamics, in particular mixed vibrational-electronic coherences, have on energy and charge transfer kinetics.

This chapter will focus on current theory and experimental methods attempting to understand and characterize coherences. The latter half of this chapter will review previous observations of coherences in Bacterial Reaction Centers and Bacteriochlorophyll a.

Section 3.1 Theoretical Modeling

Multidimensional spectroscopy is particularly suited for studying coherent signals like those initially observed in the BRC using pump-probe spectroscopy [5]. The ability to distinguish excitation and detection frequencies (ω_1,ω_3) together with the selectivity of the phase matching conditions allow us to easily determine which light-matter interaction pathways result in coherent dynamics during t_2 (Figure 3.1). For simple model systems, all the pathways resulting in coherence can be easily enumerated, providing a particularly useful tool when considering different possible physical origins. In most systems the origins considered are due to electronic superposition states, nuclear vibrational superposition states, or mixtures of these two. In this section we will outline three prominent models of coherences commonly considered in coherence studies and will discuss several less common phenomena contributing to coherent dynamics.

Simple Model Systems

After the initial observation of coherences using 2DES in the Fenna-Matthews-Olson antenna complex, many theoretical studies attempted to model the 2DES signals expected for coherences in different types of systems. The approach used across studies share many commonalities, including use of the semi-classical approach, describing the electric field of the light classically and the system quantum mechanically. Standard treatment also includes assuming only resonant excitation interactions; the electric-dipole and rotating-wave approximations; and considering an isotropically oriented sample. Most theoretical studies also implement the Born-Oppenheimer approximation for nonadiabatic dynamics and the secular approximation for systems with weak system-bath coupling, though a few which include nonsecular terms will be described later in this section. The secular approximation eliminates coherence-coherence and population-coherence transfer mechanisms. Several of these studies treat coupling to the bath [121–123] or disorder in the system explicitly [26].

Purely Vibrational Model

The first model we'll consider here represents coherences between two vibrational states on the same electronic state (Figure 3.2) that is coherences which are purely due to a quantum superposition of vibrational states ("purely vibrational"). A similar model was used to describe the coherences observed in the initial observations of coherences in the BRC [5]. There are several studies which treat this model in a very similar fashion [26,69,121,123–125]; working with the harmonic approximation for vibrational motion along one nuclear coordinate and a diabatic representation of electronic states. A typical Hamiltonian used for a displaced harmonic oscillator is shown in Equation (3.1) [121],

$$H = |g\rangle(\Omega\left\{b^{\dagger}b + \tfrac{1}{2}\right\})\langle g| + |\mathrm{a}\rangle(\Omega\left\{b^{\dagger}b + \tfrac{1}{2} - \mathrm{d}\tfrac{b^{\dagger}+b}{\sqrt{2}}\right\} + \varepsilon_{\mathrm{a}})\langle \mathrm{a}| \qquad (3.1)$$

with ground and excited electronic states, |g⟩ and |a⟩, harmonic ladder operators b and $b^{\dagger}$ operating on a vibration with frequency Ω. The excited state is displaced along the nuclear coordinate, q, by dimensionless displacement d (see Figure 3.2). The displacement is related to the coupling of an electronic transition to a different vibrational quantum (0-0 → 1-1) and can also be described by the Franck-Condon factor. The displaced harmonic oscillator is comprised of two diabatic electronic states with one Franck-Condon active vibrational mode per electronic state. This model is generally only extended for a single Franck-Condon allowed vibration as vibronic coupling (coupling of an electronic transition to vibrational modes) is fairly weak (or $d \ll 1$) in chlorin molecules and the probability of exciting a higher lying vibrational mode is low.

Applying the selection rules for Feynman pathways from a 2DES experiment we can easily enumerate 8 rephasing and 8 nonrephasing pathways that result in signals that oscillate with the vibrational frequency, Ω, during t_2 (Rephasing pathways are shown in Figure 3.2). Of the 8 rephasing pathways, three pairs of two have the same (ω_1,ω_3) values so that when all 8 pathways are modelled there are five distinct peaks in the 2D coherence map (defined in in detail in Section 3.3) (Figure 3.2) which form a “chair” pattern where the left edge is aligned with the zero phonon 0-0 transition frequency. Butkus, et al. have characterized the amplitude of different signals as a function of the Huang-Rhys factor [126]. They show that the diagonal signal in Figure 3.2 at (A,A) and off-diagonal at (A+Ω,A) should have comparable amplitude and opposite phase and that the upper off-diagonal at (A,A+Ω) is roughly half the amplitude of the previous peaks [126]. The 2D map in Figure 3.2 shows the expected spectral location of different coherent modes for an ideal displaced oscillator system. In reality, molecular systems have large inhomogeneous broadening which effectively smears each of the 5 signals in Figure 3.2 along the diagonal. This is demonstrated in the largely vibrational coherence map modelled by Butkus, et al in another study which models an electronic dimer with vibrational modes and coupling to a disordered bath [26].

This displaced oscillator model provides a good approximation for qualitative and quantitative behavior of molecular vibrational contributions in a 2DES spectrum, as will be demonstrated in Chapter 4, and has been previously remarked on in 2DES studies of

Chlorophyll a [77]. There are, however, several shortcomings to this model. It assumes harmonic electronic potentials but anharmonicity effects are large in chlorophyll molecules [127]. This model also assumes that the vibrational frequency is the same on both electronic states. Vibrational spectra of chlorins show that this is true for most vibrational modes (within experimental resolution). However there are several modes where the ground and excited state vibrational frequencies different by about ~5 cm^{-1} [128,129]. Differences in the ground and electronic vibrational frequency leads to deviations from the "chair" pattern in Figure 3.2. The displaced oscillator model also assumes that $\mu_{electronic}$ does not change with the nuclear coordinate, q_{vib} (Condon Approximation) [130]. These and other effects will be considered when interpreting the coherence maps of BChla in Chapter 4.

One final note about vibrational coherences is that their decoherence rates are impacted by the disorder and coupling to the bath, in addition to the lifetime of vibrational population relaxation (on the order of several picoseconds in Chlorophyll a [131]) and the excited electronic state lifetime.

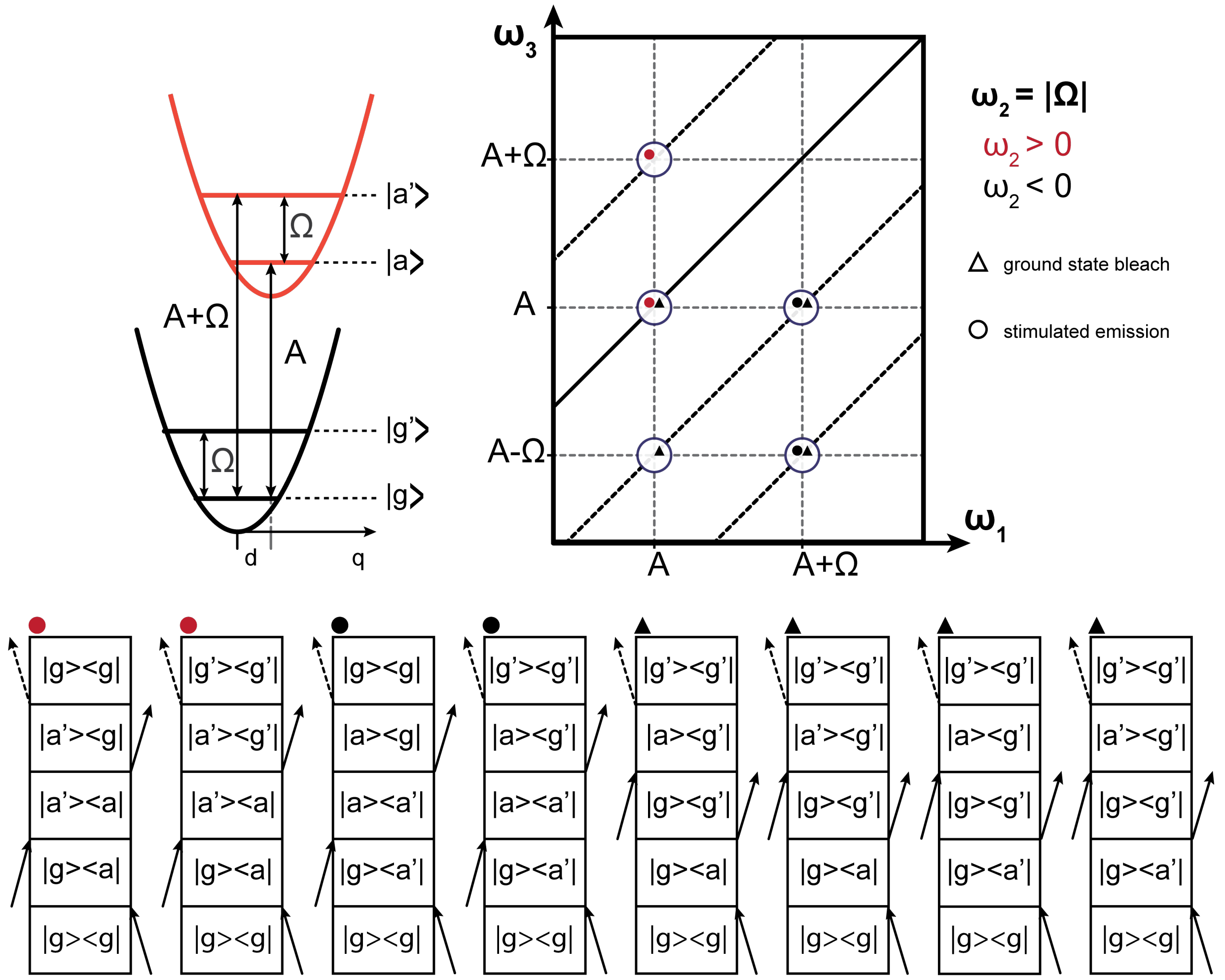

Figure 3.2 Vibrational Displaced Oscillator. (Top left) Jablonski diagram of a 4-level displaced oscillator. Two electronic states, ground |g⟩ and excited state |a⟩, are represented by a harmonic potential which each have two vibrational modes, the zeroth |n⟩ and first |n'⟩ vibrational mode with frequency Ω, which is assumed to be the same on the ground and excited state. The excited state is shifted along the nuclear coordinate, q, with respect to the ground state by some displacement d. The displacement, d, is related to the reorganization energy $(\lambda = \Omega * d^2/2)$ and the Huang-Rhys factor $(S = d^2/2)$ of vibrational mode Ω which describes the vibronic coupling between electronic and vibrational degrees of freedom. Only one excited vibrational mode is included per electronic state as the Huang-Rhys factors in chlorins are small and the probability of excitation to a higher vibrational state is low. (Top right) Coherence map showing the expected distribution of Rephasing coherence signals. The key to the right describes the sign and type of each signal. In the vibrational displaced oscillator all coherences oscillate with the vibrational frequency, Ω, and pathways are limited to ground state bleach and stimulated emission. (Bottom) Double-sided Feynman diagrams for each of the 8 signals shown in the 2D map. Based on models by [121,126].

Purely Electronic Model

The second model system to consider is an electronic dimer (Figure 3.3) which produces coherences oscillating with the excitonic difference frequency, ΔE, during t_2. This model was used in the interpretation of coherences in the Fenna-Matthews-Olson antenna complex [6,64,106], as the frequency of observed modes coincided with expected exciton difference frequencies calculated based on an electronic Hamiltonian with no vibrational modes. It was also invoked in early 2DES coherence studies of the Bacterial Reaction Center [59,132], and has been modelled in several theoretical studies [26,45,121,126,133–136]. The electronic dimer model is comprised of two strongly coupled two-level systems resulting in delocalized excitonic states. Many treatments use a homodimer with identical electronic frequencies. A typical electronic dimer excited state Hamiltonian is shown in Equation (3.2) [121]:

$$H_{exc} = \epsilon_1|e_1\rangle\langle e_1| + \epsilon_2|e_2\rangle\langle e_2| + (J_{ab}|e_1\rangle\langle e_2| + J_{ba}|e_2\rangle\langle e_1|) \tag{3.2}$$

After diagonalization of this Hamiltonian, the singly excited state energies are given by $\varepsilon_{e_1,e_2} = \frac{1}{2}(\epsilon_1 + \epsilon_2) \pm \frac{1}{2}\sqrt{(\epsilon_2 - \epsilon_1)^2 + 4J^2} = \epsilon \pm J$ for a homodimer ($\epsilon_1 = \epsilon_2 = \epsilon$), where J is the coupling and is usually Coulombic [26,137] and assumed to be independent of nuclear coordinate. The doubly excited state energy is given by $\varepsilon_f = 2\epsilon - \Delta$, where Δ is the bi-exciton binding energy which is typically assumed to be negligible [126]. Analyzing the third order polarization, as described in Chapter 2, results in 4 rephasing and 4 nonrephasing coherence signals (Rephasing signals in Figure 3.3) which all oscillate with the exciton difference frequency, $\Delta E = |\varepsilon_{e_1} - \varepsilon_{e_2}|$, during t_2. Of the 4 pathways for each signal, two groups of two have the same (ω_1,ω_3) values so only two distinct peaks are expected in the 2D coherence maps (Figure 3.3). These peaks are distributed

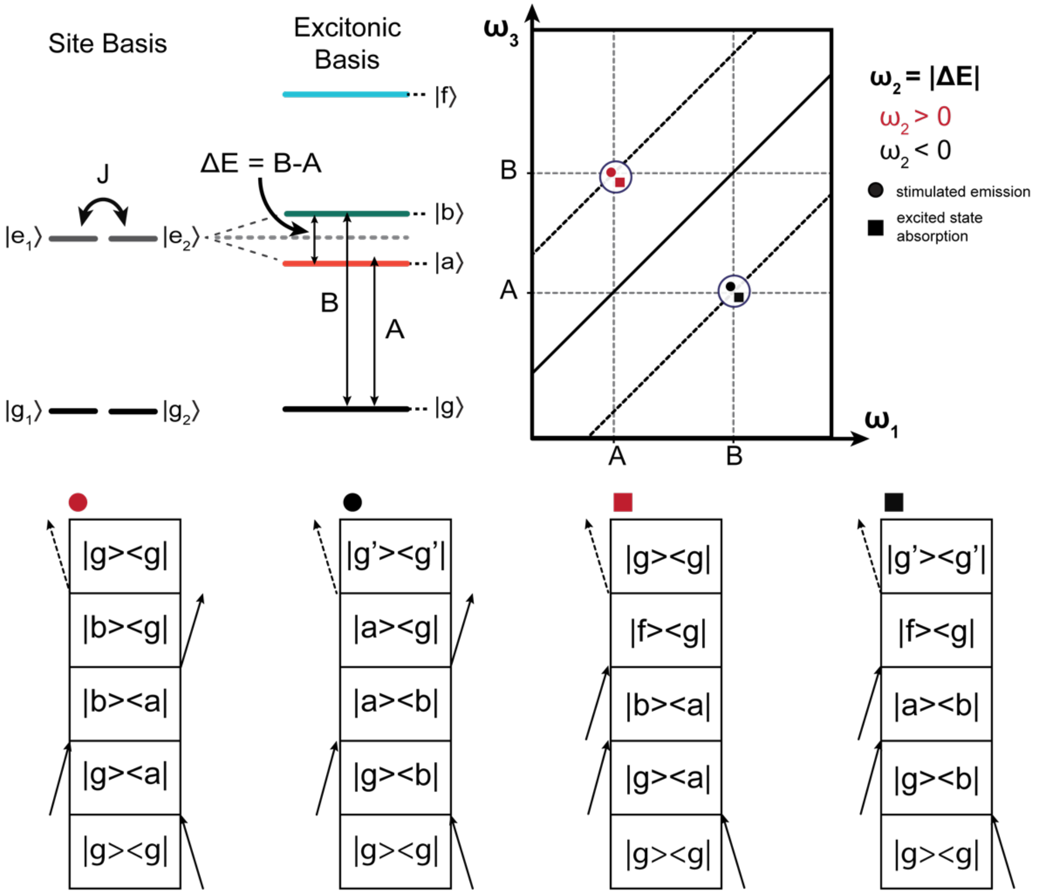

Figure 3.3 Electronic Dimer Model. (Top left) Jablonski diagrams showing an electronic dimer with degenerate electronic transitions (|e$_1$⟩,|e$_2$⟩) coupled by some coupling J in the site basis. The diagonalized excitonic basis shows the splitting of the energy levels into two delocalized singly excited states (|a⟩,|b⟩) and a doubly-excited state (|f⟩). (Top right) 2D map showing the expected distribution of Rephasing coherence signals; sign of oscillation is indicated by the color of the symbol. In an electronic dimer all coherences oscillate at the exciton difference frequency, ΔE = B – A, where B and A are the individual excitonic frequencies. (Bottom) Double-sided Feynman diagrams illustrating the light-matter interactions corresponding to the signals in the 2D map.

symmetrically about the diagonal ($\omega_1 = \omega_3$) line with equal amplitude and are expected to oscillate in phase with one another [26,126,137].

A major source of debate in the coherence community is with regards to the assertion that electronic coherences in protein complexes could last for picoseconds [58,59,66,106]. Given that electronic coherences are due to superposition states of two different electronic states, the electronic dephasing which is measured to be on the order of a few tens femtoseconds in similar antenna proteins [138,139] should limit the observation windows for the coherences. Several of these early studies had proposed that the protein environment is able to extend these electronic dephasing times via correlated fluctuations in the electronic energy gap [58] and that the protein even helps to maintain correlation between electronic states on a long timescale [64,66]. Others have proposed that the longevity of the observed coherences is due to mixing between electronic and vibrational degrees of freedom [60,61,69–72,140], where rapidly decaying electronic coherences transfers to a vibrational coherence which have longer dephasing times.

Mixed Vibrational-Electronic Model

This brings us to our final simple model system, the mixed vibrational-electronic (vibronic) dimer (Figure 3.4). This model was initially proposed by Womick & Moran [141] and typically consists of a coupled dimer of two-level vibrational displaced oscillators. In this model, the excitonic splitting is determined by the electronic coupling and the coupling to vibrational levels is expressed by the nuclear coordinate displacements. This type of model has been used in several theoretical studies [25,69,70,123,136,137,142–146] and has been increasingly applied to explain the origin of coherences in photosynthetic protein complexes.

The 2D coherence distribution for the vibronic model includes contributions similar to the electronic dimer and intramolecular vibrational modes similar to the monomeric displaced oscillator. There are many new signals which arise from the coupling which oscillate at the exciton difference frequency, ΔE; the vibrational frequency, Ω; as well as sum and difference frequencies of these two frequencies, $\Delta E \pm \Omega$. This model exhibits complicated amplitude and phase behavior, which have been examined and discussed in detail in a study by Butkus, et al. that looks at four different cases with varying coupling strengths, J, vibrational frequencies, and Huang-Rhys factors [137].

A main feature of the vibronic model is the role that vibrational levels have in bridging energy gaps between electronic states [141]; the vibrational-electronic resonance can also lead to non-adiabatic energy transfer on the excited state and amplified Raman coherences on the ground electronic state [70,142,147]. This type of resonance has also been shown experimentally to enhance weak or dark states via intensity borrowing from a stronger state [76]. Several theoretical models have shown that vibronic coupling enhances the speed of energy transfer in reaction centers at 77 K [71,72] and light-harvesting proteins at cryogenic temperatures [70] and room temperature [144].

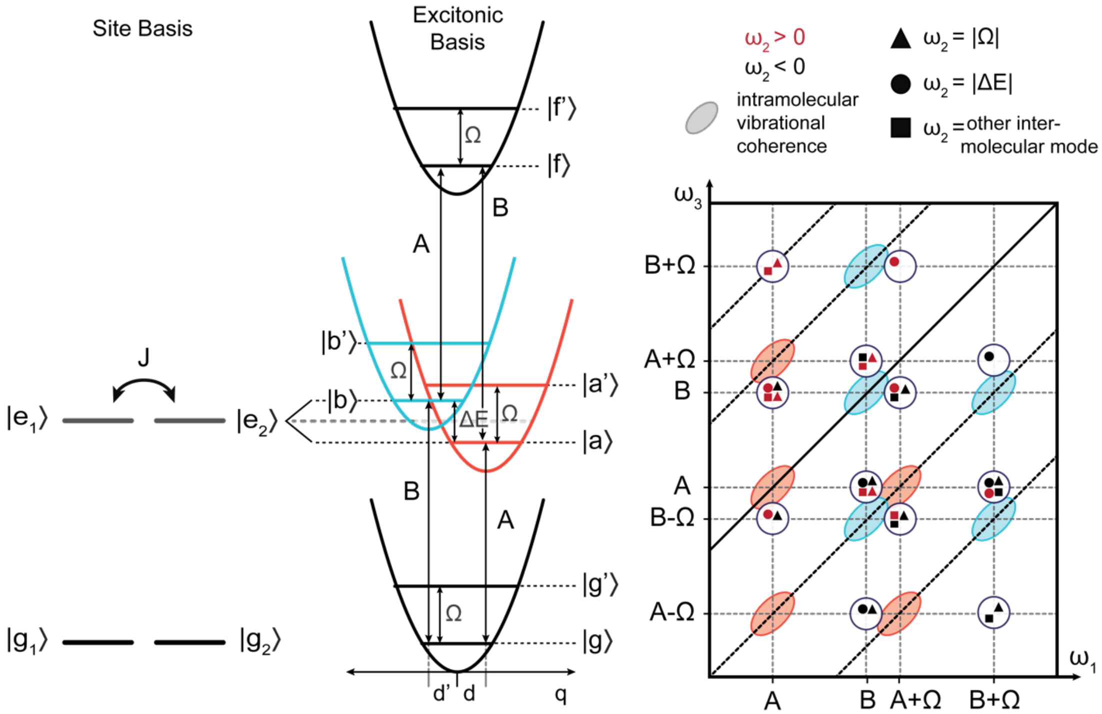

Figure 3.4 Mixed Vibrational-Electronic Model. (Left) Cartoon Jablonski diagrams for the electronic contributions to the undiagonalized site basis and the 8-level system of electronically coupled displaced oscillators. Two singly-excited electronic states, |a⟩ and |b⟩, each have two vibrational levels, |n⟩ and |n'⟩, as does the doubly excited state, |f⟩, and the ground state, |g⟩. Vibrational levels are spaced by frequency Ω for all four electronic states. Exciton binding energy is assumed to be small such that F = A+B. (Right) 2D map showing the expected distribution of coherence signals. Each excitonic transition, |a⟩ and |b⟩, have signals which correspond to intramolecular vibrations the same as shown in Figure 3.2; for conciseness these signatures are represented by colored ovals. Additionally, the electronic dimer pathways from Figure 3.3 are also present in this model but are depicted explicitly. The vibronic model results in coherences at the exciton difference frequency, ΔE, the vibrational frequency, Ω, and the sum and difference of these two frequencies. The key above the 2D map labels which of these frequencies each signal oscillates at and with what sign. [26,137]

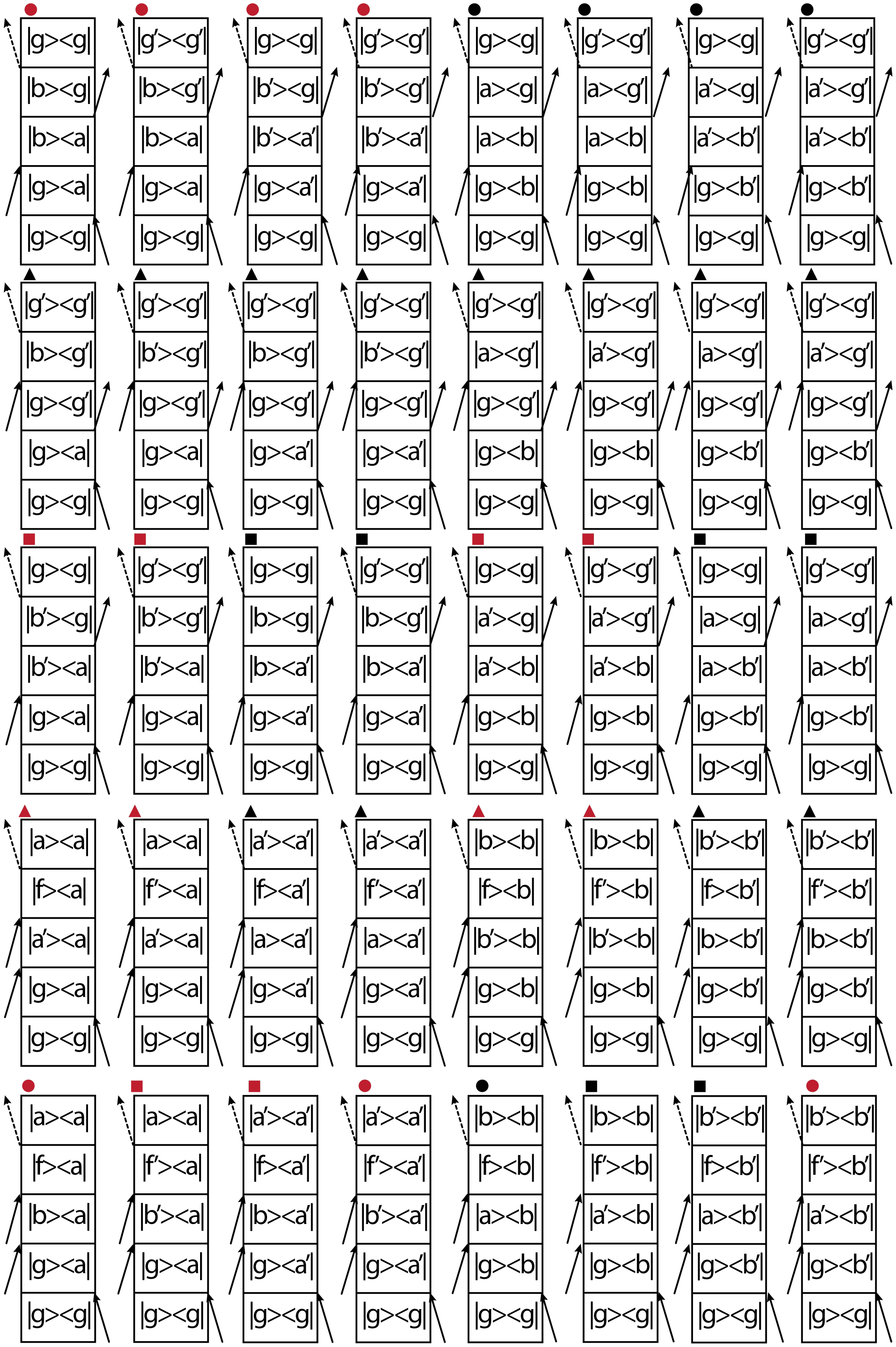

Figure 3.5 Mixed Vibrational-Electronic Model Double-sided Feynman diagrams for signals unique to the mixed vibrational-electronic model (neglecting intramolecular pathways which are shown in Figure 3.2). Cartoon 2D map for these signatures is presented in Figure 3.4. [26,137]

Coherence Transfer

A final note to close out the review of theoretical descriptions of coherence is that there have been several experimental observations of coherence transfer signals, which arise from nonsecular pathways [61,118,148–152]. As mentioned at the beginning of this chapter, most theoretical studies of coherences have made the secular approximation, neglecting terms including coherence transfer and population to coherence transfer (Figure 3.6). There are however a few theoretical studies which have treated nonsecular terms [45,153]. One of these studies primarily focuses on the improved modelling of the BRC special pair band temperature-dependence by including charge transfer states [45]. This study also includes nonsecular terms and shows that coherence transfer is likely to occur when charge transfer states are included [45].

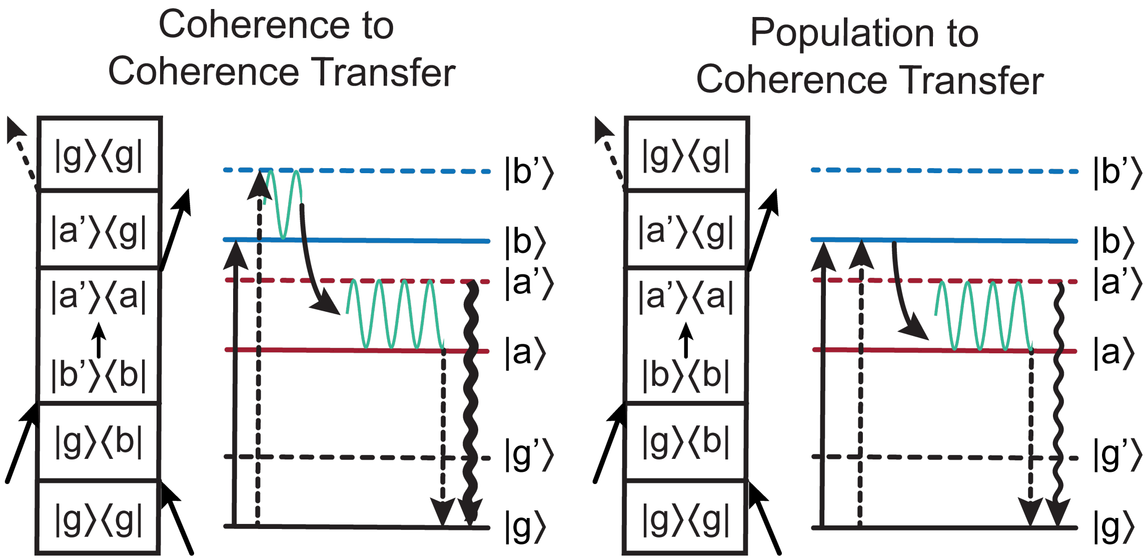

Figure 3.6 Coherence Transfer Pathways. If the secular approximation is neglected several new pathways emerge where coherence transfer is allowed [45,153]. (Right) DSFD and LMID depicting coherence to coherence transfer. (Right) DSFD and LMID depicting population to coherence transfer.

Section 3.2 Coherences in Bacterial Reaction Centers and Constituent Monomers

Coherences in the Bacterial Reaction Center

As mentioned at the beginning of this chapter, the first observation of coherences in any photosynthetic protein complex were in Bacterial Reaction Centers (BRC) at cryogenic temperatures [5]. These studies were performed on R-26 mutant BRCs from *Rhodobacter sphaeroides* as well as the D_{LL} mutant BRCs from *Rhodobacter capsulatus* using 45- and 80-fs pulses centered on the lower excitonic special pair state, P_*. R-26 BRCs lack the carotenoid but perform energy and charge transfer similar to the wild type reaction centers, whereas D_{LL} BRCs lack the A-branch BPheoa and do not perform charge transfer. The study reported weak, low-frequency periodic modulations of the total pump-probe signal in both BRCs, but more prominently in the D_{LL} mutant which remains in the P_-* state for a longer time than RCs which proceed to charge separation. These oscillations persisted on a picosecond timescale, indicating that coherent vibrational relaxation for certain modes occur on the same timescale as charge transfer processes. In this initial study they considered several possible explanations for these oscillations including vibrational wavepacket motion on the excited electronic state, impulsive Raman excitation of ground electronic state wavepacket motion, and electronic superposition state of different electronic states. The first two proposals can be described as purely vibrational in origin and the third as a purely electronic process.

The conclusion of this initial study was that the long-lived coherences originated from excited electronic state vibrational wavepacket motion delocalized across multiple molecules. The authors proposed that charge transfer occurred adiabatically, modulated by the oscillating delocalized charge distribution on the special pair, and that this may explain the rapidity and efficiency of charge transfer. This initial study was expanded upon by follow-up studies that showed these coherences persisted up to room temperature [56,97] and coherences were present with longer dephasing rates in membrane-bound BRCs [97–99,102]. Studies on a host of mutant BRCs determined that these coherences were delocalized across both special pair molecules and the surrounding protein matrix [30,57,103,154]. Studies which saw P-band coherences form following downhill energy transfer from the B*- and H*-bands suggested a functional importance of these low frequency coherences in the BRCs [51]. Low-frequency coherences have also been observed in spontaneous fluorescence of BRCs, strengthening the assignment of coherences to excited electronic state vibrational wavepacket motion [100]. Other transient absorption studies also observed low-frequency coherences following energy transfer of B* to P* and suggested that rapid energy transfer could create vibrational wavepackets in the upper exciton state, P_{+}^{*} [41,101]. The results of nearly a decade of intense scrutiny of coherent oscillations in BRCs using transient absorption spectroscopy indicate that long-lived low-frequency oscillations on P* are due to delocalized interdimer vibrational wavepacket motion [57].

Not long after the first observation of coherences in photosynthetic proteins using two-dimensional electronic spectroscopy (2DES) in the Fenna-Matthews-Olson antenna complex using [6], two-color electronic coherence photon echo experiments by Lee, et al. resolved coherent oscillations due to electronic superposition states between the B*- and H*-bands of chemically oxidized R-26 BRC from *Rho. Sphaeroides* at 77 K & 180 K. These coherences persisted for several hundred femtoseconds, longer than the electronic dephasing rates of the individual states and longer than the downhill energy transfer process to the special pair, which the authors interpreted to indicate strong correlations between the surrounding protein environment and the B* and H* transition energies. This strong correlation was taken to indicate that the protein protects electronic coherences allowing them to persist long enough to enhance energy transfer processes [58]. In a follow-up two-color coherence photon echo study by Ryu, et al. the coherences between the B*- and H*-bands were reexamined considering vibrational, electronic, and a mixed vibrational-electronic model. The conclusions of this study were that the coherences between the B*- and H*-bands were due to vibrational-electronic mixing between excited electronic states of B* and H* pigments; a 685 cm^{-1} bacteriochlorophyll vibrational mode nearly resonant with the excitonic energy gap of these two states is excited on the ground state of B and is enhanced due to excited state vibronic mixing [60].

A 2DES study also of chemically oxidized R-26 BRCs from *Rho. sphaeroides* and covering the B*- and H*-bands saw oscillatory signals in the cross peaks of B* and H* in the 500 – 700 cm^{-1} range [59]. This study reported 2DES data using both an all-parallel pulse polarization scheme and a double-crossed polarization scheme which selectively excited pathways between nonparallel transitions. In their cross-polarized data they saw two persisting oscillatory modes at ~570 & 750 cm^{-1}. Given the selectivity of the pulse scheme used they were able to eliminate the possibility that these coherences were due to purely vibrational coherences; this initial work concluded that these two modes were electronic in origin [59]. In a follow-up study by the same group, Paleček, et al. [61] showed that the coherences discussed in [59] were due to mixed vibrational-electronic coherences. Paleček, et al. showed how initial excitation of electronic coherences in the

B*-H* crosspeaks could rapidly decay to long-lived ground state vibrational coherences. This follow up study shows some of the clearest evidence of vibronic coherence signatures to date.

Many additional coherence frequencies are present in the study by Paleček, et al. which exhibit destructive-interference signatures at the diagonal peaks; the authors propose a mechanism termed Energy Transfer Induced Coherence Shifts (ETICS) whereby rapid energy transfer from H* to B* and from B* to P* results in the excitation of a ground electronic state vibrational coherence. The “shift” into the ground state acquires a π phase shift which interferes destructively with the ground state bleach pathway at the diagonal peak position. This type of signature is also evident in our observations of coherences in the BRC. However, similar signatures are also present in our monomeric data on Bacteriochlorophyll a and Chlorophyll a, where we do not expect to see any energy transfer. These results are discussed in detail in the Chapters 4-6.

The first 2DES study to look at coherences in BRCs which undergo charge transfer were performed on several different mutants which shifted the P_-* band around; the goal of this study was to correlate changes in energy transfer with coherent oscillatory behavior [62]. While some of the BRCs studied can perform charge separation this study only presents data up to 1 ps, before appreciable charge separation has occurred. This study observes many coherences with similar frequencies to those reported previously in [59] and later in [61] which they interpret as vibronic in origin given the relative amplitudes of different signatures and by comparing which modes are present in different BRC mutants.

A very recent 2DES study on a Q_A-devoid BRC mutant A(M260)W from *Rho. sphaeroides* similar to the mutant studied in this thesis is the first published 2DES study to show strong coherences in the P_-* region [63]. Interestingly this study only resolves low-frequency coherences, in keeping with the early pump-probe studies of the P_-* band, despite also covering part of the B*-band which has been shown to have several high frequency coherence modes [59,60]. All of these coherence results for the BRC are summarized in Table A.2.

Coherences in Bacteriochlorophyll a

An important consideration in the above-mentioned studies of coherence in bacterial reaction centers was the coherent behavior of monomeric solutions of Bacteriochlorophyll a. Many of the BRC studies reference resonance Raman studies of BRCs when comparing the frequencies of coherence modes observed and generally find good agreement which is important in considering the origin of coherences and has been integral in the assignment of vibrational and vibronic origin in several studies [57,60–63]. Early room temperature coherence studies of monomeric BChla did not resolve prominent coherent oscillations [155]; coherence studies of the BRC following this study used this information to inform their conclusions, specifically that coherences in BRCs were not due to intramolecular vibrational modes. Not long after this initial study, another transient absorption study failed to see BChla coherences at room temperature, however, was able to resolve a single low-frequency coherence at 4.2 K [105]. In 1997 a 3-pulse photon echo study by Arnett, et al. observed room temperature coherent oscillations in Bacteriochlorophyll a in tetrahydrofurane and pyridine solutions, several of which were in the same frequency regime as the low-frequency oscillations observed in the

BRC [111,112]. The first 2DES study of BChla in several different solvents found that the majority of oscillatory signals were due to the solvent with the exception of two higher frequency modes, 550 & 730 cm^{-1}, which were present in all the different samples. This study was used to strengthen the assignment of coherence in the Fenna-Matthews-Olson complex as electronic in origin [115]. However, an ultrafast pump probe study of Chlorophyll a published a year prior to the study on BChla with 2DES showed a large number of oscillatory modes which were interpreted as vibrational in origin given their frequency match to resonance Raman and their phase-behavior [114]. Several 2DES studies of coherence in Chla also saw many strong coherence modes which were assigned to vibrational origin [77,116].The vibrational properties of BChla and Chla are not very different from one another. Huang-Rhys factors in both molecule are $S \cong 0.01$ [127,129], with Chla being slightly more strongly vibronically coupled than BChla. Recently a 2DES study of coherences in BChla also showed several low-frequency modes which were assigned to vibrational origins [78]. These coherence results for BChla are summarized in Table A.1.

Section 3.3 Signal Analysis Method

The most straightforward method for analyzing coherences in 2DES data involves 1) fitting and subtracting out exponential population dynamics, 2) Fast-Fourier transformation with respect to t_2 to generate a three-dimensional frequency solid, and 3) analysis of the most prominent coherence modes with respect to frequency and two-dimensional phase and amplitude distribution. Some coherence studies have focused on the oscillatory signals in single 2D point (ω_1,ω_3) [6,64,106] or the (t_1,t_2) for a single

ω_3 [58,60], but considering the full 3D matrix simultaneously provides a more rigorous way to compare to the toy models in Section 3.1.

Most experimental coherence studies to date have focused on coherences of the real rephasing signal. The rephasing signal contains similar information as the nonrephasing signal but is sometimes preferred due a higher signal to noise ratio; the real rephasing signal is used instead of the real absorptive signal because it offers better pathway selectivity. Recently coherence studies have analyzed the complex rephasing signals, which provide an additional method for separating out coherence pathways based on the sign of the oscillations. This was first proposed in a theoretical study of coherences in quantum dots [120] and first demonstrated in a 2DES study of coherences in P3HT photovoltaic materials [119]. This method of coherence analysis has notably been used to explain destructive interference signatures in BRCs [61].

In this thesis 2DES data is fit using a user-defined multi-exponential model which includes damped oscillatory terms, allowing for the simultaneous fit of exponential population dynamics and oscillatory coherence dynamics. This model is used to fit the entire 2DES data simultaneously using a global search algorithm, explained in detail elsewhere [156]. The exponential portion of the fit is subtracted from the 2DES data, leaving an oscillatory residual signal. If no oscillatory signals are included in the fitting model slow oscillatory signals may be fit as fast decay components, resulting in a distorted residual. For this reason, it is important to include damped oscillators in the fitting model especially in systems with strong low-frequency coherences. In the case of the BRC and BChla presented in this thesis, low-frequency modes are not very prominent, and choice of fitting model was not found to be critical.

After removal of the populations kinetics, the oscillatory residual is Fourier transformed with respect to t_2 using a Fast Fourier Transform (FFT) function in Matlab. Data is typically zero-padded from 350 to 1000 points. In the case where either the real or imaginary part of the signal is analyzed separately, both the $+\omega_2$ and $-\omega_2$ contain the same information and the size of the matrix can be reduced by half. This is particularly important as an interpolated full resolution 2DES data set can be several gigabytes in size. In the case where we want to look at the separated positive and negative coherence frequency components, $\pm\omega_2$, we perform the fitting for the real and imaginary parts of the rephasing data separately; this is necessary because the fitting algorithm cannot work with complex valued data. Following subtraction of the fit from the real and imaginary parts, the complex residual is reconstructed by adding the components together $Re[S_{res}] + i \cdot Im[S_{res}]$. The rest of the analysis is the same as for the real rephasing signals except that the full FFT matrix must be retained as the $+\omega_2$ and $-\omega_2$ contain different information.

Following Fourier transformation to ω_2 coherence frequency, the data can be analyzed in a variety of ways. Often the first analysis used is to take the Frobenius norm of the 3D frequency solid (3.3) to look at which modes are present in the data. The Frobenius norm sums over the ω_1 and ω_3 axes, resulting in an amplitude spectrum of ω_2 representing all of the oscillatory components present. The Frobenius norm is given by:

$$|S(\omega_2)| = \sqrt{\sum_{i,j} \left| S\left(\omega_{1,i}, \omega_{3,j}, \omega_2\right) \right|^2} \quad (3.3)$$

Frobenius spectra for BChla and the BRC are presented in Chapters 4 & 5. Peaks in the Frobenius spectra correspond to prominent coherence modes and the baseline of the spectrum represents the amount of oscillatory noise in the spectrum. A useful first step in interpreting the coherence data is to compare the frequencies of peaks in the Frobenius spectrum with values from the vibrational spectroscopy literature and exciton difference frequencies, in the case of a system with multiple coupled transitions.

Several factors can contribute to ambiguity when trying to attribute a certain peak frequency to one of the model systems presented in Section 1.1. The width of a peak in the Frobenius spectrum is affected by multiple factors and is fundamentally limited by the lifetime of the oscillatory mode being resolved. In the case of rapidly dephasing electronic coherences, the width is expected to be quite large, whereas typical linewidths for Chlorophyll and Pheophytin vibrations have been measured using hole-burning to be < 5 cm^{-1} [131]. Experimentally, the factor that most affects the peak widths is the coherence frequency resolution, $\Delta\omega_2$, determined by the length of the t_2 scan. For most experiments presented here the t_2 scan is 3,500 fs which corresponds to $\Delta\omega_2 = 9.6$ cm^{-1}. The width of peaks can be impacted by inhomogeneous effects where the same mode may have a slightly different frequency or dephasing rate in different parts of the 2D spectrum. Additionally, if a sample has many coherences, closely spaced modes which cannot be resolved by the experiment may appear as one broad peak. This is particularly evident in the low-frequency region of Frobenius spectra of both BChla (Figure 4.6) and the BRC (Figure 5.6) as BChla and BPheoa have very spectrally congested vibrational spectra (See Table A.4). A final note is that the maximum resolvable coherence frequency is determined by the Nyquist frequency, which is defined as half the sampling rate. For the experiments presented here, the sampling rate of the waiting time, t_2, is 10 fs which corresponds to a Nyquist frequency of 1,667 cm^{-1}. Because our ability to resolve high frequency modes is also impacted by the duration of our pulses, which for the experiments presented in this thesis range from 9 – 14.5 fs, we cannot confidently resolve coherence frequencies greater than 1,110 cm^{-1} (Nyquist frequency using the largest pulse duration).

Another standard way to represent the coherence data is to plot the 2D (ω_1,ω_3) distribution for given coherence frequency, ω_2. These plots are referred to as coherence maps if plotting the absolute value of the FT signal, and phase maps if plotting the phase angle of the FT signal. Plotting the coherence data in this way allows for comparison with the expected coherence maps for the toy models presented in Section 1.1 as well as the real absorptive signal. Several coherence maps are presented for BChla and the BRC in Chapters 4 and 5. If analyzing the complex signal of either rephasing or nonrephasing, comparing the amplitude distribution for a given coherence frequency of the -ω_2 and +ω_2 can help in interpreting a mode where the model assignment is not clear from the real signal maps. By identifying the magnitude and sign of the (ω_1,ω_2,ω_3) frequencies that lead to a particular signal, we can develop new models to explain the system being studied. This approach has been used in understanding signals in both the BChla and the BRC data sets which are not readily explained by the simple models in Section 1.1.

When comparing coherence signals to the toy models and theoretical studies described in Section 1.1 it is important to also consider the impact that the experimental apparatus has on the coherences observed. Several recent studies have characterized the impact that the laser spectrum has on the coherences excited, where the pulse bandwidth and pulse duration can act as a filter for specific coherence pathways [157] or even distort the coherence signatures [158]. The filtration effects of pulse duration and bandwidth were exploited in early studies we did on Chlorophyll a to filter specific subsets of pathways based on the vibrational displaced oscillator model [77]. Two-Color Rapid

Acquisition Coherence Spectroscopy (T-RACS) utilizes the amplitude shaping capabilities of the AOPDF pulse shaper (Dazzler, Fastlite) to shape the two pumps so they are centered about the different transition energies of the DSFD pathways in Figure 3.2 [77]. The shaped pump spectra pathway selectivity made it possible to resolve individual pathways with a fixed t_1, such that the waiting time could be scanned out to long times at a decreased overall acquisition time. This study presents some of the first 2DES coherence data of Chlorophyll a and demonstrated the importance of the pulse spectra in exciting specific coherence pathways [77].

Section 3.4 Time-Frequency Analysis Methods

In addition to the standard Fast Fourier Transform analysis described in the previous section, we can implement time-frequency analysis methods previously used primarily in signal processing and in characterizing ultrafast pulses. Several coherence studies have begun using sliding window Fourier Transforms and wavelet analysis to comment on the temporal dynamics of coherences present in transient absorption [159] and 2DES data [66,160,161]. These and other time-frequency methods are very enticing tools as they could help us resolve dynamical behavior of coherences along t_2. In particular, mixed vibrational-electronic models theorize that electronic coherences should rapidly decay or transfer to a vibrational coherence which should result in time-dependent frequency shifts. Being able to resolve these kinds of dynamics would be a very useful and more direct way to confirm the presence of vibronic signatures in coherence maps.

The pros and cons of several different time-frequency analysis methods have been characterized elsewhere [162]. Briefly, Sliding Window Fourier Transform methods where a window function is convolved with the t_2 domain data is able to resolve some time-dependent behavior of coherence modes but is limited by the time-frequency uncertainty relationship. This method is most useful in a system with few coherence modes which are well spaced apart spectrally; in the case of BChla containing systems, which typically contain many closely spaced vibrational frequencies, a sliding window Fourier transform method cannot offer reliable conclusions. Sliding window Fourier transform methods may be mode appropriate if using an experiment that selectively excites a few modes such as Two-color Rapid Acquisition Coherence Spectroscopy (T-RACS) [77] or highly selective pulse polarization schemes [59,61].

Wavelet transform methods work around the time-frequency uncertainty relationship by convolving the t_2 domain data with an oscillatory wavepacket function. Scaling the wavelet functions changes which oscillatory component in the signal data is constructively amplified. In this analysis method the temporal resolution is frequency dependent, as the ability to resolve low frequency modes requires a large temporal window. This method also suffers from frequency bleed-through, that is systems like those studied here with many prominent modes within 100 cm^{-1} of one another, the wavelet convolution is not selective enough to distinguish between them. Attempting to make conclusions about individual modes or general behavior of the system being studied is then muddled.

The time-frequency analysis method found with the fewest drawbacks in the study by Volpato & Collini, a Smoothed-pseudo Wigner-Ville method, is difficult to implement in Matlab as it requires symbolic integration which Matlab is poorly suited for and so has not yet been implemented in coherence analysis [162]. Sliding window Fourier transform and Wavelet analysis methods have been used although due to the frequency bleed-through described above must be interpreted with caution. Time-frequency analysis still require careful consideration and should be tested before being integrated into routine coherence analyses.

CHAPTER 4 2DES OF MONOMERIC BACTERIOCHLOROPHYLL A

Bacteriochlorophyll a (BChla) is the most prominent chromophore in Bacterial Reaction Centers of several well studied species of purple bacteria and is also found in abundance in purple bacterial light harvesting complexes. While there have been an abundance of vibrational spectroscopy studies, including various types of Raman spectroscopy [163–174], spectral Hole Burning (HB) [175], and Fluorescence Line Narrowing (FLN) experiments (10, 21), and steady state measurements (many summarized in [176]) performed on monomeric BChla, there have only been a few ultrafast electronic spectroscopy studies of this system [78,105,111–113,115,155]. Given the prominence of this molecule in bacterial photosynthesis, BChla is an important model system for understanding the behavior of bacterial photosynthetic protein complexes.

In this chapter we will start by reviewing some basic properties of Bacteriochlorophyll a before presenting 2DES results of monomeric BChla in solution. The final portion of this chapter will describe the coherences observed in monomeric BChla samples. In Chapter 6, the BChla results presented here will be compared with the coherences observed in the Bacterial Reaction Center protein complex (Chapter 5).

Section 4.1 Bacteriochlorophyll a Properties

Structure & Electronic Spectra

Bacteriochlorophyll a is one type of porphyrin derivative found in photosynthetic protein complexes. Figure 4.1 shows the structure of BChla; BChla is a large multi-ring planar molecule with very low symmetry and measures about 10 Å on each side. In the center of the hydrocarbon macrocycle are four nitrogen atoms which bind to a magnesium ion, Mg^{2+}, in the center of the structure. Bacteriopheophytin a (BPheoa) is another tetrapyrrolic molecule found in Bacterial Reaction Centers that is very similar in structure to BChla but lacks the Mg^{2+} ion. Different types of Bacteriochlorophyll and Bacteriopheophytin molecules are distinguished from one another by the side chains bound to the edges of the macrocycle, and bacteriochlorins are differentiated from chlorins, commonly found in plants, by increased hydration and lower conjugation.

The electronic structure of porphyrins are generally described by the Gouterman model [177] where there are four electronic transitions, two of which are in the Q-band in the visible-near IR region and two which are in the Soret band in the UV region. Figure 4.2 shows room temperature linear absorption spectra of the Q-band of monomeric BChla in several solutions. The two peaks in the Q-band are referred to as Qy and Qx, named for the transitions' polarization direction along the macrocycle in Figure 4.1. The two peaks in the Soret band are also aligned along the x and y axes in Figure 4.1, but will not be discussed in this thesis. This model of four electronic excited states is common for most porphyrin molecules. However, several recent studies of the Q-band structure in chlorophyll a (Chla) have found evidence of vibronic mixing between the Qy and Qx

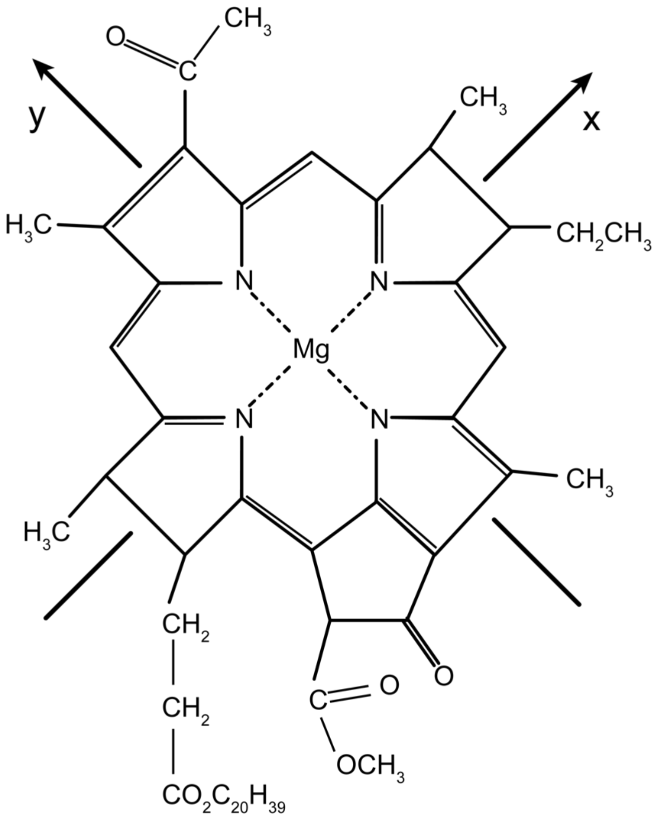

Figure 4.1 Bacteriochlorophyll a structure. Like other chlorin molecules, BChla has a central Magnesium ion. BChla is more hydrated than its chlorophyll analogue. The Gouterman model predicts two perpendicular transition dipoles, oriented along the **x** and **y** axes, denoted in the above diagram [177].

transitions, obscuring the assignment of specific peaks [130,176]. The study by Reimers, et al. [176] develops a model for the electronic and vibrational properties of 32 porphyrins and related macrocycles, and also predicts vibronic coupling between Qx and Qy transitions of BChla but to a much lower degree than in Chl a.

Part of the reason for this lower predicted coupling strength between Qy and Qx in BChla is the large energy gap between these transitions; at room temperature in isopropanol the Qx band is >4000 cm^{-1} higher in frequency than the Qy band [176]. There are three main features in the room temperature linear absorption spectra in Figure 4.2: the lowest energy electronic transition is the Qy band peaked at ~12,850 cm^{-1} (778 nm),

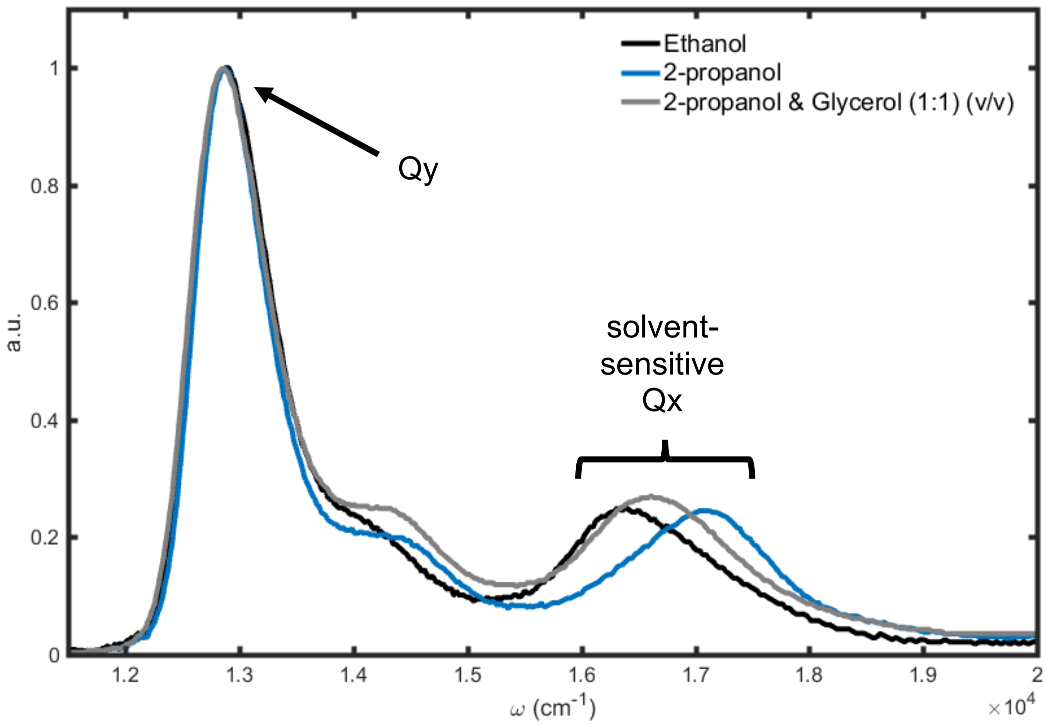

Figure 4.2 Room temperature linear absorption spectra of Bacteriochlorophyll a in several solvents. The visible-near IR portion of the BChla absorption spectrum is presented, where the strongest peak corresponds to the lowest energy electronic state, Qy. A shoulder on the blue-edge of Qy is a vibronic shoulder of Franck-Condon active vibrational modes, and the bluest peak corresponds to second lowest energy electronic state, Qx. The spectral location of Qx is very sensitive to solvent coordination to the central Mg^{2+}. In addition to the 4 nitrogen molecules, the Mg^{2+} is coordinated by one solvent molecule in isopropanol (2-propanol) and by two solvent molecules in ethanol [164]. The increased coordination results in redshift of ~30 nm or ~750 cm^{-1}. The mixed 2-propanol:glycerol solvent shows a shift between the 5- and 6-coordinated case, potentially evidence for a mixture of 5- and 6-coordinated molecules.

to the blue of Qy is a vibrational sideband, and finally the Qx band is found at ~16,000 cm^{-1}.

Mg^{2+} Coordination

For the three solvents used in Figure 4.2 the Qy band remains relatively static with some small shifts (~2 nm) whereas the Qx band shifts by nearly 750 cm^{-1} (30 nm) depending on the choice of solvent. This behavior has been well documented in metalloporphyrins and is related to the number of solvent molecules which are coordinated with the BChla monomers [164,176,178–181]. The Mg^{2+} ion in the center of

BChla (and Chla) is coordinated by the 4 nitrogen atoms in the center of the macrocycle (Figure 4.1); in solution the Mg^{2+} acquires up to two additional nucleophilic coordination partners (or ligands) from solvent molecules which can participate from either side of the macrocycle plane (See Figure 1 in Fujiwara, et al. for clarification [180]). The number of additional ligands is related to the nucleophilicity of the solvent, the presence of competing solvent molecules (water is a strong coordinating aggregator in metalloporphyrin solutions [178,182]), and the stericity of the solvent. The solution of BChla in isopropanol in Figure 4.2 is composed of mainly 5-coordinated molecules, evident by the blue-shifted Qx band [179]. Upon 6-coordination, the Qx band red-shifts, as seen for BChla in ethanol in Figure 4.2 [164]. Addition of glycerol to the isopropanol solution results in a slight red shift of the Qy band and a red-shift of Qx (Figure 4.2) in between the 5- and 6-coordinated cases discussed above. This location of Qx likely indicates a mixture of 5- and 6-coordinated BChlas in solution.

Coordination to the Mg^{2+} can also lead to aggregation in BChla and Chla samples in nonpolar solvents, where keto-side groups of one molecule coordinate with the Mg^{2+} of another [182]; this aggregate behavior also occurs in dry films and can be mediated by water molecules in solution. Additionally, coordination has been shown to be temperature-dependent [179] and in the case of frozen samples, coordination is freezing-rate dependent. Coordination number has also been shown to impact the vibrational frequencies in metalloporphyrins [178,180,183], which could serve as a useful tool in distinguishing between coherences on molecules with different coordination numbers in the reaction center. Unfortunately for this study, most of the vibrational modes which are coordination sensitive are outside the resolvable frequency range of our current experimental apparatus.

Vibrational Structure

Both BChla and BPheoa have a large number of vibrational modes which have been well characterized by many vibrational spectroscopy approaches, including Raman spectroscopies [163–174], spectral Hole Burning (HB) [175], and Fluorescence Line Narrowing (FLN) experiments (10, 21). BChla and BPheoa have many vibrational modes in common [171,184]. Several of the prominent vibrational modes observed in chlorins like Chla and bacteriochlorins like BChla are common with the vibrational structure of base porphyrins [185] and several studies have assigned the origin of the bacteriochlorin vibrations to specific macrocycle skeletal vibrations [127,165]. The vibrational modes for several studies are summarized in Table 4.1. The majority of Raman studies resonantly excite the Soret or Qx bands, as the fluorescence signals from excitation of Qy are very strong. A few experiments on dry BChla films where fluorescence is largely quenched have been able to directly excite the Qy band [169,171]; these experiments are summarized in Table 4.1 for easy comparison with the coherence modes. The vibronic coupling strengths in chlorins and bacteriochlorins are generally weak with Huang-Rhys factors typically $S \leq 0.01$ [127]. A Hole Burning study of the Qy band of Chla measured the vibrational lifetimes to be on the order of a picosecond at 5 K [131]. Many of these vibrations are similar in frequency to BChla modes and have similar structural assignments [165], so we can also expect the Qy vibrational modes to have similar lifetimes in BChla.

Deviations from Basic Model in Porphyrins

Several experimental [128,175] and theoretical studies [127,129] have characterized differences in the ground and excited state vibrational frequencies of both Chla and BChla. Differences in the ground and excited state vibrational frequencies correspond to asymmetry of the absorption and emission spectra for a given electronic transition. Deviations of the absorption and emission bands from mirror symmetry are evidence of deviation from the “basic model” of porphyrin electronic bands [127,186], which utilizes several assumptions including the harmonic approximation, the Condon approximation, and linear electron-phonon coupling. This asymmetry is also indicated by the derivation of two sets of differing Franck-Condon factors from Hole Burning (HB) and Fluorescence Line Narrowing (FLN) spectroscopies [130,187]. These Franck-Condon factors are necessary for calculating radiative and nonradiative electronic processes. Several studies have focused on addressing this asymmetry and developing new models to accurately describe the electronic and vibrational structure of these porphyrins, and in doing so improve models of photosynthetic electronic energy transfer [188].

A recent study of vibronic coupling in Chla Qy band has found evidence that the Condon approximation, which assumes an electronic transition has no dependence on nuclear coordinates, is not valid and leads to vibrationally induced mixing of electronic states [130]. A BChla study by Rätsep, et al. [127] combines FLN experiment with HB data [175], RR data [189], and density functional theory to model the vibrational structures of the ground and excited states. In this study they eliminate two possible explanations for the band asymmetry, anharmonicity of the electronic states and Franck-

Condon progressions, and provide evidence that Duschinsky rotations are responsible for the large band asymmetries [127].

Most theoretical models of electronic transitions assume Duschinsky rotations, the rotation of ground or excited state nuclear coordinate planes about the vertical energy axis, are negligible [190]. When Duschinsky rotations are present, a vertical transition from a vibrational mode on one electronic state to another results in a linear combination of vibrations along multiple nuclear coordinates [191]. Duschinsky rotations have been previously invoked to describe the behavior of several molecules and complexes, including theoretical modelling of the Green Fluorescent Protein chromophore [192], ultrafast transient absorption of cresyl violet [193], fluorescence spectra of Chla in Light Harvesting Complex II [187], Raman spectra of etioporphyrins [194], and in UV spectra of (E)-Phenylvinylacetylene [188]. Additionally, a theoretical study by Sando, et al. [191] has shown that Duschinsky rotations could increase the rate of electron transfer in molecular systems.

Table 4.1 Select vibrational studies of monomeric BChla and BPheoa. Vibrational spectroscopy studies with the most similar experimental conditions as the 2DES presented in this thesis. Additional studies are summarized in Table A.4.

Reference	[171] Czarnecki, et al.		[169] Diers & Bocian		[184] Lutz, et al.	
Experiment Type	NIR RR		NIR RR		Resonance Raman	
T	25 K		15 K		35 K	
Band Excited	BChla Qy	BPheoa Qy	BChla Qy	BChla Qx	BChla Qx	BPheoa Qx
λ₀ (nm)	800	750	750	568	579	528.7
Vibrational Frequencies (cm^{-1})	90	90	88	164	140	145
	126	126	164	190	170	183
	154	137	190	257	198	220
	166	150	235	288	262	235
	181	163	257	310	295	250
	191	183	340	353	355	269
	203	220	359	383	384	290
	225	233	383	423	423	345
	242	243	396	440	442	372
	259	264	423	458	570	391
	287	272	509	487	595	425
	329	280	536	685	635	473
	344	328	567	733	670	525
	359	338	581	800	687	567
	363	356	655	864	712	585
	375	372	685	908	735	617
	383	383	733	1033	765	658
	405	393	776	1120	795	688
		420	800	1135	855	712
			843	1340	897	724
			864	1544	927	753
			908	1614	952	780
			1182		970	840
			1290		1005	881
			1382		1035	935
			1527		1065	964
			1614		1117	995
					1140	1038
					1162	1060
					1212	1103
					1242	1134
					1290	1215
					1342	1242
					1377	1282
					1402	1326
					1418	1348
					1450	1377
					1470	1400

Section 4.2 2DES of Bacteriochlorophyll a

As outlined in the previous section, there are many aspects of our understanding of the electronic and vibrational structure of porphyrins, including Bacteriochlorophyll a and especially Chlorophyll a, that are evolving and require additional experiments with which to test theoretical models. In our 2DES experiments on Bacteriochlorophyll a, we will examine some ways that the current models for the electronic and vibrational structure succeed and where they fall short. This work on 2DES also serves as an important control study for comparing against the multichromaphoric Bacterial Reaction Center (BRC) data.

Experimental Parameters

2DES experiments on BChla were performed using the hybrid diffractive-optic and pulse-shaping based setup described in Chapter 2.2 using pump and probe pulses generated by a Degenerate Optical Parametric Amplifier (DOPA), described in Chapter 2.2. The pump and probe spectra are shown in the top and right panels of Figure 4.3, respectively. For this experiment we centered the pump spectrum to the blue of the Qy peak; this was done so that we would have the pump bandwidth to excite any accessible vibrational frequencies on the Qy state. Centering the pump bandwidth to 750 nm resulted in some amplitude shaping of the pump spectrum due to the pulse shaper. The probe bandwidth is centered on Qy and retains nearly the entire 200 nm bandwidth of the DOPA output. The pump and probe were compressed to 14.3 and 10 fs, measured with PSI (based on SPEAR [195]) and Multiphoton Intrapulse Interference Phase Scan (MIIPS [196]), respectively. Using a SHG FROG the autocorrelation FWHM was measured to be 23.7 fs. The pump and probe pulse energies were 7.8 μW (15.6 nJ) and

10.4 μW (20.8 nJ) and were focused to spot sizes of 0.0298 mm^2 and 0.0159 mm^2, respectively.

Table 4.2 2DES of BChla Experimental Parameters

Pump Duration (fs)	Probe Duration (fs)	Pump Energy (μW)	Probe Energy (μW)
14.3	10	7.8	10.4

BChla samples were prepared from dry powder purchased from Sigma Aldrich. Samples were prepared in a dry N_2-pressurized glove box with solvents degassed with

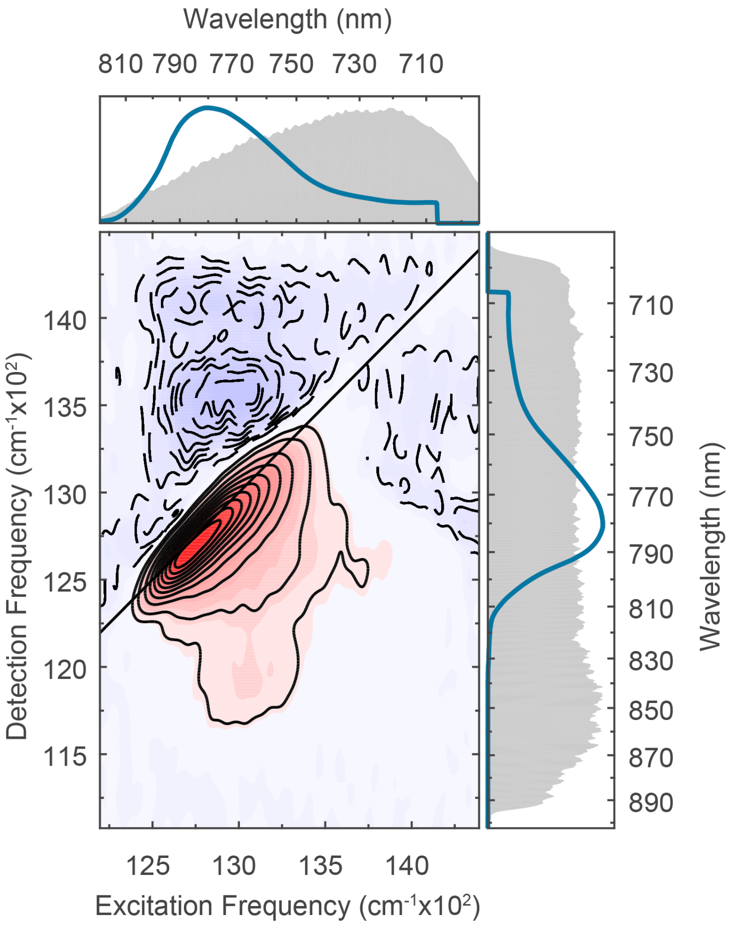

Figure 4.3 2DES of BChla monomer in isopropanol at 77K. (Center) The t_2 = 200 fs real Absorptive 2DES spectrum shows a strong positive diagonal peak corresponding to the Q_y transition, which shows a large inhomogeneous broadening along the diagonal. Cross peaks above and below the diagonal line ($\omega_1 = \omega_3$) are due to excited state absorption and ground state bleach signals, respectively. (Top) The 77K linear absorption spectrum for BChla in isopropanol (blue) is shown with the pump spectrum (grey); the pump spectrum is centered to the blue of the Q_y peak so as to probe excited state vibrational coherences. (Right) The 77K linear absorption spectrum (blue) is shown with the probe spectrum (grey) which is centered on the Q_y band.

N_2 gas. For the experiments presented in this thesis, BChla powder was dissolved in degassed isopropanol to achieve an OD(776 nm) = 0.39 in a $l = 380\ \mu m$ pathlength cell ($C = 0.159\ mM$ using $\varepsilon(775.5\ nm, isopropanol) = 6.55x10^4 \frac{1}{M\ cm}$ [197]). The sample was loaded into a LN2 cryostat (MicrostatN, Oxford Instruments) and held at 77 K. Attempts to measure the 2DES signal at room temperature have not yet been successful, as a large scatter signal grows within a few seconds of exposure to the laser. This may be due to exposure to oxygen which could damage the sample, or due to the build up some triplet state. The data presented here was taken by scanning the coherence time $-10 \leq t_1 \leq 390\ fs$ in 10 fs steps, and the waiting time $-50 \leq t_2 \leq 3500\ fs$ in 10 fs steps.

The 77 K real absorptive spectrum of BChla (Figure 4.3) shows a strong peak corresponding to the Qy transition along the diagonal at ($\omega_1 \cong 12{,}740$ cm^{-1}, $\omega_3 \cong 12{,}700$ cm^{-1}), showing a small redshift in the detection frequency that appears almost instantaneously following excitation. The Qy peak shows large inhomogeneous broadening along the diagonal, as well as negative ESA signals above the diagonal and positive GSB signatures below the diagonal. The lifetime of the Qy excited state is on the order of tens of nanoseconds [197], significantly longer than the 3.5 ps scan analyzed here. Figure 4.4 shows several real absorptive and real rephasing 2D spectral for different waiting times. Over the course of the 3.5 ps scan the Qy peaks remain roughly constant. Several off-diagonal peaks in the real absorptive spectra (top column, Figure 4.4) above and below the diagonal decay slowly. The Qy band also retains the inhomogeneous broadening for the entire 3.5 ps scan, indicating slow spectral diffusion. Several t_2 traces at various (ω_1,ω_3) points in the real rephasing 2D spectrum are shown in Figure 4.5; the t_2 trace along the diagonal shows a slight increase in rephasing signal, which attribute to laser power drift. This power drift does not significantly affect the coherent dynamics, determined by comparison with other experimental data sets.

Section 4.3 Coherences in Bacteriochlorophyll a

Until recently, only a few time-resolved electronic spectroscopy experiments had been performed on BChla. One of the earliest coherence studies on BChla at room temperature concluded that BChla exhibited no coherent dynamics [155]. Several studies shortly thereafter observed a low-frequency coherence at 4.2 K [105] and several strong coherence modes at room temperature [111,112]. The results of this earliest study were referenced in several studies of coherences in BRCs [57] and other BChla containing protein complexes [115,138]. More recent ultrafast studies have reported additional contradictory results; a pump probe study on BChla in various solvents observed several low-frequency modes [113] whereas a 2DES study of BChla in multiple solvents reported that most coherences were due to nonresonant solvent response and only two coherences were due to the BChla [115]. The most recent study of coherences in BChla used 2DES, reporting primarily low frequency coherences and proposing that these low-frequency vibrations were coupled [78]. The frequencies of coherences observed in BChla and some experimental parameters from these studies are summarized in Table 4.3.

The data presented here were taken with higher coherence resolution and shorter pulses than most of the previous coherence studies on BChla. Given the waiting time scanning parameters and the pulse durations used for this experiment, the FT coherence frequency, ω_2, frequency resolution is $\Delta\omega_2 = 9.8\ cm^{-1}$ and the Nyquist frequency is $\omega_2 = 1{,}166\ cm^{-1}$. The fit to the full real rephasing signal is shown in Figure 4.5, along with the oscillatory residuals at various (ω_1,ω_3) in the real rephasing spectrum. 2D points were chosen based on the vibrational displaced oscillator coherence amplitude distribution (Figure 3.2). The diagonal peak (circle, Figure 4.5) shows complicated oscillatory behavior indicative of a sum of oscillators with different

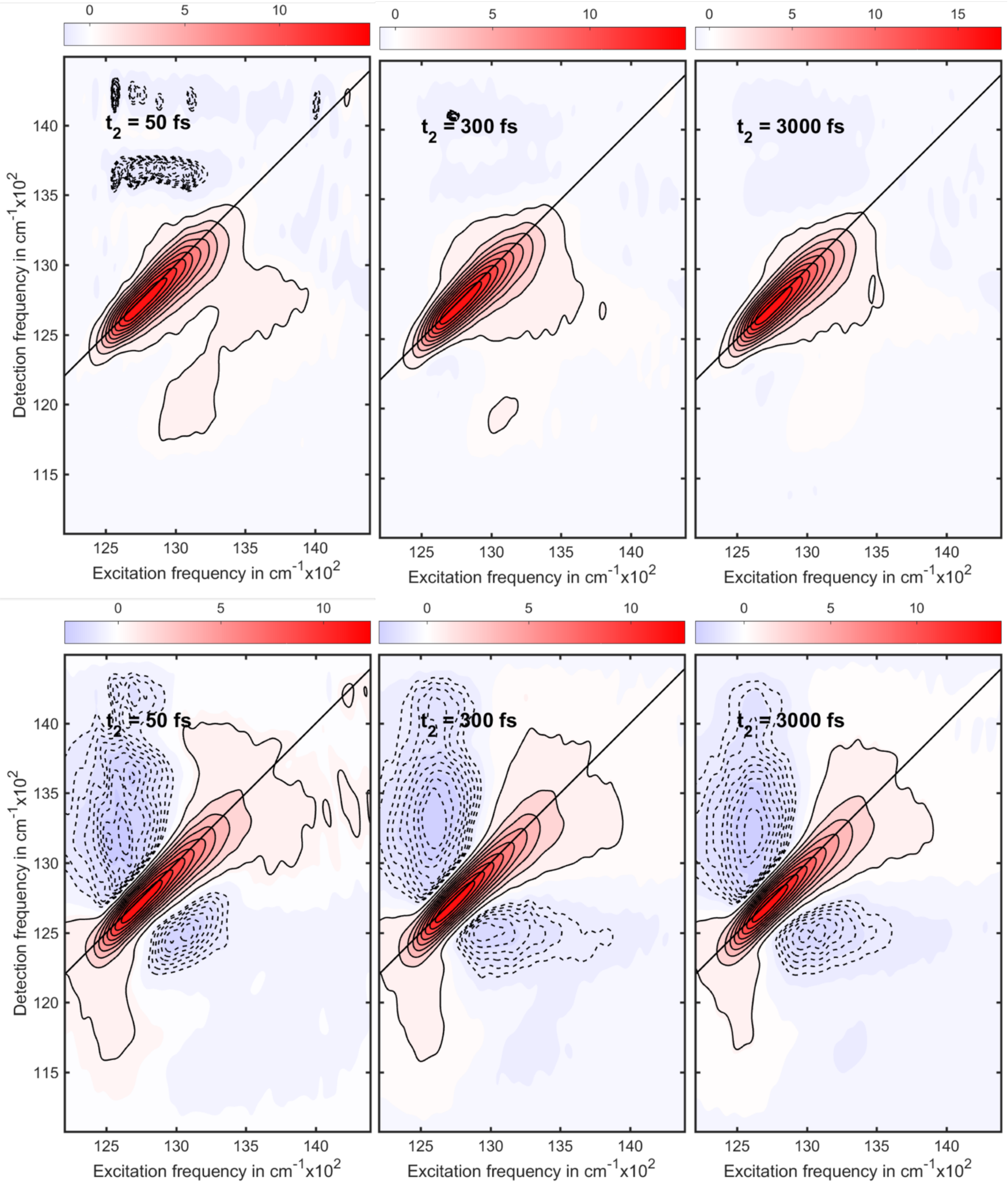

Figure 4.4 Real absorptive (top) and real rephasing (bottom) spectra of monomeric BChla in isopropanol at 77K at several waiting times. t_2 = 50 fs (left), 300 fs (center), and 3000 fs (right). Real absorptive data were studied in kinetic analysis of the population dynamics. The real rephasing signal is used in coherence analysis in order to take advantage of the selectivity of specific pathways.

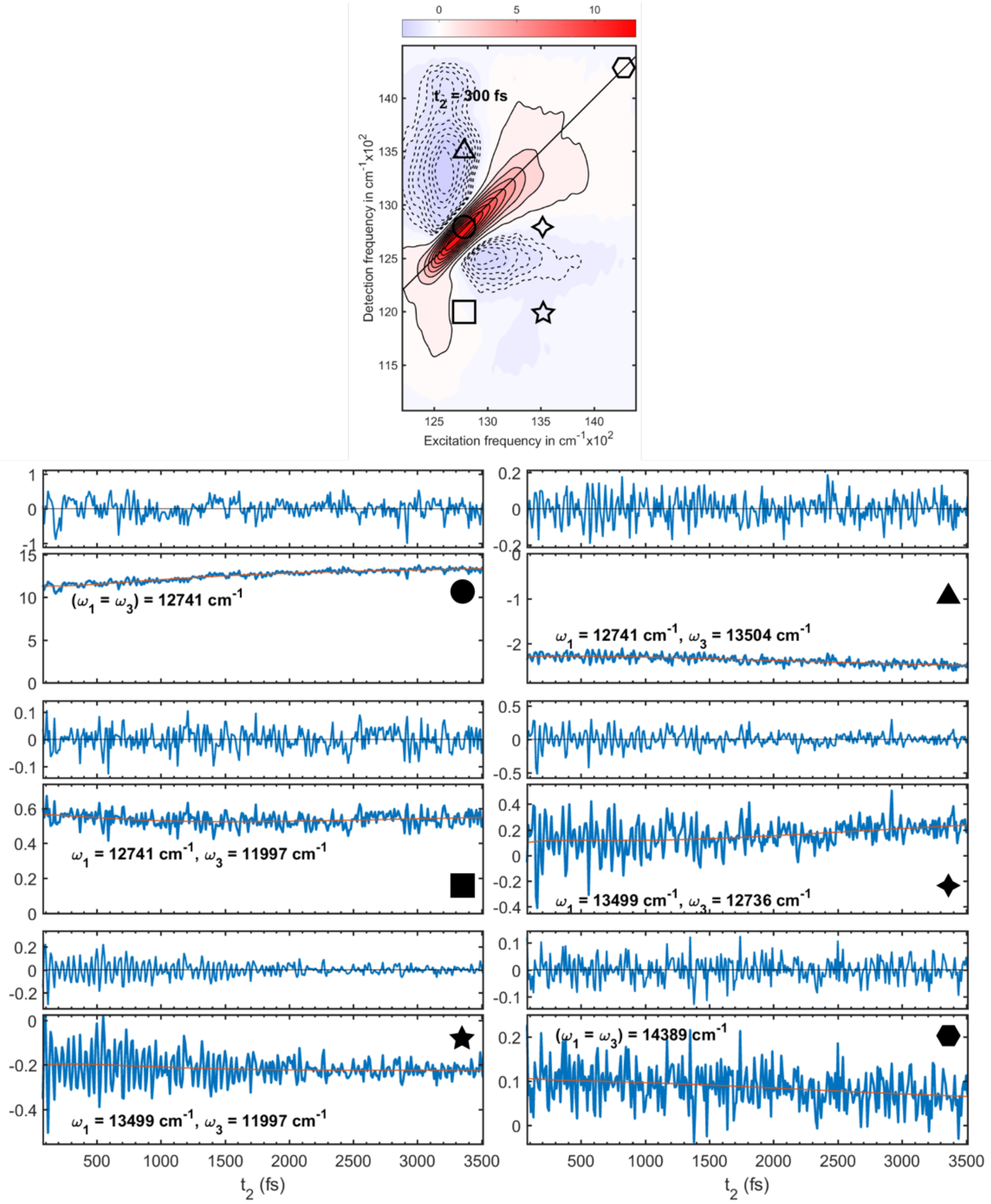

Figure 4.5 Coherent oscillations in t_2 traces of the real rephasing signal of BChla real rephasing 2DES data. (Bottom) Several t_2 traces are shown for different points in the 2DES spectrum of BChla in isopropanol at 77 K. (Top) 2D real rephasing spectrum at t_2 = 300 fs with symbols showing location of t_2 traces plotted below. For each 2D point the t_2-dependence of the full signal is shown (blue) with the fit trace (orange); above the full signal is shown the residual signal following subtraction of the exponential terms of the fit. (Top left t_2 trace) The t_2 trace through the Q_y peak at ($\omega_1 = \omega_3$ = 12,741 cm^{-1}) shows a strong positive signal with small oscillatory signals on top; the residual shows oscillatory behavior at multiple frequencies. (Bottom right t_2 trace) A t_2 trace at ($\omega_1 = \omega_3$ = 14,389 cm^{-1}), far from where we expect see oscillatory signal demonstrates the noise background present in the 2DES data, showing oscillatory signals which are 1/10th the signals along the Q_y diagonal. (Remaining t_2 traces) t_2 traces chosen at points corresponding to signals for a ω_2 = 740 cm^{-1} coherences using the vibrational displaced oscillator model. t_2 traces at (ω_3 = 13,499 cm^{-1}) in particular show strong oscillatory signals similar to those expected from a single mode.

frequencies, whereas the residuals of several off-diagonal peaks show strong oscillations at what looks like a single frequency (triangle and 5-point star, Figure 4.5). These off-diagonal peaks are spaced about ~740 cm^{-1} away from the diagonal line.

Table 4.3 Summary of Coherence Studies of Bacteriochlorophyll a. *Coherence/Phase map plotted for this mode.

Reference	[198] Chachisvilis, et al.	[111] Arnett, et al.	[113] Shelly, et al	[115] Fransted, et al.	[78] Yue, et al.	This Study
Experiment Type	TA	3PE	PP	2DES	2DES	2DES
T	4.2 K	N/A (RT)	RT	N/A (RT)	RT	77 K
Pump/Probe Pulse Duration (fs)	86/86	13/13	60/60	15.6/15.6	35/35	14.3/10
Coherence resolution (cm^{-1})	51	16.7	2.78	22.4 - 33.4	66.7	9.8
Coherence Modes (cm^{-1})	104	185	63	550	80	36
		210	81	730	160	69
		340	91/92		200	201*
		480	108		280	232
		560	127		340	348*
		730	165		400	385
		790	195			454
		890	210			573*
		1180				621
						689
						740*
						768
						903*
						1032
						1058
						1192
						1251
						1316
						1473
						1486
						1542

Frobenius Spectrum

Fourier transforming the real rephasing residual transforms the waiting time, t_2, to the coherence frequency, ω_2. Taking the Frobenius norm of the 3D-frequency solid, summing over ω_1 and ω_3 as described in Equation 3.3, generates the Frobenius spectrum (Figure 4.6). The Frobenius spectrum shows several prominent peaks sitting atop a noise pedestal. The frequencies of these peaks are summarized in Table 4.3 (and with BRC

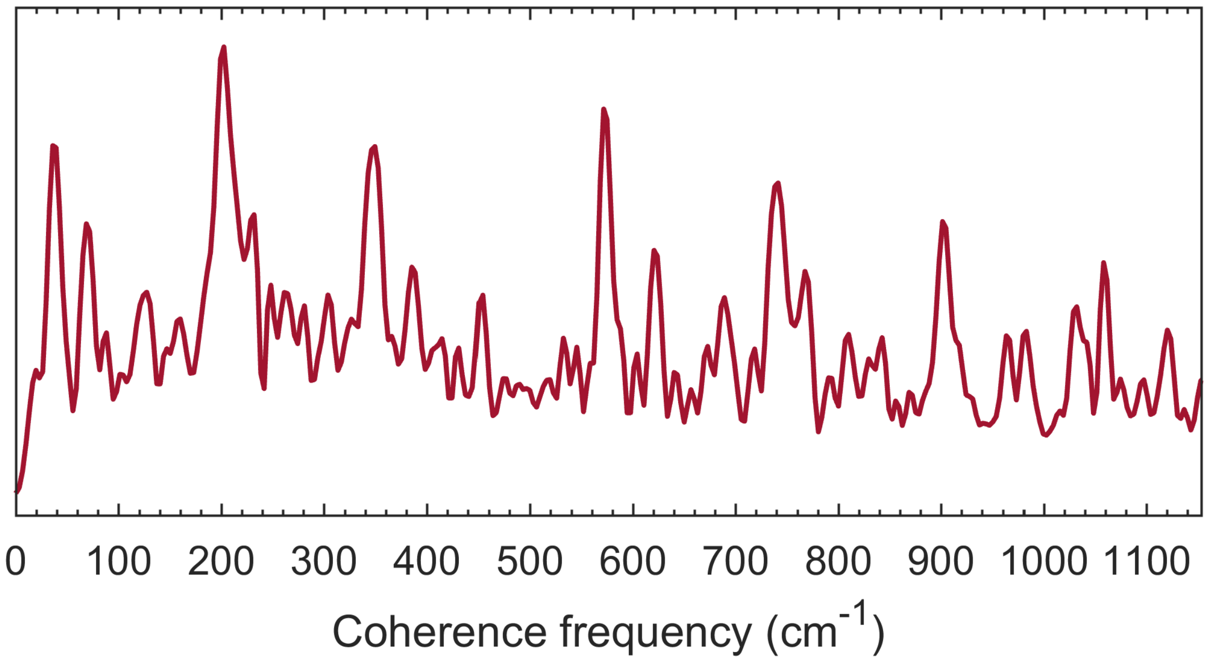

Figure 4.6 Frobenius spectrum for monomeric BChla in isopropanol. The Frobenius spectrum is calculated for the entire 2D spectrum and is normalized by the integrated spectral amplitude. Several prominent peaks are present (Peak frequencies listed in Table 4.3) which correspond well to known vibrational modes (Table 4.1)

coherence frequency in Table A.3). Comparison of the peak frequencies from the Frobenius spectrum (Table 4.3) with the vibrational frequencies in Table 4.1 suggests that these modes are vibrational in origin. For several of these frequencies there are small differences in the frequency observed here versus in the vibrational spectroscopy experiments, however many of the observed modes in Figure 4.6 are within the experimental resolutions of the vibrational spectroscopy experiments. This Frobenius spectrum shows reproducible peaks frequencies when compared across data sets from different experimental runs, within the experimental $\Delta\omega_2$ resolution, with peak amplitudes sensitive to the bandwidth of the pump and probe spectra.

Coherence Maps

Figure 4.7 and Figure 4.8 show coherence amplitude maps for several prominent peaks from the Frobenius spectrum in Figure 4.6. Several diagonal lines are drawn on each of the coherence maps; in addition to the diagonal line at $(\omega_1 = \omega_3)$ there are lines offset from the diagonal line by factors of the coherence frequency $(\omega_1 = \omega_3 \pm n \cdot \omega_2)$. The vibrational displaced oscillator and electronic dimer described in Section 3.1 each predict coherence signals offset from the diagonal by the coherence frequency, which is the vibrational mode or the exciton difference frequency, respectively. Additionally, only the vibronic model from Section 3.1 predicts signatures which lie off of these diagonal lines. These lines serve as a qualitative guide for interpreting the origin of the coherence amplitude. Also drawn on top of the coherence maps in Figure 4.7 and Figure 4.8 are

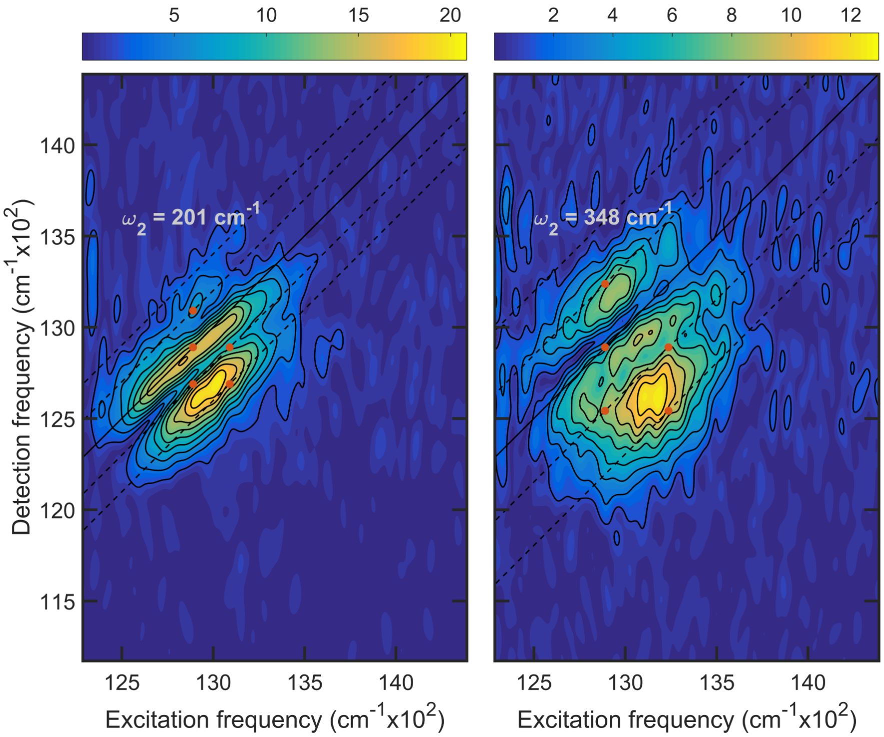

Figure 4.7 Low-frequency real rephasing coherence maps of BChla in isopropanol. Coherence frequencies (ω_2 = 201 & 348 cm^{-1}) were chosen from the prominent peaks in the Frobenius spectrum (Figure 4.6). Orange circles are overlaid in the chair pattern from the displaced oscillator model (Figure 3.2) centered at the Q_y peak. The inhomogeneous broadening in this system smears the coherence signals along the diagonal.

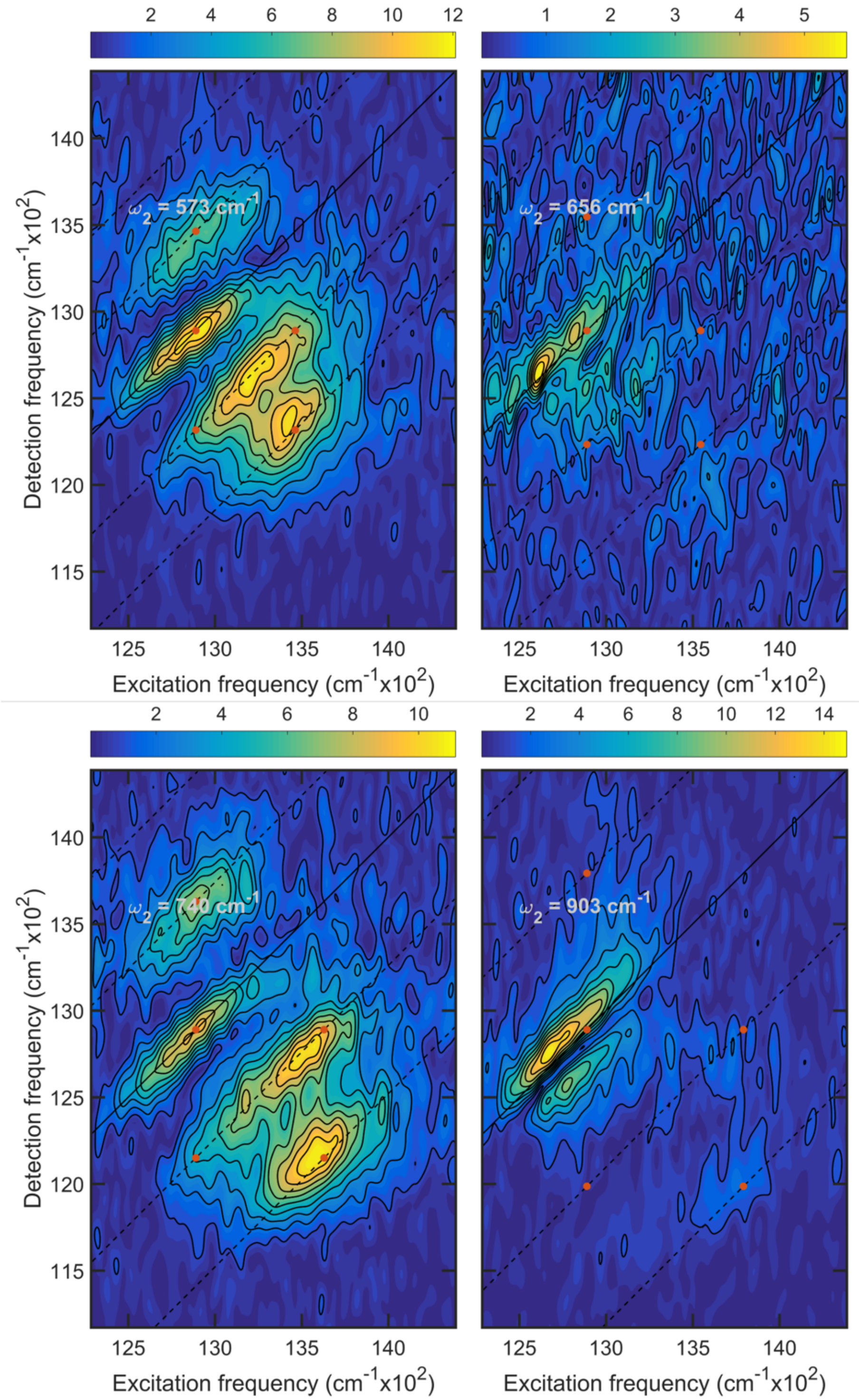

Figure 4.8 High-frequency real rephasing coherence maps of BChla in isopropanol. Coherence frequencies (ω_2 = 573, 740, & 903 cm^{-1}) were chosen from the prominent peaks in the Frobenius spectrum (Figure 4.6). Coherence frequency ω_2 = 656 cm^{-1} is plotted for comparison to a BPheoa mode in the BRC data in Chapter 5. Orange circles are overlaid in the chair pattern from the displaced oscillator model (Figure 3.2) centered at the Q_y peak. The inhomogeneous broadening in this system smears the coherence signals along the diagonal.

orange circles in the characteristic chair pattern of the vibrational displaced oscillator (Figure 3.2).

The majority of signals in these maps match the chair distribution well, with several caveats. The low-frequency modes in Figure 4.7 show significant signal between the diagonal lines, which would indicate a vibronic coherence based on the models presented in Section 3.1. It is however unlikely that these low frequency modes could be related to vibronic coherence, as Qy is well isolated from the next nearest electronic transition (Qx is ~4000 cm^{-1} to the blue) and the samples are low enough concentration to assume each molecule is an isolated monomer. Similar behavior of the low-frequency modes was also observed in Chlorophyll a in unpublished data; these signals may be due to a Stokes shift but this requires further consideration. The current explanation for this behavior is that pathways with opposite phase interfere with one another for the low-frequency modes as the spacing between pathways is smaller. In the high-frequency modes, the ω_2 = 573 & 741 cm^{-1} show the best agreement with the displaced oscillator chair model, but the ω_2 = 901 cm^{1} also shows weak signals in the expected distribution (Figure 4.8). The signals off the diagonal in the ω_2 = 903 cm^{-1} map are much weaker than the diagonal peak, which we attribute to the limited pump bandwidth. The ω_2 = 656 cm^{-1} coherence map does not correspond to a prominent peak in the Frobenius spectrum (Figure 4.6) but is shown for the purpose of comparison to an interesting mode in the BRC, to be discussed in detail in Chapter 6.

Other unexplained signatures in the coherence maps are nodal lines near the diagonal in the ω_2 = 348 and 903 cm^{-1} maps. These signatures look similar to destructive interference signals recently observed in Bacterial Reaction Centers by Paleček, et al. [61]; in this study the authors propose a mechanism for these destructive signatures based on ultrafast energy transfer between the chromophores of the BRC. In the case of the spectrally isolated Qy band of monomeric BChla we do not expect any energy transfer to occur, nor do the population dynamics show evidence for energy transfer. We can confirm that these signatures are due to destructive interference by looking at the complex rephasing coherence signal; this analysis method is similar to the real rephasing analysis and is described in Chapter 3. Figure 4.9 shows the $+\omega_2$ and $-\omega_2$ coherence maps for the 6 coherence modes from Figure 4.7 and Figure 4.8. The ω_2 = ±901 cm^{-1} coherence maps clearly show signal amplitude along the diagonal line. Taking the real part of the complex rephasing signal then adds out-of-phase signals, resulting in the destructive interference signature in Figure 4.7 and Figure 4.8. Looking at the separate sign components of the coherence frequency was first demonstrated by Song, et al. [119] and the destructive phenomenon was first described by Paleček, et al. [61]. The ω_2 = 348 cm^{-1} looks as though the nodal line is due to a lack of amplitude on the diagonal, as opposed to destructive interference effects. Understanding these signal is a work in progress that will be facilitated by ongoing theory collaborations.

The complex rephasing signal analysis also allows us to separate out some of the pathways from the vibrational displaced oscillator in Figure 3.2; two of the 8 pathways should oscillate with the $+\omega_2$ and the other 6 with $-\omega_2$. Looking at the high-frequency modes in Figure 4.9 we can see the separation of one diagonal and the single crosspeak above the diagonal from the second diagonal peak and the below-diagonal components, as expected for a displaced harmonic oscillator (Figure 3.2).

Figure 4.10 and Figure 4.11 show phase angle maps for the coherence modes

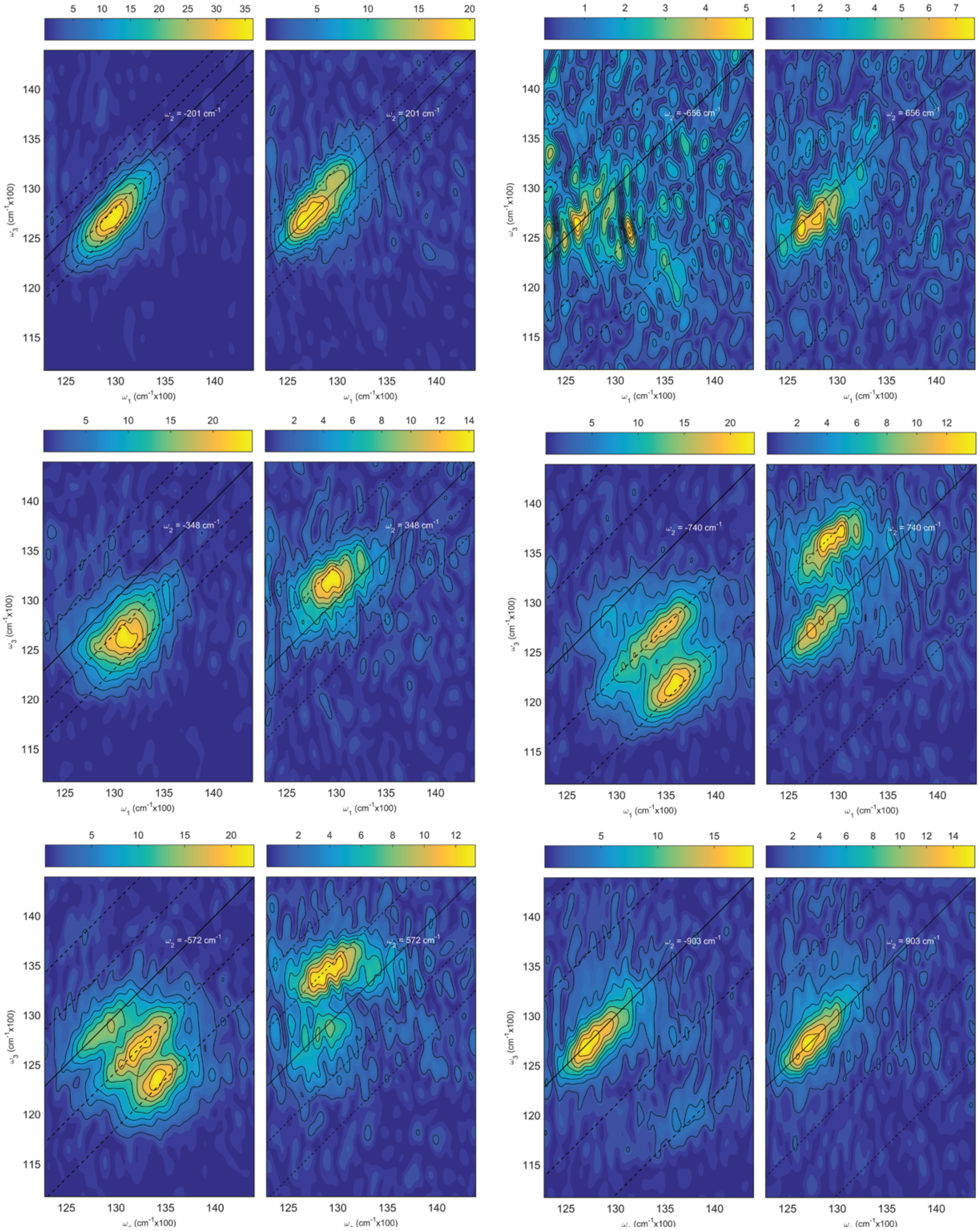

Figure 4.9 Coherence maps from the complex rephasing signal of BChla in isopropanol. Following Fourier transformation of the complex residual, described in Chapter 3, the $+\omega_2$ and $-\omega_2$ coherence maps can be plotted to further distinguish different coherence pathways. Low-frequency maps show one peak per $+\omega_2$ and $-\omega_2$ map above and below the diagonal, respectively. Higher-frequency maps show more peaks maintain the relationship with sign of coherence frequency and location in relation to the diagonal line, with the exception of the peaks on the diagonal. The additional information from using the complex rephasing data strengthens the assignment of these modes to a vibrational coherence and serves as a marker for the BRC.

plotted in Figure 4.7 and Figure 4.8. These phase maps show diagonal bands of phase roughly corresponding to the amplitude peaks in the coherence maps, similar to the predicted phase behavior for a vibrational coherence in a vibronic dimer in the presence of disorder [26]. The phase between neighboring peaks (moving across the phase map in the antidiagonal direction) should be π. The measured phase between neighboring peaks roughly matches this distribution for some of the signals, however there are several deviations from this behavior. Notably, the phase map for the ω_2 = 903 cm^{-1} mode (Figure 4.11), which shows destructive interference-type signatures in the coherence map, shows a π phase jump about the diagonal line where there is a node in the coherence map. Similar behavior is seen in the ω_2 = 656 cm^{-1}.

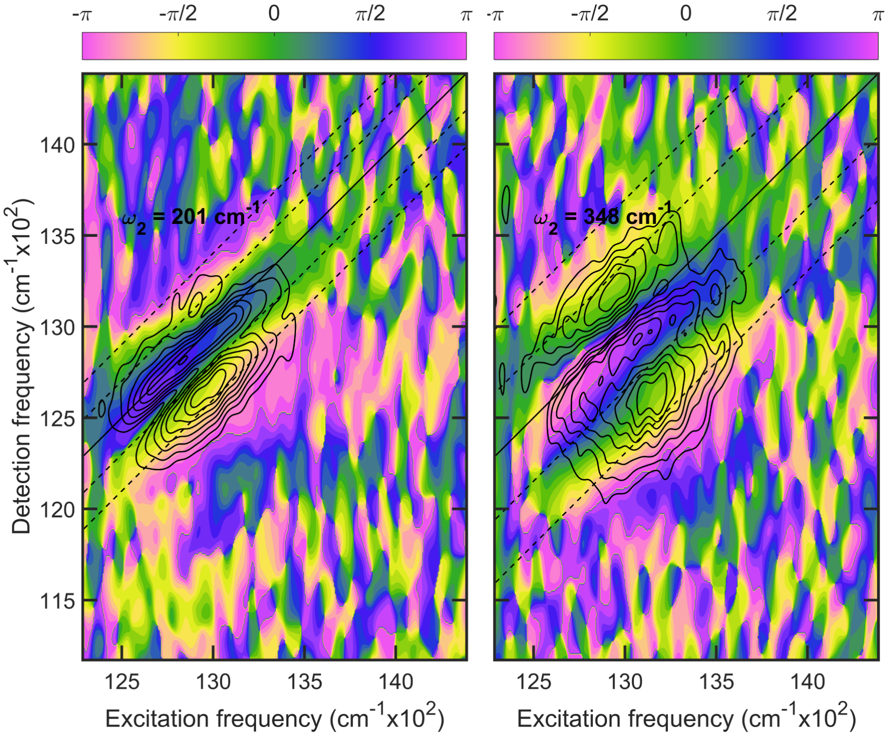

Figure 4.10 Low-frequency real rephasing phase maps for BChla in isopropanol. Phase maps were adjusted for t_2 truncation at t_2 = 80 fs but dividing by a constant phase. For this system phase is banded along the diagonal and adjacent peaks are ~π out of phase. Black contours indicate the 10-100% coherence amplitude.

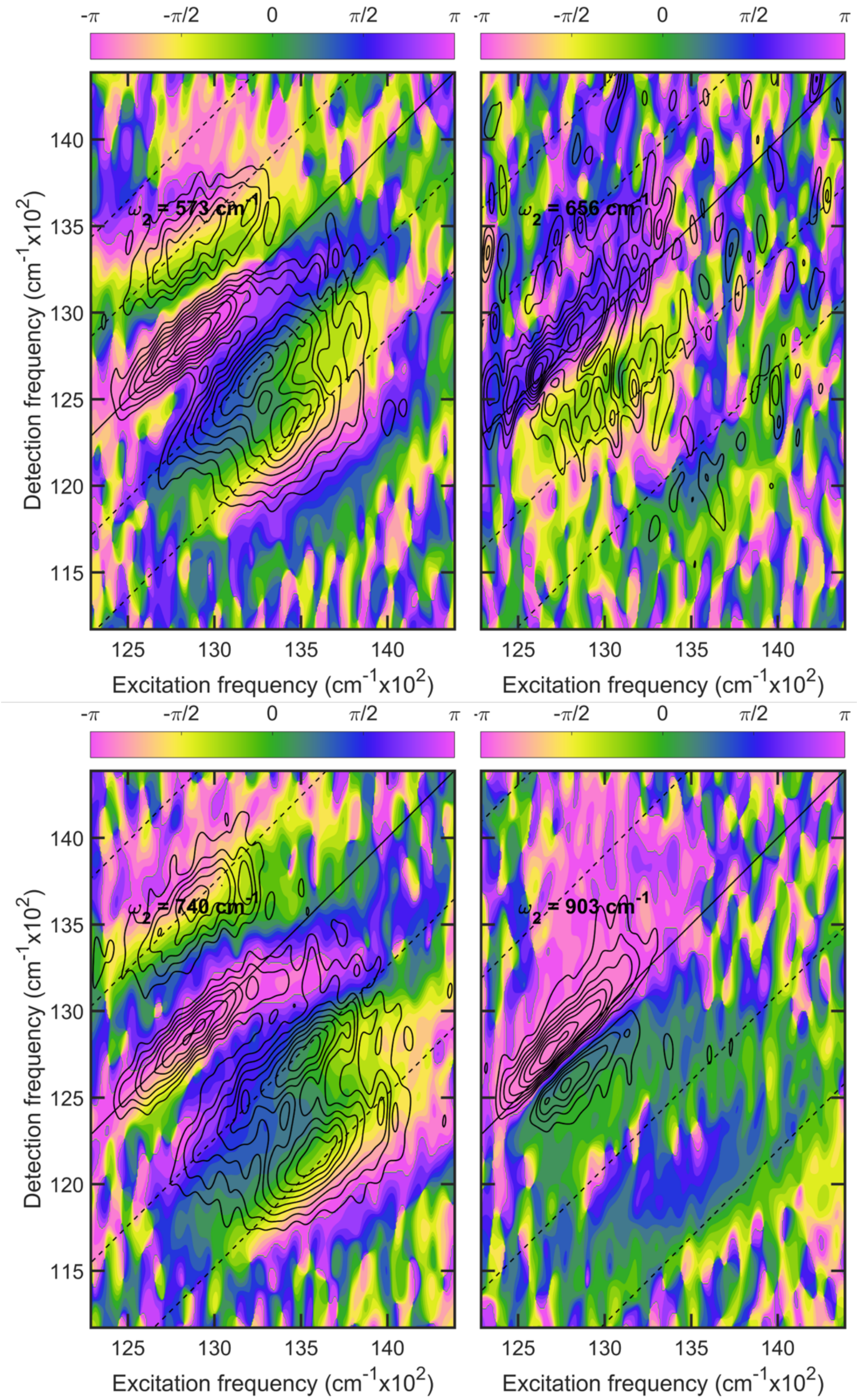

Figure 4.11 High-frequency real rephasing phase maps of BChla in isopropanol. Phase maps were adjusted for t_2 truncation at t_2 = 80 fs but dividing by a constant phase. For this system phase is banded along the diagonal and adjacent peaks are ~π out of phase. Black contours indicate the 10-100% coherence amplitude.

Destructive Interference Signatures & Solvent Considerations

The observation of the destructive interference signals in the BChla real rephasing coherence maps for $\omega_2 = 903\ cm^{-1}$ similar to signatures previously proposed to result from rapid energy transfer [61] was unexpected given our experimental conditions and seemed to suggest several possible explanations: 1. The mechanism for destructive interference has a more general explanation than that proposed by Paleček, et al. [61], or 2. Rapid energy transfer is occurring in our BChla samples. Considering explanation 2., we could hypothetically be seeing energy transfer from the Qy band to the Qx band or from the Qy band to solvent molecules, however the Qx band is > 4,000 cm^{-1} higher in energy than the Qy band and we are incapable of exciting any vibrational modes that could be related to vibronic coupling between Qy and Qx in this experiment. The second possibility, that we are indirectly observing energy transfer from the BChla to coordinated solvent molecules seemed more plausible. A weak 810 cm^{-1} mode in the Frobenius spectrum in Figure 4.6 does not match well with BChla vibrational modes (Table 4.1), but is close to a prominent resonance Raman mode of our solvent, isopropanol, at 820 cm^{-1}. The coherence map at ω_2 = 810 cm^{-1} showed a similar destructive interference signatures as in the $\omega_2 = 903\ cm^{-1}$ coherence map in Figure 4.8, suggesting these features might arise from the same mechanism. In addition to energy transfer from BChla to coordinated solvent molecules, we also considered several phenomena including metal-enhanced nonresonant Raman excitation of solvent modes, vibrational resonance coupling of the solvent via the coordinated Mg^{2+} [183,199–201] , and excitation of solvent vibrations via impulsive solvent dissociation. In any of these cases we would expect changing the solvent to change the frequencies where we could see the destructive interference signatures. In the case of vibrational resonance coupling, the effect would only be visible if a molecule vibrational mode was near resonant with the solvent vibrational mode; fortunately, the BChla has a large number of vibrational modes such that it is likely we could find a suitable solvent to test this theory. We performed additional 2DES experiments on BChla in ethanol, which is a 6-coordinating solvent and has a vibrational spectrum easily distinguishable from isopropanol. These experiments did not show evidence that we were exciting solvent molecules and rather showed very similar Frobenius spectra and coherence maps as the BChla data presented in this chapter. With these considerations, it seems likely that there must be an alternative explanation for the destructive interference signatures observed in the BChla other than that proposed by Paleček, et al [61].

Conclusions

Given the correspondence of peaks in the Frobenius spectrum (Figure 4.6) to well characterized vibrational modes of BChla and the agreement of the coherence map amplitude distributions for prominent modes (Figure 4.7 and Figure 4.8) with those simulated for a vibrational displaced oscillator (Figure 3.2), the coherences observed in BChla are likely vibrational in character. The prominence of many coherence modes has not been previously reported in this molecule [78,113,115,155,198], although the study by Arnett, et al. [111] showed several similar frequencies as those most prominent in this work. Additionally, this study did not observe any significant solvent effects. The characterization of the coherences in BChla is an important step in understanding the coherences present in the large pigment-protein complexes and offers strong evidence that vibrational effects are prominent in ultrafast spectroscopy of BChla.

CHAPTER 5 2DES OF BACTERIAL REACTION CENTERS

The well-separated bands of the BRC Qy region and the availability of many mutant strains, which allow for control over energy and charge transfer properties, make the BRC an excellent system for studying photosynthetic energy and charge transfer. For the same reasons, the BRC is well suited for studying the origin and role of coherent dynamics in photosynthetic processes and is also well suited for testing out theoretical models of coherence including vibronic coherence models.

Past observations of coherences in the BRC are outlined in detail in Chapter 3. Briefly, the majority of 2DES experiments performed on BRCs have studied oxidized reaction centers (R-26 *Rhodobacter sphaeroides*) which transfer energy to P but do not undergo charge transfer [59–61]. These studies have observed a large number of coherent modes with frequencies that roughly correspond to BChla vibrational modes. More recent work on BRCs treated with reducing agents have seen similar modes [62], and a recent study focused on the P_-* band has observed a few low frequency modes [63], similar to early pump-probe observations in the BRC [57]. A summary of several coherence studies of the BRC is presented in Table 5.3.

The following chapter presents the results of our 2DES on two BRC mutants, the W(M250)V and D_{LL} BRC mutants, using the broadband Degenerate Optical Parametric Amplifier (DOPA) light source described in Chapter 2.2, spanning the visible and near-IR frequencies. Following some general remarks about the signals observed in the t_2 domain signals, the coherence signals are presented and briefly discussed. A detailed comparison of the coherences observed in the BRC and those presented on BChla in Chapter 4 comprises Chapter 6.

This work on the W(M250)V BRC mutant is some of the first 2DES performed on bacterial reactions which undergo charge separation. Sister studies of the populations kinetics have solidified the single-pathway model for charge separation and have resolved the weak upper-exciton P_+* [4]. The results presented in this section and Chapter 6 are in preparation for publication and are some of the highest signal-to-noise coherence signals presented in this system.

Section 5.1 2DES of BRCs

BRC Samples

In order to perform high-repetition rate experiments on Bacterial Reaction Centers (BRCs) we have studied two mutants of *Rhodobacter capsulatus* BRC which do not form the long-lived $P^+Q_A^-$ state; W(M250)V and D_{LL} (Figure 5.1). The W(M250)V mutant results from a single amino acid mutation from a valine to a tryptophan which blocks binding of the A-branch quinone [36]. This mutant otherwise behaves like the WT, undergoing rapid energy transfer to P_-* followed by charge separation to $P^+H_A^-$. The second mutant, D_{LL}, results from several point mutations that modify one M-branch alpha helix until it looks like its mirror-partner L-branch. This series of mutations results in an absence of the A-branch BPheo molecule [34] which is evident in a reduced absorbance in the H-band of the linear absorption spectrum compared to WT & W(M250)V (Figure 5.1). This mutation also has several effects on the protein function: energy transfer along the BPheo-containing B-branch to P* occurs similarly to the WT, however charge separation does not occur due to changes in redox potentials [35,202]. This functionally altered D_{LL} mutant allows us to perform some control experiments; for kinetic experiments we can confidently determine the population kinetics of the P_-^* state and for coherence experiments we can use the results when considering the role of charge separation in the observed coherent modes present.

While the W(M250)V and D_{LL} mutant BRCs of *Rh capsulatus* have been well studied by transient absorption spectroscopies [36,40,203], there have not been many vibrational studies of this species and no crystal structures exist, to date. Sequence similarity between BRCs from *Rh. capsulatus* and well-studied purple bacteria species like *Rhodobacter sphaeroides* [203] and *Rhodopseudomonas viridis* has been used to justify the application of studies on these species in interpreting results from the *Rh capsulatus*, as we will also do here.

W(M250)V and D_{LL} BRCs purified proteins in 10 mM Tris Base, pH 7.8 with 0.1% Deriphat 160 C buffer were provided by Chris Kirmaier and Dewey Holten at the University of Washington in St. Louis. The W(M250)V and D_{LL} samples were grown and purified by Phil Laible at Argonne National Laboratory and Steven Boxer and Jessica (Chuang) Seeliger, respectively. BRCs were treated with sodium ascorbate and terbutryn before concentration. Terbutryn is added to ensure that the $P^+Q_B^-$ state does not form as it binds competitively with free quinone [36]; there is a small chance that a small percentage of W(M250)V samples still have Q_A or that charge transfer may occur along the B-branch to Q_B. Sodium ascorbate is added to the samples in order to reduce the P^+ state between laser shots, ensuring that each successive pulse sequence is interacting with the sample in its ground state. Samples were mixed with glycerol to achieve a (1:1) (v/v) ratio to form

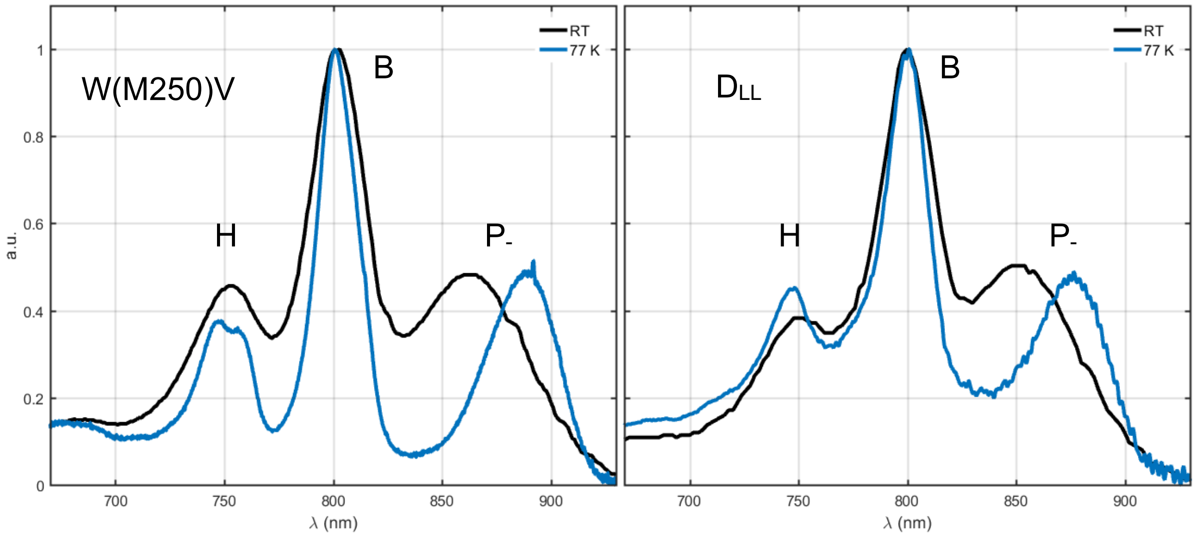

Figure 5.1 Linear absorption spectra for the W(M50)V (left) and D_{LL} (right) BRC mutants. Spectra are shown at room temperature and cryogenic (77K) temperatures. Room temperature spectra were taken using a UV-Vis spectrometer. The 77 K spectra were taken using a CCD spectrometer and a broadband white light source. Spectra are normalized to the peak of the B-band at around 800 nm. There were difficulties in properly subtracting the background of the 77 K D_{LL} spectrum on the blue edge, but this should not effect the location of the band peaks.

a good glass upon freezing. In the W(M250)V BRC 77 K linear absorption spectrum in Figure 5.1 the H*-band shows two peaks. We also see splitting of the B*-band in the 2DES data; splitting of the B*-band in the BRC has been shown to be glycerol-concentration dependent [204].

Samples were prepared to balance the differing optical densities of the three Q_y bands of interest; the B*-band has greater than twice the optical density of the other two bands (Figure 5.1). The sample used in the experiment presented for W(M250)V was prepared with OD(P_-*, 862 nm) = 0.176 at room temperature. BRC samples were loaded in a 380 μm path length cell and held at 77 K during the experiments.

Table 5.1 Experimental Conditions

	Pump Duration (fs)	Probe Duration (fs)	Pump Energy (μW)	Probe Energy (μW)
W(M250)V BRC	14.5	10.3	10.9	14.1
DLL BRC	11.8	14.3	11.8	14.3

Experimental Parameters

2DES experiments were performed using the experimental setup detailed in Chapter 2.2 and with pump and probe pulses from the Degenerate Optical Parametric Amplifier (DOPA) described in Chapter 2.3. Spectra of the pump and probe pulses used in the W(M250)V (D_{LL}) experiment is shown in Figure 5.2 (Figure 5.13) and were compressed to 14.5 fs (14.3 fs) and 10.3 fs (9.9 fs), measured using PSI (based on SPEAR [195]) and Multiphoton intrapulse interference phase scan (MIIPS [196]), respectively. Using SHG FROG the autocorrelation FWHM was measured to be 24.8 fs. Pump and probe energies used in these experiments are listed in Table 5.1. At 77K the B-band optical density increases by about 60% compared to the room temperature OD. For each experiment the coherence time, t_1, was scanned $0 < t_1 < 390$ fs in 10 fs steps; the waiting time, t_2, was scanned $-50 < t_2 < 3500$ fs in 10 fs steps.

Stick spectra in Figure 5.2 & Figure 5.13 show the location of the excitonic energies of the BRC determined through global kinetic fit by Niedringhaus, et al. [4] and are defined in

Table 5.2. Included in the excitonic model is the upper P state, P_+^*, which we assign a spectral location of 11,900 cm^{-1}. As discussed briefly in Chapter 1 the upper-excitonic state of the special pair P has been historically difficult to assign and various experimental and theoretical treatments have placed it anywhere in the range of 12,345 – 12,820 cm^{-1} at cryogenic temperatures [27,33,42–44]. Much of the difficulty is related to the low dipole strength associated with this transition and the overlap of several different transitions in the same spectral region. In Niedringhaus, et al. we were able to resolve the P_+^* state by fitting both the linear absorption spectrum and 2DES spectra [4].

Additionally, as will be discussed in detail in Section 5.3 the P_{+}* is evident in coherence maps of W(M250)V data via transition dipole strength borrowing from B*-band transitions. The excitonic energies presented in

Table 5.2 were determined by fitting to the linear absorption spectrum of W(M250)V BRCs, although some of the constraints were informed by the D_{LL} 2DES data. With the exception of the H_A peak location, which is not present in the D_{LL} BRC, the majority of the spectrum looks similar to W(M250)V BRCs (Figure 5.1). It is worth noting, however, that the lower-exciton of P, P_{-}*, is blue-shifted in comparison to the W(M250)V P_{-}* peak. This behavior is consistent with spectra previously presented on W(M250)V [40]

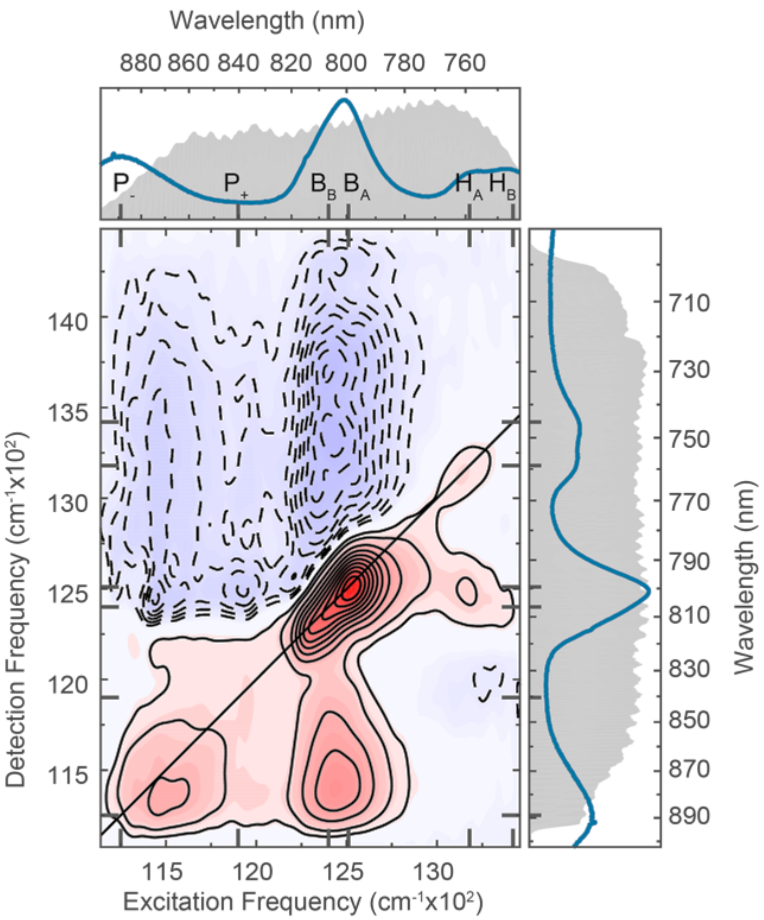

Figure 5.2 Real Absorptive 2D Spectrum of W(M250)V BRC mutant at 77 K and t_2 = 200 fs. 77 K Linear absorption spectrum (blue) with the experiment pump (above) and probe (right) spectra shown in grey with labeled stick spectrum for the excitonic spectrum of states (Table 5.2) [4].

and D_{LL} [35], but indicates that judgement should be applied when considering the P-exciton locations in D_{LL}.

Table 5.2 Excitonic Energy Levels and exciton difference frequencies in the W(M250)V BRC [4].

Excitonic States		P_{-}*	P_{+}*	B_{B}*	B_{A}*	H_{A}*	H_{B}*
	(cm^{-1})	11,250	11,900	12,400	12,510	13,180	13,420
P_{-}*	11,250	0	650	1,150	1,260	1,930	2,170
P_{+}*	11,900	-	0	500	610	1,280	1,520
B_{B}*	12,400	-	-	0	110	780	1,020
B_{A}*	12,510	-	-	-	0	670	910
H_{A}*	13,180	-	-	-	-	0	240
H_{B}*	13,420	-	-	-	-	-	0

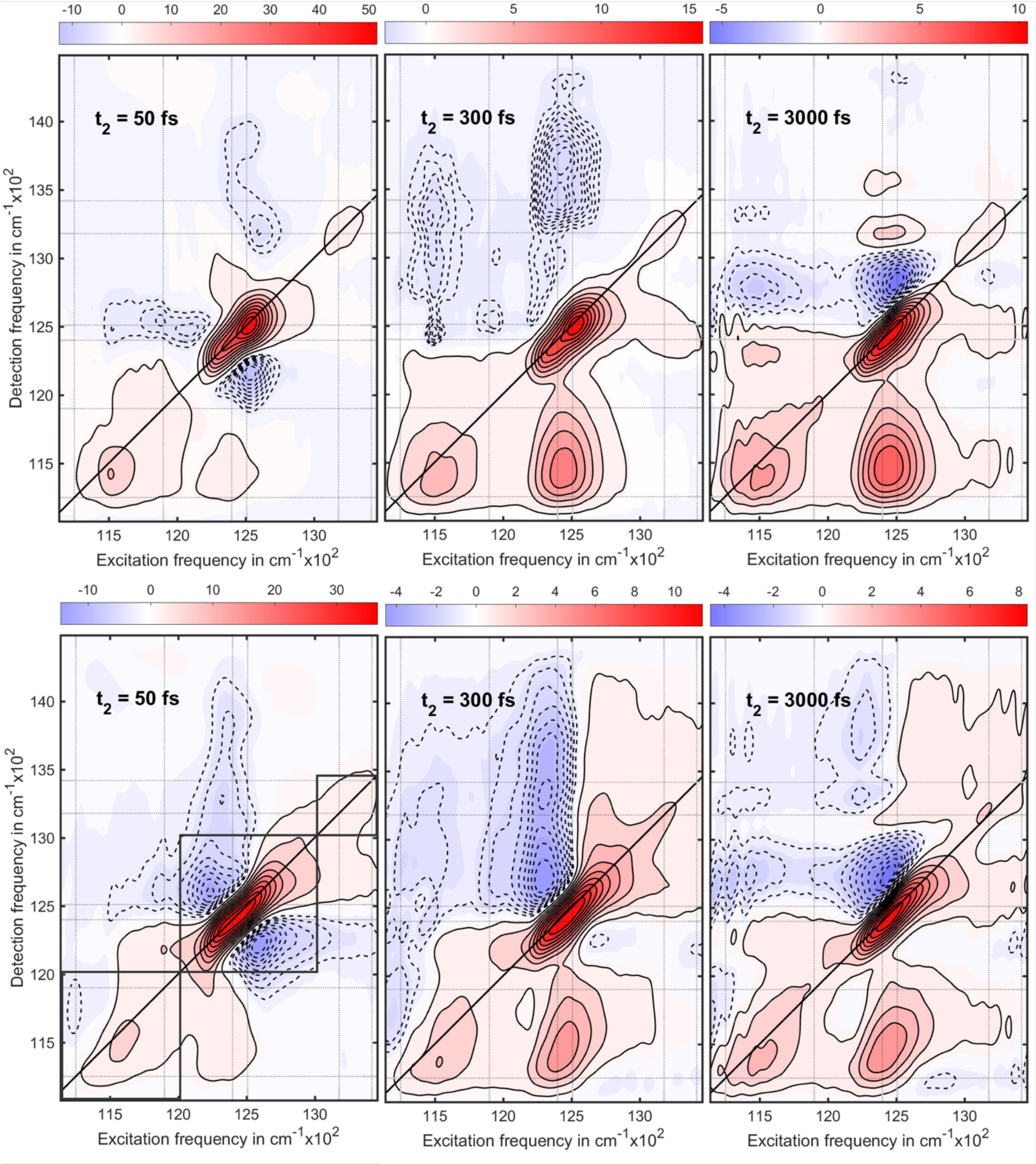

Figure 5.3 Real absorptive (top) and real rephasing (bottom) spectra of W(M250)V BRC mutant. t_2 = 50 fs (left), 300 fs (center), and 3000 fs (right). Real absorptive data were studied in kinetic analysis of energy and charge transfer. The real rephasing signal is used in coherence analysis in order to take advantage of the selectivity of specific pathways. Boxes in t_2 = 50 fs real rephasing figure (lower left) show the regions integrated over for Frobenius spectra in Figure 5.7.

Real Rephasing 2DES of W(M250)V BRC

Figure 5.3 shows the real rephasing spectra of the W(M250)V BRC at several waiting times. At early times we see three strong positive amplitude features along the diagonal ($\omega_1 = \omega_3$) corresponding to the P_-^*, B^*, and H^* bands. The P_+^* is visible at early times along the diagonal at 11,900 cm^{-1} but is much weaker than the neighboring diagonal peaks and very rapidly decays due to internal conversion to P_-^*. At t_2 = 50 fs (Figure 5.3, left column) we already see evidence of downhill energy transfer between the B^* and P_-^* bands and between H^* and B^* as cross peaks below the diagonal. Cross peaks between the A- and B-branch B^* and H^* molecules are evident by the antidiagonal distribution of the two peaks. At slightly longer times (t_2 = 300 fs) we see evidence for energy transfer from H^* to P_-^* as a lower-diagonal cross peak at ω_3 = 11,500 cm^{-1}. After energy transfer occurs to P_-^* the charge separated states form several picoseconds later, with the electron moving from P_-^* to $P^+B_A^-$ and finally to $P^+H_A^-$, evident in the excited state absorption signatures at ω_3 = 12,750 cm^{-1} and ω_3 = 13,400 cm^{-1}. A detailed analysis of the kinetics of these samples is described by Niedringhaus, et al. [4]. Figure 5.4 summarizes the energy and charge transfer pathways and timescales. Also evident in the early time spectra in Figure 5.3 is a large inhomogeneous broadening of the two B-bands. In the Magic-angle polarization 2D spectra there is a clear separation of B_A and B_B peaks following energy transfer to P-* [4], though this is not evident from the P-polarized spectra.

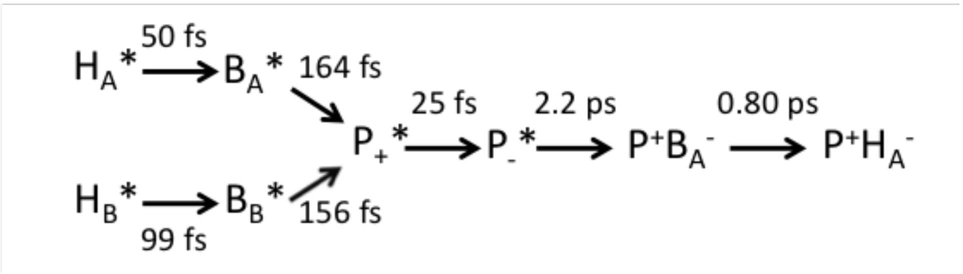

Figure 5.4 Energy and Charge Transfer Pathways and Rates for the BRC. From Niedringhaus, et al. [4].

After charge separation, the B_A* peak shows evidence for spectral diffusion as a loss of elongation along the diagonal, whereas the B_B* peak retains the diagonal elongation due to maintained correlation. These differences are attributed to local electronic perturbations upon electron transfer, which only proceeds along the A-branch, and induces Stark shifts of the molecules and the surrounding protein environment. Stark shifts are also evident at both B* peaks after charge separation to the $P^+H_A^-$ state, found to be 205 & 135 cm^{-1} for the B_A* and B_B* bands, respectively (B_A* 12,510 cm^{-1} → 12,715 cm^{-1}; B_B* 12,400 cm^{-1} → 12,535 cm^{-1}) [4].

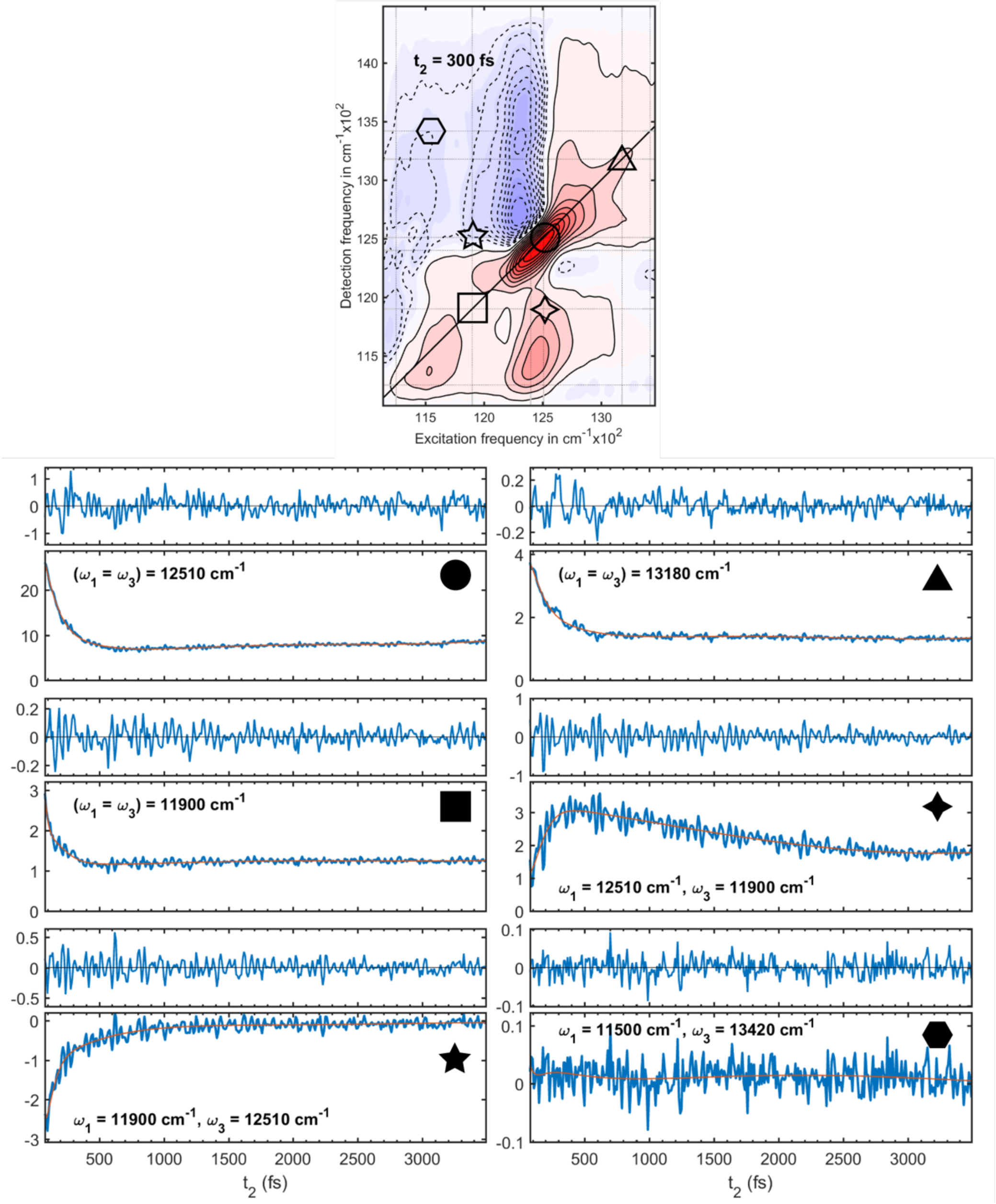

Figure 5.5 Coherent oscillations in BRC t_2 traces. (Bottom) t_2 traces shown for several points in the W(M250)V 2D maps for the real rephasing signal. (Top) 2D real rephasing spectrum at t_2 = 300 fs with symbols showing location of t_2 traces plotted below. For each t_2 trace the lower plot shows the total real rephasing signal including population kinetic (blue) with the exponential portion of the global kinetic fit (orange), in a subfigure above is shown the residual signal after subtraction of the exponential portion of the global kinetic fit revealing oscillations. Three traces show full and residual signal along the diagonal at excitonic energies corresponding to B_A* (top left), H_B* (top right), and P_+* (middle left): two show cross peaks between B_A* and P_+* (middle right) and P_+* and B_A* (bottom left); and one shows the signals far from the diagonal where we expect to see little to no signal (bottom right). Residual signals on the diagonal for P_+* and H_B *show about twice the signal amplitude as the noise residual. The B_A* diagonal and cross peak traces show very strong oscillatory amplitude.

Section 5.2 Coherences in W(M250)V BRCs

Previous reports of coherences have mainly focused on the B and H bands [59,61], but even in this somewhat limited region these studies have observed a rich spectrum of coherences. In our experiment with broader pulse bandwidth and BRCs which undergo charge separation, we expect to see similar coherences to those previously observed and potentially additional modes due to our coverage of the P* bands. New modes not present in previous work on the BRC might also indicate a connection to charge transfer but would be difficult to find direct evidence of. Previously reported coherence frequencies are summarized in Table 5.3 for convenience.

Coherent oscillations are strong enough in the 2DES BRC data to be visible on the full signal t_2 trace, as shown in Figure 5.5. Figure 5.5 shows several t_2 traces from different (ω_1,ω_3) points in the real rephasing 2D spectrum. Figure 5.5 shows the total signal, the exponential portion of the fit trace from the global kinetic analysis, and the residual signal after subtracting the fit. Comparing the maximum amplitude of the absolute value of the residual to the maximum amplitude of the absolute value of the total signal, including kinetic contributions, allows us to consider the effects coherences may have on the global kinetic fits to the data. This comparison for signals along the diagonal is less than 10% of the total signal however signals at cross peaks show a slightly higher percentage (around 25%); this is due to the lower relative signal strength in cross peaks compared to diagonal peaks. The residual amplitude in a region where we expect to see no coherence signal shows a residual which is about the same amplitude as the full signal. Comparing the amplitude of the oscillatory residuals in Figure 5.5 we see that the signals on the B_A*

diagonal and the ($\omega_1 = B_A^*$, $\omega_3 = P_-^*$) cross peak are 2-5 times stronger than other peak locations in the 2D spectrum, and that residuals in all locations where we expect to see signal are at least 2 times larger than the noisy residual.

Table 5.3 Summary of Coherence Studies of the BRC. *Coherence/Phase map plotted for this mode.

Reference	[99] Vos, et al.	[59] Westenhoff, et al.	[60] Ryu, et al.	[61] Paleček, et al.	[62] Flanagan, et al.	[63] Ma, et al.	This Study
Experiment Type	Pump Probe	2DES	2CPE	2DES	2DES	2DES	2DES
T	10 K	80 K	77 K	77 K	77 K	RT	77 K
Pump/Probe Pulse Duration (fs)	30/~30	17/17	45/45	17/17	8/12	18/18	14.5/10.3
Coherence resolution (cm^{-1})	8.3	-	16.7	20.6	33.4	16.7	9.8
Coherence Modes (cm^{-1})	15	90	50	195	180	33	101
	69	190	80	325	330	63	131
	92	220	125	560	560	153	144
	122	310		650	650	235	173
	130	390		720	730		189
	153	575		890	890		206
	191	645		1150	1040		225
	329	710			1170		336
							363
							392
							408
							555
							572
							611
							637
							656
							689
							712
							728
							741
							758
							774
							849
							905
							1003
							1068
							1597

Frobenius Spectra

The Frobenius spectrum in Figure 5.6 shows the amplitude of oscillating frequencies ω_2 for the entire 2D dataset calculated using Eq. 3.3 with the Fourier-transformed 3D-frequency solid after population dynamics subtraction. The Frobenius spectrum in Figure 5.6 shows many prominent peaks far above the background pedestal. Given the waiting time, t_2, scanning parameters and the pulse temporal widths, the 2DES experiment can resolve coherences up to a Nyquist frequency of 1,150 cm^{-1} (given 14.5 fs pump pulse) with $\Delta\omega_2$ = 9.5 cm^{-1} resolution (given the 3,500 fs scan). The peaks present in Figure 5.6 are summarized in Table 5.3 and Table A.3 in the appendix and closely match those seen in the BChla monomer data set in Chapter 4; a direct comparison of the Frobenius spectra for the W(M250)V BRC and monomeric BChla is shown in Figure 6.1. There have been numerous vibrational spectroscopy experiments

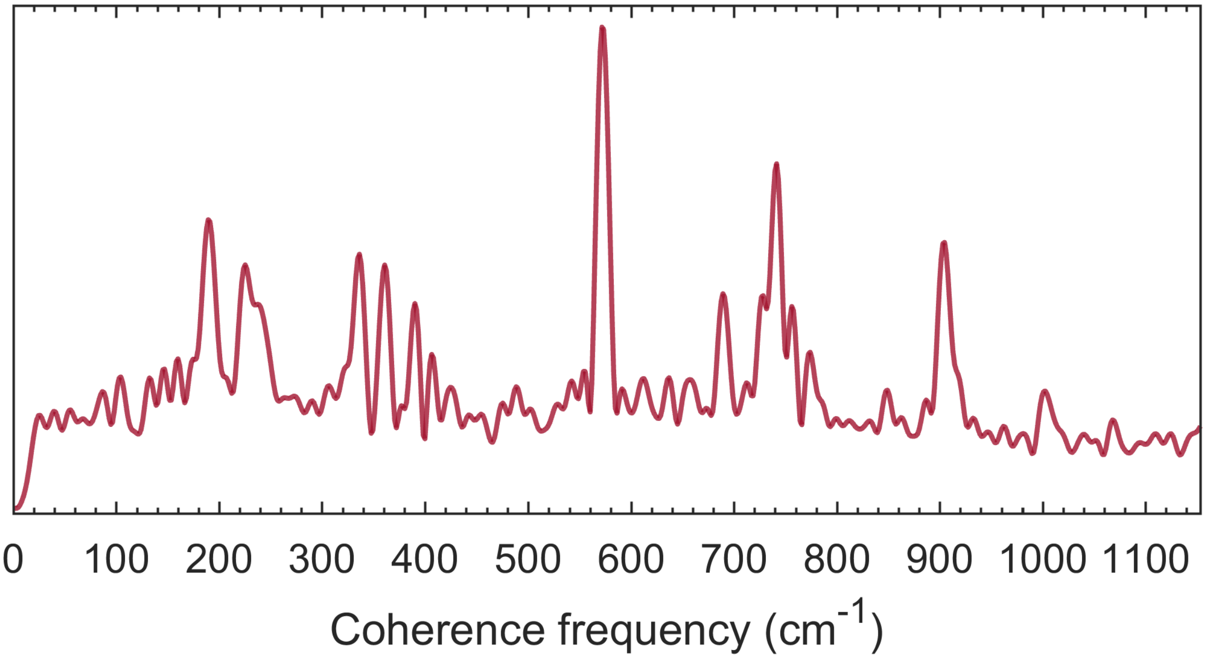

Figure 5.6 Frobenius spectrum of the W(M250)V BRC mutant. The spectrum is calculated by taking the square root of the sum over ω_1 and ω_3 axes of the 3D frequency solid, as described in Chapter 3.3. The spectrum is normalized by the integrated coherence amplitude.

on BRCs including resonance Raman [163,171,189,205–211], and Fourier transformed Infrared spectroscopy (FTIR) [212]. Table 5.4 contains a summary of select vibrational studies of the BRC (Table A.7 in the appendix provides a broader summary of vibrational spectroscopy of the BRC). From these vibrational spectra we see that all the prominent peaks match vibrational modes from experiments.

Taking advantage of the excitation and detection frequency selectivity of the 2D spectra we can compare Frobenius spectra of different electronic bands. Figure 5.7 shows Frobenius spectra where the summation ranges for ω_1 and ω_3 are truncated to regions around the P_-*, B*, and H* diagonal peaks (regions shown in t_2 = 50 fs real rephasing map in Figure 5.3); the majority of the ω_2 amplitude is in the B region, with the lowest ω_2 amplitude on H. If we consider the bandwidth of the pulses used in the experiment and the relative dipole strengths of the three electronic transitions, we can explain why the B*-band hosts the majority of the coherence amplitude. In Chapter 3 we briefly discussed the role that the pump and probe spectral play in selectively exciting specific coherence pathways. Considering first the 8 coherence pathways present in the purely vibrational mode (Figure 3.2). which all depend on some combination of the vibrational frequency plus or minus the electronic transition energy being studied. The B*-band is centered in the middle of both the pump and probe spectra such that all 8 of the ground state bleach and stimulated emission signals from Figure 3.2 are probed. In contrast, only two ground state bleach pathways are accessible for H given the bandwidth of the pump relative to the H*-band, and only stimulated emission pathways can be excited on P_-*$_-$ considering the bandwidth of both the pump and probe pulses. If we additionally consider the expected number of pathways for a mixed vibrational-electronic

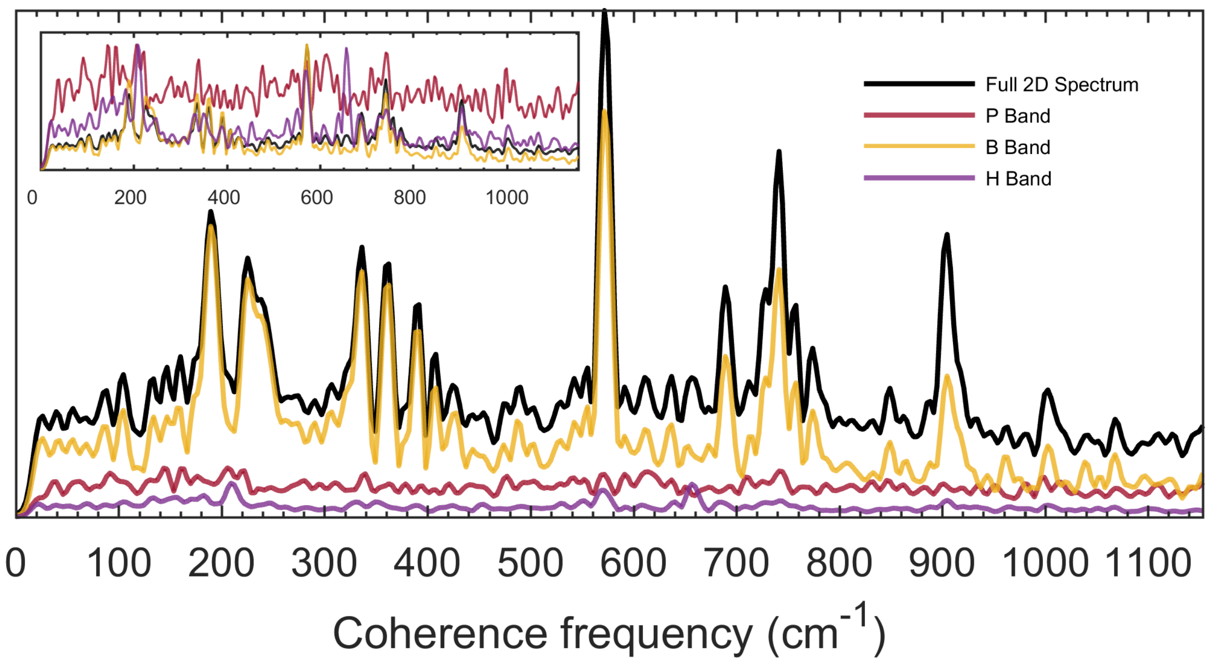

Figure 5.7 Frobenius Spectra for the W(M250)V BRC mutant over different regions of the 2D spectrum including the P_-*, B*, and H* diagonal peaks (regions shown in t_2 = 50 fs real rephasing map of Figure 5.3. The main figure shows the relative coherence amplitude of the full 2D spectrum (same as red curve trace in Figure 5.6) with the Frobenius spectra calculated for three diagonal regions located on P_-* (red), B_A* and B_B* (yellow), and H_A* and H_B* (purple. In the main figure the traces are normalized by their integrated spectral amplitude. The inset figure shows the same four traces normalized to the maximum.

vibronic coherence model (Figure 3.4) there are many more pathways localized around the diagonal peak of the higher energy electronic transition compared to the lower energy electronic 0-0 transition. If P_-* and the B* states are vibronically coupled, we would expect to see a stronger signal amplitude localized on B* relative to P_-*.

Table 5.4 Select vibrational spectroscopy studies of BRCs at cryogenic temperatures.

Reference	[213] Cherepy, et al.			[171] Czarnecki, et al.		
Experiment Type	SERDS RR			NIR RR		
T	95 K			25 K		
Band Excited	P_-*	B*	H*	P_-*	B*	H_B*
λ_o (nm)	870	800	760	894	805	750
Vibrational Frequency (cm^{-1})	36	85	90	72	56	64
	64	125	121	96	87	94
	82	159	139	130	118	124
	101	186	184	137	137	138
	132	219	209	143	163	140
	168	332	232	144	185	153
	179	357	282	179	190	184
	204	382	336	203	220	184
	262	566	359	240	231	209
	291	624	377	252	240	237
	332	685	397	268	264	244
	476	725	415	280	280	266
	520	735	567	291	295	274
	560	746	618	316	326	285
	577	843	629	326	335	331
	616	893	658	335	357	339
	688	920	692	357	364	384
	733	943	720	364	375	397
	763	966	728	381	384	417
	780	999	737	393	393	
	790	1022	744	406	400	
	897	1115	753			
	926	1133	773			
	949	1162	794			
	970		839			
	1010		845			
	1039		852			
	1060		860			
	1109		881			
	1131		899			
	1154		921			
	1170		929			
	1195		935			
	1255		969			
	1283		980			
	1609		998			
	1618		1015			
	1650		1056			
	1681		1074			
			1107			
			1139			
			1169			
			1195			
			1215			
			1233			
			1312			

The B*-band Q_y transition has about twice the OD of either the P_-* or H*-bands (Figure 5.1) although the dipole strengths of the individual B* transitions are smaller than the P_-* dipole strength [4]; we would expect signals along the P_-* and H*-bands to be 16 times weaker than the B-band signals. A final note when considering the relative amplitude of ω_2 amplitude on P_-* is that the pump and probe spectra are only able to cover the blue edge of the P^*_- transition (Figure 5.2).

Coherence Maps

Figure 5.8 and Figure 5.9 show the distribution of the absolute value of several low- and high-frequency coherence frequencies, ω_2, as a function of ω_1 and ω_3 in coherence maps. The frequencies shown are selected by looking at the peak locations in the Frobenius spectrum in Figure 5.6. Chapter 6 will outline an in-depth comparison of the coherences observed in the W(M250)V BRC, presented in this chapter, and BChla from Chapter 4. The following discussion will outline some of the general features seen in the W(M250)V coherence maps.

Dashed diagonal lines drawn at $\omega_1 = \omega_3 \pm n \cdot \omega_2$ in Figure 5.8 & Figure 5.9 are added to aid in interpretation of the signatures relative to the simple models from Chapter 3. Orange circles in the "chair" pattern characteristic to a purely vibrational model are overlaid on the maps at ω_2 = B_A* & B_B*. The low-frequency modes in Figure 5.8 show significant deviation from the chair diagram along the B-band, whereas the high-frequency modes shown in Figure 5.9 show better agreement with several notable differences. For coherence maps at ω_2 = 741 & 905 cm^{-1}, the higher excitation energy pathways ($\omega_1 = E + \Omega$ in Figure 3.2) are attenuated due to the limited pump bandwidth. Additionally the ω_2 = 572 cm^{-1} in Figure 5.9 shows the peaks at the B*-band diagonal line shifted away from the diagonal line; this feature has been observed in previous coherence studies of the BRC [61] and will be discussed in detail in Chapter 6. “Chair” patterns are not overlaid on the P_-* or H*-bands due to the lack of pump and probe coverage necessary to resolve this pattern and the general weakness of coherence amplitude along these bands. In the case of the ω_2 = 656 cm^{-1} mode in Figure 5.9 we see strong signals at ω_1 = H*-band which are distributed in ω_3 in a way consistent with vibrational coherence.

Coherence maps of the Fourier transformed complex rephasing signal (Figure 5.12) separate out the Fourier transformed coherence frequency components by sign ($\pm\omega_2$). The strong signals along the B*-band show similar sign behavior as in BChla (Figure 4.9) and the vibrational discplaced oscillator (Figure 3.2). In the vibrational displaced oscillator and electronic dimer, signatures above the diagonal ($\omega_1 = \omega_3$) oscillate with $+\omega_2$ and those below the diagonal oscillate with $-\omega_2$ (Section 3.1). Signals in Figure 5.12 which do not follow this behavior are not explained by these two simple models. There are some weak signatures below the diagonal at several positive coherence frequencies (+ω_2) at the (B*,P_-*) cross peak (Figure 5.12); these signatures could possibly indicate vibronic coupling between B* and P_-* or could be evidence for energy transfer which is modulated by vibrational wavepacket motion on B*.

Phase maps, or the phase angle part of the FT real rephasing signal, are presented in Figure 5.10 and Figure 5.11. Phase maps have been used in several theoretical models to distinguish between types of coherence signatures [26,70,137]; comparing the relative phase between two peaks from the coherence maps can be helpful in distinguishing between vibrational, electronic, and vibronic signatures. The phase maps in Figure 5.10 and Figure 5.11 show strong phase jumps of $\sim\pi$ near the diagonal line, where there are destructive-interference type signatures in the coherence maps. This behavior is not well characterized by any of the theoretical models presented in Chapter 3, but may be consistent with the model for energy transfer-induced coherence shifts by Paleček, et al. [61]. Interestingly, the phase around the signals labeled 1-4 in the coherence maps (Figure 5.8 and Figure 5.9) show a horizontal banding that extends to B (Figure 5.11). This behavior indicates that signals at locations 1-4 are in phase with the upper diagonal signatures on B.

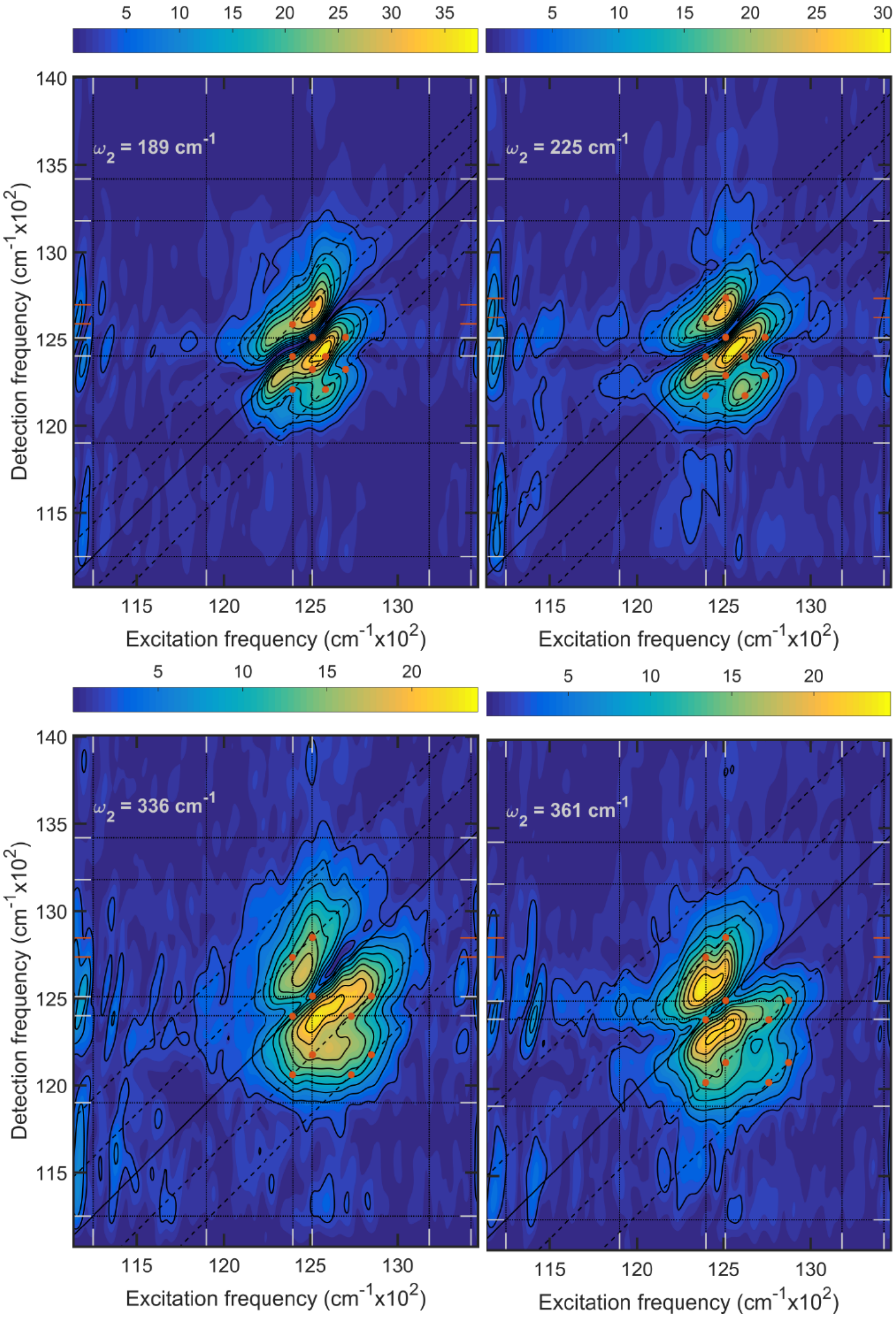

Figure 5.8 Low-frequency Real Rephasing 2D Coherence Amplitude Maps of W(M250)V BRC. Overlaid on the 2D maps are diagonal lines at ($\omega_1 = \omega_3$) and ($\omega_1 = \omega_3 \pm n\omega_2$) for several n, as well as vertical and horizontal lines which correspond to the excitonic energies found from global kinetic fitting [4]. Orange circles are overlaid in the vibrational coherence chair pattern at the exciton energies for B_A* and B_B* to highlight where we expect to see vibrational coherence signals on the B* band. Black contours are drawn at 10 – 100% of the maximum of the coherence amplitude.

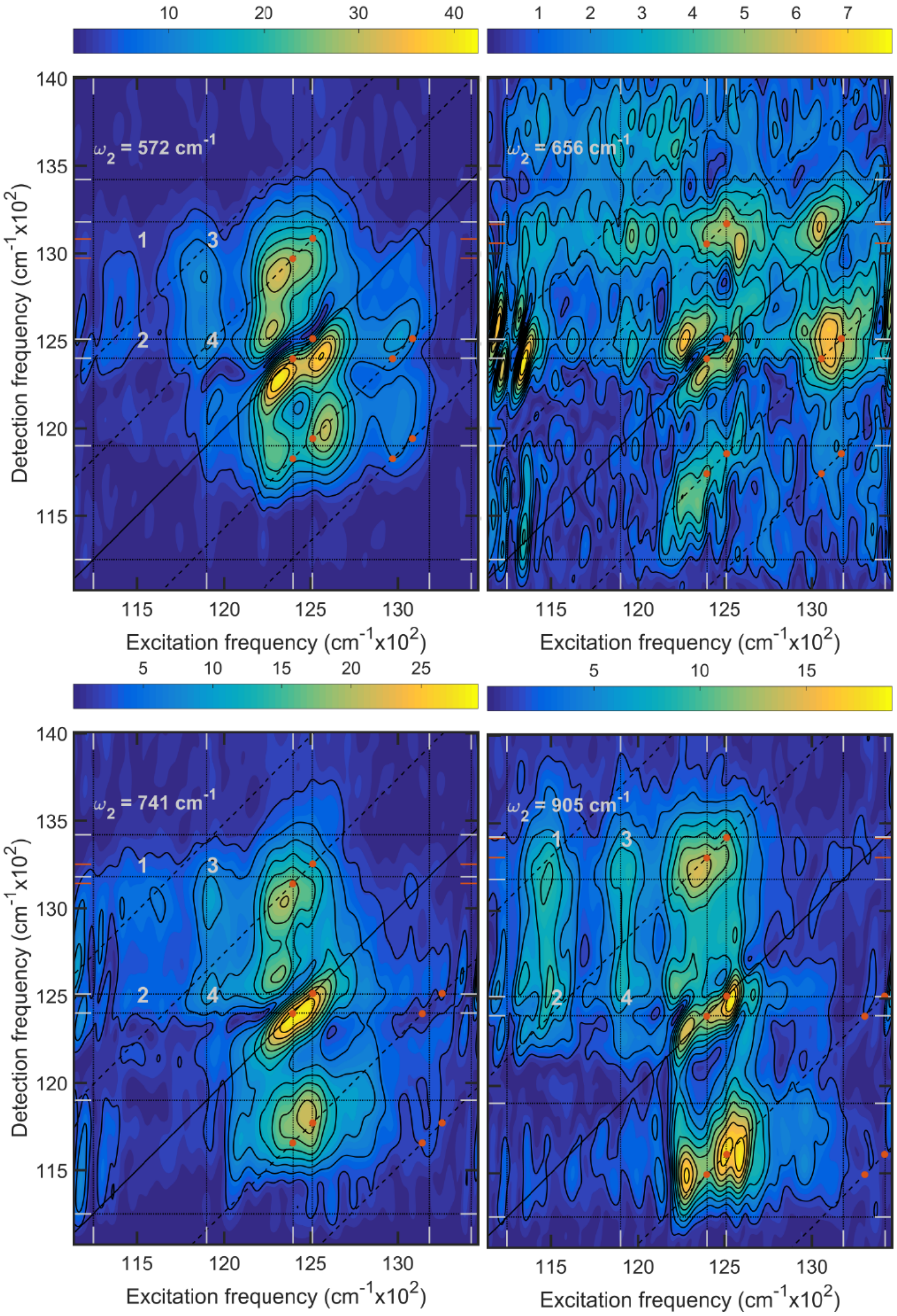

Figure 5.9 High-frequency Real Rephasing 2D Coherence Amplitude Maps of W(M250)V BRC. Numerical labels (1-4) refer to four signals found in similar spectral locations across several coherences maps; the location of these signatures is not explained by either simple electronic nor simple vibrational models from Chapter 3. Overlaid on the 2D maps are diagonal lines at ($\omega_1 = \omega_3$) and ($\omega_1 = \omega_3 \pm n\omega_2$) for several n, as well as vertical and horizontal lines which correspond to the excitonic energies found from global kinetic fitting [4]. Orange circles are overlaid in the vibrational coherence chair pattern at the exciton energies for B_A* and B_B* to highlight where we expect to see vibrational coherence signals on the B* band. Black contours are drawn at 10 – 100% of the maximum of the coherence amplitude.

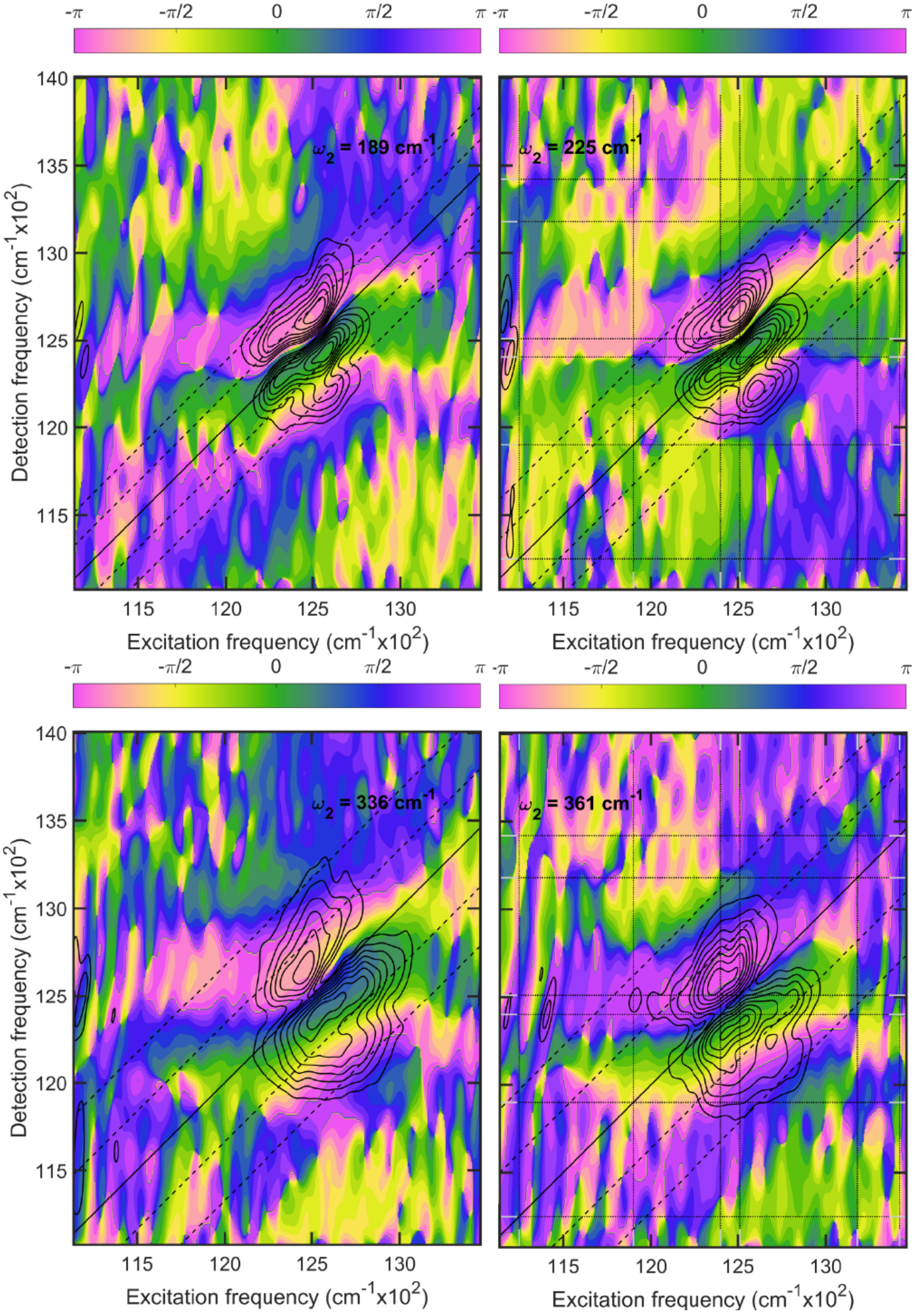

Figure 5.10 Low-frequency Real Rephasing 2D Coherence Phase Maps of W(M250)V BRC. Overlaid on the 2D maps are diagonal lines at ($\omega_1 = \omega_3$) and ($\omega_1 = \omega_3 \pm n\omega_2$) for several n, as well as vertical and horizontal lines which correspond to the excitonic energies found from global kinetic fitting [4]. Filled contours represent the oscillatory phase with black contours at 10 – 100% of the maximum of the coherence amplitude.

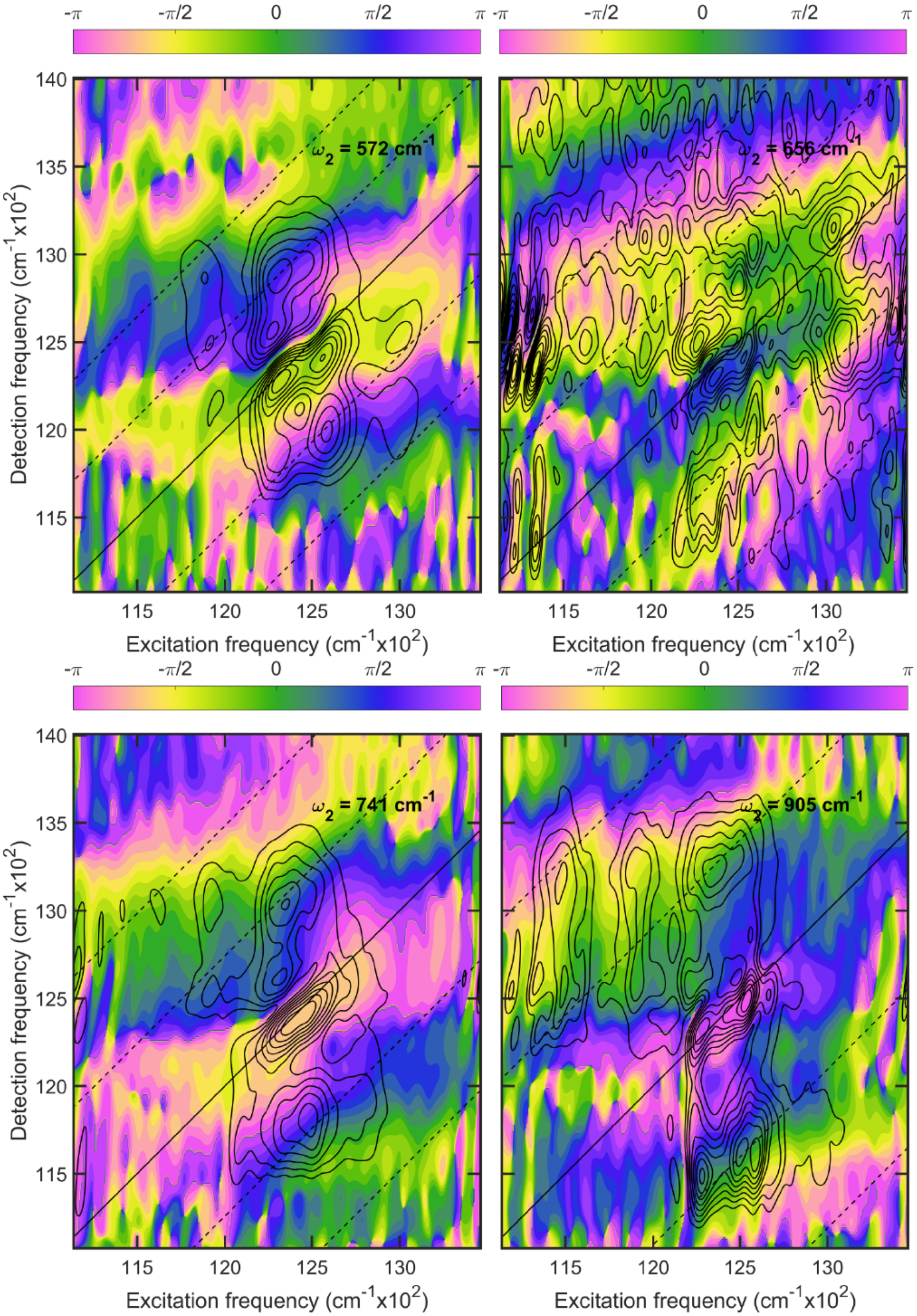

Figure 5.11 High-frequency Real Rephasing 2D Coherence Phase Maps of W(M250)V BRC. Overlaid on the 2D maps are diagonal lines at ($\omega_1 = \omega_3$) and ($\omega_1 = \omega_3 \pm n\omega_2$) for several n, as well as vertical and horizontal lines which correspond to the excitonic energies found from global kinetic fitting [4]. Filled contours represent the oscillatory phase with black contours at 10 – 100% of the maximum of the coherence amplitude.

High-frequency Above-Diagonal Signatures

In addition to the strong signals localized at the B-band there are prominent signals in all the high-frequency maps shown in Figure 5.9 which have been labeled 1-4 for clarity. These signals cannot be explained by the simple vibrational model considered in Chapter 3, which only considers two electronic states with two vibrational levels each. This model is widely used for systems with chlorin molecules which have weak vibronic coupling ($S \cong 0.01$ for BChla [127]) such that excitation to higher-lying vibrational quanta would be extremely weak. The P-band has been observed to have a greatly enhanced vibronic coupling ($S \cong 0.1$ [27,214]) in which case it may be pertinent to extend the 4-state model in Chapter 3 to include higher-lying vibrational excitations. A 6-state model (two electronic states with three vibrational states each) could explain some of signals labeled 1-4 if these modes were harmonics of the vibrational mode. However the agreement of the coherence frequency these signatures are observed at with known BChla vibrational modes suggests higher-lying vibrational states are not involved. We do not see strong harmonics of known vibrational modes in the Frobenius spectrum.

The spacing between signatures 1 & 2 (3 & 4) in Figure 5.9 is roughly equal to ω_2. In all instances signatures 1 & 2 appear at $\omega_1 = 11{,}500\ \text{cm}^{-1}$, which differs from the excitonic energy assigned to P_- due to the partial overlap of our pump and probe with the P_-^* band (Figure 5.2). Signature 2 is found at $\omega_3 \cong 12{,}510\ \text{cm}^{-1}$ or the excitonic energy for B_A^* which might suggest an electronic coherence as in Figure 3.3, however the exciton difference frequency expected between B_A^* and P_-^*, $1{,}260\ \text{cm}^{-1}$ (Table 5.2), is much higher in energy than coherence frequencies in Figure 5.9 and does not match any peaks in our data (Table 5.3). If we instead use the excitation frequency of the P_-* peak from our real absorptive data (Figure 5.3), ω_1 = 11,500 cm^{-1}, for P_-*, the exciton difference frequency with B_A* is 1,010 cm^{-1}. Though the modes in Figure 5.9 do not match either exciton difference frequency between P_-* and B_A*, we do see an increase in signal amplitude at signal locations 1 & 2 with increasing ω_2; for example, signals at 1 & 2 for ω_2 = 905 cm^{-1} are enhanced relative to the ω_2 = 572 cm^{-1} mode.

We have now assigned P_+* band to an excitonic energy of 11,900 cm^{-1} which corresponds to the excitation frequency of signals 3 & 4. However before making this assignment several other explanations were considered. The excitation frequency of signals 3 & 4 is in a very-low absorbance region of the linear absorption spectra in Figure 5.1 which was generally assigned to the vibronic progression of P_-*. We considered that signals 3 & 4 were due to a strongly coupled vibration of P_-* with a very high probability of excitation; this proposal would require that the strongly-coupled vibrational mode was coupled to additional vibrational modes so that during t_2 the system would oscillate with the difference frequency of the two excited vibrational modes. This difference frequency would have to match the frequency of a known vibrational mode of monomeric BChla, where we observe these signals. Even given the relative enhancement of vibronic coupling on the special pair relative to monomeric BChla, the coupling of one vibrational mode to several others has not previously been reported in the BRC or BChla studies and would require a large amount of coincidence to give rise to the signatures seen in Figure 5.9. A simpler explanation that is consistent with the kinetic fitting performed on the 2DES data [4] is that these signatures arise from the P_+* state, explaining the consistent excitation frequency and the spacing of signals 3 & 4 of about ω_2. This was tentatively assigned as the upper excitonic state of P, P_+*, until the independent global kinetic analysis assigned P_+* to 11,900 cm^{-1} [4].

We do not see much coherence amplitude along the diagonal for either P_-* or P_+* states in any coherence maps. In the case of P_- this has been attributed to the pulse bandwidth used in our experiments, and for P_+ is consistent with its weak dipole strength and rapid internal conversion to P_-*. We therefore believe that we are able to see the signals labeled 1-4 primarily due to the involvement of the B-band transitions which results in dipole intensity borrowing. The enhancement of weak or dark transitions due to vibrationally-assisted coupling to a strong electronic transition has been previously modelled [142]; 2DES coherence maps demonstrating an ability to resolve weak or dark states have previously been reported in molecular systems [76,215]. Our current theory regarding the origin of these coherences involves vibronic coupling between the P*-bands and one or both B* transitions and is discussed in further detail in Chapter 6.

Coherence maps for the complex rephasing signal (Figure 5.12) further divide the coherence signals by the sign of the coherence frequency, $\pm\omega_2$, as described in Chapter 3. The distribution of B*-band coherence signals in the $\pm\omega_2$ maps for higher frequency modes show a similar distribution as we would expect for a vibrational displaced oscillator (Figure 3.2). Notably, the signatures labeled 1-4 oscillate with $+\omega_2$; this information can help us constrain pathways to help us develop a model that gives rise to these signatures.

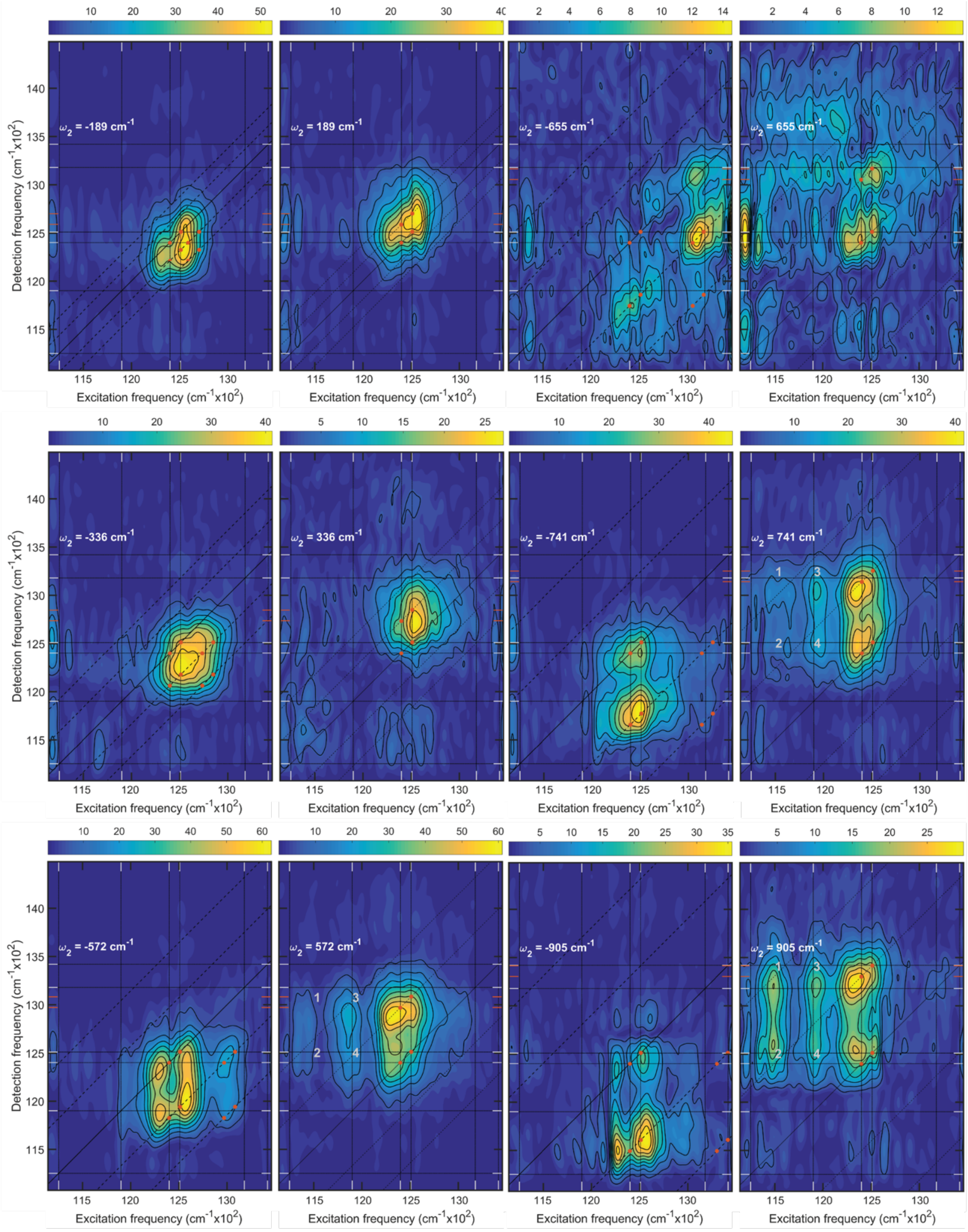

Figure 5.12 Coherence maps from the complex rephasing signal of W(M250)V BRC. Following Fourier transformation of the complex residual, described in Chapter 3, the $+\omega_2$ and $-\omega_2$ coherence maps can be plotted to further distinguish different coherence pathways. Low-frequency maps show one peak per $+\omega_2$ and $-\omega_2$ map above and below the diagonal, respectively. Higher-frequency maps show more peaks maintain the relationship with sign of coherence frequency and location in relation to the diagonal line, with the exception of the peaks on the diagonal.

Section 5.3 Comparison of D_{LL} and W(M250)V Coherences

Results & Discussion

Experimental parameters for the D_{LL} experiments are given in Section 5.2 and Table 5.1. The D_{LL} samples were prepared with OD(P_-*, 850 nm) = 0.105 at room temperature. Figure 5.13 shows the pulse spectra used for the D_{LL} experiments; the pump was able to better cover the P_-* peak in these experiments but the overall weaker signal strength due to scatter meant that the coherences observed on P_-* are still very weak (Figure 5.16 & Figure 5.17). Figure 5.14 shows real absorptive and real rephasing D_{LL} 2D spectra at several waiting times. At t_2 = 50 fs cross peaks between B* and P_-* and H_B*

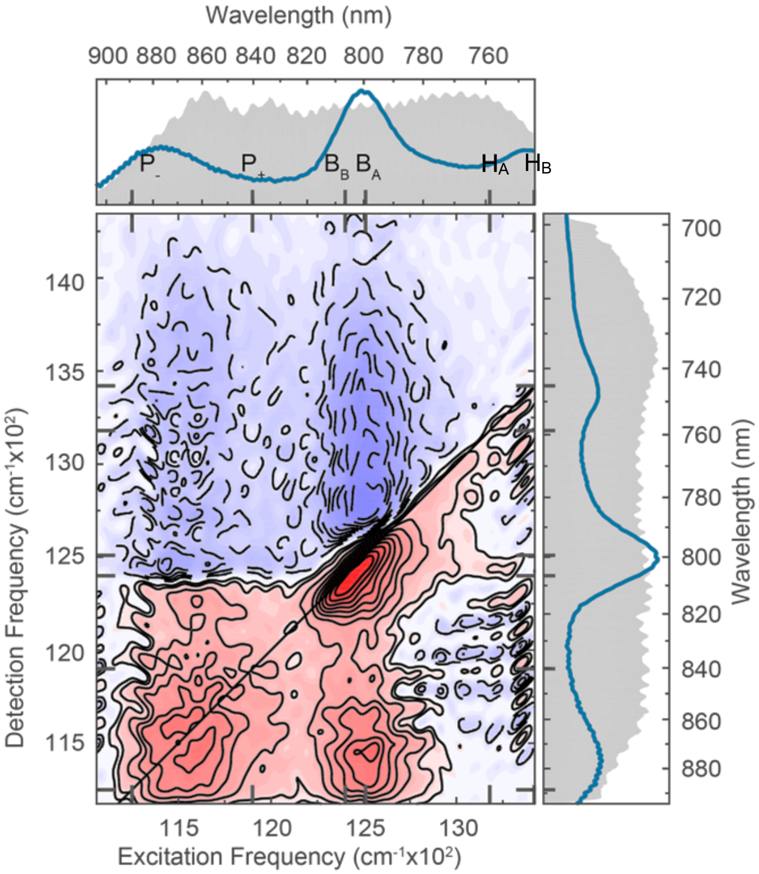

Figure 5.13 Real Absorptive 2D Spectrum of D_{LL} BRC mutant at 77 K and t_2 = 200 fs. 77 K linear absorption spectrum (blue) with the experiment pump (above) and probe (right) spectra shown in grey with labeled stick spectrum for the excitonic spectrum of states extracted for the W(M250)V data (Table 5.2).

and B* are present below the diagonal indicating rapid downhill energy transfer similar to the W(M250)V data (Figure 5.4). After initial downhill energy transfer to P_-*, the P_-* state decays to the ground state on a timescale greater than a nanosecond as no charge transfer occurs in this mutant. The diagonal peak in the H-band is weaker due to the lack of H_A*, and no A-branch H*-B* cross peak is present. The energy transfer timescales are

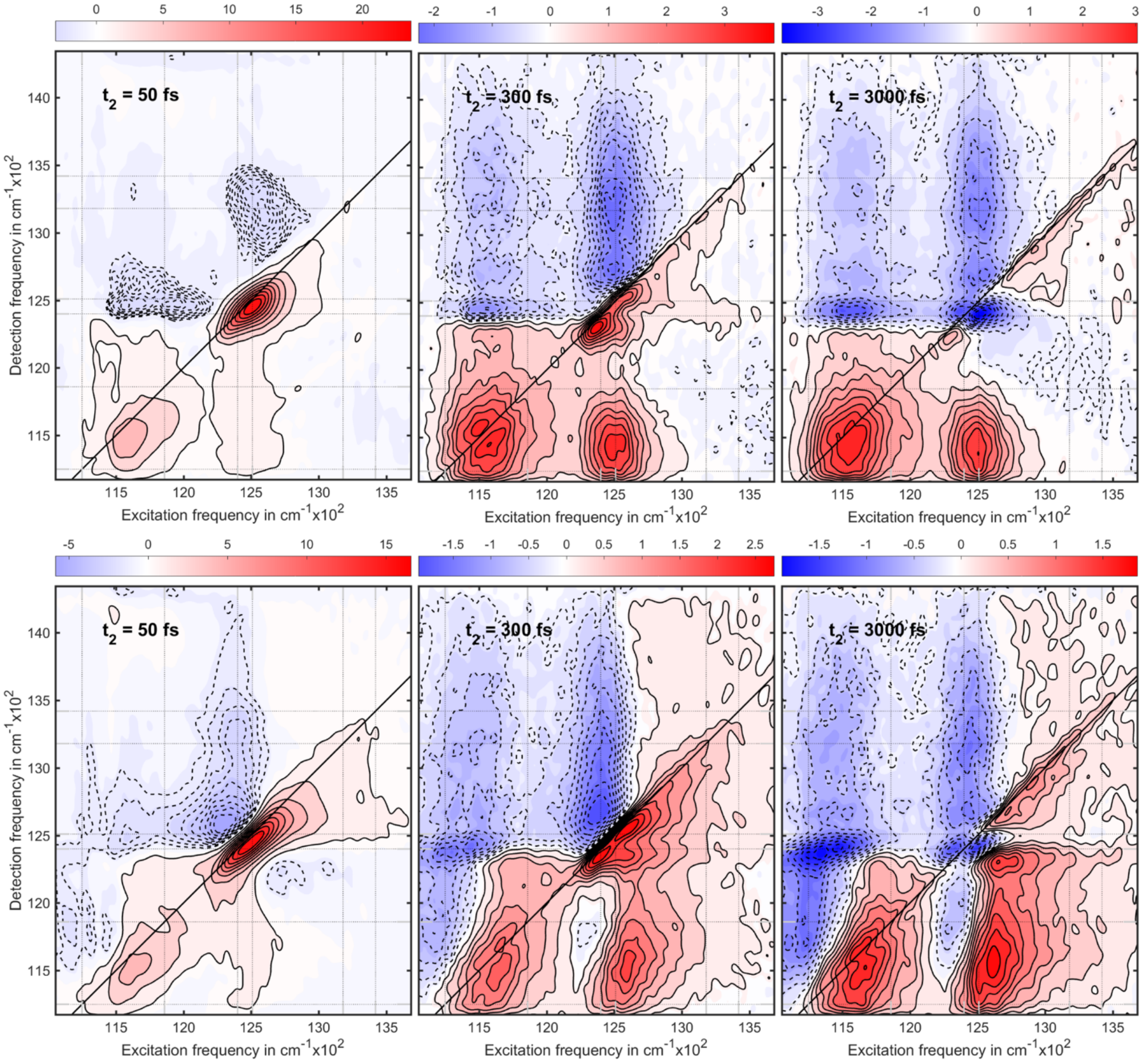

Figure 5.14 2DES Real absorptive (top) and real rephasing spectra (bottom) of D_{LL} BRC mutant. t_2 = 50 fs (left), 300 fs (center), and 3000 fs (right). Real absorptive data were studied in kinetic analysis of energy and charge transfer. The real rephasing signal is used in coherence analysis in order to take advantage of the selectivity of specific pathways.

in agreement with the corresponding pathways in the W(M250)V mutant (Figure 5.4) [4], showing that D_{LL} serves as a control for charge transfer processes. The signatures along the H*-band diagonal at long times (right column, Figure 5.14) suggests that there is still population on H_B* at 3 ps however, we expect all population to have transferred to P_-* by this time. A possible explanation for these features is scatter from the pumps or a combination of pump and probe, which manifests along the diagonal [216]. This sample was difficult to work with and did exhibit significant scatter. We are considering other possible explanations for these signatures as well.

Figure 5.15 shows the Frobenius spectrum of the D_{LL} experiment (red) compared to the W(M250)V Frobenius spectrum (black) from Figure 5.6. The noise floor for the D_{LL} data set is significantly higher than the W(M250)V set but there are several prominent peaks at roughly the same positions as in the W(M250)V spectrum (Summarized in Table A.3). Notable differences are the absence of the ~220 cm^{-1} peak in the low-frequency

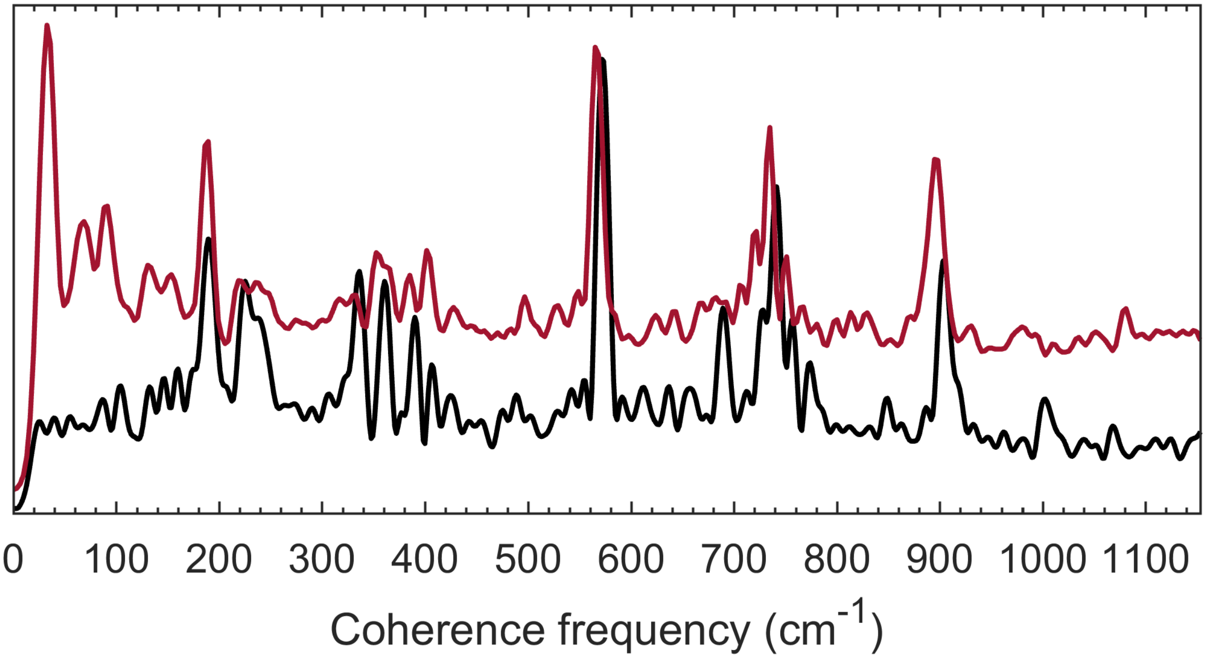

Figure 5.15 Frobenius spectrum of D_{LL} (red) overlaid on the Frobenius spectrum of W(M250)V (black) for comparison. Both spectra are normalized by their integrated coherence amplitude.

range and the 656 & 680 cm^{-1} peaks in the high-frequency range. The absence of the 656 & 680 cm^{-1} modes compared to the W(M250)V Frobenius spectrum may be explained entirely by the absence of the A-branch BPheoa molecule since the ~650 cm^{-1} mode is a prominent vibrational BPheoa mode [163,181]. The ~180, ~360, ~570, ~740, and ~900 cm^{-1} modes are still present in the D_{LL} mutant and have roughly the same "chair" amplitude distribution in the coherence maps (Figure 5.16, Figure 5.17) as the W(M250)V coherence maps (Figure 5.8, Figure 5.9) but with much lower signal to noise (S/N) related to scatter issues due to the poor glass quality of the sample.

The high-frequency coherence maps in Figure 5.17 show weak amplitude in the same spectral regions as signatures 1-4 in the W(M250)V high-frequency coherence maps (Figure 5.9). Though the S/N is weak, the presence of these signatures in D_{LL} may indicate that origin of these signatures is not directly related to charge transfer processes in the BRC but is rather a feature of the structure.

Vibronic Coupling of B_A and H_A

As demonstrated in the regional Frobenius spectra of W(M250)V BRC in Figure 5.7, the majority of the coherence amplitude is localized on the B*-band, with the exception of the ω_2 = 656 cm^{-1} map which shows significant amplitude on the H-band. Comparing to resonance Raman studies of monomeric BChla and BPheoa shows a vibrational mode at a frequency of about 650 cm^{-1} present in both molecule's spectra however much this mode is a strong peak in BPheoa and a very weak mode in BChla [163,181]. Resonance Raman studies selectively exciting the P_-*-, B*-, and H*-bands of BRCs showed a ~650 cm^{-1} mode on the H*-band at both 95 K & 278 K which not present in either P_-*- or B*-bands [213]. This suggests that the 656 cm^{-1} we see in the W(M250)V Figure 5.9 originates from a BPheoa vibrational mode and not a BChla vibrational mode. Comparison of the H*-band diagonal Frobenius spectrum to the P_-*- and B*-band spectra in Figure 5.7 shows that the 656 cm^{-1} mode is much more prominent on H* than the other two regions. In the total 2D Frobenius spectrum this frequency is very weak and only slightly above the background noise floor. Examining the 2D distribution of this mode in Figure 5.9 shows ground state bleach signals on H*, as expected for a strong BPheoa vibrational mode, but additional amplitude distributed in the B*-bands and in above-diagonal features around $\omega_1 = P_-$*, P_+*, which are unexpected for an intramolecular vibration. The presence of the 656 cm^{-1} mode along the B*- and P_-*-bands could suggest coupling between the three bands as excitation at B* or P* does not involve downhill energy transfer beginning from H*, which could potentially be periodically modulated by strong nuclear motion. The exciton difference frequencies between the H_A* and B_A* states extracted from our global kinetic fitting [4] is 670 cm^{-1}, in which case this vibrational BPheoa mode is nearly resonant with the energy gap between the B_A* and H_A* states.

Previous 2DES coherence studies of oxidized BRCs which focused on the B*- and H*-bands have shown evidence for vibronic coherences between B* and H* for ω_2 = 575 & 645 cm^{-1} using a vibrational coherence-suppressing pulse polarization scheme [59,61]. In the latter of these studies, Palecek, et al. show peaks corresponding to initial excitation of electronic coherence between B* and H* molecules which then rapidly converts to long lived ground state vibrational coherence [61]. Our data supports these results through the distribution of the 656 cm^{-1} mode in the B*- and P*-bands of W(M250)V and the lack of this mode in the H_A*-deficient D_{LL} (Figure 5.17).

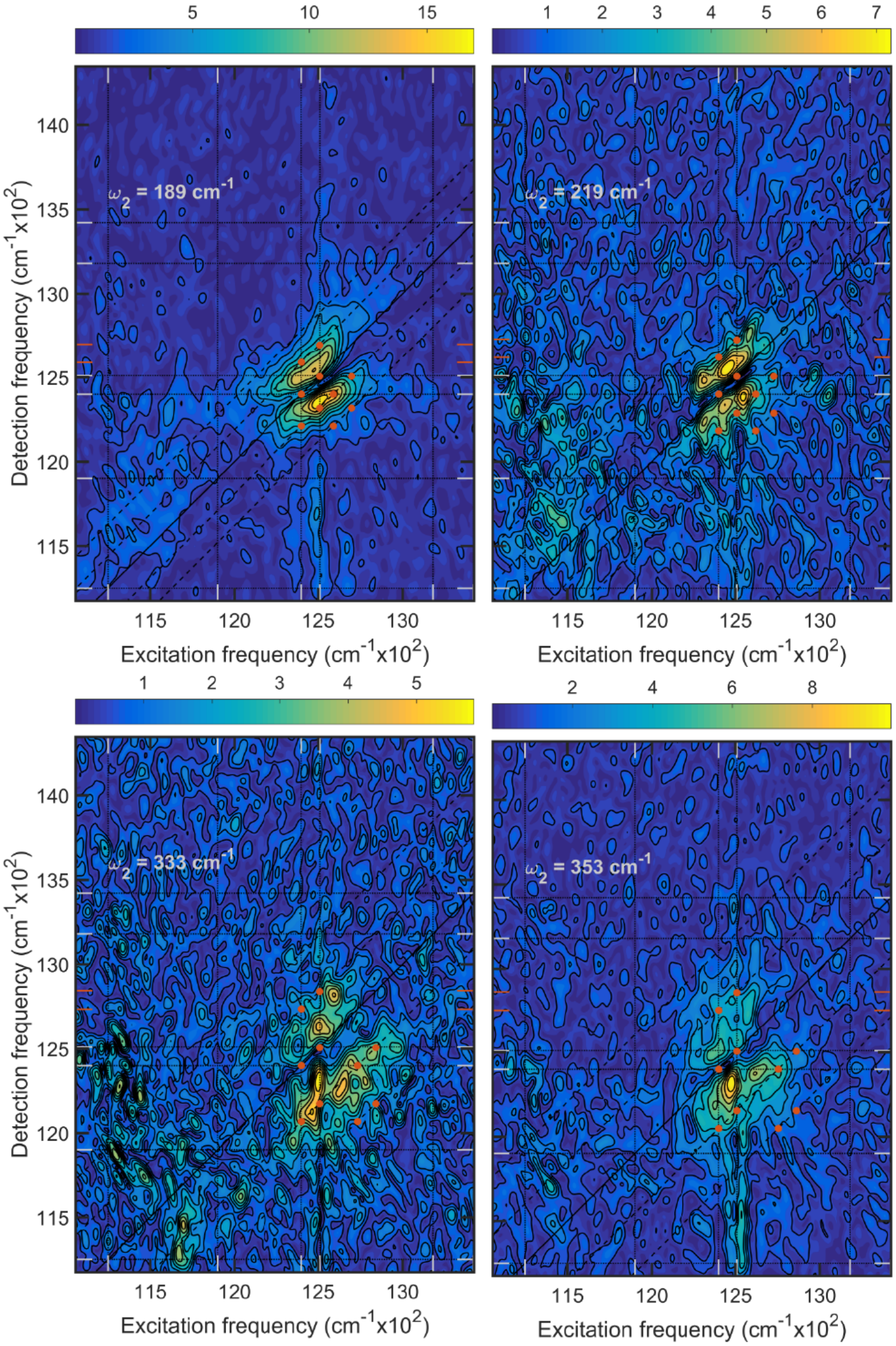

Figure 5.16 Low-frequency Real Rephasing 2D Coherence Amplitude Maps of D_{LL} BRC. Overlaid on the 2D maps are diagonal lines at ($\omega_1 = \omega_3$) and ($\omega_1 = \omega_3 \pm n\omega_2$) for several n, as well as vertical and horizontal lines which correspond to the excitonic energies found from global kinetic fitting [4]. Orange circles are overlaid in the vibrational coherence chair pattern at the exciton energies for B_A* and B_B* to highlight where we expect to see vibrational coherence signals on the B* band. Black contours are drawn at 10 – 100% of the maximum of the coherence amplitude.

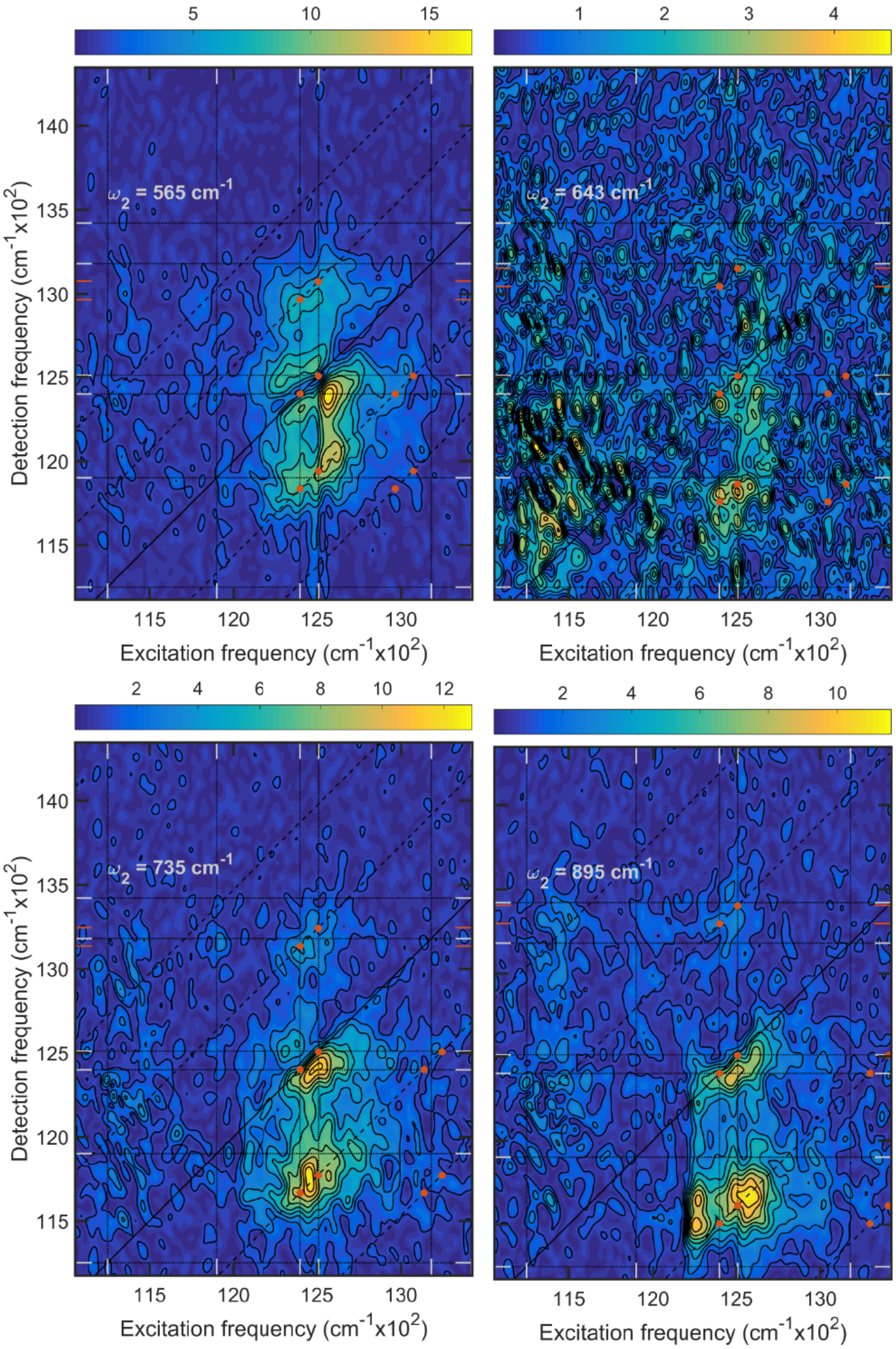

Figure 5.17 High-frequency Real Rephasing 2D Coherence Amplitude Maps of D_{LL} BRC. Overlaid on the 2D maps are diagonal lines at ($\omega_1 = \omega_3$) and ($\omega_1 = \omega_3 \pm n\omega_2$) for several n, as well as vertical and horizontal lines which correspond to the excitonic energies found from global kinetic fitting [4]. Orange circles are overlaid in the vibrational coherence chair pattern at the exciton energies for B_A* and B_B* to highlight where we expect to see vibrational coherence signals on the B* band. Black contours are drawn at 10 – 100% of the maximum of the coherence amplitude.

Section 5.4 Conclusions

Using broadband 2DES we have observed coherences in two BRC mutants: W(M250)V BRC, which is functionally similar to wild type proteins, and D_{LL}, which lacks the A-branch BPheoa and does not perform charge separation. Both of these mutants showed a large number of prominent coherences (Figure 5.6 and Figure 5.15), whose frequencies are very similar to vibrational modes of the BRC (Table 5.4, Table A.5) and the BChla monomer (Table A.4). In both BRCs, the majority of the coherence amplitude was localized on the B*-band (Figure 5.7), likely both because of its high OD and because it is well centered in both the pump and probe pulse spectra used in these experiments (Figure 5.2 and Figure 5.14). We are also able to see coherences in the H*-band and weak coherences in the P_-* band (Figure 5.7). The real rephasing coherence maps show a similar amplitude distribution along the B-band as we might expect for vibrational coherences on two spectrally-overlapped monomers (Figure 5.9). In addition to these signatures that are vibrational in origin, four peaks far above the diagonal (more prominent in the W(M250)V coherence maps Figure 5.9) are not explained by the purely vibrational or purely electronic models for coherence described in Chapter 3. These signals are tentatively assigned as signatures of vibronic coupling between B* and P*.

CHAPTER 6 COMPARISON OF COHERENCES IN BACTERIOCHLOROPHYLL A MONOMERS & THE BACTERIAL REACTION CENTER

In Chapter 4 and Chapter 5 we presented results from broadband Two-dimensional electronic spectroscopy (2DES) on monomeric Bacteriochlorophyll a (BChla) and Bacterial Reaction Centers (BRCs), respectively. Both monomeric BChla and the BRCs show a large number of coherent modes. In this chapter, we directly compare the signatures of coherence in monomeric BChla in isopropanol and the W(M250)V BRC.

Section 6.1 Vibrational Contributions

The conclusions of Chapter 4 and Chapter 5 were that the coherences present in both the BChla and BRC were largely vibrational in character. This conclusion was reached given the similarity of coherence frequencies to known vibrational modes of each system (Table A.1 and Table A.2) and because the amplitude distribution in coherence maps is similar to that expected from a simple vibrational displaced oscillator model (Figure 3.2).

Figure 6.1 shows the Frobenius spectra from W(M250)V (red) and BChla (yellow) overlaid on one another; both spectra are normalized by their integrated spectral amplitude and show similar background pedestals. Blue lines indicate the locations of vibrational frequencies from resonance Raman studies of monomeric BChla [163,169,171] also listed in Table 4.1; these lines are only plotted for modes that were good agreement with the frequencies of prominent peaks from the BChla and BRC spectra. The criterion used to determine good agreement was whether the peak frequencies from our Frobenius spectra ($\omega_{2,peak}$) plus or minus half our experimental resolution ($\omega_{2,peak} - \frac{1}{2}\Delta\omega_2 \leq \omega_{2,peak} \leq \omega_{2,peak} + \frac{1}{2}\Delta\omega_2$, $\Delta\omega_2 = 9.8\ cm^{-1}$) were within the range defined by the literature frequencies ($\Omega_{lit,peak}$) plus or minus half each studies' experimental resolution ($\Omega_{lit,peak} - \frac{1}{2}\Delta\Omega_{lit,peak}, \Omega_{lit,peak} + \frac{1}{2}\Delta\Omega_{\mathrm{lit,peak}}$). Additionally, purple and green lines drawn below the Frobenius spectra indicate exciton difference frequencies (ΔE) from a theoretical model of BRCs at 77 K [27] and from our global fitting analysis of 2DES and linear absorption spectra of W(M250)V (Excitonic energies and difference frequencies listed in Table 5.2) [4]. In the case of vibronic coupling we expect to see a vibrational frequency which is able to bridge the excitonic energy gap to achieve

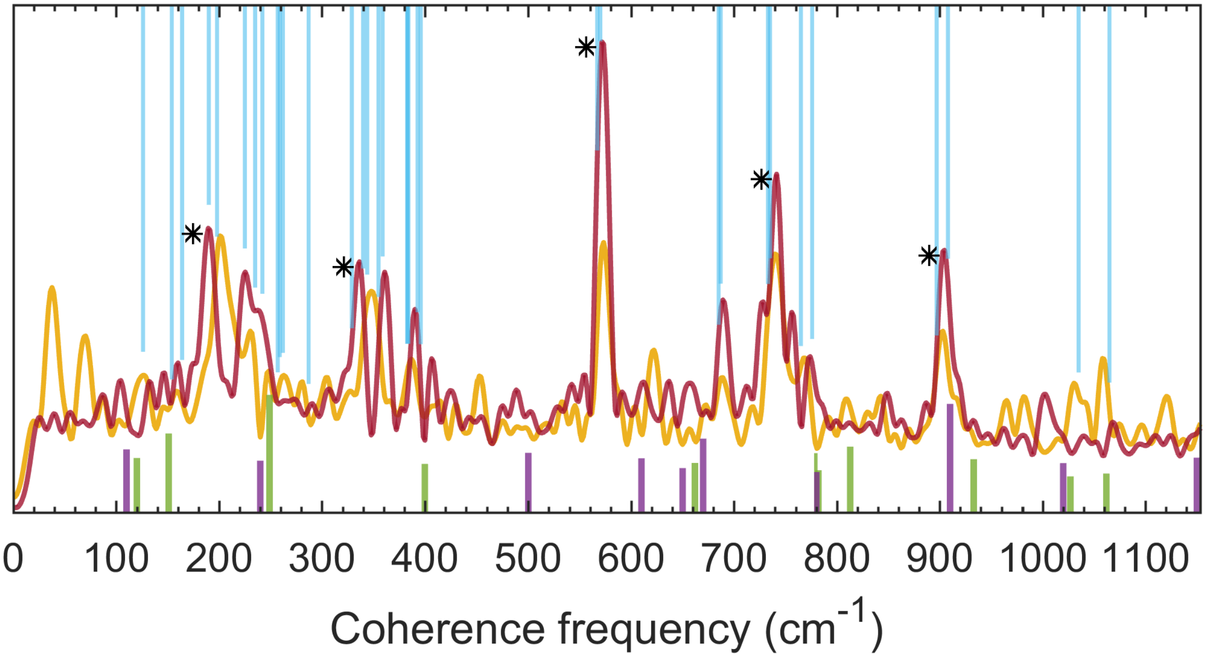

Figure 6.1 Frobenius spectra of W(M250)V (red) overlaid on the spectrum for monomeric BChla (yellow). For comparison purposes, lines are drawn for vibrational modes from resonance Raman experiments [163,169,171] (above, blue) and excitonic difference frequencies from two excitonic models (below, purple [27] and green [4] from Table 5.2). Asterisks indicate prominent modes in both sample spectra.Spectra are normalized by their integrated spectral amplitude.

resonance. In Figure 6.1 we see that there are several exciton difference frequencies which are close in frequency to several vibrational frequencies, indicated by the purple/green and blue lines respectively.

The peak amplitudes of BChla and the BRC in Figure 6.1 for the low-frequency peaks are similar in amplitude while the higher-frequency modes are stronger in W(M250)V (red) compared to BChla (yellow) (Figure 6.1). Comparing the BRC Frobenius spectrum to the BChla spectrum, we see that the high-frequency modes have nearly the same frequency (within a few wavenumbers). There are also several prominent low-frequency peaks in both Frobenius spectra in the same rough spectral region, though the agreement in frequencies is off by tens of wavenumbers. Qualitatively, the low frequency peaks in the BChla spectrum look like broad peaks that likely are due to multiple modes too close in frequency to resolve with our experimental conditions (coherence resolution $\Delta\omega_2 = 9.8$ cm^{-1}). The low-frequency peaks in the BRC Frobenius spectrum are better separated though they still show signs of spectral. The differences in the low-frequency modes are likely due to perturbations of the BChla vibrational frequencies due to protein-pigment and pigment-pigment interactions in the BRC. A resonance Raman study which excited the three main bands of the BRC (P_-*-, B*-, and H*-bands) showed shifts in the low frequency region of the vibrational spectrum around 200 cm^{-1} across the different electronic bands [213].

Judging by the Frobenius spectra alone, the BRC coherences are very similar to those in the monomer BChla. There are no prominent peaks in the BRC spectrum that are not also present in the BChla spectrum. It is worth noting that any short lived electronic coherences either due to a purely electronic origin like in Figure 3.3 or a mixed vibronic origin like in Figure 3.4 would be short lived and so would show a very weak signal. Additionally, we demonstrated in Chapter 5 that the B*-band dominates the Frobenius spectrum due to its large oscillator strength relative to the P_-*- and H*-bands, and the centering of the pump and pulse spectra about 800 nm where the B*-band peaks. It is possible that any coherence signatures of electronic or vibronic coupling involving the special pair (P*) or BPheoa (H*) molecules would be too weak to resolve in the Frobenius spectrum Figure 6.1.

The real rephasing coherence maps for the three high-frequency peaks at $\omega_2 \cong$ 570, 740, & 900 cm^{-1} for both BChla and W(M250)V BRC are shown in Figure 6.2. The BChla maps and the signatures about the B*-band ($\omega \cong$ 12,500 cm^{-1}) in the BRC maps show signal amplitude distribution very similar to that expected for a vibrational displaced oscillator (Figure 3.2). Examining the diagonal peak shapes for the Qy band in the BChla maps and the B-band of the BRC maps, we see that only the ω_2 = 741 cm^{-1} mode of the BRC shows diagonal elongation similar to the inhomogeneous broadening in the BChla maps. The other two high-frequency BRC maps at ω_2 = 572 and 904 cm^{-1} shows more complicated structure, including nodal behavior reminiscent of the destructive interference features in the ω_2 = 902 cm^{-1} map of BChla. For all three BRC coherence maps presented in Figure 6.2 there are also signal peaks immediately above the diagonal that are not present in the BChla maps. The most significant departure from the BChla monomeric maps are the signals labeled 1-4 in the BRC coherence maps.

The low-frequency coherence maps at $\omega_2 \cong$ 200 & 350 cm^{1} for BChla and the BRC are shown in Figure 6.3, along with coherence maps at ω_2 = 656 cm^{-1}. The $\omega_2 \cong$ 350 cm^{-1} are similar in both samples whereas the $\omega_2 \cong$ 200 cm^{-1} maps differ, with the BRC map showing nodal structure along the diagonal similar to the ω_2 = 573 and 905 cm^{-1} maps. As discussed in Chapter 5, the 656 cm^{-1} peak in the W(M250)V Frobenius spectrum is likely a BPheoa vibrational mode given its frequency [163] and absence from the H_A-deficient D_{LL} spectrum (Section 5.3). To confirm this assignment, we show that the coherence map at ω_2 = 656 cm^{-1} in the BChla shows very weak signal at this frequency.

There are additional coherence signals in the BRC maps which are not well explained by the vibrational displaced oscillator, including peaks along ω_1 ~ 12,300 cm^{-1} which look distinct from the peaks we would expect for the B_B band at ω_1 = 12,400 cm^{-1}. Generally, the coherence maps of the BRC show a higher degree of structure compared to BChla monomers and show additional signatures not explained by the purely vibrational or electronic models.

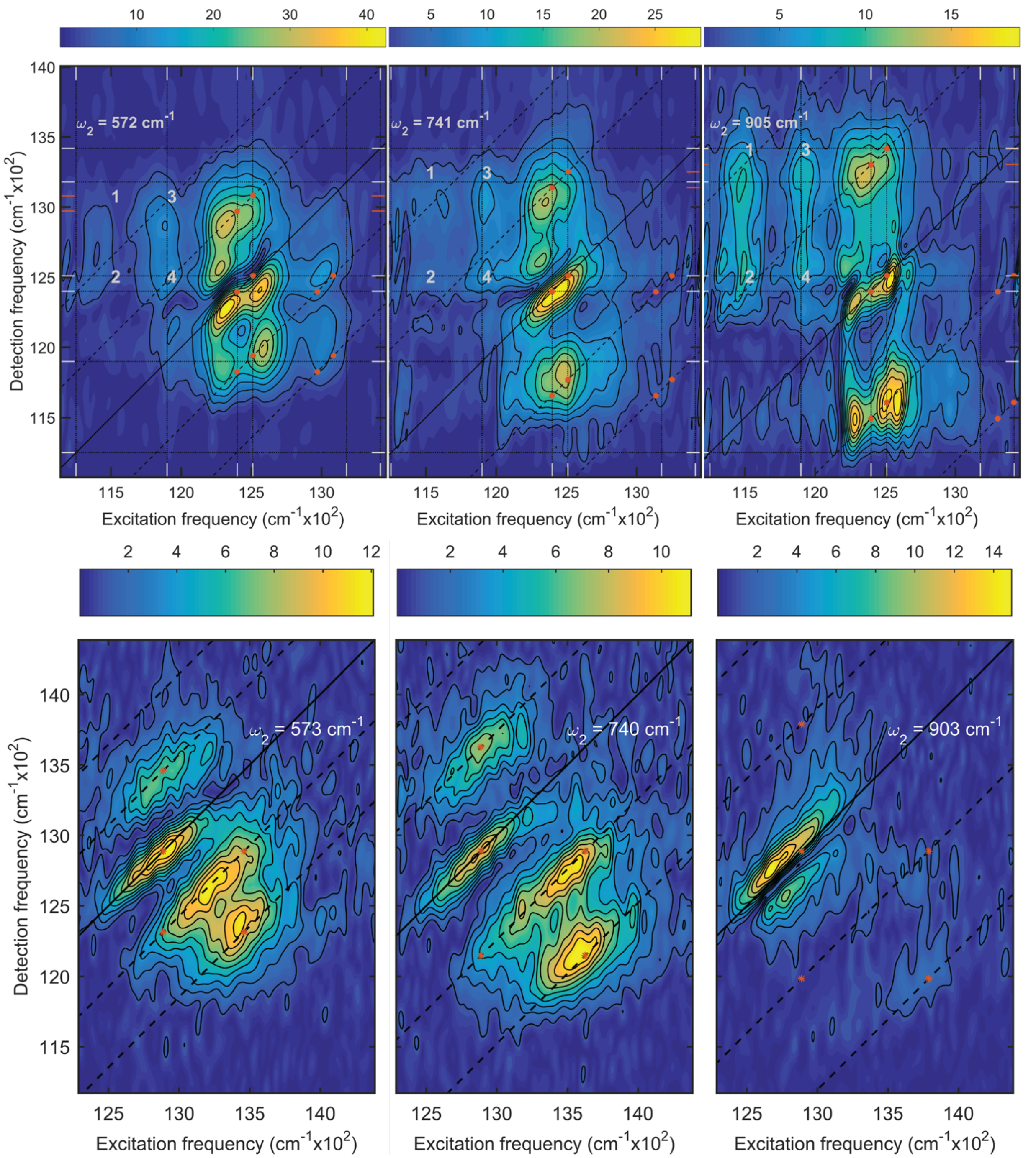

Figure 6.2 Comparison of high-frequency real rephasing coherence maps of the BRC (top) and BChl a (bottom). Coherence maps from Figure 4.6 and Figure 5.6 are reproduced here to aid in comparison. Orange circles are overlaid in the chair pattern from the displaced oscillator model (Figure 3.2) centered on the B* bands (top) and the Q_y peak (bottom) . Overlaid on the 2D maps are diagonal lines at ($\omega_1 = \omega_3$) and ($\omega_1 = \omega_3 \pm n\omega_2$) for several n. Vertical and horizontal lines which correspond to the excitonic energies found from global kinetic fitting are drawn on the BRC coherence maps (top) [4]. Black contours are drawn at 10 – 100% of the maximum of the coherence amplitude.

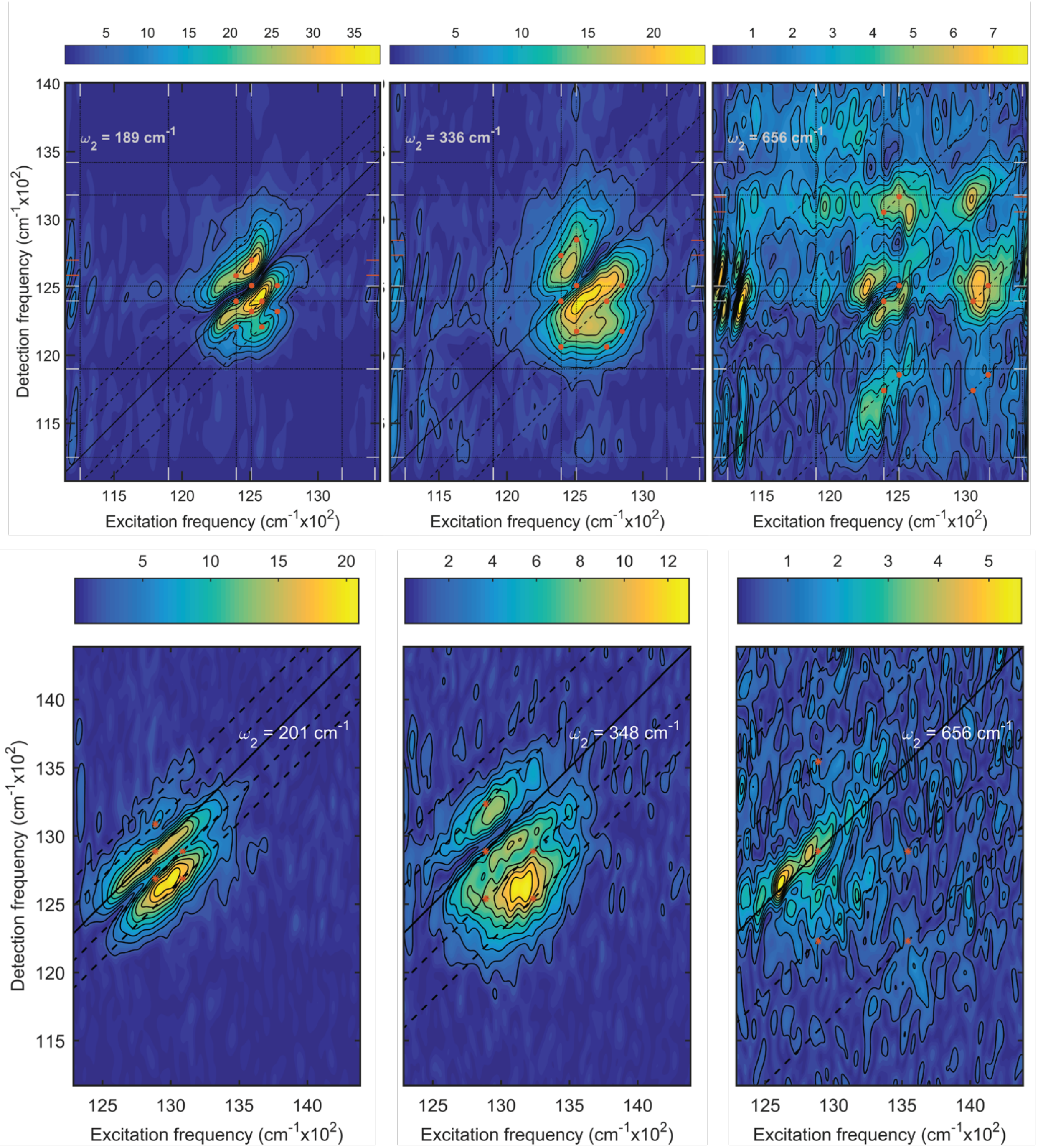

Figure 6.3 Comparison of low-frequency and 656 cm^{-1} real rephasing coherence maps of the BRC (top) and BChl a (bottom). Coherence maps from Figure 4.6 and Figure 5.6 are reproduced here to aid in comparison. Orange circles are overlaid in the chair pattern from the displaced oscillator model (Figure 3.2) centered on the B* bands (top) and the Q_y peak (bottom). Overlaid on the 2D maps are diagonal lines at ($\omega_1 = \omega_3$) and ($\omega_1 = \omega_3 \pm n\omega_2$) for several n. Vertical and horizontal lines which correspond to the excitonic energies found from global kinetic fitting are drawn on the BRC coherence maps (top) [4]. Black contours are drawn at 10 – 100% of the maximum of the coherence amplitude.

Section 6.2 Vibronic Contributions

We will now focus our discussion on the signals labeled 1-4 in W(M250)V BRC high-frequency coherence maps in Figure 6.2. In Chapter 5 we discussed several possible mechanisms that could give rise to these signals, eliminating strongly coupled vibrational modes of the lower-exciton (P_{-}*) given the consistent excitation frequency of signatures 3 & 4 for different coherence modes and the assignment of P_{+}* to $\omega = 11{,}900$ cm^{-1}, the excitation frequency of signals 3 & 4 [4]. Signals 1-4 oscillate during the 2DES time delays (t_1,t_2,t_3) at ($-P_n^*$,$+\Omega$,$+B_A^*$) or ($-P_n^*$,$+\Omega$,$+(B_A^*+\Omega)$) where the subscript n indicates either the upper or lower excitonic peak and Ω is the coherence frequency which closely matches known vibrational modes. The excitation and detection frequencies corresponding P_n^* and B_A^* transitions suggest coupling between the special pair and A-branch monomeric BChla. In the case of purely electronic coherence between P_{-}^* or P_{+}^* and B_A^*, we would expect to see cross peaks 2 & 4 at $\omega_3 \cong B_A^*$ but these should oscillate with the excitonic difference frequencies, $\omega_2 = \Delta E = 1{,}260$ & 610 cm^{-1} respectively (Table 5.2). The fact that we additionally see signals above the (P_n^*,B_A^*) crosspeaks (signals labeled 1 & 3) for many coherence frequencies, and that these signals are present at several coherence frequencies that match known vibrational modes suggests there is more at play than a purely electronic origin. These factors and the similarity of these coherence frequencies with both known vibrational modes and excitonic difference frequencies suggests that these signatures arise from vibronic coupling. Comparing these signals to the vibronic model presented in Chapter 3 suggests these signals 1-4 arise from excited state absorption to a bi-excitonic state of P* and B*. It is, however, surprising that signals 1 & 3 are at the same detection frequency $\omega_3 \sim B_A^* + \omega_2$. This suggests that the pathways for signals on P_-^* and P_+^* involve the same states and can possibly be explained by the rapid internal conversion of P_+^* to P_-^* which we have measured to be 25 fs [4]. In Figure 6.4 we present our current hypothesis for signals 1-4 which involves excited state absorption of a vibronically coupled system of strongly coupled molecular sites P_A, P_B, and B_A. The states involved in the coherences pathways proposed in Figure

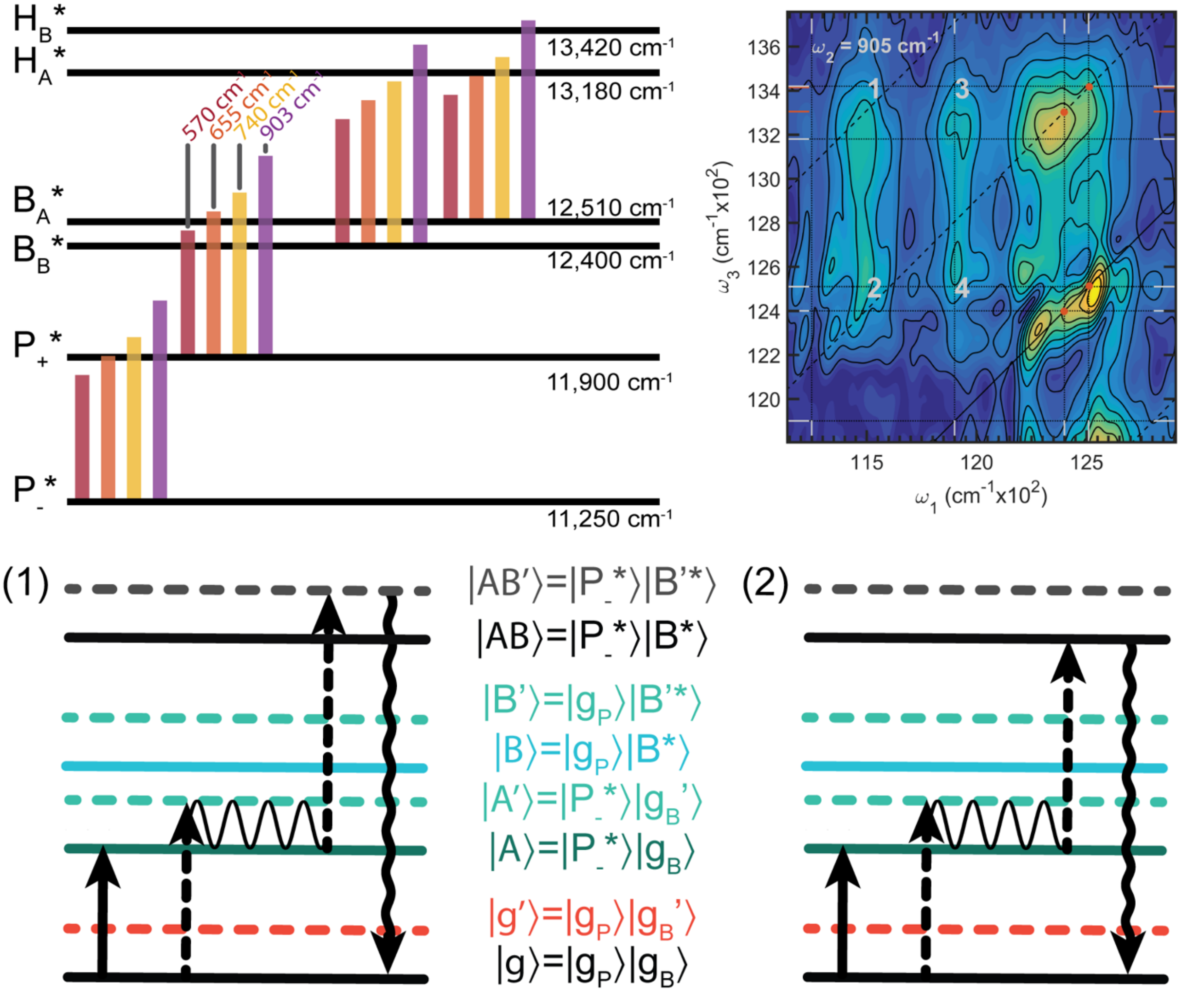

Figure 6.4 Proposed vibronic origin of BRC signals. (Top left) Excitonic energy Jablonski diagram of the 6 excitonic electronic states from Niedringhaus, et al [4] with proportional vibrational frequencies, representing vibrationally-assisted resonance between states. (Top right) Windowed real rephasing W(M250)V BRC coherence map for $\omega_2 = 903\ cm^{-1}$, highlighting signals 1-4. (Bottom) Proposed Light-Matter Interaction Pathways that give rise to signals 1 & 2. Signals 3 & 4 are explained by a similar mechanism where $|P_-^*\rangle$ is replaced with $|P_+^*\rangle$ and internal conversion takes place following the second pump interaction. Delocalized excitonic states are derived from simulations using a reduced model of the BRC starting with model parameters from Jordanides, et al. [27]. The details of the simulation will be included in a publication in preparation.

6.4 result from a large degree of delocalization across these molecules following diagonalization of the Hamiltonian. The details of this model are the subject of a manuscript in preparation.

Briefly, correctly modelling the signals labeled 1-4 in Figure 6.2 requires first reproducing the location of the upper-exciton, P_+*. This can be accomplished by including special pair charge transfer states. Including special pair charge transfer states has previously been demonstrated to better describe the temperature-dependence of the P_-* band than models which do not include these states [45]. Another departure from typical models of the BRC electronic structure required for modeling these signals is strong coupling between the special pair molecules, P_A and P_B, and the monomeric BChla, which in this model is B_A. Typical models of the BRC include P_n-B_n coupling strengths of about 100 cm^{-1} [27], which does not result in large delocalization between these molecules. The signatures of vibronic coherence we see in the coherence maps in Figure 6.2 suggest a large degree of delocalization and a shared ground state between P_n and B_n molecules (Figure 6.4). Supporting this prediction, modeling signals 1-4 requires strong coupling, $J > 100\ cm^{-1}$, which results in very delocalized states. The model described in Figure 6.4 is a reduced model of the total BRC electronic structure, only including the special pair states (though only states involving P_-* are shown) and one monomeric BChla which has one active ground and excited state vibrational mode. The exact details of this model, and any updates on this model following the submission of this thesis, will be the subject of a publication in progress.

In attempting to understand the origin of these signals we also considered coherence transfer processes and Energy Transfer Induced Coherence Shifts

(ETICS) [61]. Coherence transfer processes like those shown in Figure 3.6 result from coupling between off-diagonal density matrix terms and are typically neglected in models of molecular systems (Secular approximation) [14,190]. A theoretical model of the BRC special pair that did not make the Secular approximation showed that coherence transfer effects could be significant in systems where states with very different reorganization energies were coupled to one another [45]. Signals 1 & 2 would then be explained by preparation of a vibrational coherence on the excited state of P_-* which is rapidly transferred to the B_A excited state. A similar mechanism would explain the signatures along the P_+ band but would first involve rapid internal conversion to P_- in order to explain the similarity of detection frequencies of signals 1 & 3. These effects would likely be very weak however and would imply uphill energy transfer from the P-band to the B-band.

Section 6.3 Destructive Interference Signatures

A recent study of coherences in oxidized BRCs from *Rh.* sphaeroides by Paleček, et al. [61] observed nodes along the diagonal line in coherence maps for many different coherence frequencies. These signatures were proposed to be due to destructive interference of signals oscillating at $+\omega_2$ and $-\omega_2$ which added destructively when the real part of the signal was taken. The explanation offered by Paleček, et al. involves a $+\omega_2$ coherence signal originating on the excited electronic state acquiring a π phase shift, which then destructively interferes with $-\omega_2$ ground state coherences. This phase shift is acquired when rapid energy transfer away from the electronic state demotes the excited state coherence to the ground state [61] in the ETICS mechanism. As noted previously, we see several signatures of destructive interference on the B*-band in the coherence maps of the BRC (Figure 6.2 and Figure 6.3) very similar to those observed by Paleček, et al. [61]. Extending this model to rapid energy transfer between B* and excitonic states of P* could hypothetically explain the signals we see above the diagonal labeled 1-4. In a model where P* is strongly coupled to B_A*, following rapid energy transfer from the P_-* and P_+* excited states to charge separated states or internal conversion (for P_+*) could demote excited state vibrational coherences to the ground state where the probe pulse could interact with the B_A* transition. In this case we would expect to see signatures 1-4 grow in following the rapid internal conversion at $\omega_1 = P_+$* (25 fs) or following charge separation (~2500 ps) [4]. In the study by Paleček, et al. [61] the authors perform a polarization-selective 2DES such that they are able to suppress purely vibrational coherence, allowing them to resolve two dominant coherence frequencies. This allows the authors to examine the time-dependent dynamics of the two coherence modes directly, whereas our all-parallel experiment excited many coherences simultaneously, making it very difficult to determine t_2-dependent behavior without additional analysis.

In Figure 6.5 and Figure 6.6 are several coherence maps generated following a Sliding Window Fourier Transform (SWFT) method to analyze the t_2-dependent behavior of the three high-frequency coherence modes highlighted in Figure 6.2. This analysis is performed on the $0 \leq t_2 \leq 3500$ fs real rephasing data of BChla and W(M250)V BRC via Matlab's spectrogram function using a 490 fs wide Tukey window function, centered at different points along t_2, where t_c is the temporal center of the window. The 490 fs window yields a coherence frequency resolution of $\Delta\omega_2 = 68$ cm^{-1}. Several of the maps plotted in Figure 6.5 and Figure 6.6 are slightly different in frequency than those plotted by taking the Fourier transformation of the full t_2 trace; we can attribute these differences to the decreased frequency resolution from using the SWFT though it is also possible that these frequencies indicate real peaks which rapidly shift over the course of t_2.

In addition to coherence maps at two values of t_c, Figure 6.5 and Figure 6.6 show t_c-dependent traces at several points in the 2D coherence maps. For most coherences shown, these t_c traces decay by the end of the scan at 3,500 fs. There are a few exceptions in both BChla and the BRC; the diagonal peak of the $\omega_2 \sim 903$ cm^{-1} mode for BChla in Figure 6.5 shows a spike at around 1,700 fs and the B-diagonal peak for the same mode in the BRC map in Figure 6.6 shows a similar increase in signal but at a slightly later time. What is clear from the maps for $\omega_2 \sim 740$ cm^{-1} in the BRC are that the temporal dynamics of the signals 1-4 are very similar to those which correspond to excited state vibrational modes on B* (Figure 6.6). t_c traces at 2D points corresponding to signals 1-4 show no sign of growing in on the time scale of charge separation or any energy transfer rates in the BRC. The spectrogram results suggest that ETICS does not explain signals 1-4, though this method is not sensitive to short-lived signals like those that would be expected from internal conversion between P_+* and P_-*.

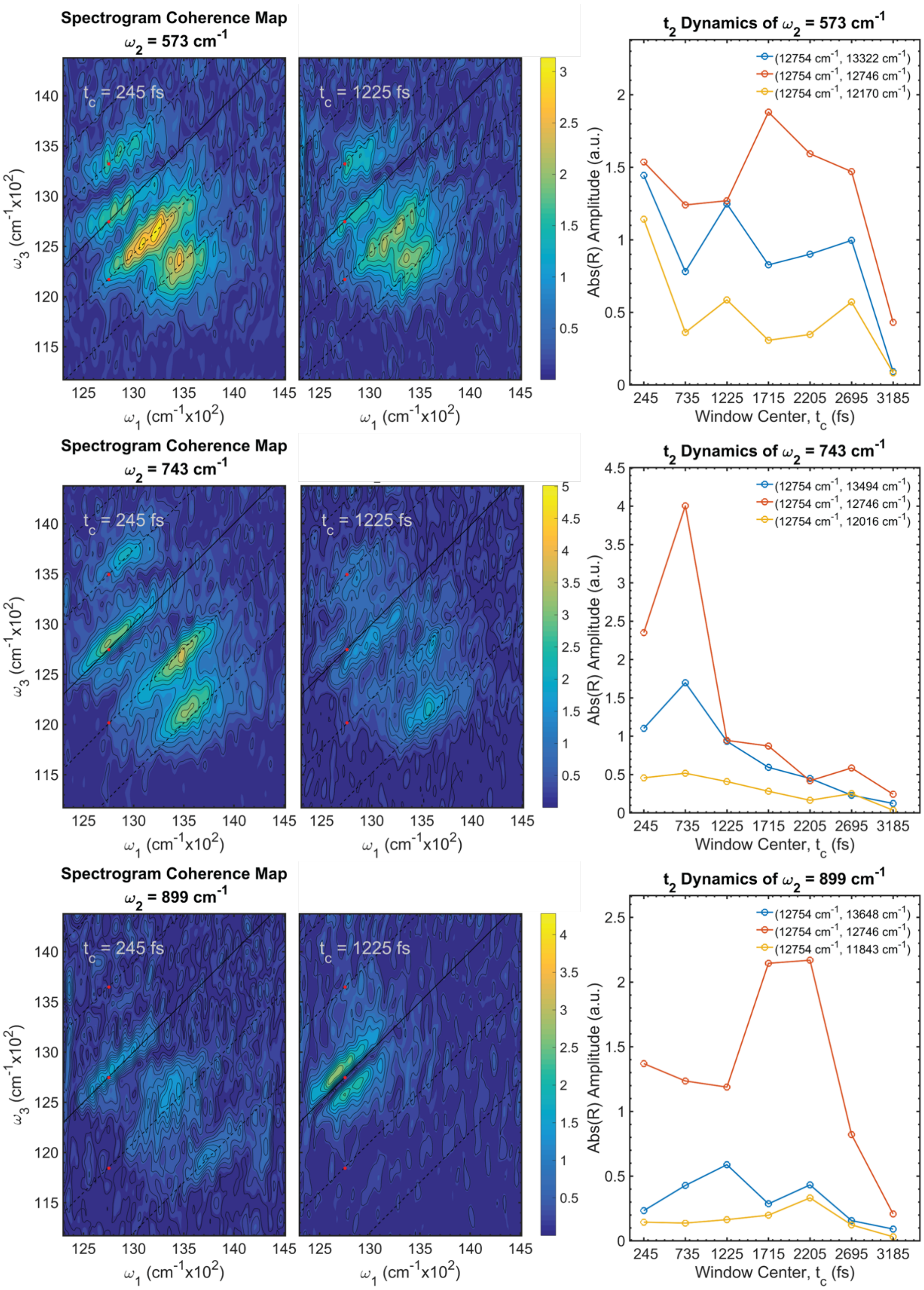

Figure 6.5 Bacteriochlorophyll a Sliding-window Fourier Transform (SWFT) Maps. $0 \leq t_2 \leq 3500$ fs. Real rephasing data was analyzed using a SWFT with a 490 fs width Tukey window ($\Delta\omega_2 = 68$ cm^{-1}). (Left & center) Coherence maps plotted for two time points where the window function was centered at t_c = 245 & 1225 fs for the peaks closest in frequency to ω_2 = 573, 740, and 903 cm^{-1} modes. (Right) SWFT coherence amplitude at several (ω_1,ω_3) points, denoted by red circles in the coherence maps, as a function of t_c show the time-dependence of coherence signals.

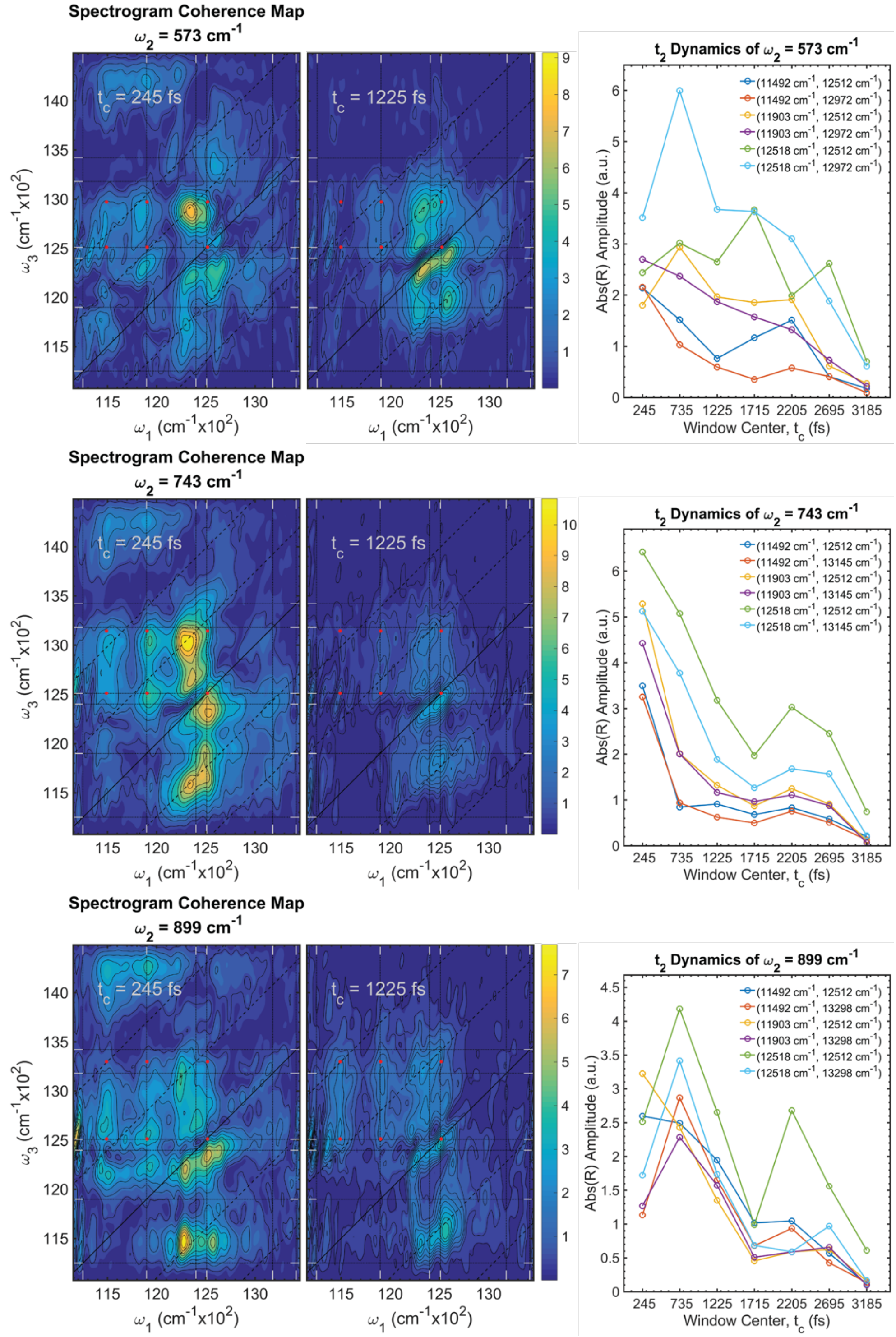

Figure 6.6 W(M250)V BRC Sliding-Window Fourier Transform (SWFT) Maps. $0 \leq t_2 \leq 3500$ fs. Real rephasing data was analyzed using a SWFT with a 490 fs width Tukey window ($\Delta\omega_2 = 68$ cm^{-1}). (Left & center) Coherence maps plotted for two time points where the window function was centered at $t_c = 245$ & 1225 fs for the peaks closest in frequency to $\omega_2 = 572$, 741, and 905 cm^{-1} modes. (Right) SWFT coherence amplitude at several (ω_1,ω_3) points, denoted by red circles in the coherence maps, as a function of t_c show the time-dependence of coherence signals.

We have also performed a frequency-isolating analysis technique which windows a specific coherence frequency from the 3D frequency cube (ω_1,ω_2,ω_3) using a Gaussian window and inverse Fourier transforms (IFFT) to the time domain to perform a similar t_2-dependent analysis as performed by Paleček, et al [61]. In Paleček, et al, the π phase shift attributed to ETICS was resolved by fitting sinusoids to the portion of the t_2 traces following energy transfer. The fit was then extrapolated for the entire t_2 region, revealing a mismatch between the signal and fit at early times preceding energy transfer; the poor fit at early t_2 was attributed to a π phase shift [61]. Using our IFFT analysis we can perform a similar fitting; in Figure 6.7 and Figure 6.8 we show IFFT t_2 traces for the prominent high-frequency coherence modes of BChla and the W(M250)V BRC, respectively. To test whether the signals above the diagonal (labeled 1-4) are due to an ETICS-like process due to internal conversion from P_+* to P_-* or charge separation from P_-*, we fit t_2-traces in the region following energy transfer to P_+* (~200 fs) and before charge separation (~2000 fs) to a single sinusoid and extrapolate this fit for the entire t_2 axis. Looking for π phase shifts at early times ($0 \leq t_2 \leq 200\, fs$) we see some t_2 traces that show what looks like a π phase shift in the $\omega_2 \cong 570$ cm^{-1} of both the BRC and BChla, seeming to support the hypothesis that these signatures are due to an ETICS-like process. However, if we fit the early times to a single sinusoid we see that the frequency is shifted from later times, and what looks like a π phase shift is due to frequency mismatch.

These results support the results of the spectrogram analysis; that the signals labeled 1-4 in Figure 6.2 do not exhibit any time dependence that can be correlated with energy or charge transfer events in the BRC. Additionally, this analysis suggests that several coherence frequencies undergo a rapid frequency shift within the first few hundred fs. In the case where excited state and ground state vibrational modes have significantly different frequencies, decay of an excited state vibration to the ground could result in frequency shifts. It is worth noting that the coherence maps at t_c = 245 and 1225

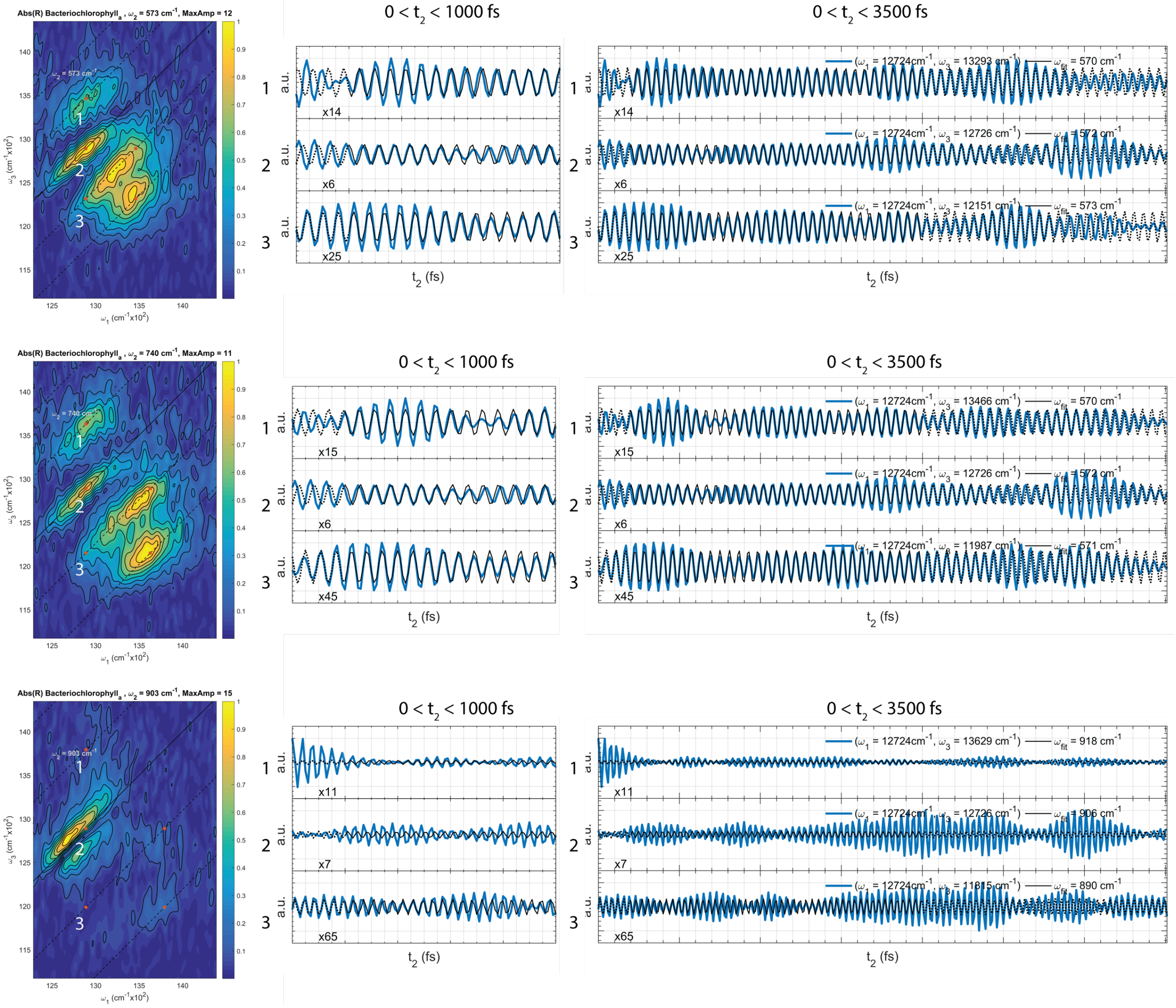

Figure 6.7 Inverse Fourier Transformed t_2 traces of BChla in isopropanol. Inverse Fourier transformed spectra were generated by windowing the 3D frequency data (ω_1,ω_2,ω_3) about a specific coherence frequency (for the BChla ω_2 = 572, 740, & 903 cm^{-1}) using a Gaussian window function. Following windowing, the data was inverse Fourier transformed with respect to ω_2, yielding the data as a function of (ω_1,t_2,ω_3) but with fewer oscillatory components. t_2 traces are shown for select points (ω_1,ω_3) corresponding to the peak locations of signals labeled 1-3 (left column). These t_2 traces (blue) are shown with a single sinusoidal fit (black, solid – fit region, dashed - extrapolated) (right column); the first picosecond is shown to highlight rapid frequency shifts within the first few hundred femtoseconds (center column). These t_2 traces are sometimes better fit with multiple sinusoids.

fs for $\omega_2 \sim 903$ cm^{-1} in BChla (Figure 6.5) show that the destructive interference signals grow in at later times, which could be consistent with these types of frequency shifts.

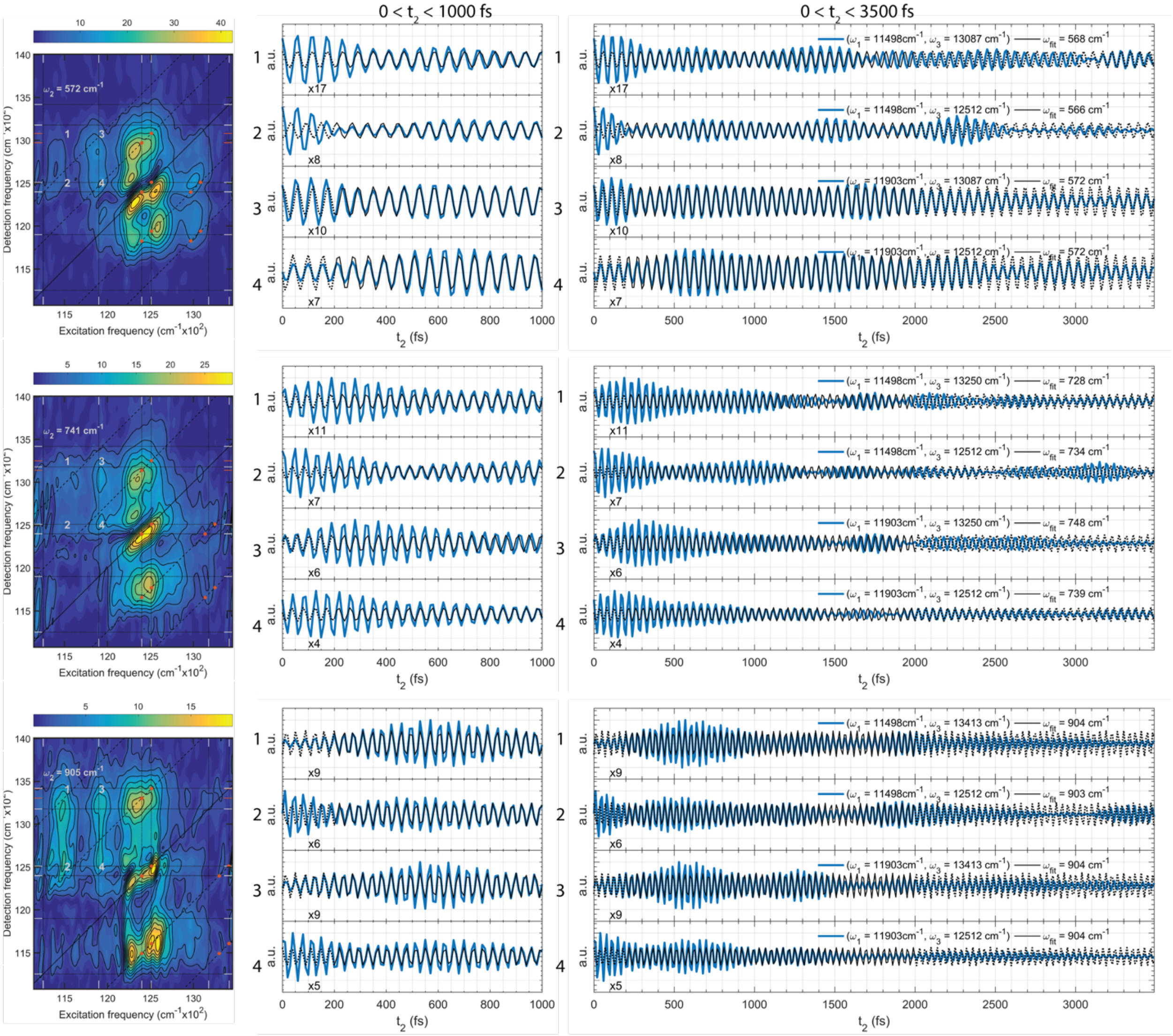

Figure 6.8 Inverse Fourier Transformed t_2 traces of W(M250)V BRC. Inverse Fourier transformed spectra were generated by windowing the 3D frequency data (ω_1,ω_2,ω_3) about a specific coherence frequency (for the BRC ω_2 = 573, 741, & 905 cm^{-1}) using a Gaussian window function. Following windowing, the data was inverse Fourier transformed with respect to ω_2, yielding the data as a function of (ω_1,t_2,ω_3) but with fewer oscillatory components. t_2 traces are shown for select points (ω_1,ω_3) corresponding to the peak locations of signals labeled 1-4 (left column). These t_2 traces (blue) are shown with a single sinusoidal fit (black, solid – fit region, dashed - extrapolated) (right column); the first picosecond is shown to highlight rapid frequency shifts within the first few hundred femtoseconds (center column). These t_2 traces are sometimes better fit with multiple sinusoids.

Section 6.4 Conclusions

The coherences observed in the BChla and W(M250)V BRC share many of the same frequencies, closely matching known vibrational frequencies of monomeric BChla (Figure 6.1). Notably, there are no prominent modes in the W(M250)V Frobenius spectrum that are not also present in the BChla Frobenius spectrum Figure 6.1. The coherence maps of both the BChla and W(M250)V (Figure 6.2 and Figure 6.3) show signatures distributed in a pattern characteristic of purely vibrational coherences as determined by the displaced oscillator model in Chapter 3 (Figure 3.2). There are several notable differences in the W(M250)V coherence spectra, however, in particular the four signals labeled 1-4 (Figure 6.2) which lie far above the diagonal line and are not well described by either purely vibrational or purely electronic models.

We consider several possible mechanisms which could explain these signals but are able to eliminate contributions due to rapid energy transfer (ETICS) using a Sliding Window Fourier Transform analysis and an Inverse Fourier Transform windowing method. Our current hypothesis is that these signatures are a result of vibronic coupling of the special pair molecules to the A-branch Bacteriochlorophyll a, suggesting a higher P-B_A coupling strength than previously reported. The vibronic coupling evident by signals 1-4 is the focus of a manuscript in progress.

CHAPTER 7 CONCLUSIONS

Section 7.1 Summary

In this thesis I have performed cryogenic two-dimensional electronic spectroscopy (2DES) experiments (Chapter 2) in order to study the coherent oscillatory signals (Chapter 3) in two systems, the Bacterial Reaction Center (BRC) and its most-prominent molecular constituent BChla as a monomer in solution. These experiments utilized broadband pulses to simultaneously study the three Qy electronic bands of the BRC, which allows us to better characterize the electronic structure and behavior of this system. This is some of the first 2DES work to study BRCs which perform charge separation and shows some of the clearest signatures of coherence in this system to date. Additionally, this work comprises the first 2DES to observe and characterize a large number of coherent signals on monomeric BChla in solution, which had previously been determined to only have a few weak coherent oscillations [115,155].

We observe many coherent oscillatory signals in both monomeric BChla in solution (Chapter 4) and two BRC mutants, W(M250)V and D_{LL} (Chapter 5). Analysis of the coherent signals shows that the BChla coherences are vibrational in origin, as might be expected for a molecular monomer with many Franck-Condon active vibrations [127], and additionally determine that the majority of coherence signals in the BRC are vibrational in origin as well. By comparing the coherence signals in BChla versus the BRC we are able to identify additional signatures in the BRC that are not explained by a vibrational displaced oscillator or an electronic dimer model (Chapter 6). These signatures can be explained by vibronic coupling between the special pair and monomeric BChla molecules of the BRC, indicating a larger coupling strength between these sites than previously considered [27]. Additionally, these signatures of vibronic coupling resolve the upper-exciton of P (P_+*) which is very weak in the full 2DES signal but whose coherences signals are enhanced due to the vibronic coupling with B [142]. We have demonstrated the ability of coherence analysis of 2DES to resolve weak electronic transitions and glean information about the excitonic structure of the BRC. Although it is difficult to comment on the functional relevance of the observed coherences in the BRC, the coherence studies clearly demonstrate the existence of vibrational-electronic resonances that have been proposed in other work [60–63] to enhance energy and charge separation processes. We hope that the rich spectroscopic information provided by our 2D data and coherence analysis will inspire modeling of the role of vibrational-electronic resonance in the energy transfer and charge separation processes of the BRC.

In addition to my work on BChla and BRCs, I have studied coherences in Chlorophyll a (Chla) using 2DES and Two-Color Rapid Acquisition Coherence Spectroscopy (T-RACS) [77], which are also vibrational in origin. I had also begun studying coherences in molecular dyads [217], which mimic the coupling of the BRC special pair, using 2DES. In my analysis of the coherence signals, I have developed additional coherence analysis techniques for our lab, including complex signal analysis, presented in this thesis for the complex rephasing signals (based on the analysis presented by Paleček, et al. [61]), and various time-frequency analysis techniques in order to characterize the temporal dynamics of coherences.

Section 7.2 Future Work

The ultimate goal of studying coherences in photosynthetic protein complexes is to determine whether or not coherent oscillations are themselves functionally-relevant or whether they report on functionally-important vibrational electronic resonances. Unfortunately, establishing a causal link between our observations and the rapid and efficient energy and charge transfer processes in the BRC is challenging for several reasons. While the work in this thesis moves our understanding of coherences in two key systems forward, it is inconclusive about the functionality of observed coherences. The structure and function of the BRC are inextricably linked, making it difficult to selectively change energy gaps and vibrational frequencies without substantial structural changes. Our studies of D_{LL}, which does not undergo charge separation was a first attempt to link coherence and charge separation. We found that it appears to show similar coherence signatures to W(M250)V, indicating that charge separation does not initiate new coherent signatures. Recent work on the Fenna-Matthews-Olson antenna complex has shown that coherences are relatively unaffected by mutations [108], in contrast to the early work of Vos and Martin that showed the sensitivity of low-frequency modes to mutations near the special pair [103,154].The work in this thesis also raises some questions about BChla vibrations, as we have seen signatures which have previously been attributed to rapid energy transfer [61] as well as coherences that show amplitude distributions previously attributed to vibronic coupling (Chapter 4.3). In order to address these and other open questions, I would like to propose the following follow-up experiments:

- Additional 2DES studies and modeling of BChla and Chla monomers in order to: better characterize the time-dependent behavior of vibrational coherences; investigate the mechanism giving rise to destructive-interference signatures; and investigate the mechanism giving rise to the vibronic-looking signatures in the low-frequency coherence maps.
- 2DES Stark Spectroscopy of BRCs. Linear Stark spectroscopy has previously been used to measure the Stark shifts of the BRC B*-band following charge separation [29] but linear methods are limited in spectrally congested systems. 2DES Stark Spectroscopy was recently developed [218] and demonstrated to identify charge transfer and excitonic states in TIPS-pentacene [219]. Performing 2DES Stark spectroscopy on BRCs could allow us to measure and better characterize charge transfer states, and could potentially allow us to resolve coherences involved in charge separation processes.
- 2DES of W(M252)V BRCs from *Rhodobacter sphaeroides*; this species of purple bacteria has been studied and characterized much more extensively than the species studied in this thesis, *Rhodobacter capsulatus*. Though it is usually assumed that the structure, spectra, and dynamics of the *Rh. sphaeroides* BRC are applicable to *Rh. capsulatus* given their amino acid sequence similarities [203], our assignment of P_+^* far to the red of assignments using *Rh. sphaeroides* [27] suggests there may be significant structural differences. Studying the W(M252)V, the *Rh. sphaeroides* mutant analogue of W(M250)V, would allow us to characterize these differences.

- Polarization-selective 2DES of the BRC. Several multidimensional spectroscopy studies have previously demonstrated the strength of full control of each pulses' polarization for selectively exciting or suppressing certain coherence signals [59,61,94]. The polarization scheme used in studies by the Zigmantas group which selectively suppresses signals due to intramolecular vibrations [59,61] would allow us to better characterize vibronic coherence contributions in the BRC. This setup requires control of each pulse polarization and implementing total polarization control into the interferometer described in Chapter 2.2 represents a challenge.
- Development of robust time-frequency analysis techniques. As mentioned in Chapter 3.4, Volpato and Collini [162] have well characterized several time-frequency analysis techniques in terms of their reliability. Using some of the suggestions from this text to develop a reliable time-frequency analysis method for interpreting coherence data is essential for all-parallel 2DES experiments or systems with many coherence frequencies.
- 2DES of molecular dyads. Linked hydroporphyrin molecules have been designed and synthesized to mimic strong coupling like that seen in the special pair of the BRC [217]; analyzing the coherence signals in this system could help us better understand how electronic coherence effects manifest in 2DES data.
- 2DES of Bacteriopheophytin a. In Chapter 5 we discuss coherence signals which are due to a vibrational mode unique to the Bacteriopheophytin a (BPheoa) in BRCs. To better characterize this mode in the BRC data, we should also perform coherence studies of BPheoa monomers in solution.

- Additional 2DES of W(M250)V BRCs with shifted pump and probe spectra. As discussed in Chapter 5 and Chapter 6, the coherence spectrum of the W(M250)V BRC was dominated by contributions from the B-band, due in part to the spectra of both the pump and probe pulses being centered about the B-band. The light source used to generate the pump and probe pulses is centered about 800 nm but we can use pulse shapers to modify the pump and pulse spectra, primarily through amplitude shaping, to better excite coherences on the P*- and H*-bands.
- 2DES of W(M250)V BRCs using different probe light sources. Using a continuum or ultraviolet (UV) probe we can study a larger portion of the BRC spectrum. The continuum probe would allow us to monitor Qx dynamics following excitation of the Qy bands while the UV probe would interrogate amino acids in the surrounding protein.

APPENDIX A SUMMARY TABLES

This Appendix includes several reference tables summarizing literature values for coherences (Section A.1) and vibrational modes (Section A.2). The coherence frequencies resolved in Bacteriochlorophyll a (BChla) monomers (Table A.1) and Bacterial Reaction Centers (BRC) (Table A.2) presented in the literature, as well as the coherence frequencies presented in this thesis (Table A.3). Vibrational spectroscopy results from various Raman techniques, Fluorescence line narrowing and hole-burning techniques are summarized for monomeric BChla and Bacteriopheophytin a (Table A.4a&b) and the BRC (Table A.5a,b,&c).

Section A.1 Coherence Frequencies

Table A.1 Coherence modes in Bacteriochlorophyll a Summary

Reference	[198] Chachisvilis, et al.	[111] Arnett, et al.	[113] Shelly, et al	[115] Fransted, et al.	[78] Yue, et al.
Experiment Type	TA	3PE	PP	2DES	2DES
T	4.2 K	N/A (RT)	RT	N/A (RT)	RT
Pump/Probe Pulse Duration (fs)	86/86	13/13	60/60	15.6/15.6	35/35
Coherence resolution (cm^{-1})	51	16.7	2.78	22.4 - 33.4	66.7
Coherence Modes (cm^{-1})	104	185	63	550	80
		210	81	730	160
		340	91/92		200
		480	108		280
		560	127		340
		730	165		400
		790	195		
		890	210		
		1180			

Table A.2 Coherence modes in Bacterial Reaction Centers Summary

Reference	[98] Vos, et al.	[220] Westenhoff, et al.	[60] Ryu, et al.	[61] Paleček, et al.	[62] Flanagan, et al.	[63] Ma, et al.
Experiment Type	Pump Probe	2DES	2CPE	2DES	2DES	2DES
Pump/Probe Pulse Duration (fs)	30/~30	17/17	45/45	17/17	8/12	18/18
Coherence resolution (cm^{-1})	8.3	-	16.7	20.6	33.4	16.7
Coherence Modes (cm^{-1})	15	90	50	195	180	33
	69	190	80	325	330	63
	92	220	125	560	560	153
	122	310		650	650	235
	130	390		720	730	
	153	575		890	890	
	191	645		1150	1040	
	329	710			1170	

Table A.3 Prominent Peaks in BRC Frobenius Spectra. Criteria for "prominence" determined using Matlab's findpeaks function with "MinPeakHeight" criteria after subtracting a smoothed fit to the background of the Frobenius spectrum. The "MinPeakHeight" criteria was: ≥ 30% for BChla; ≥ 7.5% of the maximum for W(M250)V; and ≥ 10% for DLL.

BChl a in isopropanol	W(M250)V BRC	DLL BRC
ω_2 (cm^{-1})	ω_2 (cm^{-1})	ω_2 (cm^{-1})
36	101	33
69	131	72
202	144	91
232	173	131
349	189	154
385	206	189
454	225	219
572	336	238
621	363	251
689	392	353
741	408	385
768	555	402
901	572	529
1032	611	549
1058	637	565
1192	656	683
1251	689	705
1316	712	722
1473	728	735
1486	741	751
1542	758	764
	774	898
	849	1081
	905	1176
	1003	1349
	1068	
	1597	

Section A.2 Vibrational Frequencies

Table A.4a Bacteriochlorophyll a and Bacteriopheophytin a Vibrational Frequencies

Reference	[163] Lutz, et al.		[164] Cotton & Van Duyne						[221] Renge, et al.			
Experiment Type	RR		RR						FLN			
T	35 K		RT						5 K			
Molecule & Solvent	BChla	BPheoa	BChla, pyridine	BChla, bis-pyridine	BChla, ethanol	$(BChla)_3$	(BChl-pyrazine)n	BChl hydrate	BChla, TEA		Bpheoa, i-Am2O	
Band	Qx	Qx	B						Qy, Ground State	Qy, Excited State	Qy, Ground State	Qy, Excited State
λ_o (nm)	528.7	579	457.9						703.2		755	
Vibrational Frequency (cm^{-1})	140	145	899	772	794	689	351	1283	82	166	150	148
	170	183	950	792	965	1285	565	1332	164	194	187	183
	198	220	965	893	1027	1335	589	1360	196	342	346	337
	262	235	1017	1065	1139	1360	635	1376	219	379	461	444
	295	250	1029	1120	1154	1427	694	1419	232	449	564	560
	355	269	1064	1139	1167	1531	717	1525	342	564	588	622
	384	290	1117	1153	1215	1589	754	1553	270	591	622	666
	423	345	1142	1175	1245	1609	765	1592	370	624	659	683
	442	372	1159	1216	1284		1291	1608	380	653	678	703
	570	391	1211	1252	1332		1338	1627	397	680	711	720
	595	425	1247	1288	1359		1365	1637	568	701	724	732
	635	473	1283	1335	1380		1418	1652	591	727	739	745
	670	525	1335	1358	1389		1524		624	757	753	774
	687	567	1360	1382	1490		1535		643	773	776	838
	712	585	1382	1392	1516		1569		683	795	841	850
	735	617	1392	1417	1531		1595		697	845	878	868
	765	658	1427	1446	1579		1654		706	879	898	887
	795	688	1451	1458	1597		1679		729	917	922	903
	855	712	1463	1490	1657				763	950	934	949
	897	724	1497	1519					775	967	962	1033
	927	753	1529	1531					795	980	980	1058
	952	780	1589	1577					847	1011	997	1107
	970	840	1609	1594					879	1033	1061	1165
	1005	881	1671	1675					897	1044	1098	1197
	1035	935							923	1096	1106	1230
	1065	964							950	1104	1134	1250
	1117	995							967	1147	1177	1303

	1140	1038							980	1169	1227	1350
	1162	1060							1005	1186	1357	1382
	1212	1103							1026	1253	1381	
	1242	1134							1043	1323	1396	
	1290	1215							1113	1335		
	1342	1242							1135	1350		
	1377	1282							1159	1381		
	1402	1326							1174	1482		
	1418	1348							1211	1508		
	1450	1377								1543		
	1470	1400								1622		
	1545	1465										
	1615	1498										
	1650	1508										
	1670	1525										
	1700	1553										
		1612										
		1630										
		1665										
		1698										

Table A.4b Bacteriochlorophyll a and Bacteriopheophytin a Vibrational Frequencies, Continued.

Reference	[205] Mattioli, et al.		[168] Lutz	[169] Diers & Bocian			[171] Czarnecki, et al.		[175] Zazubovich, et al.		[127] Rätsep, et al
Experiment Type	RR		RR	NIR RR			NIR RR		HB		ΔFLN
T	RT		10 K & 20 K	15 K			25 K		5 K		4.5 K
Molecule & Solvent	BChla	BPheoa	BChla	BChla	BChla	BChla	BChla	BPheoa	BChla, TEA	BChla, glycerol:water/LDAO	BChla, TEA
Band	Qy	Qy	Qx	B	Qx	Qy	Qy	Qy	Qy		Qy
λ_o (nm)	1064	1064	580	407	568	750	800	750	700 - 800		780.2
Vibrational Frequency (cm^{-1})	731	654	59	383	164	88	90	90	164	161	84
	893	720	93	567	190	164	126	126	192	195	167
	1016	874	135	752	257	190	154	137	236	238	13
	1119	932	174	908	288	235	166	150	260	285	191
	1139	993	195	930	310	257	181	163	286	341	214
	1158	1101		987	353	340	191	183	341	373	239
	1288	1133		1066	383	359	203	183	353	383	256
	1359	1238		1120	423	383	225	220	379	402	345
	1519	1549		1135	440	396	242	233	395	420	368
	1596	1582		1160	458	423	259	243	421	453	388
	1657	1618		1241	487	509	287	264	454	483	407
	1687	1670		1290	685	536	329	272	564	531	423
	1740	1703		1356	733	567	344	280	589	565	442
		1743		1534	800	581	359	328	676	592	473
				1553	864	655	363	338	725	676	506
				1614	908	685	375	356	744	711	565
					1033	733	383	372	760	724	587
					1120	776	393	383	774	742	623
					1135	800	405	393	787	760	684
					1340	843		420	836	772	696
					1544	864			858	787	710
					1614	908			882	799	727
						1182			915	839	776
						1290				864	803
						1382				886	845
						1527				915	858
						1614				932	890
										953	915
										977	967
										993	980
										1008	101
										1031	1019

										1047	166
										1062	1089
										1099	105
										1115	1117
										1141	1137
										1154	1158
										1175	1180
										1185	1190
										1223	1211
										1257	1229
										1287	1252
										1335	1289
										1351	1378
										1377	1466
										1388	1519

Table A.5a Vibrational Frequencies of the Bacterial Reaction Center

Reference	[205] Mattioli, et al.		[206] Shreve, et al.	[212] Nabedryk, et al.				[181] Mattioli, et al.		[222]Palaniappan, et al.				
Experiment Type	RR		NIR RR	FTIR				RR		RR				
T	RT		278 K	100 K				RT		200 K				
RC	R-26, Rh. Sphaeroides		R-26, Rh.sphaeroides	WT, Rh. Sphaeroides	L(L131)H	L(M160)H	L(L131)H + L(M260)H	R-26, Rh. Sphaeroides		2.4.1, Rh. Sphaeroides				
Band	P, Reduced	P, Oxidized	P-					P, Reduced	P, Oxidized	P, Reduced	B, Reduced	B, Oxidized	H, Reduced	H, Oxidized
λ_o (nm)	1064		850					1064		850	800	800	752	752
Vibrational Frequency (cm^{-1})	728	669	36	1402	1404	1403	1403	335	669	1463	1430	1449	1446	1447
	894	1306	71	1460	1459	1458	1459	565	1306	1488	1452	1461	1461	1467
	1014	1438	94	1479	1479	1480	1478	728	1348	1494	1480	1467	1473	1483
	1136	1407	127	1551	1552	1549	1550	894	1407	1514	1492	1483	1490	1500
	1143	1485	202	1573	1561	1575	1570	1013	1485	1530	1507	1500	1507	1506
	1528	1500	337	1645	1644	1644	1604	1135	1500	1540	1520	1518	1524	1523
	1576	1548	685	1683	1657	1664	1620	1528	1548	1561	1533	1524	1534	1533
	1584	1576	730	1692	1678	1678	1634	1607	1576	1566	1545	1543	1548	1551
	1607	1587	898	1705	1684	1696	1643	1620	1600	1591	1570	1573	1568	1560
	1620	1600		1713	1692	1718	1662	1653	1641	1613	1569	1595	1580	1568
	1653	1641		1752	1710	1752	1685	1679	1717	1628	1591	1599	1591	1587
	1679	1657			1753		1733	1691		1640	1610	1618	1612	1602
	1691	1681					1745	1734		1648	1626	1628	1620	1641
	1734	1697					1753	1740		1670	1641	1638	1631	1661
	1741	1717								1678	1652	1661	1640	1690
		1741								1697	1672	1683	1659	1700
										1719	1689	1690	1683	1714
										1744	1693	1718	1697	1724
											1697	1735	1703	1740
											1726		1719	
											1746		1722	
													1742	
													1750	

Table A.5b Vibrational Frequencies of the Bacterial Reaction Center, Continued.

Reference	[209] Palaniappan, et al.				[171] Czarnecki, et al.				[210] Czarnecki, et al.	
Experiment Type	RR				NIR RR				NIR RR	
T	200 K				25 K				25 K	
RC	WT, Rh. Sphaeroides		H(M202)L, Rh. Sphaeroides		H(M202)L	WT	H(M202)L	WT	2.4.1, Rh. sphaeroides	
Band	P	B	P	B	P-		B		P-	B
λo (nm)	865	800	865	800	865		800		894	805
Vibrational Frequency (cm^{-1})	72	60	60	58	60	72	58	60	72	87
	96	85	83	67	83	96	67	85	96	118
	129	114	114	82	114	129	82	114	130	135
	144	161	129	103	154	144	103	161	137	137
	179	183	144	114	183	179	114	183	141	163
	203	218	154	140	203	203	140	218	144	184
	236	229	183	160	232	236	160	229	178	187
	268	252	203	171	251	268	171	252	202	188
	291	274	232	181	268	291	181	274	236	220
	335	332	251	212	289	335	212	332	240	231
	364	355	268	223	335	364	223	355	252	240
	381	381	289	235	365	381	235	381	268	264
	417	397	335	254	377	417	254	397	291	294
		416	365	276	398		276	416	316	326
			377	315	417		315		326	355
			398	332			332		332	364
			417	350			350		364	384
				381			381		381	
				397			397			
				416			416			

Table A.5c Vibrational Frequencies of the Bacterial Reaction Center, Continued.

Reference	[214] Cherepy, et al.		[213] Cherepy, et al.								[189] Frolov, et al.			
Experiment Type	RR		RR								RR			
T	95 K	278 K	95 K	278 K	95 K	278 K	95 K	278 K	77 & RT	77 & RT	77 & RT	77 & RT
RC	R-26, Rh. sphaeroides		R-26, Rh. sphaeroides								R-26, Rh. sphaeroides			
Band	B		P		B		H		B, Oxidized		B, Reduced	
λo (nm)	800		870	850	800		760		800	810	800	810
Vibrational Frequency (cm^{-1})	84	117	36	33	85	122	90	563	187	185	187	187
	121	177	64	70	125	182	121	606	221	218	220	211
	160	212	82	96	159	217	139	620	234	234	232	219
	186	332	101	127	186	332	184	651	265	270	335	330
	219	355	132	145	219	355	209	673	292	293	356	355
	334	384	168	187	332	384	232	685	312	310	362	364
	358	397	179	204	357	569	282	713	335	329	382	383
	383	418	204	332	382	621	336	724	357	353	394	392
	398	436	262	484	566	682	359	735	363	363	417	398
	417	464	291	563	624	721	377	748	383	382	566	567
	436	478	332	586	685	731	397	765	393	391	583	584
	464	512	476	622	725	744	415	797	398	397	624	624
	479	569	520	685	735	761	567	844	417	417	684	685
	511	621	560	730	746	843	618	879	435	435	712	710
	568	682	577	900	843	892	629	897	446	445	726	727
	624	721	616	932	893	920	658	930	461	460	732	730
	685	731	688	1011	920	1002	692	972	479	477	736	735
	726	744	733	1050	943	1018	720	993	510	509	746	746
	736	761	763	1070	966	1064	728	1010	538	528	760	759
	747	843	780	1099	999	1114	737	1023	566	566	787	788
	765	892	790	1163	1022	1132	744	1050	584	584	799	890
	843	920	897	1257	1115	1158	753	1065	624	623	841	897
	894	947	926	1278	1133	1165	773	1103	654	654	847	927
	921	970	949		1162		794	1117	666	664	869	
	945	1002	970				839	1134	684	684	895	
	967	1018	1010				845	1161	705	705	966	
	1000	1064	1039				852	1230	712	711	999	
	1021	1114	1060				860		726	725	1062	
	1065	1132	1109				881		736	731	1163	
	1082	1158	1131				899		746	735		
	1101	1165	1154				921		761	746		
	1116		1170				929		787	760		
	1133		1195				935		799	786		
	1163		1255				969		830	797		
	1185		1283				980		840	825		
	1229		1609				998		847	839		
	1242		1618				1015		871	847		
	1269		1650				1056		895	869		
	1280		1681				1074		921	892		
	1302						1107		944	921		
	1336						1139		967	944		
	1346						1169		999	966		
	1369						1195		1010	999		
	1382						1215		1020	1009		
	1393						1233		1026	1019		
	1465						1312		1066	1026		
	1516						1374		1101	1065		

	1534						1392		1115	1101		
	1579						1469		1131	1115		
	1652								1162	1129		
	1673								1186	1158		
									1217	1186		
									1230	1217		
									1242	1229		
									1269	1242		
									1281	1269		
									1303	1282		
									1337	1303		
									1346	1337		
									1357	1343		
									1369	1357		
									1376	1368		
									1386	1376		
									1395	1386		
									1438	1395		
									1448	1435		
									1469	1447		
									1500	1468		
									1536	1519		
									1585	1535		
									1610	1582		
									1658	1610		
									1677	1650		
										1678		

APPENDIX B BRC SAMPLE CONSIDERATIONS

Section B.1 Sample Preparation

Both W(M250)V and DLL BRC mutants were provided to us by Chris Kirmaier and Dewey Holten at the University of Washington in St.Louis. The W(M250)V and DLL samples were grown and purified by Phil Laible at Argonne National Laboratory and Steven Boxer and Jessica (Chuang) Seeliger, respectively.

Both samples were kept in 10 mM Tris pH 7.8, 0.1% Deriphat 160-C buffer. Before each experiment, BRC samples were treated with 40 mM terbutryn, enough to achieve a 25:1 ratio to the BRC, and 400 mM sodium ascorbate, enough to achieve a 100:1 ratio with the BRC. Terbutryn is added to ensure that the $P^+Q_B^-$ state does not form as it binds competitively with free quinone [36]; there is a small chance that a small percentage of W(M250)V samples still have Q_A or that charge transfer may occur along the B-branch to Q_B. D_{LL} is also treated with terbutryn for consistency. Although charge separation does not occur along the A-branch in these samples there is a small chance that it could occur along the B-branch. Sodium ascorbate is added to the samples in order to reduce the P+ state between laser shots, ensuring that each successive pulse sequence is interacting with the sample in its ground state.

After adding the reagents, samples are left to sit at room temperature for 10 minutes to allow the terbutryn to react with the RCs; following this treatment the samples are run at 2,000 g for 2 minutes in a refrigerated centrifuge so as to form a pellet of undissolved terbutryn. Early experimental attempts showed that poorly dissolved terbutryn aggregates at low-temperatures causing significant scattering problems for optical experiments. The supernatant of the centrifuged mixture is extracted and two wash steps with 30 kDalton centrifuge filters are used to reconcentrate the sample to achieve high enough concentrations for experiments. Following sample reconcentration the sample is mixed with glycerol with a 1:1 (v/v) ratio to achieve a good quality glass upon freezing.

Several initial attempts at D_{LL} experiments at cryogenic temperatures were unsuccessful as the samples became opaque when cooled using our liquid nitrogen cryostat. The samples were prepared using the same solvents and reagents as the W(M250)V experiments so it was proposed that the samples may not be completely purified. Additional steps were added to the prep for finer filtration however this did not prevent the temperature-dependent opacity. We were eventually successful in performing cryogenic 2D experiments after finding the opacity was freezing rate dependent and that a good glass was formed when the sample was flash frozen.

Section B.2 Additional BRC Sample Preparation Notes:

- Vacuum grease used in preparing well sealed sample cells builds up on the cell windows over time and can trap solvent or water from wash steps, resulting in a cloudy opaque layer upon freezing. To avoid this problem sample cell windows should periodically be washed using toluene or benzene; vacuum grease is not soluble in most solvents typically used in cleaning optics.
- Sodium ascorbate should be prepared weekly as it degrades over time.

- Initial studies of the W(M250)V mutant at room temperature with stationary samples found that the BRCs were not performing charge transfer, or were closed with the P^+ stuck in a reduced state.
- O-phenanthroline was tested as an alternative to sodium ascorbate, but was found to be less effective in reducing P^+ between laser shots.
- Glycerol is very hygroscopic; if using glycerol in a sample preparation, draw "fresh" glycerol for each prep. from a container which should be sealed from the air.

Section B.3 W(M250)V/DLL BRC Sample Preparation Procedure

Components

- Treatment of RCs with Terbutryn for quinone removal/inactivation
- Treatment of RCs with sodium ascorbate for P+ reduction
- Reconcentration of RCs for proper OD

Chemicals to Gather/prepare

- 40 µM BRCs (concentration provided by Chris Kirmaier, concentration may be different than what is actually available; can measure this with an OD measurement)
- "Buffer A" – 10 mM Tris base, 0.1% Deriphat, pH 7.8
- 40 mM terbutryn in ethanol
- 400 mM sodium ascorbate in buffer A, prepare a fresh solution weekly
- Freshly drawn glycerol
- 3% Deriphat in buffer A

Equipment

- 10 μL, 100 μL, 1000 μL pipettes & corresponding tips
- Gloves
- Ice & Cooler
- Small tube racks
- 2 1.5 mL Eppendorf tubes
- 3 centrifuge filters (Amicon ultra – 0.5 mL filters)
- 6 centrifuge filter tubes (Amicon ultra – 0.5 mL filters)
- 2 small (~0.5 mL) Eppendorf tubes

Procedure

Notes: Save pipette tips and tubes which came in contact with RCs for washing/sample reclamation after the prep. Perform all prep steps in dim/dark lighting conditions; do not need to black out door windows. Sample is robust but it is better to err on the side caution.

1. Pull aliquots out of LN2 storage needed for the. Allow sample to thaw on ice in a cooler for however long it takes (typically ~5 hours).

Once samples thaw. In an Eppendorf tube:

2. place 500 μL buffer A and add 33.3 μL (for a OD(800 nm) ~= 0.3) of the 40 μM sample.
3. Add 5 μL of sodium ascorbate and 12.5 μL of terbutryn.
4. Allow solution to stand for 10 min at room temperature.
5. Set up the small centrifuge to cool to 4˚C. Centrifuge the Eppendorf for 5 min at 10,000 g (with balance Eppendorf). This step creates a pellet of undissolved terbutryn, which we suspect causes scatter problems.

First centrifuge filtration step:

6. Into a centrifuge filter (in filter tube), add 500 μL of the sample, avoiding the terbutryn pellet. Run this (with balance) for 5 min at 14,000 g.
7. Dump the filtered liquid at below the filter and add the remaining sample from the Eppendorf into the filter and run for 30 min at 14,000 g.
8. Into a second centrifuge tube, flip the filter with the concentrate. Run for 2 min at 1,000 g.
9. Add 500 μL of buffer A to the concentrated sample and add 5 μL sodium ascorbate.

Second centrifuge filtration step: Repeat steps 6-9.

Mixing final volume with glycerol:

10. Measure the concentrated sample while pipetting it into one of the small tubes. The final sample volume after concentration should be between 15 – 20 μL.
11. To the small tube, add equal volume glycerol.
12. Add 3% deriphat solution to the sample such that the final deriphat concentration is 0.1% (add no more than 1 μL, should be around 0.4 μL).
13. Hand mix this, flipping and rolling the tube. After sample is well mixed with glycerol, centrifuge for 1 min at 5,000 g to push sample to the bottom of the tube.
14. Load sample into sample cell and measure the OD. Note that the 77K OD will be roughly twice the RT OD. DLL has only been observed freezing well when frozen rapidly (dunked in LN2). Other possible sources of sample issues are related to the windows; vacuum grease is not soluble in most cleaning solutions we typically use.

APPENDIX C BACTERIOCHLOROPHYLL A SAMPLE CONSIDERATIONS

Section C.1 Sample Preparation

Bacteriochlorophyll a (BChla) sample preparation is fairly straightforward. Powdered BChla is purchased in a purified form from Sigma Aldrich. Powdered sample is measured using a scale as best as possible. This step is performed in room atmosphere. The sample is then moved to a pressurized N2 filled glove box where it is dissolved in the solvent desired to a higher concentration than the final desired concentration. The solvent must be degassed with N2 gas prior to sample preparation to remove any oxygen. The data presented in Chapter 4 was for BChla dissolved in isopropanol, but BChla dissolves well in alcohols and many other solvents [197]. The OD of the high-concentration stock sample is measured in a UV-Vis spectrometer to determine the concentration. A portion of this stock is diluted with additional solvent. Several alcohols will form a good glass upon freezing without addition of glycerol, but the sample cell must be sealed with epoxy to prevent evacuation of the sample cell during the cryostat pump-down procedure. Using a 5-minute quick setting epoxy around the seal of the sample cell works well and can be purchased from a hardware store.

Section C.2 Additional BChl a Preparation Notes

- BChla occasionally relaxes to a triplet state which can be transferred to an oxygen molecule, resulting in volatile oxygen radicals that can damage the BChla.

To avoid this, solvents used must be degassed of O2 by flowing N2 gas through the sample in a glove bag for approximately 10 minutes. BChla samples should be prepared and handled in a N2-pressurized glove bag.

- Samples contaminated with water are likely to form aggregates. Ensure windows and any preparation tools are completely dry. Aggregated samples can be identified by a shoulder on the red edge of the Qy band, broadening of the Qy band and decreased Qy band OD
- Glycerol is very hygroscopic; if using glycerol in a sample preparation, draw “fresh” glycerol for each prep. from a container which should be sealed from the air.

REFERENCES

[1] J. I. Priestley, Philos. Trans. **62**, p. 425 (1775).

[2] R. E. Blankenship, *Molecular Mechanisms of Photosynthesis* (Blackwell Science Ltd, Oxford, UK, 2008).

[3] J. Hecht, Appl. Opt. **49**, F99 (2010).

[4] A. Niedringhaus, V. R. Policht, R. Sechrist, A. Konar, P. D. Laible, D. F. Bocian, D. Holten, C. Kirmaier, and J. P. Ogilvie, Proc. Natl. Acad. Sci. **115**, 3563 (2018).

[5] M. H. Vos, J. C. Lambry, S. J. Robles, D. C. Youvan, J. Breton, and J. L. Martin, Proc. Natl. Acad. Sci. U. S. A. **88**, 8885 (1991).

[6] G. S. Engel, T. R. Calhoun, E. L. Read, T.-K. Ahn, T. Mančal, Y.-C. Cheng, R. E. Blankenship, and G. R. Fleming, Nature **446**, 782 (2007).

[7] G. D. Scholes, G. R. Fleming, L. X. Chen, A. Aspuru-Guzik, A. Buchleitner, D. F. Coker, G. S. Engel, R. van Grondelle, A. Ishizaki, D. M. Jonas, J. S. Lundeen, J. K. McCusker, S. Mukamel, J. P. Ogilvie, A. Olaya-Castro, M. A. Ratner, F. C. Spano, K. B. Whaley, and X. Zhu, Nature **543**, 647 (2017).

[8] G. D. Scholes, G. R. Fleming, A. Olaya-Castro, and R. van Grondelle, Nat. Chem. **3**, 763 (2011).

[9] I. McConnell, G. H. Li, and G. W. Brudvig, Chem. Biol. **17**, 434 (2010).

[10] E. Romero, V. I. Novoderezhkin, and R. van Grondelle, Nature **543**, 355 (2017).

[11] J. Otsuki, J. Mater. Chem. A **6**, 6710 (2018).

[12] D. M. Jonas, Annu. Rev. Phys. Chem. **54**, 425 (2003).

[13] A. Chenu and G. D. Scholes, Annu. Rev. Phys. Chem. **66**, 69 (2015).

[14] L. Valkunas, D. Abramavicius, and T. Mančal, *Molecular Excitation Dynamics and Relaxation* (Wiley-VCH Verlag GmbH & Co. KGaA, 2013).

[15] R. E. Blankenship, PLANT Physiol. **154**, 434 (2010).

[16] M. F. Hohmann-Marriott and R. E. Blankenship, Annu. Rev. Plant Biol **62**, 515 (2011).

[17] N. Y. Kiang, J. Siefert, Govindjee, and R. E. Blankenship, Astrobiology **7**, 222 (2007).

[18] T. Mirkovic, E. E. Ostroumov, J. M. Anna, R. van Grondelle, Govindjee, and G. D. Scholes, Chem. Rev. **117**, 249 (2017).

[19] S. Sadekar, J. Raymond, and R. E. Blankenship, Mol. Biol. Evol. **23**, 2001 (2006).

[20] F. Fassioli, A. Olaya-Castro, S. Scheuring, J. N. Sturgis, and N. F. Johnson, Biophys. J. **97**, 2464 (2009).

[21] M. K. Sener, J. D. Olsen, C. N. Hunter, and K. Schulten, Proc. Natl. Acad. Sci. U. S. A. **104**, 15723 (2007).

[22] G. D. Scholes and G. R. Fleming, J. Phys. Chem. B **104**, 1854 (2000).

[23] G. R. Fleming and R. Van Grondelle, Curr. Opin. Struct. Biol. **7**, 738 (1997).

[24] U. Ermler, G. Fritzsch, S. K. Buchanan, and H. Michel, Structure **2**, 925 (1994).

[25] S. Polyutov, O. Kühn, and T. Pullerits, Chem. Phys. **394**, 21 (2012).

[26] V. Butkus, D. Zigmantas, D. Abramavicius, and L. Valkunas, Chem. Phys. Lett. **587**, 93 (2013).

[27] X. J. Jordanides, G. D. Scholes, and G. R. Fleming, J. Phys. Chem. B **105**, 1652 (2001).

[28] L. Huang, G. P. Wiederrecht, L. M. Utschig, S. L. Schlesselman, C. Xydis, P. D. Laible, D. K. Hanson, and D. M. Tiede, Biochemistry **47**, 11387 (2008).

[29] M. A. Steffen, K. Lao, and S. G. Boxer, Science (80). **264**, 810 (1994).

[30] M. H. Vos, C. Rischel, M. R. Jones, and J. L. Martin, Biochemistry **39**, 8353 (2000).

[31] Z. Guo, S. Lin, and N. W. Woodbury, J. Phys. Chem. B **117**, 11383 (2013).

[32] J. P. Allen and J. C. Williams, J. Bioenerg. Biomembr. **27**, 275 (1995).

[33] J. Breton and A. Vermeglio, *The Photosynthetic Bacterial Reaction Center* (Springer US, Boston, MA, 1988).

[34] S. J. Robles, J. Breton, and D. C. Youvan, Source Sci. New Ser. **248**, 1402 (1990).

[35] J. I. Chuang, S. G. Boxer, D. Holten, and C. Kirmaier, Biochemistry **45**, 3845 (2006).

[36] P. D. Laible, C. Kirmaier, C. S. M. Udawatte, S. J. Hofman, D. Holten, and D. K. Hanson, Biochemistry **42**, 1718 (2003).

[37] J. Deisenhofer, O. Epp, K. Miki, R. Huber, and H. Michel, Nature **318**, 618 (1985).

[38] M. H. Stowell, T. M. McPhillips, D. C. Rees, S. M. Soltis, E. Abresch, and G. Feher, Science **276**, 812 (1997).

[39] K. M. Faries, L. L. Kressel, M. J. Wander, D. Holten, P. D. Laible, C. Kirmaier, and D. K. Hanson, J. Biol. Chem. **287**, 8507 (2012).

[40] K. M. Faries, N. P. Dylla, D. K. Hanson, D. Holten, P. D. Laible, and C. Kirmaier, J. Phys. Chem. B **121**, 6989 (2017).

[41] D. C. Arnett, C. C. Moser, P. L. Dutton, and N. F. Scherer, J. Phys. Chem. B **103**, 2014 (1999).

[42] G. Hartwich, H. Scheer, V. Aust, and A. Angerhofer, BBA - Bioenerg. **1230**, 97 (1995).

[43] S. R. Meech, A. J. Hoff, and D. A. Wiersma, Proc. Natl. Acad. Sci. **83**, 9464 (1986).

[44] O. Rancova, R. Jankowiak, A. Kell, M. Jassas, and D. Abramavicius, J. Phys. Chem. B **120**, 5601 (2016).

[45] T. Mančal, L. Valkunas, and G. R. Fleming, Chem. Phys. Lett. **432**, 301 (2006).

[46] W. Zinth and J. Wachtveitl, ChemPhysChem **6**, 871 (2005).

[47] R. S. Knox, Photosynth. Res. **48**, 35 (1996).

[48] R. van Grondelle, J. P. Dekker, T. Gillbro, and V. Sundstrom, Biochim. Biophys. Acta - Bioenerg. **1187**, 1 (1994).

[49] R. A. Friesner and Y. Won, Biochem. Biophys. Acta **977**, 99 (1989).

[50] C. Kirmaier and D. Holten, Photosynth. Res. **260**, 225 (1987).

[51] M. H. Vos, J. Breton, and J.-L. Martin, J. Phys. Chem. B **101**, 9820 (1997).

[52] M. E. Van Brederode, J. P. Ridge, I. H. M. Van Stokkum, F. Van Mourik, M. R. Jones, and R. Van Grondelle, Photosynth. Res. **55**, 141 (1998).

[53] L. Huang, N. Ponomarenko, G. P. Wiederrecht, and D. M. Tiede, Proc. Natl. Acad. Sci. **109**, 4851 (2012).

[54] S. Lin, J. Jackson, A. K. W. Taguchi, and N. W. Woodbury, J. Phys. Chem. B **102**, 4016 (1998).

[55] H. Zhou and S. G. Boxer, J. Phys. Chem. B **102**, 9139 (1998).

[56] M. H. Vos, F. Rappaport, J.-C. Lambry, J. Breton, and J. L. Martin, Nature **363**, 320 (1993).

[57] M. H. Vos and J. L. Martin, Biochim. Biophys. Acta - Bioenerg. **1411**, 1 (1999).

[58] H. Lee, Y.-C. Cheng, and G. R. Fleming, Science **316**, 1462 (2007).

[59] S. Westenhoff, D. Paleček, P. Edlund, P. Smith, and D. Zigmantas, J. Am. Chem. Soc. **134**, 16484 (2012).

[60] I. S. Ryu, H. Dong, and G. R. Fleming, J. Phys. Chem. B **118**, 1381 (2014).

[61] D. Paleček, P. Edlund, S. Westenhoff, and D. Zigmantas, Sci. Adv. **3**, e1603141 (2017).

[62] M. L. Flanagan, P. D. Long, P. D. Dahlberg, B. S. Rolczynski, S. C. Massey, and G. S. Engel, J. Phys. Chem. A **120**, 1479 (2016).

[63] F. Ma, E. Romero, M. R. Jones, V. I. Novoderezhkin, and R. van Grondelle, J. Phys. Chem. Lett. 1827 (2018).

[64] G. Panitchayangkoon, D. Hayes, K. A. Fransted, J. R. Caram, E. Harel, J. Wen, R. E. Blankenship, and G. S. Engel, Proc. Natl. Acad. Sci. U. S. A. **107**, 12766 (2010).

[65] J. R. Caram, N. H. C. Lewis, A. F. Fidler, and G. S. Engel, J. Chem. Phys. **136**, 104505 (2012).

[66] B. S. Rolczynski, H. Zheng, V. P. Singh, P. Navotnaya, A. R. Ginzburg, J. R. Caram, K. Ashraf, A. T. Gardiner, S. H. Yeh, S. Kais, R. J. Cogdell, and G. S. Engel, Chem **4**, 138 (2018).

[67] A. Nemeth, F. Milota, T. Mančal, V. Lukeš, H. F. Kauffmann, and J. Sperling, Chem. Phys. Lett. **459**, 94 (2008).

[68] P. F. Tekavec, J. a Myers, K. L. M. Lewis, and J. P. Ogilvie, Opt. Lett. **34**, 1390 (2009).

[69] N. Christensson, H. F. Kauffmann, T. Pullerits, and T. Mančal, J. Phys. Chem. B

116, 7449 (2012).

[70] V. Tiwari, W. K. Peters, and D. M. Jonas, Proc. Natl. Acad. Sci. U. S. A. **110**, 1203 (2013).

[71] F. D. Fuller, J. Pan, A. Gelzinis, V. Butkus, S. S. Senlik, D. E. Wilcox, C. F. Yocum, L. Valkunas, D. Abramavicius, and J. P. Ogilvie, Nat. Chem. **6**, 706 (2014).

[72] E. Romero, R. Augulis, V. I. Novoderezhkin, M. Ferretti, J. Thieme, D. Zigmantas, and R. van Grondelle, Nat. Phys. **10**, 676 (2014).

[73] E. Collini, C. Y. Wong, K. E. Wilk, P. M. G. Curmi, P. Brumer, and G. D. Scholes, Nature **463**, 644 (2010).

[74] K. Hoki and P. Brumer, in *Procedia Chem.* (2011), pp. 122–131.

[75] P. Brumer and M. Shapiro, Proc. Natl. Acad. Sci. U. S. A. **109**, 19575 (2012).

[76] A. A. Bakulin, S. E. Morgan, T. B. Kehoe, M. W. B. Wilson, A. W. Chin, D. Zigmantas, D. Egorova, and A. Rao, Nat. Chem. **8**, 16 (2016).

[77] S. S. Senlik, V. R. Policht, and J. P. Ogilvie, J. Phys. Chem. Lett. **6**, 2413 (2015).

[78] S. Yue, Z. Wang, X. Leng, R. Zhu, H. Chen, and Y. Weng, Chem. Phys. Lett. **683**, 591 (2017).

[79] J. D. Hybl, A. W. Albrecht, S. M. Gallagher Faeder, and D. M. Jonas, Chem. Phys. Lett. **297**, 307 (1998).

[80] L. Lepetit, G. Chériaux, and M. Joffre, J. Opt. Soc. Am. B **12**, 2467 (1995).

[81] R. Boyd, in 3rd ed. (Academic Press, San Diego, 2003), p. 578.

[82] A. Weiner, *Ultrafast Optics IV* (Springer New York, New York, NY, 2004).

[83] P. Berman and V. S. Malinovsky, *Principles of Laser Spectroscopy and Quantum Optics* (Princeton University Press, 2011).

[84] S. Mukamel, *Principles of Nonlinear Optical Spectroscopy*, 1st ed. (Oxford University Press, New York, 1995).

[85] M. T. Zanni and R. M. Hochstrasser, Curr. Opin. Struct. Biol. **11**, 516 (2001).

[86] M. Cho, Chem. Rev. **108**, 1331 (2008).

[87] J. A. Myers, K. L. Lewis, P. F. Tekavec, and J. P. Ogilvie, Opt. Express **16**, 17420

(2008).

[88] F. D. Fuller and J. P. Ogilvie, Annu. Rev. Phys. Chem. **66**, 667 (2015).

[89] J. P. Ogilvie, M. L. Cowan, M. Armstrong, A. Nagy, and R. J. D. Miller, Ultrafast Phenom. Xiii **71**, 571 (2003).

[90] J. P. Ogilvie and K. J. Kubarych, in *Adv. At. Mol. Opt. Phys.* (2009), pp. 249–321.

[91] F. D. Fuller, D. E. Wilcox, and J. P. Ogilvie, Opt. Express **22**, 1018 (2014).

[92] A. M. Siddiqui, G. Cirmi, D. Brida, F. X. Kärtner, and G. Cerullo, Opt. Lett. **34**, 3592 (2009).

[93] A. Niedringhaus, Dissertation 12 (2017).

[94] G. S. Schlau-Cohen, A. Ishizaki, T. R. Calhoun, N. S. Ginsberg, M. Ballottari, R. Bassi, and G. R. Fleming, Nat. Chem. **4**, 389 (2012).

[95] T. Wilhelm, J. Piel, and E. Riedle, Opt. Lett. **22**, 1494 (1997).

[96] J. Breton, J. L. Martin, G. R. Fleming, and J. C. Lambry, Biochemistry **27**, 8276 (1988).

[97] M. H. Vos, M. R. Jones, C. N. Hunter, J. Breton, and J. L. Martin, Proc. Natl. Acad. Sci. U. S. A. **91**, 12701 (1994).

[98] M. H. Vos, M. R. Jones, C. N. Hunter, J. Breton, J. C. Lambry, and J. L. Martin, Biochemistry **33**, 6150 (1994).

[99] M. H. Vos, M. R. Jones, P. McGlynn, C. N. Hunter, J. Breton, and J. L. Martin, Biochim. Biophys. Acta - Bioenerg. **1186**, 117 (1994).

[100] R. J. Stanley and S. G. Boxer, J. Phys. Chem. **99**, 859 (1995).

[101] D. M. Jonas, M. J. Lang, Y. Nagasawa, T. Joo, and G. R. Fleming, J. Phys. Chem. **100**, 12660 (1996).

[102] M. H. Vos, M. R. Jones, and J. L. Martin, Chem. Phys. **233**, 179 (1998).

[103] C. Rischel, D. Spiedel, J. P. Ridge, M. R. Jones, J. Breton, J. C. Lambry, J. L. Martin, and M. H. Vos, Proc. Natl. Acad. Sci. U. S. A. **95**, 12306 (1998).

[104] V. a. Shuvalov and a. G. Yakovlev, FEBS Lett. **540**, 26 (2003).

[105] M. Chachisvilis, H. Fidder, T. Pullerits, and V. Sundström, J. Raman Spectrosc. **26**,

513 (1995).

[106] G. Panitchayangkoon, D. V. Voronine, D. Abramavicius, J. R. Caram, N. H. C. Lewis, S. Mukamel, and G. S. Engel, Proc. Natl. Acad. Sci. **108**, 20908 (2011).

[107] R. Hildner, D. Brinks, J. B. Nieder, R. J. Cogdell, and N. F. van Hulst, Science (80-.). **340**, 1448 (2013).

[108] M. Maiuri, E. E. Ostroumov, R. G. Saer, R. E. Blankenship, and G. D. Scholes, Nat. Chem. **10**, 177 (2018).

[109] E. Thyrhaug, R. Tempelaar, M. Alcocer, K. Žídek, D. Bína, J. Knoester, T. L. C. Jansen, and D. Zigmantas, 1 (2017).

[110] A. P. Spencer, W. O. Hutson, and E. Harel, Nat. Commun. **8**, 14732 (2017).

[111] D. C. Arnett, T.-S. Yang, and N. F. Scherer, in *Seventh Int. Conf. Time-Resolved Vib. Spectrosc.* (Los Alamos Naitonal Labs: Sante Fe, NM, 1997), pp. 131–135.

[112] D. C. Arnett, L. D. Book, C. C. Moser, P. L. Dutton, and N. F. Scherer, Laser Chem. **19**, 195 (1999).

[113] K. R. Shelly, E. C. Golovich, and W. F. Beck, J. Phys. Chem. B **110**, 20586 (2006).

[114] J. Du, T. Teramoto, K. Nakata, E. Tokunaga, and T. Kobayashi, Biophys. J. **101**, 995 (2011).

[115] K. A. Fransted, J. R. Caram, D. Hayes, and G. S. Engel, J. Chem. Phys. **137**, 125101 (2012).

[116] R. Moca, S. R. Meech, and I. a. Heisler, J. Phys. Chem. B **119**, 8623 (2015).

[117] E. Collini and G. D. Scholes, Science **323**, 369 (2009).

[118] E. Thyrhaug, S. A. Bogh, M. R. Carro-Temboury, C. S. Madsen, T. Vosch, D. Zigmantas, C. Stahl Madsen, T. Vosch, and D. Zigmantas, Nat. Commun. **8**, 15577 (2017).

[119] Y. Song, C. Hellmann, N. Stingelin, and G. D. Scholes, J. Chem. Phys. **142**, (2015).

[120] J. Seibt, T. Hansen, and T. Pullerits, J. Phys. Chem. B **117**, 11124 (2013).

[121] D. Egorova, Chem. Phys. **347**, 166 (2008).

[122] V. Butkus, L. Valkunas, and D. Abramavicius, J. Chem. Phys. **137**, 44513 (2012).

[123] V. Perlík, C. Lincoln, F. Sanda, J. Hauer, and F. Šanda, J. Phys. Chem. Lett. **5**, 404 (2014).

[124] D. A. Farrow, E. R. Smith, W. Qian, and D. M. Jonas, J. Chem. Phys. **129**, 174509 (2008).

[125] T. Mančal, A. Nemeth, F. Milota, V. Lukeš, H. F. Kauffmann, and J. Sperling, J. Chem. Phys. **132**, 184515 (2010).

[126] V. Butkus, D. Zigmantas, L. Valkunas, and D. Abramavicius, Chem. Phys. Lett. **545**, 40 (2012).

[127] M. Rätsep, Z.-L. L. Cai, J. R. Reimers, and A. Freiberg, J. Chem. Phys. **134**, 24506 (2011).

[128] E. J. Peterman, S. O. Wenk, T. Pullerits, L. O. Pâlsson, R. van Grondelle, J. P. Dekker, M. Rögner, and H. van Amerongen, Biophys. J. **75**, 389 (1998).

[129] M. Rätsep, J. Linnanto, and A. Freiberg, J. Chem. Phys. **130**, 194501 (2009).

[130] J. L. Hughes, B. Conlon, T. Wydrzynski, and E. Krausz, Phys. Procedia **3**, 1591 (2010).

[131] R. A. Avarmaa and K. K. Rebane, Spectrochim. Acta Part A Mol. Spectrosc. **41**, 1365 (1985).

[132] E. L. Read, H. Lee, and G. R. Fleming, Photosynth. Res. **101**, 233 (2009).

[133] H. van Amerongen, R. van Grondelle, and L. Valkunas, *Photosynthetic Excitons* (WORLD SCIENTIFIC, 2000).

[134] T. Mančal and L. Valkunas, New J. Phys. **12**, 65044 (2010).

[135] T. Mančal, N. Christensson, V. Lukeš, F. Milota, O. Bixner, H. F. Kauffmann, and J. Hauer, J. Phys. Chem. Lett. **3**, 1497 (2012).

[136] D. Egorova, J. Chem. Phys. **140**, 212452 (2014).

[137] V. Butkus, L. Valkunas, and D. Abramavicius, J. Chem. Phys. **140**, 34306 (2014).

[138] S. Savikhin, D. R. Buck, and W. S. Struve, Chem. Phys. **223**, 303 (1997).

[139] H.-G. Duan, V. I. Prokhorenko, R. J. Cogdell, K. Ashraf, A. L. Stevens, M. Thorwart, and R. J. D. Miller, Proc. Natl. Acad. Sci. **114**, 8493 (2017).

[140] M. Ferretti, V. I. Novoderezhkin, E. Romero, R. Augulis, A. Pandit, D. Zigmantas,

and R. van Grondelle, Phys. Chem. Chem. Phys. **16**, 9930 (2014).

[141] J. M. Womick and A. M. Moran, J. Phys. Chem. B **115**, 1347 (2011).

[142] A. Chenu, N. Christensson, H. F. Kauffmann, and T. Mančal, Sci. Rep. **3**, 2029 (2013).

[143] V. Butkus, A. Gelzinis, R. Augulis, A. Gall, C. Büchel, B. Robert, D. Zigmantas, L. Valkunas, and D. Abramavicius, J. Chem. Phys. **142**, 212414 (2015).

[144] V. Perlík, J. Seibt, L. J. Cranston, R. J. Cogdell, C. N. Lincoln, J. Savolainen, F. Šanda, T. Mančal, and J. Hauer, J. Chem. Phys. **142**, 212434 (2015).

[145] V. Perlík and F. Šanda, J. Chem. Phys. **147**, 84104 (2017).

[146] V. Butkus, J. Alster, E. Bašinskaitė, R. Augulis, P. Neuhaus, L. Valkunas, H. L. Anderson, D. Abramavicius, and D. Zigmantas, J. Phys. Chem. Lett. **8**, 2344 (2017).

[147] A. W. Chin, J. Prior, R. Rosenbach, F. Caycedo-Soler, S. F. Huelga, and M. B. Plenio, Nat. Phys. **9**, 113 (2013).

[148] M. Khalil, N. Demirdöven, A. Tokmakoff, N. Demirdöven, and A. Tokmakoff, J. Chem. Phys. **121**, 362 (2004).

[149] F. Ding, E. C. Fulmer, and M. T. Zanni, J. Chem. Phys. **123**, 94502 (2005).

[150] A. J. Musser, M. Liebel, C. Schnedermann, T. Wende, T. B. Kehoe, A. Rao, and P. Kukura, Nat. Phys. **11**, 352 (2015).

[151] J. Brazard, L. A. Bizimana, T. Gellen, W. P. Carbery, and D. B. Turner, J. Phys. Chem. Lett. **7**, 14 (2016).

[152] Z. Guo, B. P. Molesky, T. P. Cheshire, and A. M. Moran, Top. Curr. Chem. **375**, 87 (2017).

[153] K. Hyeon-Deuk, Y. Tanimura, and M. Cho, J. Chem. Phys. **127**, 75101 (2007).

[154] M. H. Vos, M. R. Jones, J. Breton, J. C. Lambry, and J. L. Martin, Biochemistry **35**, 2687 (1996).

[155] S. Savikhin and W. S. Struve, Biophys. J. **67**, 2002 (1994).

[156] F. D. Fuller, Observations of Coherence in Oxygenic Photosynthesis, University of Michigan, 2014.

[157] F. V De, A. Camargo, L. Grimmelsmann, H. L. Anderson, S. R. Meech, I. A. Heisler, F. V. D. A. Camargo, L. Grimmelsmann, H. L. Anderson, S. R. Meech, and I. A. Heisler, Phys. Rev. Lett. **118**, 33001 (2017).

[158] R. Tempelaar, A. Halpin, P. J. M. Johnson, J. Cai, R. S. Murphy, J. Knoester, R. J. D. Miller, and T. L. C. Jansen, J. Phys. Chem. A **120**, 3042 (2016).

[159] S. Rafiq and G. D. Scholes, J. Phys. Chem. A **120**, 6792 (2016).

[160] S. Rafiq, J. C. Dean, and G. D. Scholes, J. Phys. Chem. A **119**, 11837 (2015).

[161] V. I. Novoderezhkin, E. Romero, J. Prior, and R. van Grondelle, Phys. Chem. Chem. Phys. **19**, 5195 (2017).

[162] A. Volpato and E. Collini, Opt. Express **23**, 20040 (2015).

[163] M. Lutz, J. Kleo, and F. Reiss-Husson, Biochem. Biophys. Res. Commun. **69**, 711 (1976).

[164] T. M. Cotton and R. P. Van Duyne, J. Am. Chem. Soc. **103**, 6020 (1981).

[165] M. Lutz, in *Adv. Infrared Raman Spectrosc. 11*, edited by R. J. H. Clark and R. E. Hester (Wiley Heyden, 1984), pp. 211–300.

[166] R. J. Donohoe, H. A. Frank, and D. F. Bocian, Photochem. Photobiol. **48**, 531 (1988).

[167] J. R. Diers and D. F. Bocian, J. Phys. Chem **98**, 12884 (1994).

[168] M. Lutz, Biospectroscopy **1**, 313 (1995).

[169] J. R. Diers and D. F. Bocian, J. Am. Chem. Soc. **117**, 6629 (1995).

[170] A. Ivancich, M. Lutz, and T. A. Mattioli, Biochemistry **36**, 3242 (1997).

[171] K. Czarnecki, J. R. Diers, V. Chynwat, J. P. Erickson, H. a. Frank, and D. F. Bocian, J. Am. Chem. Soc. **119**, 415 (1997).

[172] Y. Koyama and L. Limantara, Spectrochim. Acta Part A Mol. Biomol. Spectrosc. **54**, 1127 (1998).

[173] J. R. Diers, Q. Tang, C. J. Hondros, C.-Y. Chen, D. Holten, J. S. Lindsey, and D. F. Bocian, J. Phys. Chem. B **118**, 7520 (2014).

[174] A. Gall, A. a. Pascal, and B. Robert, Biochim. Biophys. Acta **1847**, 12 (2014).

[175] V. Zazubovich, I. Tibe, and G. J. Small, J. Phys. Chem. B **105**, 12410 (2001).

[176] J. R. Reimers, Z.-L. Cai, R. Kobayashi, M. Rätsep, A. Freiberg, and E. Krausz, Sci. Rep. **3**, 2761 (2013).

[177] M. Gouterman, J. Mol. Spectrosc. **6**, 138 (1961).

[178] K. Ballschmiter and J. J. Katz, J. Am. Chem. Soc. **91**, 2661 (1969).

[179] T. A. Evans and J. J. Katz, Biochim. Biophys. Acta - Bioenerg. **396**, 414 (1975).

[180] M. Fujiwara and M. Tasumi, J. Phys. Chem. **90**, 250 (1986).

[181] T. A. Mattioli, A. Hoffmann, D. G. Sockalingum, B. Schrader, B. Robert, and M. Lutz, Spectrochim. Acta Part A Mol. Spectrosc. **49**, 785 (1993).

[182] K. Ballschmiter and J. Katz, Biochim. Biophys. Acta - Bioenerg. **256**, 307 (1972).

[183] J. R. Kincaid, L. M. Proniewicz, K. Bajdor, A. Bruha, and K. Nakamoto, J. Am. Chem. Soc. **107**, 6775 (1985).

[184] M. Lutz and J. Kleo, Biochim. Biophys. Acta - Bioenerg. **546**, 365 (1979).

[185] A. K. Mandal, M. Taniguchi, J. R. Diers, D. M. Niedzwiedzki, C. Kirmaier, J. S. Lindsey, D. F. Bocian, and D. Holten, J. Phys. Chem. A **120**, 9719 (2016).

[186] K. K. Rebane, *Impurity Spectra of Solids: Elementary Theory of Vibrational Structure*, 1st ed. (Springer US, Boston, MA, 1970).

[187] J. Pieper, J. Voigt, and G. J. Small, J. Phys. Chem. B **103**, 2319 (1999).

[188] C. W. Müller, J. J. Newby, C.-P. Liu, C. P. Rodrigo, and T. S. Zwier, Phys. Chem. Chem. Phys. **12**, 2331 (2010).

[189] D. Frolov, A. Gall, M. Lutz, and B. Robert, J. Phys. Chem. A **106**, 3605 (2002).

[190] A. M. Kelley, *Spectroscopy and Condensed-Phase Molecular Spectroscopy and Photophysics* (Wiley, 2013).

[191] G. M. Sando, K. G. Spears, J. T. Hupp, and P. T. Ruhoff, J. Phys. Chem. A **105**, 5317 (2001).

[192] R. Gnanasekaran, Chem. Phys. Lett. **587**, 61 (2013).

[193] T. Fuji, T. Saito, and T. Kobayashi, Chem. Phys. Lett. **332**, 324 (2000).

[194] J. A. Shelnutt, L. D. Cheung, R. C. C. Chang, N.-T. Yu, and R. H. Felton, J. Chem. Phys. **66**, 3387 (1977).

[195] D. E. Wilcox and J. P. Ogilvie, J. Opt. Soc. Am. B **31**, 1544 (2014).

[196] B. Hou, J. H. Easter, J. A. Nees, Z. He, A. G. R. Thomas, and K. Krushelnick, Opt. Lett. **37**, 1385 (2012).

[197] J. Connolly, B. Samuel, and A. Frederick, Photochem. Photobiol. **36**, 565 (1982).

[198] M. Chachisvilis, H. Fidder, T. Pullerits, and V. Sundstrom, J. Raman Spectrosc. **26**, 513 (1995).

[199] T. G. Spiro and J. M. Burke, J. Am. Chem. Soc. **98**, 5482 (1976).

[200] C. Veas and J. L. McHale, J. Am. Chem. Soc. **111**, 7042 (1989).

[201] A. S. Rury, L. E. Goodrich, M. G. I. Galinato, N. Lehnert, and R. J. Sension, J. Phys. Chem. A **116**, 8321 (2012).

[202] J. I. Chuang, S. G. Boxer, D. Holten, and C. Kirmaier, J. Phys. Chem. B **112**, 5487 (2008).

[203] N. P. Dylla, K. M. Faries, R. M. Wyllie, A. M. Swenson, D. K. Hanson, D. Holten, C. Kirmaier, and P. D. Laible, FEBS Lett. **590**, 2515 (2016).

[204] C. Kirmaier, D. Holten, and W. W. Parson, Biochim. Biophys. Acta - Bioenerg. **810**, 49 (1985).

[205] T. A. Mattioli, A. Hoffmann, B. Robert, B. Schrader, and M. Lutz, Biochemistry **30**, 4648 (1991).

[206] A. P. Shreve, N. J. Cherepy, S. Franzen, S. G. Boxer, and R. a Mathies, Proc. Natl. Acad. Sci. **88**, 11207 (1991).

[207] N. J. Cherepy, A. P. Shreve, L. J. Moore, S. Franzen, S. G. Boxer, and R. A. Mathies, J. Phys. Chem. **98**, 6023 (1994).

[208] T. A. Mattioli, J. C. Williams, J. P. Allen, and B. Robert, Biochemistry **33**, 1636 (1994).

[209] V. Palaniappan, C. C. Schenck, and D. F. Bocian, J. Phys. Chem. **99**, 17049 (1995).

[210] K. Czarnecki, V. Chynwat, J. P. Erickson, H. A. Frank, and D. F. Bocian, J. Am. Chem. Soc. **119**, 2594 (1997).

[211] N. J. Cherepy, A. P. Shreve, L. J. Moore, S. G. Boxer, and R. A. Mathies, J. Phys. Chem. B **101**, 3250 (1997).

[212] E. Nabedryk, J. P. Allen, a K. Taguchi, J. C. Williams, N. W. Woodbury, and J. Breton, Biochemistry **32**, 13879 (1993).

[213] N. J. Cherepy, A. P. Shreve, L. J. Moore, S. G. Boxer, and R. A. Mathies, Biochemistry **36**, 8559 (1997).

[214] N. J. Cherepy, Electronic and Nuclear Dynamics of the Bacterial Photosynthetic Reaction Center and Chlorosomes from Resonance Raman Intensities, University of California, Berkeley, 1996.

[215] E. E. Ostroumov, R. M. Mulvaney, R. J. Cogdell, and G. D. Scholes, Science (80-.). **340**, 52 (2013).

[216] K. L. M. Lewis, Two-Dimensional Electronic Spectroscopy of the Photosystem II D1D2-Cyt. b559 Reaction Center Complex: Experiment and Simulation, University of Michigan, 2011.

[217] H. S. Kang, N. N. Esemoto, J. R. Diers, D. M. Niedzwiedzki, J. A. Greco, J. Akhigbe, Z. Yu, C. Pancholi, G. Viswanathan Bhagavathy, J. K. Nguyen, C. Kirmaier, R. R. Birge, M. Ptaszek, D. Holten, and D. F. Bocian, J. Phys. Chem. A **120**, 379 (2016).

[218] A. Loukianov, Development of Two-Dimensional Stark Spectroscopy for the Investigation of Photosynthetic Charge Separation, University of Michigan, 2017.

[219] A. Loukianov, A. Niedringhaus, B. Berg, J. Pan, S. S. Senlik, and J. P. Ogilvie, J. Phys. Chem. Lett. **8**, 679 (2017).

[220] S. Westenhoff and D. Paleček, J. … (2012).

[221] I. Renge, K. Mauring, and R. Avarmaa, J. Lumin. **37**, 207 (1987).

[222] V. Palaniappan, P. C. Martin, V. Chynwat, H. A. Frank, and D. F. Bocian, J. Am. Chem. Soc. **115**, 12035 (1993).